Unsteady Nonlinear Aerodynamic Modeling and Applications

Mohamed Y. Zakaria

Dissertation submitted to the Faculty of the
Virginia Polytechnic Institute and State University
in partial fulfillment of the requirements for the degree of

Doctor of Philosophy
in
Engineering Mechanics

Muhammad R. Hajj, Chair
Saad A. Ragab
Robert A. Canfield
Maurush Patil

March 4, 2016
Blacksburg, Virginia

Keywords: Unsteady nonlinear aerodynamics, Wind tunnel testing, Flow Visualization, Frequency response, Flutter, Energy Harvesting, High angles of attack and Flapping flight

Unsteady Nonlinear Aerodynamic Modeling and Applications

Mohamed Y. Zakaria

Abstract

Unsteady aerodynamic modeling is indispensable in the design process of rotary air vehicles, flapping flight and agile unmanned aerial vehicles. Undesirable vibrations can cause high frequency variations in motion variables whose effects cannot be well predicted using quasi-steady aerodynamics. Furthermore, one may exploit the lift enhancement that can be generated through unsteady motion for optimum design of flapping vehicles. Additionally, undesirable phenomena like flutter and ensuing limit cycle oscillations can be exploited for harvesting energy. In this dissertation, we focus on modeling the unsteady nonlinear aerodynamic response and present various applications where unsteady aerodynamics are very relevant.

The dissertation starts with experiments for measuring unsteady loads on a NACA-0012 airfoil undergoing a plunging motion under various operating conditions. We supplement these measurements with flow visualization to obtain better insight into phenomena causing enhanced lift. For the model, we present the frequency response function for the airfoil at various angles of attack. Experiments were performed at reduced frequencies between 0.1 and 0.95 and angles of attack up to 65°. Then, we formulate an optimization problem to unify the transfer function coefficients for each regime independently to obtain one model that represents the global dynamics. An optimization-based finite-dimensional (fourth-order) approximation for the frequency responses is developed. Converting these models to state-space form and writing the entries of the matrices as polynomials in the mean angle of attack, a unified unsteady model was developed. In a second set of experiments, we measured the unsteady plunging forces on the same airfoil at zero forward velocity. The aim is to investigate variations of the added forces associated with the oscillation frequency of the wing section for various angles of attack. Data of the measured forces are presented and compared with

predicted forces from potential flow approximations. The results show a significant departure from those estimates, specially at high frequencies indicating that viscous effects play a major role in determining these forces.

In the second part of this dissertation, we consider different applications where unsteady loads and nonlinear effects play an important role. We perform a multi-objective aerodynamic optimization problem of the wing kinematics and planform shape of a *Pterosaur replica* ornithopter. The objective functions included minimization of the required cycle-averaged aerodynamic power and maximization of the propulsive efficiency. The results show that there is an optimum kinematic parameter as well as planform shape to fulfill the two objectives. Furthermore, the effects of preset angle of attack, wind speed and load resistance on the levels of harvested power from a composite beam bonded with piezoelectric patch are determined experimentally. The results point to a complex relation between the aerodynamic loading and its impact on the static deflection and amplitudes of the limit cycle oscillations as well as the level of power harvested. This is followed by testing of a centimeter scale micro wind turbine that has been proposed to power small devices and to work as a micro energy harvester. The experimental measurements are compared to predicted values from a numerical model.

The methods developed in this dissertation provide a systematic approach to identify unsteady aerodynamic models from numerical or experimental data that may work within different regimes. The resulting reduced-order models are expressed in a state-space form, and they are, therefore, both simple and efficient. These models are low-dimensional linear systems of ordinary differential equations, so that they are compatible with modern flight dynamic models. The specific form of the obtained added force model, which defines the added forces as function of plunging velocity and drag forces, guarantees that the resulting model is accurate over a range of high frequencies. Moreover, presented applications give a sense of the broad range of application of unsteady aerodynamics.

Acknowledgments

Completion of this study would have been impossible for me without the guidance from my advisor and colleagues and splendid teamwork spirit of Virginia Tech.

My greatest thanks are to my advisor, Prof. Muhammad Hajj, who has been both a role model and a source of encouragement and guidance throughout my time at Virginia Tech. Prof. Hajj has provided a supportive environment that has allowed me to explore my interests. I am grateful for his patience and optimism about my work as well as for giving me the freedom to work with other professors. Prof. Hajj taught me *seeing the unobvious* while explaining my results and projecting those observations to determine underpinning physics of observed responses or measured data.

It was a great honor for me to have the chance to work with Prof. Saad Ragab, whose mind-provoking comments and guidance considerably helped me in my academic pursuit. A Salute to Prof. Robert Canfield who always opened his office door for me and certainly enhanced my knowledge about aeroelasticity and optimization. He also gave me precious advice about my present and future research goals. Special thanks also go to Prof. Mayuresh Patil who always welcomed me to discuss any technical issue at any time. I always appreciated his comments and questions.

Special thanks and appreciation go to Dr. Haithem Taha for his support and guidance. He has been always there to motivate and discuss many technical problems. We spent a plenty of time to complete a lot of scientific puzzles related to my research which lead to open a lot of fruitful discussions to solve problems I faced in my work. I would like to also thank Prof. Craig Woolsey for giving me the opportunity to attend the weekly meetings for his research group. I learned a lot from the thorough discussions while attending these

meetings. Through these meetings and collaborations, I had great pleasure in working with David Allen Allen and Dr. Sevak Tahmasian.

I enjoyed sharing the office with several colleagues. Specially worth noting are Allen Hammak, Daniel Periera, Ahmed Hussein, Peter Noelen, Kedar Vaidya, Farid Jafari and Dr Mostafa Ibrahim with whom I spent most of my time during my PhD studies. Thanks also to Mohamed Zein who shared with me a lot of classes and for his support. Also, I have much fun studying days and nights with my dearest friends in Blacksburg who made my stay at Virginia Tech a great experience, Mohamed Elbadawy, Sherif AbdelHamid and Abdallah Elgohary. I also enjoyed our semi-regular Soccer playing and Wollyball. Working in the wind tunnel laboratory has truly been a pleasure. I especially enjoyed the time spent with current and former lab mates, who have taught me a great deal: They are Mohammad Haik, Kenneth Brown and Chris Denny.

I was very fortunate to visit the University of Sao Poalo and work with Dr. Flavio Marques in his wind tunnel laboratory. Conducting experiments with Daniel Periera (the fighter) was a highlight of my graduate work, in addition to working together for six month at Virginia Tech. I owe thanks to Mag. Gen. Khaled Megawer and Lt. Col. Tamer Maher for their consistent encouragement and support that made me feel safe while working towards my degree. I really enjoyed working with my colleagues from MTC, Ahmed Eliethy, Karim Taha and Tamer Saaed who were always available for help and support.

All of my love and thanks go to my wife; her love and support have not wavered. Without her fortitude I would not have been able to make it. My love goes also to our lovely daughters, Laila and Rokaya for giving me the space to work and being patient for my absence. Thanks to my loving parents Mom, Dad and my sisters, who were my first and greatest teachers. I would not be where I am without the love and support of my family.

At the end, I pray to Almighty Allah, who bestowed all of His blessings on me, to give me the strength and wisdom to use this knowledge the way He wants.

Contents

List of Figures

List of Tables

Nomenclature

AR	Wing aspect ratio
a	Minor axis of ellipse (m)
c	Airfoil chord $2b$ (m)
C_L, C_D, C_M	Lift, drag and pitching moment coefficients
$C(k)$	Unsteady aerodynamic deficiency function
D	Diameter
e	Error between measured and optimized values
E	Expectation
$\widehat{F}$	Non-dimensional frequency ($\omega c^2/\nu$)
f	Frequency (Hz)
G	Response gain function / Electromechanical coefficient
h_a	Plunging displacement (half stroke)
h_{tunnel}	Wing model height from ground, (m)
$\dot{h}(t)$	Plunging velocity (m/s)
$\ddot{h}(t)$	Plunging acceleration (m/s^2)
k	Reduced frequency $\pi f c/U_\infty$
ℓ	Wing span (m)
N	Number of blades
Np	Plunging vertical force (N)
P	Non-dimensional Laplace variable
q	Dynamic pressure, $\rho U_\infty^2/2$
R	Resistance

Re	Reynolds number, $rhoU_\infty c/\mu$
S	Power density
T	Time period
U_∞	Free stream velocity, (m/s)
U_{ref}	Reference velocity $2\pi f h_a$ (m/s)

Greek

α_o	Airfoil mean angle of attack
α_{eff}	Effective angle of attack
α_e	Elastic energy storage parameter
η	Efficiency
ω	Angular frequency of oscillation,(rad/s)
ϕ	Cycle angle
ρ	Air density, (kg/m^3)
β_e	Negative energy dissipation parameter
β_0	Dynamic twist angle
$\delta\theta$	Dynamic varying pitch angle
Γ	Flapping angle
τ	Non-dimensional time
θ	Pitch angle of the airfoil chord with respect to the free stream velocity U
$\overline{\theta}$	Section's mean pitch angle
$\overline{\theta}_a$	Pitch angle of flapping axis with respect to U
$\overline{\theta}_w$	Mean pitch angle of chord with respect to flapping axis
ν	Kinematic viscosity (m^2/s)

Superscripts

*	conjugate
^{o}	degree
$\cdot$	first derivative

Subscripts

s	quasi-steady
a	apparent mass
eff	effective
e	elastic
f	friction
g	generator
in	input
L	load
LB	lower bound
mac	mean aerodynamic chord
opt	optimum
p	propulsive power
sep	separated flow
st	stall
S	leading edge suction
UB	upper bound
xx	Power spectral density for a signal
xxx	bispectral spectral density for a signal
$-$	average

Acronyms

AoA	Angle of attack
CAD	Computer aided design
CCD	Charge-coupled device
CFD	Computational fluid dynamics
$CSMWT$	Centimeter scale micro wind turbine
fps	Frame per second
LEV	Leading edge vortex

Chapter 1

Introduction

Unsteady aerodynamics generated by body motion and/or wing flapping or flexing has been shown to play an important role in generation of propulsion and lift of natural flyers and swimmers. It is accepted that birds, bats, insects and fish exploit unsteady fluid dynamics to improve their propulsive efficiency, minimize drag, maximize lift and increase maneuverability. Consequently, similar dynamics can be exploited to design efficient engineered flyers such as micro air vehicles. Quasi-steady models have been used extensively to model time variations of aerodynamic or hydrodynamic forces such as lift and drag on flapping wings. However, such models do not address the unsteady load history as well as nonlinearities generated from the system response, which are important contributors for exploiting a phenomenon to enhance a specific performance. Figure 1.1 shows a schematic to explain how unsteady aerodynamic models can be coupled with a flight dynamic model and incorporated within a control framework. Clearly, imposing a surface deflection with a controller introduces forces that provide the input to the aircraft system to perform a specific maneuver or to correct drift from a desired path. The ability to incorporate a compact and efficient aerodynamic model of the generated forces is important to adjust both the new aerodynamic state and the controller input. Consequently, one might be able to switch between both unsteady and quasi-steady aerodynamic models that correspond to a related maneuver to feed into system dynamics block. Biological observations, coupled with developments of a small-scale manufacturing techniques and feedback control design, opened up new and interesting problems in

unsteady aerodynamics. Different approaches can be taken to analyze and model unsteady aerodynamics.

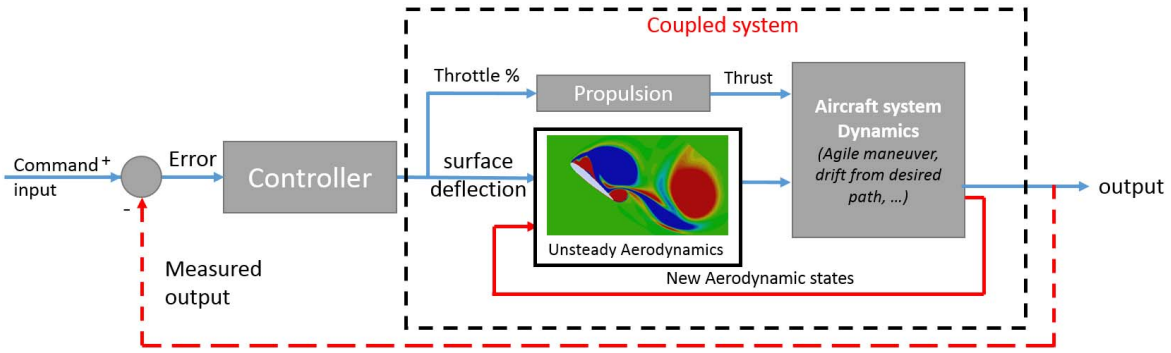

Figure 1.1: Schematic illustrating unsteady aerodynamics corrections in a flight dynamics control system of an aircraft.

The power of fidelity in such models is based on how the model is constructed. Ad-hoc models are constructed from theoretical and/or analytical formulations and reinforced with experiments or numerical techniques. These models are useful in describing specific states where the standalone theoretical models, as well as high fidelity models, failed to characterize those states. The use of high fidelity models based on experiments and CFD are expensive and time consuming. However, flight dynamicists are still in need of it in order to uncover the underpinning physics of different applications. These applications may be found in sharp maneuvers for agile unmanned air vehicles, flapping wings and bio-inspired under water vehicles, rotatory blades in helicopter and wind turbines.

Figure 1.2 illustrates aerodynamic models related to various applications. Aerodynamic models that couple with the flight dynamics model for conventional aircraft controls are often based on a quasi-steady assumption that forces and moments depend on parameters such as relative velocity and angle of attack. On the other hand, there are many of developed models that deal with the quasi-steady nonlinear assumption that is useful for describing high angles of attack applications without the inclusion of time history of unsteady forces. These models are important for small, highly maneuvering aircraft, quick response to gusts and

tracking targets. In the following two sections we will discuss linear and nonlinear unsteady

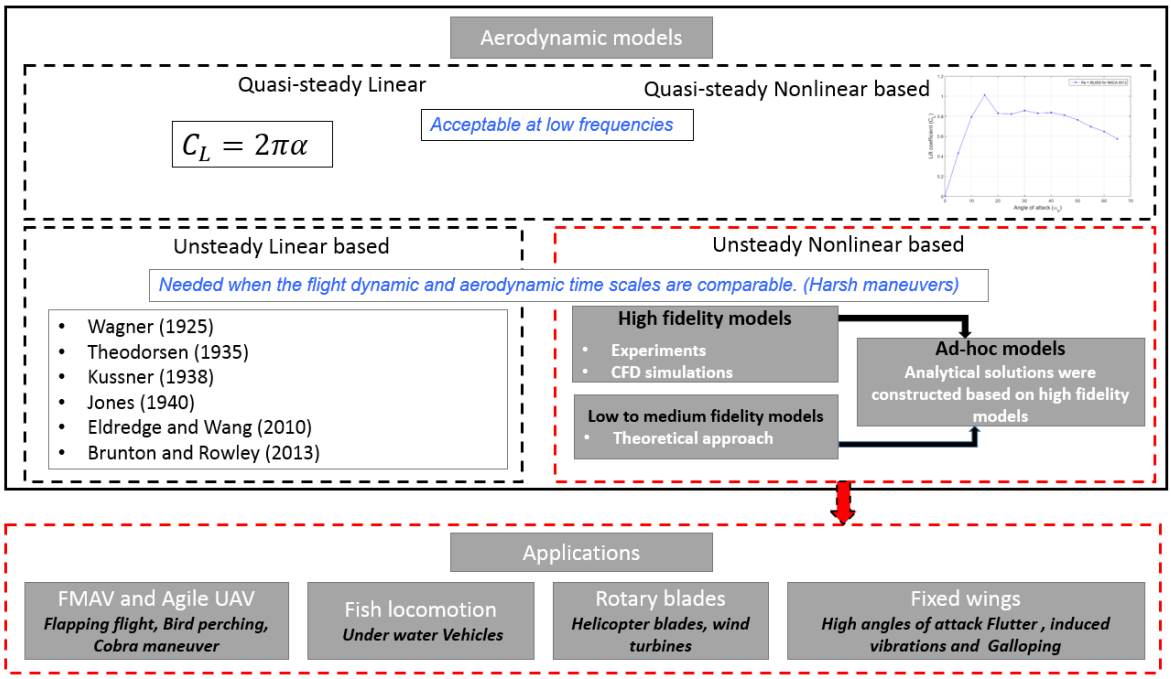

Figure 1.2: Block diagram for aerodynamic models in conjunction with the related engineering applications.

aerodynamics models that have been proposed and implemented in the literature.

1.1 Theoretical Studies

Over the period of the early theoretical foundations of Prandtl [7] and Birnbaum [8], two main constructive approaches can be distinguished. The first approach, laid down by Prandtl more than 90 years ago, is to assume that continuous sheets of voritcity emanate from the body's "sharp" edges and that the flow outside of these sheets can be modeled using inviscid assumptions. This approach has been the cornerstone of many analytical and efficient numerical unsteady aerodynamic models. The other approach is based on direct simulation of the governing Navier-Stokes equations with proper spatial and temporal discretization algorithms. Although the latter approach provides accurate solutions and detailed descriptions of the flow field, it lacks efficiency and stipulates too high of a computational burden to be used in design optimization, analysis of fluid-body-dynamics interactions, or even in studying the nonlinear dynamical characteristics of the flow field per se. On the other hand, Prandtl's approach is much more efficient and may, sometimes, lead to representations that are very convenient to some applications. Yet, it is quite limited to linearized, attached, potential flow cases and can hardly be extended to the recent interesting applications that invoke and exploit unsteady flow separation. The increased interest in biologically-inspired flights has created a substantial research activity in unsteady aerodynamics of low Reynolds number (Re) flyers. Two main aspects have been found to characterize this range of low Re flight: (i) the almost no sharp stall with a smooth lift variation over a broad range of angles of attack and (ii) the presence of a stabilized leading edge vortex (LEV) that enhances lift characteristics of such flights, see Ref. [9–11]. In addition, the experimental study of Dickinson et al. [11] and the computational results of Ramamurti and Sandberg [12] indicate that the shear force contribution to the aerodynamic loads is minimal.

The above characteristics of low Re flows have been modeled by extending Prandtl's classical theory of unsteady aerodynamics to biologically-inspired flows. Saffman and Sheffield [13] were the first to attribute the lift enhancement to an attached LEV; a concept that has

since been supported by several investigations including the recent work of Li and Wu [14]. One simple extension to Prandtl's classical theory, proposed by Minotti [15], is to add a stationary vortex with respect to the airfoil to account for the LEV effects. He also determined the optimum location of this vortex to match the experimental results of Dickinson et al. [11]. Jones [16] developed a potential flow model for the unsteady separation by shedding continuous sheets of vorticity from both the leading and trailing edges. His use of the Rott-Birkhoff equation that describes the evolution of free sheets of vorticity in potential flows along with the mathematical rigor of his formulation allowed implicit satisfaction of the Kutta condition at both edges by imposing boundlessness of the flow velocity everywhere. However, the numerical implementation was cumbersome and even diverged for cases where the simulated maneuver incorporated both low and high angles of attack. Similar approaches were proposed by Yongliang et al. [17], Pullin and Wang [18] and Ansari et al. [19]. Ramesh et al. [20] developed a new LEV shedding criterion. They used the A_0 coefficient in the Fourier series of the bound circulation distribution to serve as a criterion for predicting the onset of flow separation at the leading edge and called it the Leading Edge Suction Parameter (LESP). They showed that there is a critical value of the LESP (depending on airfoil shape and Re) that determines whether the flow is attached or separated at the leading edge, irrespective of the motion kinematics. Their LESP criterion not only predicts the onset and termination of LEV shedding but also the strength of the newly shed LEV without a need to invoke the Kutta condition. This work was extended by Ramesh et al. [21] to study limit cycle oscillations of airfoils operating at low Re. The authors concluded that the aerodynamic nonlinearities produced by intermittent LEV shedding may cause a supercritical-Hopf bifurcation.

V. OL et al. [22] and Wang and Eldredge [23] proposed a remedy for the high computational cost associated with continuous vorticity shedding from both edges as applied by Ansari et al. [19]. Instead of shedding constant-strength point vortices at each time step from both leading and trailing edges, they shed variable-strength point vortices at larger time lapses. This formulation greatly reduced the number of degrees of freedom and enhanced the efficiency of the discrete vortex model. However, they determined the strength of the free vortices at each time step by satisfying the Kutta condition at both edges, which is questionable in these highly unsteady applications, as shown by Pitt Ford and Babinsky [24], Savage

et al. [25] and invoked by Ansari et al. [19]. Hemati et al. [26] improved their varying-strength discrete vortex model by relaxing the Kutta condition and using optimal control theory to determine a law that governs the rate of change of vortex strength (i.e., instead of the Kutta condition) to minimize the discrepancy between predicted and measured forces. Their development of a compact dynamical model that governs such an unsteady flow allowed for the use of optimal control theory to better understand the flow dynamics, and more specifically, to construct the flow field from only force measurements. Brunton and Rowley [27] extended Theodorsen's model of the lift frequency response [28] to low Re flows.

Taha et al. [29] proposed a simple extension to the classical unsteady formulation. In particular, they extended Duhamel's superposition principle, commonly used in unsteady linear aerodynamics, to arbitrary unconventional lift mechanisms with emphasis on capturing the dominant nonlinear effects of LEV in insect flight. They proposed the quasi-steady circulation as the appropriate aerodynamic input that should be used in convolution with the Wagner's step response [30] in the Duhamel's principle. Then, they constructed a state- space formulation for the developed model and validated it against results from direct numerical simulations by Sun and Du [31] on the wings of several hovering insects. The model of Taha et al. [29] captures the nonlinearity of the input-output map, but its underpinning flow dynamics is Wagner's linear response. In order to capture the nonlinearity of the lift evolution dynamics, Yan et al. [32] and Taha et al. [33] revisited the classical work of Theodorsen [28] and relaxed four of its major assumptions (1) flat wake, (2) small angle of attack, (3) small disturbances to the mean flow components, and (4) time-invariant free-stream. They developed a semi-analytical model that is more efficient than classical discrete vortex models and can be applied successfully to large amplitude maneuvers. They simulated a large-amplitude canonical pitch maneuver, introduced by Eldredge et al. [34], and compared the obtained results with the computational results and experimental data of Ramesh et al. [35] and the classical unsteady model of Leishman and Nguyen [36]. The classical unsteady results deviated considerably from the experimental and computational results at large angles of attack. On the other hand, the reduced-order model developed by Yan et al. [32] produced satisfactory results for the generated lift and thus covered a gap in the classical theory of unsteady aerodynamics. Based on this model, Taha et al. [33] showed that the frequency response, and consequently

the flow dynamics, change considerably as the angle of attack increases. In particular, they showed a large departure from Theodorsen's model in the amplitude and phase for airfoils oscillating around 40^o angle of attack. This finding shows the need for developing and validating unsteady aerodynamics models that cover high angles of attack and high reduced frequencies.

1.2 Experimental Studies

In addition to the above theoretical developments, there have been several experimental investigations to study the effects of the wake structure on lift augmentation and attenuation at various reduced frequencies for pitching, plunging and surging motions, e.g., the work of Ellington et al. [37] and Jones et al. [38]. The work of Commerford and Carta [39] is one of the earliest experimental investigations of the lift response due to high frequency flow fluctuations. They placed an airfoil in the natural wake shed behind a cylinder at low Reynolds number (i.e., in the Von Karman street). The authors showed lift enhancement over potential flow theoretical predictions for angles of attack up to 20° at a reduced frequency $k = 3.9$. An optimal range of Strouhal number ($0.25 \leq S_t \leqslant 0.35$) over which high thrust efficiency and/or lift enhancement is produced was also found by several authors including Triantafyllou et al. [40], Anderson et al. [41], Ohmi et al. [42], Wang [43] and Cleaver et al. [44]. Most of these studies however, covered the relatively low angles of attack.

Rival and Tropea [45] experimentally investigated the lift augmentation and the associated unfavorable pitching moment due to dynamic stall. They elucidated the gradual transition from a bluff-body-type (multiple vortex pairs) to a mushroom-type wake at a reduced frequency $k = 0.2$. In order to have a better insight into the flow dynamics that leads to such a lift enhancement, Rival et al. [46] conducted direct-force and velocity-field measurements to analyze the development and reattachment of the LEVs from a plunging airfoil at $Re = 10,000$ and $k = 0.25$, for three different leading-edge geometries. The leading-edge shape was shown to have a direct effect on the shear layer that forms the LEV, and consequently on the development of the LEV, which we find to be contradicting to the conclusions of Usherwood and Ellington [47] at $Re = 8,000$. Panah and Buchholz [48] found out that

the LEV circulation is highly sensitive to the Strouhal number in the range $0.3 < S_t < 0.5$. Baik et al. [49] studied the flow evolution and unsteady force generation over pitching and plunging airfoils about some mean angle of attack and concluded that the Strouhal number is the most important parameter controlling the LEV maximum strength and the aerodynamic force generation.

Gursul et al. [50] described two lift enhancement mechanisms for plunging airfoils: deflected jets and convected LEVs. Stable deflected jets form at high Strouhal numbers and pre-stall conditions. Deflected jets are caused by pairing of the clockwise and counter-clockwise trailing-edge-vortices (TEVs) to form dipoles. These dipoles are asymmetric in position and strength, and therefore self-advect at an inclined direction to the free stream creating asymmetry in the flow field. This asymmetry results in high lift coefficients, even for a zero degree angle of attack. Deflected jets do not form at low Strouhal numbers due to insufficient vortex strength, nor at larger incidences due to forcing in a particular direction. Convected LEVs were determined to be an effective means for lift enhancement at post-stall angles of attack. At low Strouhal numbers, a LEV forms on the upper surface of the airfoil during the downward motion of the airfoil and then convects creating a low pressure region. As these LEVs are created by the plunging motion, the increase in lift coefficient is approximately proportional to the plunge velocity. Gursul et al. [50] concluded that this form of flow control is particularly effective when the plunging frequency equals the natural shedding frequency, its harmonics or sub-harmonics.

Pitt Ford and Babinsky [24] performed an experiment on an impulsively started flat plate at $Re = 30,000$ and angle of attack $\alpha = 15°$ to study the LEV build up. They developed a potential flow model that consisted of a bound circulation, free LEVs and free TEVs. They determined the locations and strengths of the LEVs and TEVs using the γ_2-method Graftieaux et al. [51] applied to PIV measurements. As such, they could determine the value of the bound circulation in the potential flow model that results in minimum deviation between the potential flow field and PIV measurements. Interestingly, during early stages, the optimum bound circulation was found to be Kelvin's value obtained by satisfying Kelvin's law of zero total circulation, i.e., conservation of angular momentum in inviscid flows, which is considerably different from the Kutta's value obtained by satisfying the Kutta condition

at the trailing edge. However, during later stages, the Kutta's value is closer to the optimum bound circulation than Kelvin's.

Despite many of the experimental investigations, there has been little experimental data at high angles of attack (larger than 30°), high reduced frequencies ($k > 0.1$), and transition Reynolds numbers ($Re \simeq 80,000$). Additionally, there is still a considerable need for unsteady nonlinear aerodynamic models that are (i) efficient enough to be used in optimization and control and (ii) rich enough to capture nonlinearity of the flow dynamics and potential lift enhancement mechanisms. Furthermore, while LEVs became well known as a considerable lift enhancement mechanism, there is still a lack in understanding of their dynamical behaviors. In this effort, we conduct static and dynamic plunging-oscillation experiments on a two-dimensional NACA-0012 airfoil at zero speed and at $Re = 79,900$ in the range of reduced frequencies $0.1 \leq k \leq 0.95$ and mean angles of attack α_0 between 0° and 65°. Variations in the mean and rms values of the static lift coefficient are presented. Spectral analysis is then performed to evaluate the frequency content of fluctuations at different angles of attack and flow regimes. The unsteady loads were measured at different frequencies to construct the frequency response between the plunging motion represented by its quasi-steady lift as an input and the unsteady lift as an output in the pre-stall, stall and post-stall regimes. We also use these measurements to identify and model the flow dynamics associated with lift enhancement. Then, we perform an optimization-based system identification to represent the unsteady lift by a finite dimensional dynamical system for each constructed frequency response. As such, we assess the effects of the mean angle of attack on lift build up dynamics. In addition, we performed flow visualization experiments at different reduced frequencies to gain insight into the physical concepts underpinning the lift enhancement mechanism, the associated LEV dynamics and experimental assessment of added mass forces and associated forces at high operating frequencies.

1.3 Research Objectives and Contributions

Unsteady aerodynamic modeling is widely studied in the literature, and is an effective tool to predict the actual loads on wings at different attitudes and conditions. Furthermore, one

recent application is in the field of energy harvesting. In this dissertation, we will present a model for unsteady aerodynamics and use our understanding of these aerodynamics in different applications including flapping flight and energy harvesting. The main contributions of this dissertation are as follows:

1. Frequency response measurements of the unsteady aerodynamics for plunging airfoil.
2. Modeling the added mass effects and associated forces of a two-dimensional plunging airfoil based on experimental measurements at zero flow speed.
3. Shape and kinematic optimization in forward flight of an Pterausor replica.
4. . Self-sustained flutter for initiating limit cycle oscillations of a composite beam.
5. Experimental measurements and modeling of centimeter-scale micro wind turbines.

1.4 Organization of the dissertation

Chapter 1 briefly summarizes the work done in the dissertation and its motivation, as well as introduces the previous work done in the area of unsteady aerodynamic modeling analytically and experimentally.

Chapter 2 deals with an experimental setup and force measurements of a two dimensional airfoil that is undergoing a plunging motion at high angles of attack and high reduced frequencies.

Chapter 3 explains the effect of the added forces of a two-dimensional plunging airfoil in a stationary flow at different frequencies and the approach to model this effect.

Chapter 4 describes an application of unsteady aerodynamic model in which a multi-objective optimization was held to obtain the optimal shape and kinematics of flapping wings.

Chapter 5 deals with applications of micro energy harvesters: (i) self-sustained flutter for initiating limit cycle oscillations of a composite beam and (ii) the experimental testing of a micro wind turbine energy harvester (Swirl type) that can be modeled to give the maximum power efficiency.

Chapter 2

Frequency response measurements

2.1 Introduction

In this chapter, we conduct static and dynamic plunging-oscillation experiments on a two-dimensional NACA-0012 airfoil at $Re = 79,900$ in the range of reduced frequencies $0.1 \leq k \leq 0.95$ and mean angles of attack α_0 between 0° and 65°. Variations in the mean and rms values of the static lift coefficient are presented. Spectral analysis is then performed to evaluate the frequency content of fluctuations at different angles of attack and flow regimes. The unsteady loads were measured at different frequencies to construct the frequency response between the plunging motion represented by its quasi-steady lift as an input and the unsteady lift as an output in the pre-stall, stall and post-stall regimes. We also use these measurements to identify and model the flow dynamics associated with lift enhancement. Then, we perform an optimization-based system identification to represent the unsteady lift by a finite dimensional dynamical system for each constructed frequency response. As such, we assess the effects of the mean angle of attack on lift build up dynamics. In addition, we perform flow visualization experiments at different reduced frequencies to gain insight into the physical concepts underpinning the lift enhancement mechanism and the associated LEV dynamics.

2.2 Experimental Setup

2.2.1 Wind Tunnel Facility and Operating Conditions

The experiments were conducted in an open-jet-return, low-speed wind tunnel. The test chamber has a cross section of 0.7 m × 0.7 m and a length of 1.5 m. The maximum attainable air speed is 28 m/s. The operated flow speed for the current experiments is 8.6 m/s ±0.5 %. The tunnel free stream turbulence intensity is 1% at $U_\infty = 8.6$ m/s, which corresponds to a chord Reynolds number of 79,900. The flow speed is controlled by an $AF600$ General Electric variable frequency drive. The test rig mainly consists of an oscillatory driving motor and a set of linkages connected together with a tunnel-spanning profile. The mechanism is able to perform pitch, plunge and combined motions at high setting angles of attack. The key component is the driving oscillatory rod that is connected to two threaded rear push-rod used to change the mean angle of attack of the wing. An adjustment nut is fitted along with each push-rod to allow for varying the mean angle of attack, α_0, between 0° and 65°. The motor has an operating frequency in the range of $0\ Hz < f_{motor} < 50\ Hz$ at no load conditions with a constant full stroke length $h_o = 1.93\ cm$. The main oscillatory rod is attached to a small bracket which, in turn, is attached to the mid-span wing profile at the quarter chord location. The two push-rods are attached upside down to the profile at the three quarter chord location. To achieve pure plunging motion, the push-rods are attached to the main oscillatory rod at the required mean angle of attack α_0, as shown in Fig.2.1. A foam core NACA 0012 was machined using a laser cutter and reinforced with a carbon fiber rod of diameter 4 mm at quarter chord location and the whole profile was covered by two layers of carbon fiber fabric to guarantee rigidity in span-wise direction. The carbon-fiber wing has an aspect ratio of 4.5 with a chord length of $0.14\,m$ and a span of $0.63\,m$. The wing model was mounted horizontally in the center of the test section. We use end plates (each plate is 0.25 m long and 0.15 m wide) to ensure two-dimensional flow within 2.7%. Wind tunnel blockage was less than 3.7% when the airfoil was set at the maximum angle of attack.

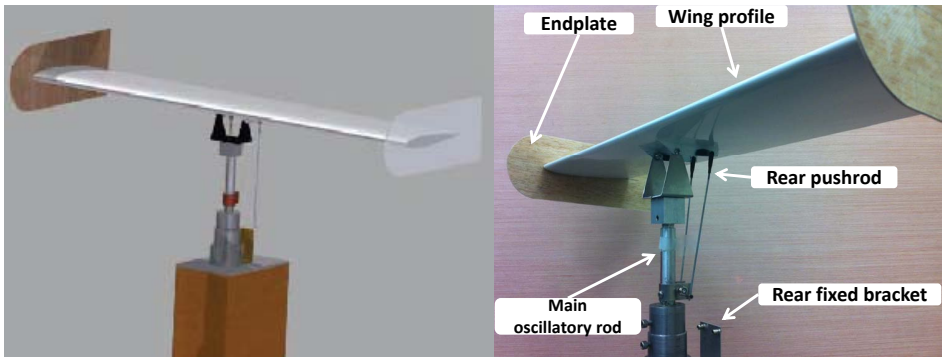

Figure 2.1: Three dimensional views of the pitch-plunge mechanism.

2.2.2 Force Balance and Data Processing

The wind tunnel is equipped with a six component strain gauge balance of strut model support system having an accuracy of 1.2% (0.05 N). The data were collected and processed using a sampling frequency rate of 2500 Hz. The measured signals were amplified by a transducer amplifier and connected to a National Instruments SCXI 1520 Multifunction DAQ. Force measurements were ensemble-averaged over three experiments and force coefficients were evaluated in terms of the dynamic pressure corresponding to the steady-state velocity, U_∞, rather than the instantaneous velocity. The wing oscillatory motion was measured using MEMS accelerometers. Two accelerometers were used for redundancy. A third accelerometer was placed on the strut balance base bracket to ensure that vibrational structural response of the balance has negligible effects, i.e., the natural frequency of the balance is away from the operating frequency. The accelerometers were calibrated using a 2 MHz variable phase synthesizer apparatus at different operating frequencies with an uncertainty of 0.5 % over the range of operating conditions. A digital protractor was used to measure the wing setting angle with an error of $\pm 0.2^\circ$. The frequency of the wing was also verified using a non-contact type optical, digital tachometer. Figure 2.2 shows the whole setup of the pitch-plunge mechanism and the tunnel facility.

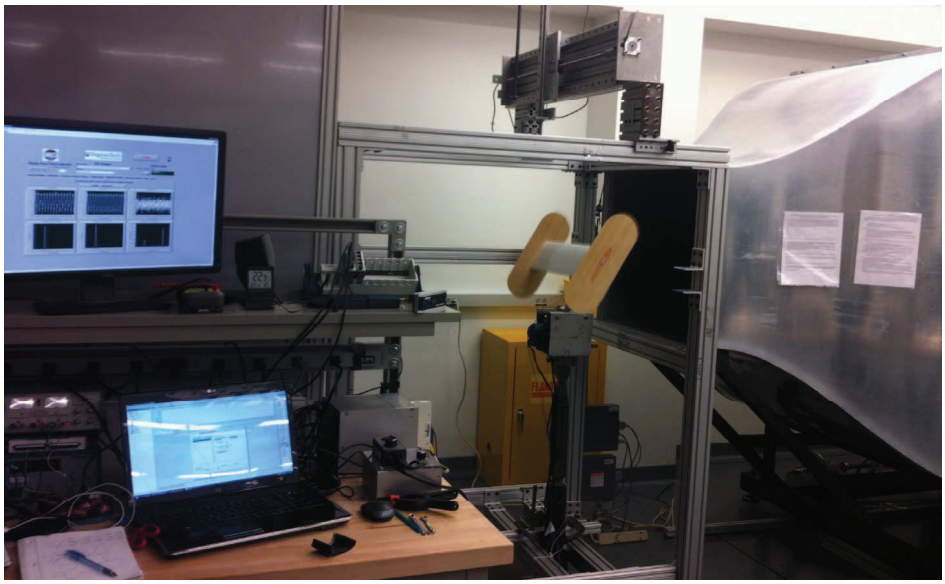

Figure 2.2: Experimental setup of the pitch-plunge mechanism in the wind tunnel facility.

2.2.3 Wind Tunnel Corrections

A common problem associated with open-jet wind tunnels is the induced pressure fluctuations in the test section. These fluctuations can limit the effective wind speed range. These fluctuations are normally attributed to a coupling between large scale coherent vortices shed from the nozzle and wind tunnel resonant modes. To determine the mean velocity at different locations, time series were measured at different positions along the spanwise direction in the presence of the wing. In addition, the vibration of the test stand from its interaction with the flow field was measured. Furthermore, the uniformity of the flow field at the nozzle outlet was assessed using a traverse system attached with a pitot tube to measure the pressure along a line perpendicular to the flow direction. Based on all of the above flow characterizations, the airfoil section was mounted at 1.48 m from the tunnel floor and 0.25 m from the nozzle outlet.

In an effort to identify the pressure fluctuations in the open-jet wind tunnel, an analytical scheme proposed by Brooks et al. [52] was used to calculate the effective angle of attack due to open-jet wind tunnel corrections. It should be noted that, since the flow is free to expand, the effects of solid and wake blockages are typically neglected for open jet flows [53], as well as the

influence of horizontal buoyancy (drop in static pressure along the test section). For an open jet flow, the remaining two corrections, downwash and streamline curvature, have a significant effect on the lift coefficient, C_L, the drag coefficient, C_D and the moment coefficient, C_M. The downwash correction is not needed when two-dimensional testing is carried out with an airfoil section that spans the tunnel width. However, in the present case, the width of the open jet exceeds the span of the airfoil by 3.5 cm. To ensure two dimensionality, end plates were used. The actual size of the end plates was taken into account in the corrections by applying the analytical method proposed by Mangler [54]. The streamline correction accounts for the free divergence of the flow from its original direction downstream of the airfoil section. In open jets, this effect is considerable because there are no tunnel walls to constrain the jet flow. The tunnel flow curvature induces more drag and changes the effective angle of attack. As a result, the measured C_D is larger and the slope of the C_L curve is smaller. Two analytical methods from Garner [55] and Brooks [52] that make use of the method of images could be used to correct for these effects. Brook's method involves additional terms for the angle of attack and pitching moment corrections, which indicates that Brook's method is of higher accuracy in comparison to Garner's method and, as such, is used in this work. The flow effective angle of attack, α_{eff}, is then given by:

$$\alpha_{\text{eff}} = \alpha_t - \frac{\sqrt{3\sigma}}{\pi} C_{Lt} - \frac{2\sigma}{\pi} C_{Lt} - \frac{4\sigma}{\pi} C_{Mt} \qquad (rad) \tag{2.1}$$

where α_t is the setting angle of attack, C_{Lt} is the measured lift coefficient, C_{Mt} is the measured pitching moment coefficient, and the nondimensional parameter σ is defined as

$$\sigma = \frac{\pi^2}{48} \left(\frac{c}{h_{\text{tunnel}}} \right)^2$$

where $h_{\text{tunnel}} = 0.7\ m$ is the wing vertical distance to the ground. Finally, a data reduction program was written to calculate the uncertainties based on Moffat [56] method considering both bias and precision errors. Eventually, the uncertainty quantification for the operating Re is $\pm 2.4\%$, k is $\pm 0.24\%$ and C_L is ± 0.05 within the respective ranges operation of 79,900, 0.1 to 0.95 and 0 to 1.

2.3 Static lift measurements and analysis

Figure 2.3 shows a comparison among the current measurements of the static lift curve at Re =79,900, the measurements of Tang and Dowell [57] at Re =313,000, and theoretical predictions. These predictions include those of the classical airfoil theory $C_L = 2\pi \sin\alpha$, the potential flow lift without leading edge suction $C_L = 2\pi \sin\alpha \cos^2\alpha$ [58], and the fit of the static lift due to a stabilized leading edge vortex $C_L = \pi \sin 2\alpha$, proposed by Berman and Wang [59] and refined by Taha et al. [29]. Based on standard statistical evaluation methods (assuming Gaussian distribution of data), uncertainty limits with a 95% confidence level were determined for each of the load measurements based on three separate runs. The plots show that the current experimental measurements are in a qualitative agreement with the measurements of Tang and Dowell [57]. Both measurements match predictions of the classical wing theory over its range of applicability up to 10°. The slight difference in the maximum lift between the current measurements and that of Tang and Dowell [57] can be attributed to the difference in the Reynolds numbers. As typical for a purely two-dimensional flow, a stabilized leading edge vortex that augments the lift cannot be realized under static conditions. As such, the predictions of the lift due to a stabilized leading edge vortex, given by $C_L = \pi \sin 2\alpha$, are higher than the current measurements. Finally, the potential flow model without leading edge suction overestimates the generated lift as it does not account for the separation effects.

Given that the leading edge of the NACA-0012 airfoil is rounded, the stall conditions observed in Fig. 2.3 correspond to those of a leading edge stall whereby an adverse pressure gradient occurs near the leading edge causing a weak separation. Also because the operating Reynolds number is 79,900, it is fair to assume that the flow over the airfoil separates even for the case of zero angle of attack and that the point of separation moves closer to the leading edge as the angle of attack is increased.

2.3.1 Power spectral density

The effects of the flow separation can also be seen from the rms values of the lift coefficient presented in Fig. 2.4. The results show that the rms value is about 0.03 for small angles of

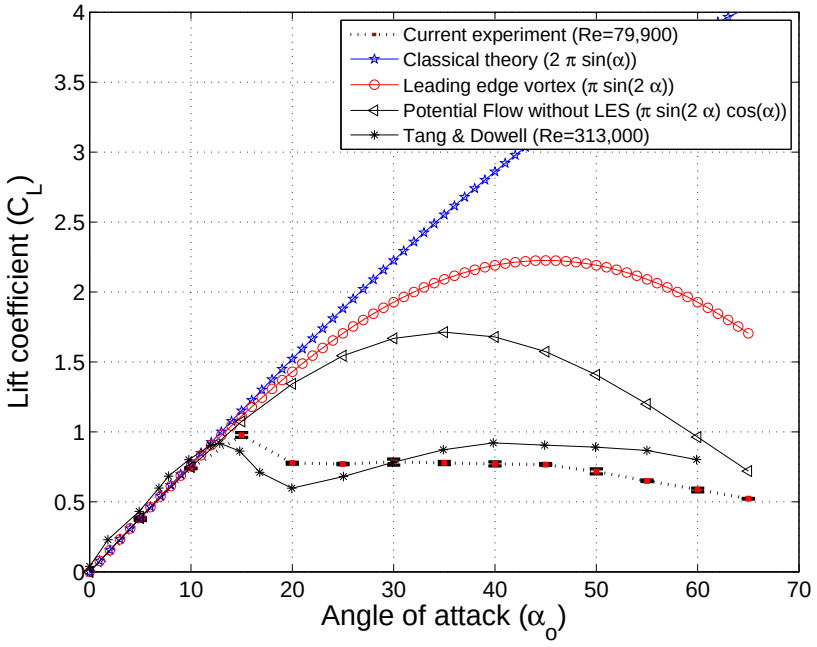

Figure 2.3: Comparison of the current steady C_L-measurements with theory and other experimental results.

attack, increases to about 0.035 in the stall regime and decreases again at angles of attack larger than 40°. As shown in Fig.2.5, the spectral density of the lift fluctuations exhibit different characteristics in the pre-stall, stall and post-stall regimes. In the pre-stall regime, $\alpha_o \leq 10°$, the spectra shown in Fig. 2.5(a) are characterized by a single peak indicating vortex shedding from the boundary layer separation. In the stall regime ($15° \leq \alpha_o \leq 35°$), the spectra presented in Fig. 2.5(b) exhibit two peaks at α_0=15°, 20° and 25° near 50 and 75 Hz and a smaller peak near 10 Hz. At α_0=30°, 35° and 40°, the spectra exhibit a broadband that extends over 25 Hz with peaks at 50 and 75 Hz. The presence of two peaks and a broadband indicate the effects of the flow separation resulting from the stall which introduces an asymmetry in the flow on the upper and lower surfaces. Spectra of the lift fluctuations at angles of attack larger than 40° show a more defined single peak similar to those observed in the pre-stall regime. Figure 2.6(a) and 2.6(b) summarize the results of the spectral analysis performed and presented in Fig. 2.5. Particularly, Fig. 2.6(a) shows that the frequency of the peak does not vary with the angle of attack. However, as shown in Fig.

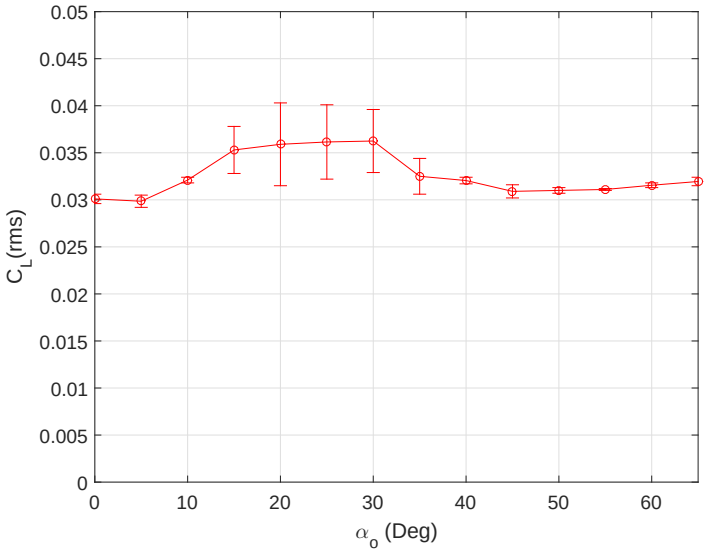

Figure 2.4: RMS of the lift coefficient the over NACA 0012 based on static measurements time series at $Re = 79,900$, $0° \leq \alpha \leq 65°$.

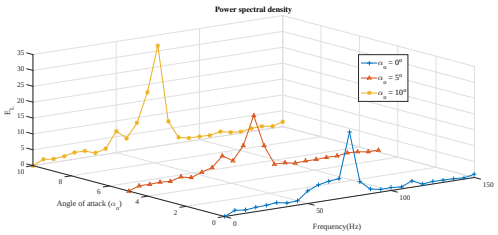

(a) Spectra in pre-stall regime

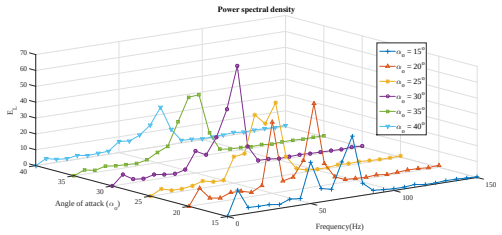

(b) Spectra in stall regime

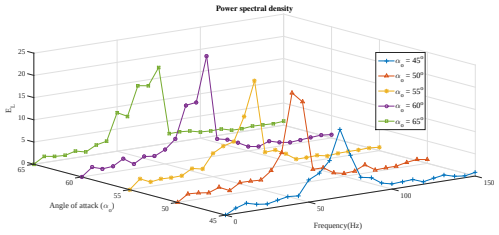

(c) Spectra in post-stall regime

Figure 2.5: Frequency spectra of the measured lift coefficient over NACA-0012 at $Re = 79,900$ in (a) pre-stall $0° \leq \alpha \leq 10°$, (b) stall $15° \leq \alpha \leq 40°$ and (c) post-stall regimes $45° \leq \alpha \leq 65°$.

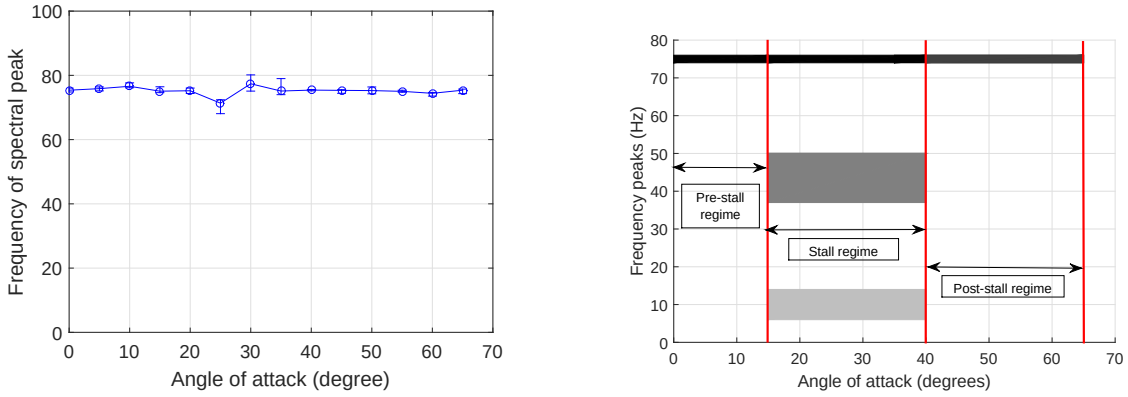

(a) (b)

Figure 2.6: Variation of the maximum peak (a) and the frequency content (b) with angles of attack at $Re = 79,900$ for NACA-0012 in the pre-stall, stall and post-stall regimes.

2.6(b), the stall regime is characterized by broader peaks and low frequency fluctuations. These differences, related to the asymmetry in the flow and resulting from the stall, can be exploited for flow control and lift enhancement through dynamic oscillations as will be shown below.

2.4 Shedding frequency for NACA 0012 at static conditions

For an oscillating airfoils, when the forced oscillation frequency matches the shedding frequency a lock-in phenomenon occurs and enhances the transient lift by multiples of their quasi-steady values. For most applications of small UAVs, the operating Reynolds number is in the range of $50,000 \leq Re \leq 300,000$. Within this range of Reynolds number, the airfoil is liable to laminar leading edge separation, which can have a significant effect on airfoil performance. When separation occurs, the flowfield over the airfoil is governed by the development of a free shear layer forming due to boundary-layer separation. At the low end of Reynolds numbers and/or high angles of attack, the shear layer fails to reattach to the airfoil surface. In contrast, at higher Reynolds numbers and/or low angles of attack, reattachment may occur, leading to the formation of a separation bubble [60].

Evidence of vortex shedding in the airfoil wake at low Reynolds number has been observed

in several other studies. Yarusevych et al. [61] conducted a thorough review by explaining the challenges and advances in the study of fundamental frequency of vortex shedding in the separated shear layer over airfoils. They experimentally investigated the flow development over NACA 0025 in the $55,000 \leq Re \leq 210,000$ at $\alpha = 0°$, $5°$, and $10°$. They identified two Re-regimes: (i) low-Re regime associated with boundary layer separation without reattachment and (ii) high-Re regime associated with separation bubble formation (reattachment takes place). They analyzed the frequency spectrum of the streamwise and normal velocity components over the airfoil upper surface. In both of the Re regimes, the chordwise stations right after separation show activities centered around a fundamental frequency f_0, which increases linearly with Re. The stations downstream the mid chord exhibit sub-harmonic response that is attributed to vortex merging. At further downstream stations corresponding to laminar-to-turbulent transition, broadband spectrum is found indicating that the rolled-up vortices in the free shear layer breakdown. The spectra of aft stations show a classical turbulent behavior ($f^{-5/3}$). According to their results, a $Re =\simeq 80,000$ should be associated with $f_0 \simeq 100$ Hz at the tested angles of attack $\alpha = 0°$, $5°$, and $10°$.

Yarusevych et al. [61] measured the velocity components at various stations to trace the change in the free shear layer frequency. However, the results presented in section 2.4 of this dissertation shows the spectra of the lift time history. Also, the independence of f_0 on α is observed in the present results too. Since the airfoil behavior is strictly dependent on the separated shear-layer behavior, at high angles of attack (poststall regime), the airfoil wake development is similar to bluff body wake [62]. However, the behavior is totally different for the case of lower angles of attack (prestall regime) when the separated shear layer fails to reattach [63]. Huang and Lin [62], Huang and Lee [64], Yarusevych and Boutilier [65] identified several distinct vortex shedding modes and argued that vortex shedding occurs in the airfoil wake only when the separated shear layer fails to reattach to the airfoil surface. Also, Yarusevych and Boutilier investigated experimentally the flow over a NACA 0018 airfoil within a range of $30,000 \leq Re \leq 200,000$. They focused on the effects of Reynolds number and separated shear layer behavior on airfoil wake development.

In a nut shell, we concluded that the contribution of the shedded vortices in the separated shear layer (centered at f_0) the lift dynamics is more pronounced than the shed vortices in

the near wake. Indeed, the convection of a free vortex on the upper surface of an airfoil has limited effects on the lift force, see [13,14,66]. These observations explain the high frequency contents in the measured signal that appears as a broadband breadth specifically in the stall regime. In addition to the fundamental frequency f_0, Yarusevych et al. [61] observed peaks at frequencies much lower than f_0 in the spectra of the normal velocity components in the wake of a NACA 0025 over $55,000 \leq Re \leq 210,000$ at $\alpha = 0°$, $5°$, and $10°$. This peak is attributed to wake shedding frequency f_s. We do not observe such a peak, however. It should be noted that according to the experimental results of Huang and Lin [67], a NACA 0012 at $Re = 79,000$ does not periodically shed vortices to its wake at angles of attack lower than $15°$. In addition, even yarusevych et al. [61] observed no peaks at f_s in the spectra of the streamwise velocity components. Only spectra of the normal velocity components exhibit peaks at f_s. Moreover, they concluded that as Re is increased towards laminar-to-turbulent transition, the wake is less coherent and the observed f_s-peaks become more broadband. This may explain why we do not observe a peak at the shedding frequency in the lift spectra at $Re = 79,900$. In the next section, we will try to shed some light on the obtained experimental results using CFD simulations and study the effects of various turbulence models.

2.5 CFD simulations for NACA 0012 at static conditions

Using (RANS) equations, Wells et al. [[68]] highlighted the effects of turbulence modeling on the simulations of vortical wake flows such as the rolled-up vortices in the near wake of a rectangular wing. They concluded that, simulations with the full Reynolds stress transport model show remarkable mean flow agreement with experimental data in the tip vortex and spiral wake due to the proper prediction of a laminar vortex core. Simulations with the Spalart-Allmaras model predicted over-diffusion of the tip-vortex. This could be explained as the Spalart-Allmaras model should be corrected to deal with the eddy viscosity term for rotating flows. In this section, we compared the experimental static lift and drag results presented by [[69]] with the results obtained from Spalart Allmaras model [[70]] at the same operating conditions. Then, we compared four different models, laminar, Spalart-Almaras, modified Spalart-Almaras and Reynolds stress transport model to analyze flow

structure of the 2D wake over a NACA-0012 airfoil at 40° angle of attack and Re=79,900. This comparison is important because using inappropriate model might lead to failure in capturing the associated shedding frequencies at high angles of attack.

2.5.1 Computational domain

ANSYS Fluent 15, is used to simulate the flow structure over a NACA-0012 airfoil at high angle of attack. The mesh is generated using the GAMBIT Modeler. To satisfy an acceptable computational accuracy, the mesh is refined in regions near the airfoil surface as well as the wake region. Firstly, we investigated the influence of the mesh size on the predicted lift and drag coefficients. However, using large number of nodes demand substantial computer memory and consequently increase the computational time. One way to examine this procedure is to increase the number of nodes until the mesh is satisfactorily fine and further refinement of the mesh produces negligible changes. The fine C-grid contains 380 points on the airfoil surface, 160 points in the radial direction and extends approximately 600 points from the trailing edge of the airfoil to the downstream boundary. The computational domain identifying the farfield boundary conditions and a zoomed-out view of the grid is shown in Fig.2.7. Although not shown here, a grid sensitivity study has been previously conducted, and this grid of 520,000 nodes was shown to be sufficiently fine for the purpose of capturing the vortex shedding. The lift and drag coefficients for different grid resolutions are shown in table 1.

Table 2.1: Mesh sensitivity analysis for SA computational model at 5^o AoA and $Re = 79,000$

Mesh elements (10^3)	C_L	C_D
62	0.492	0.042
129	0.489	0.033
256	0.475	0.032
332	0.478	0.031
520	0.480	0.031

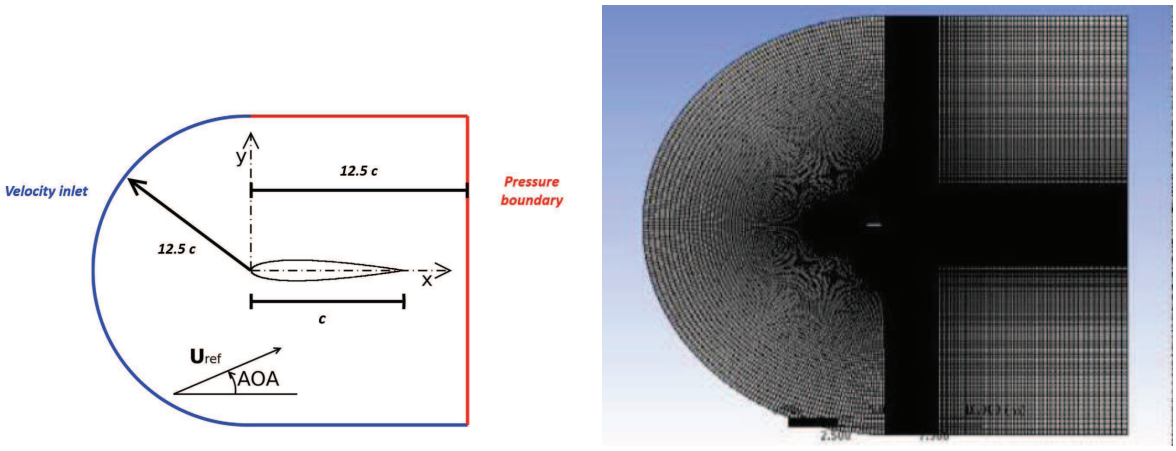

(a) Computational domain (b) Grid generation using Gambit software

Figure 2.7: Computational domain for NACA-0012 airfoil

2.5.2 Computational models

The Spalart and Allmaras [70] model is a relatively simple one-equation model that solves a modeled transport equation for the kinematic eddy (turbulent) viscosity. [71] and [72] modified the SA model to account for the numerical error associated with the vortex shedding. The modified model is a vorticity-strain based model (*Rotation Correction*). The modification should be passive in thin shear layers where vorticity and strain are very close.

The Reynolds stress model (RSM) is the most elaborate turbulence model that FLUENT provides. Abandoning the isotropic eddy-viscosity hypothesis, the RSM closes the Reynolds-averaged Navier-Stokes equations by solving transport equations for the Reynolds stresses, together with an equation for the dissipation rate. This means that five additional transport equations are required in 2D flows and seven additional transport equations must be solved in 3D. Since the RSM accounts for the effects of streamline curvature, swirl, rotation, and rapid changes in strain rate in a more rigorous manner than one-equation and two-equation models, it has greater potential to give accurate predictions for complex flows [73]. Use of the RSM is a must when the flow features of interest are the result of anisotropy in the Reynolds stresses. Among the examples are cyclone flows, highly swirling flows in combustors, rotating flow passages, and the stress-induced secondary flows in ducts.

The mean lift and drag coefficients obtained with SA model are compared with the ex-

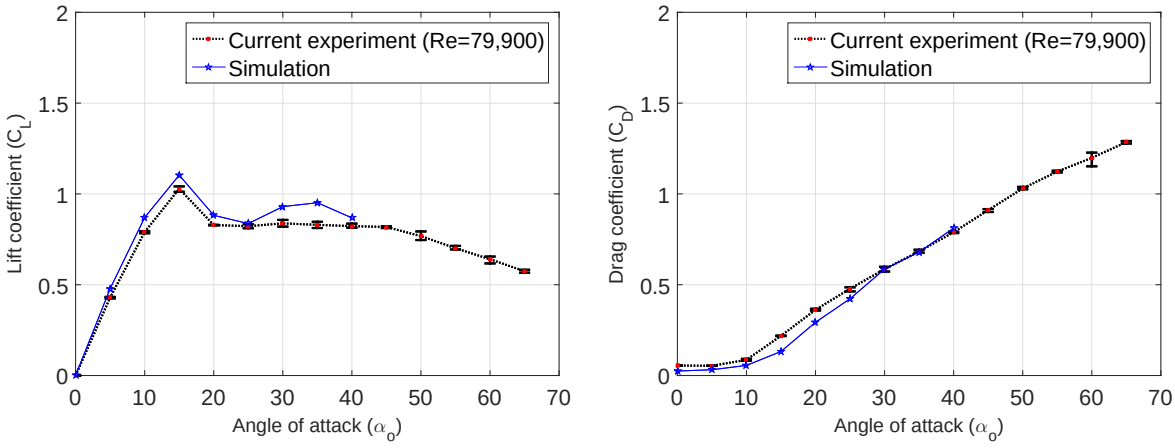

(a) Static lift curve

(b) Static Drag curve

Figure 2.8: Static mean lift and drag coefficients compared with CFD simulation using SA model at $Re = 79,900$ for NACA-0012.

perimental results up to 40° in Fig. 2.8. The results show very good agreement with the wind tunnel data and captures the same trend at stall conditions. Each simulation point corresponds to an average value over the simulation time record while excluding the transient time steps. There are some discrepancies for the range $\alpha_o = 25°$ to $\alpha_o = 40°$. As will be shown shortly, at these high angles of attack, it should be noted that vortex shedding is not observed in the wake using SA model.

Based on the previous observation with the SA model, we decided to compare a high angle of attack case using three different turbulence models and laminar flow to ensure the appropriate model for capturing the vortex shedding in the wake. Figure 2.9 shows vorticity contours for various models at $\alpha_o = 40°$ and Re=79,900 at a specific time instant (time step of 0.002 and 1500 iterations). The vorticity contours are shown in the first row. The laminar simulation and RS model almost have the same flow structure. The results organized in a way as: the first column is Spalart-Allmaras, the second column is SA modified, the third one is laminar case and the fourth is the Reynolds Stress model. The first row shows vorticity contours, second row shows pressure contours and the third represents the velocity magnitude contours. It is clear from the vorticity contours that the SA model as well as the modified one do not show the vortex shedding captured by the laminar and RS model. A closer view

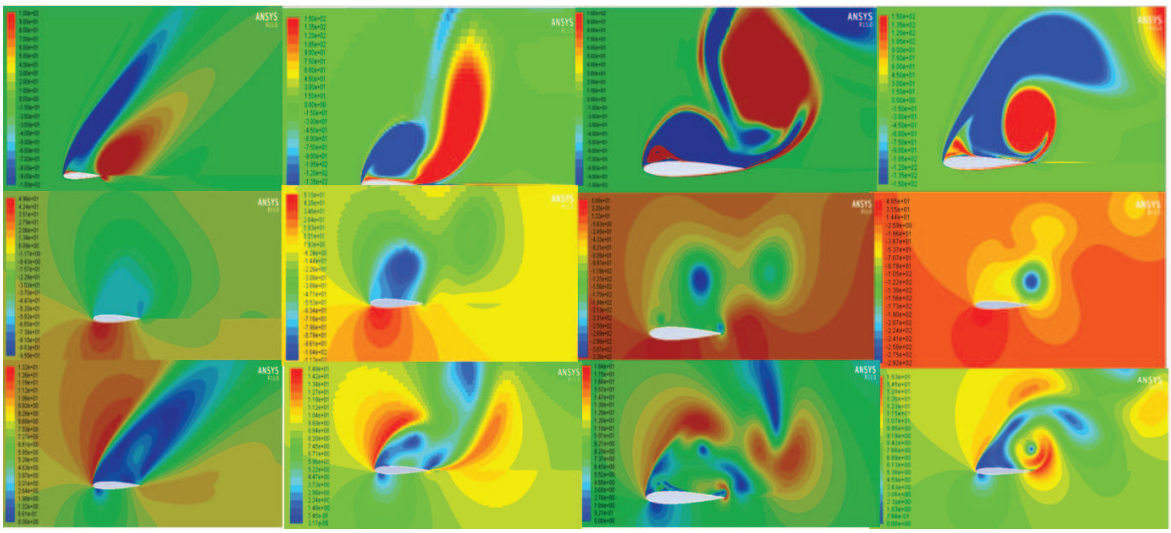

Figure 2.9: Models comparison for NACA 0012 at $Re = 79,900$ and $\alpha_o = 40°$ (SA, SA modified, laminar, Reynolds Stress). First row (Vorticity contours), second row (Pressure contours) and third row (Velocity contours).

for the laminar and RS model are shown in Fig. 2.10 and Fig. 2.11, respectively.

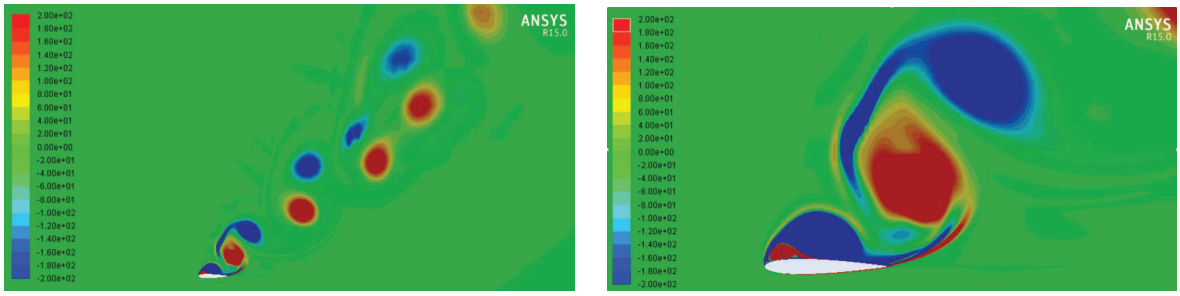

(a) Vorticity contours zoomed out view

(b) Vorticity contours zoomed in view

Figure 2.10: Vorticity contours using laminar flow model at $Re = 79,900$ for NACA-0012 at $\alpha_o = 40°$.

Figs. 2.12 and 2.13 show the lift and drag time series for both laminar and turbulent models for a period of 0.9 seconds simulation. Consequently, Figure 2.14 shows the PSD corresponding to the lift and drag history shown in figs. 2.12 and 2.13. The two models almost have the same shedding frequency around 15 Hz indicating that the vortex structure affecting the generated forces is similar in the two cases of laminar and RS models. The force coefficient

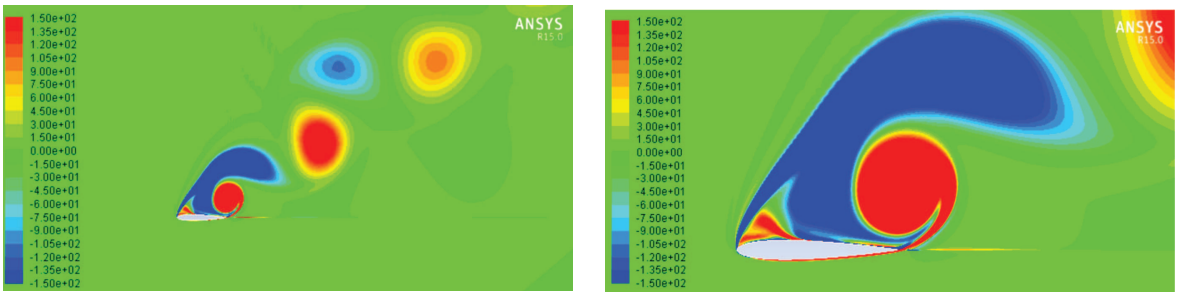

(a) Vorticity contours zoomed out view

(b) Vorticity contours zoomed in view

Figure 2.11: Vorticity contours using RS model at $Re = 79,900$ for NACA-0012 at $\alpha_o = 40°$.

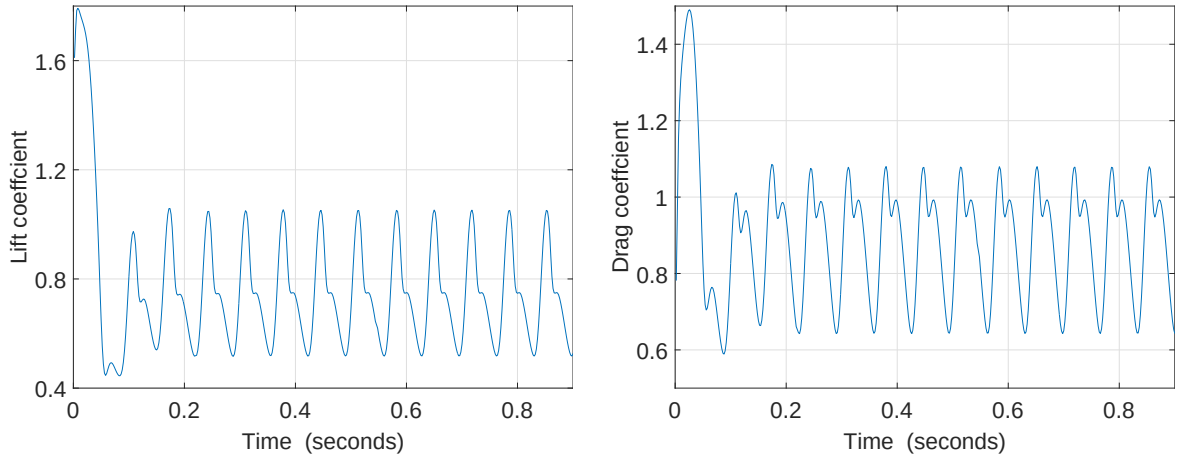

(a) Lift coefficient time history using laminar transient model

(b) Drag coefficient time history using laminar transient model

Figure 2.12: Force coefficients using laminar model at $Re = 79,900$ for NACA-0012 at $\alpha_o = 40°$.

spectra also show a well defined peak at twice the shedding frequency ($2f_s \simeq 30Hz$). The velocity spectra (to be shown later) also show two peaks at f_s and $2f_s$. The higher frequency ($2f_s$) is due to secondary vortices induced on the upper surface by the primary vortices shed from the leading and trailing edge.

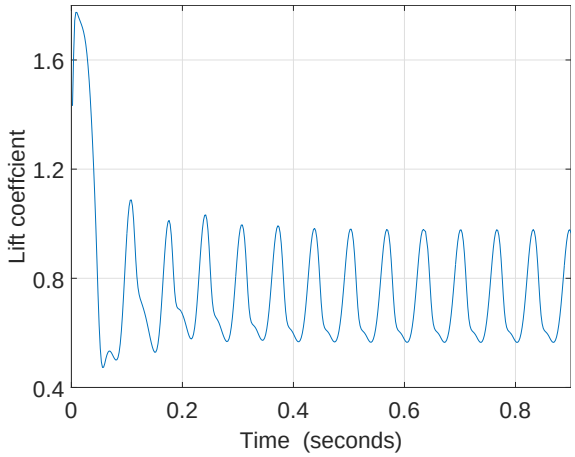

(a) Lift coefficient time history using RS model

(b) Drag coefficient time history using RS model

Figure 2.13: Force coefficients using RS model at $Re = 79,900$ for NACA-0012 at $\alpha_o = 40°$.

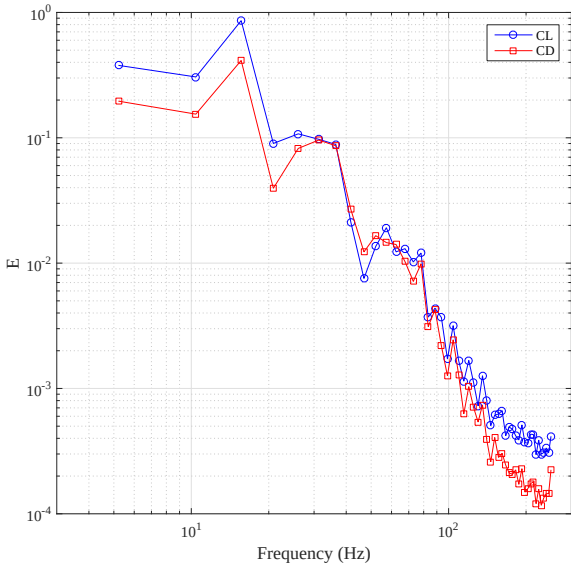

(a) Power spectra for lift and drag coefficients using laminar transient model

(b) Power spectra for lift and drag coefficients using RS transient model

Figure 2.14: Vorticity contours using RS model at $Re = 79,900$ for NACA-0012 at $\alpha_o = 40°$.

2.5.3 Shedding frequency at $40°$ angle of attack

In order to monitor the vortex shedding in the wake, we placed different probes within the flow domain and recorded the time history fluctuations for the X and Y velocities. Figure 2.15 shows the locations of probes from 1 to 10 to capture the velocity component fluctuations.

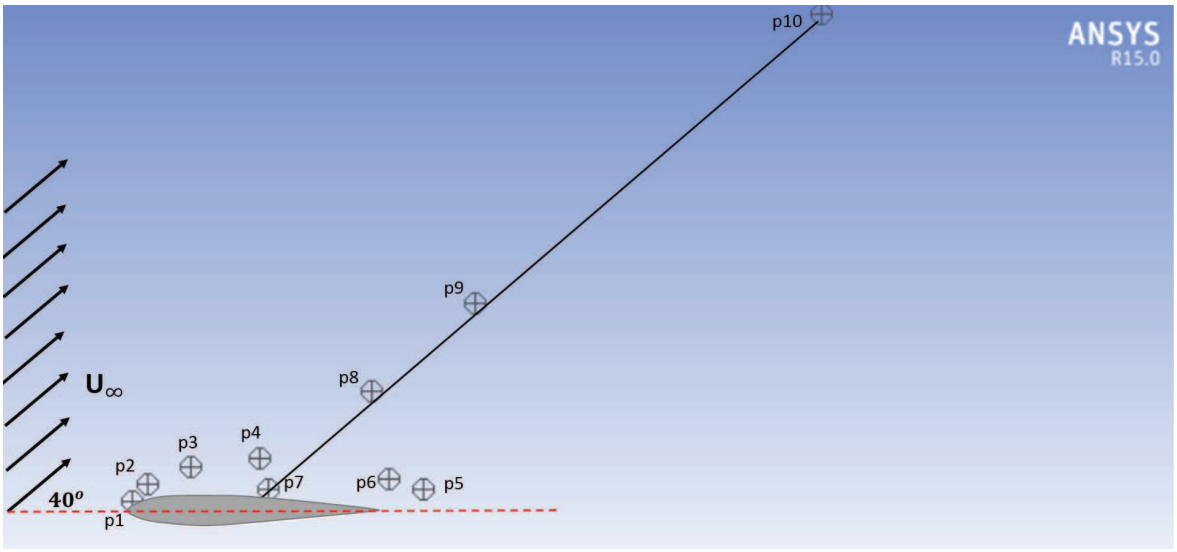

Figure 2.15: Selected probes for recording the X-velocity component time history fluctuations over NACA 0012 at $Re = 79,900$, $\alpha_o = 40°$.

Probes $1-6$ are set to be in the vicinity of the airfoil and probes $7-10$ are set to be distributed on a line drawn parallel to the undisturbed flow of length $3c$.

Figures 2.16 and 2.17 show the power spectra for the X-component velocity at the selected probe positions shown in Fig. 2.15. Figures 2.16(a) and 2.17(a) show PSD for the probes numbered 1 to 6 close to the airfoil surface. It is clear from the two figures that probes 1,2, and 3 do not indicate the vortex shedding as they do not show any peaks in the power spectra, however, probes 4, 5 and 6 show a peak frequency of 15.75 Hz. This means that the shear layer instabilities do affect the flow structure near the surface, consequently, at 40^o angle of attack the free shear layer separated from the leading edge rolls up into large vortex before it develops the classical mixing-layer type instabilities. Figures 2.16(b) and 2.17(b) show PSD for the probes numbers from 7 to 10 on the line inclined to the airfoil chord and parallel to the free stream velocity. For these probe positions, the peak frequency have the same frequency captured by probe 4, 5, and 6 of a value 15.75 Hz. The local peaks at $2f_s$ are due to secondary vortices induced on the upper surface. These results explains the lift enhancement case for an airfoil oscillating in plunge at reduced frequency near 0.7 ($k = 2\pi fc/U_\infty$) reported by Zakaria et al. [69]. This could be attributed as a lock-in phenomenon occurs between the oscillation

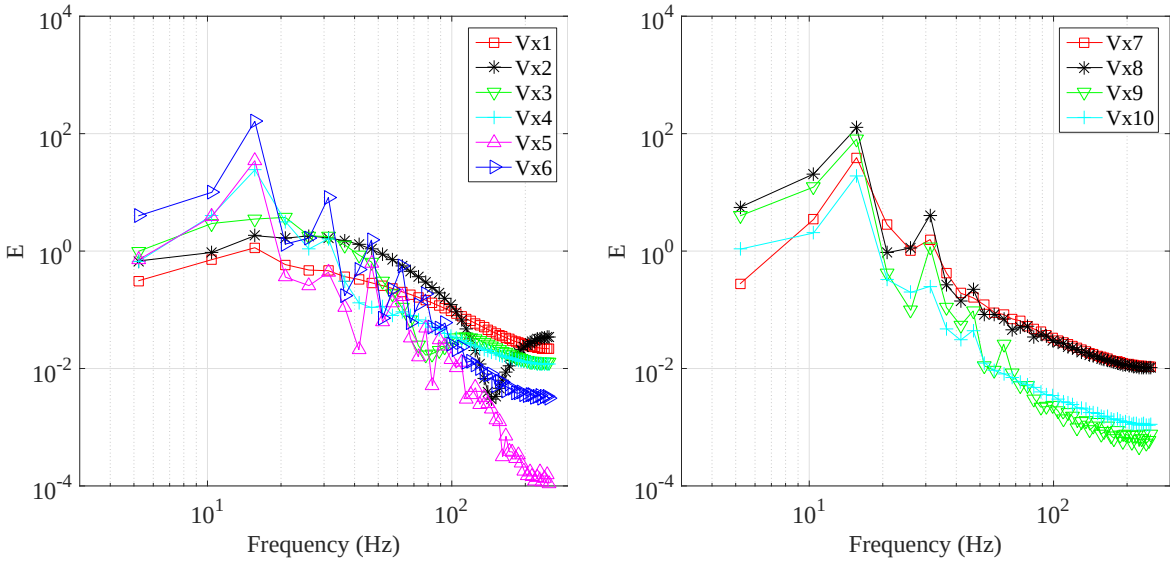

(a) Probes 1 to 6

(b) Probes 7 to 10

Figure 2.16: Power spectral density of X-velocity component time history for NACA-0012 simulated with Reynolds Stress model at specific locations shown in Fig. 2.15.

frequency and the shedding frequency which corresponds to a plunging frequency close to $\simeq 14\ Hz$ and was found to be close to the frequency obtained from simulations. Figure 2.18 shows six sequential vorticity contours for Reynolds stress model with time step of 0.01 at 40^o angle of attack. At the first time step, the free shear layer emanating from the leading edge rolls up into a large vortex on the suction side. At the same time, the boundary layer on the pressure side also separates and rolls around the sharp trailing edge forming a trailing edge vortex. As the later vortex forms it nips the suction side vortex and subsequently it breaks off from the suction side. The two vortices (the trailing edge and the nipped part of the suction side vortex) shed into the wake as a pair of counter rotating vortices. Once the two vortices are shed, the suction side vortex matures again by the vorticity of the feeding separated shear layer from the leading edge. The cycle of trailing edge vortex nipping the suction side vortex and the pair of vortices shedding into the wake repeats. It should be noted that for $70,000 \leq Re_c \leq 100,000$, a flow structure transition occurs at the angle of attack investigated. Either separation bubble formation or bubble bursting can occur for a given Reynolds number. Due to the high sensitivity of the flow to changes in experimental

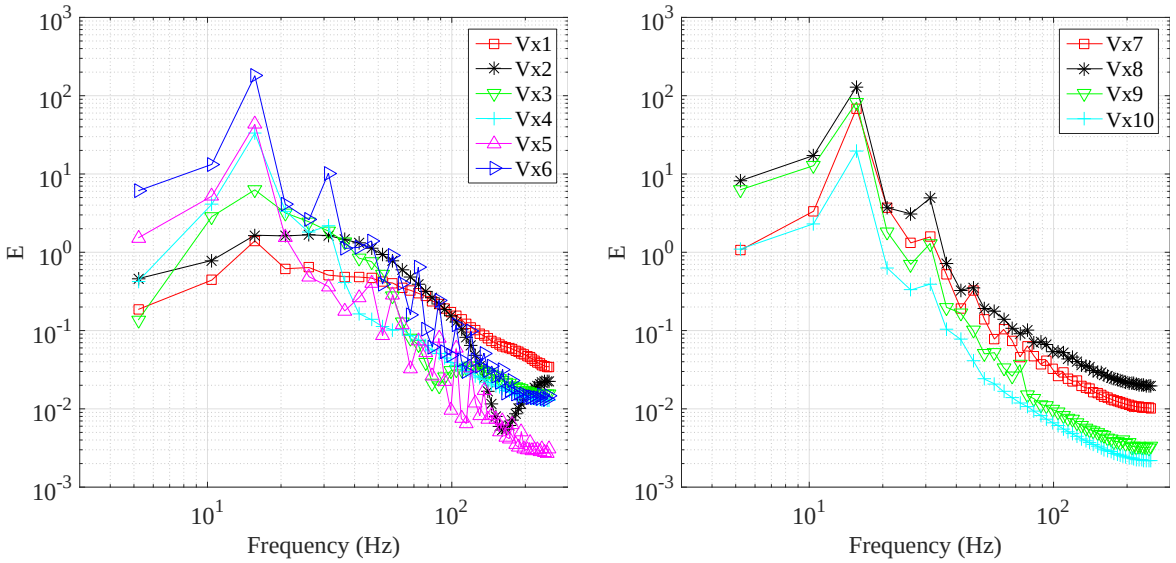

(a) Probes 1 to 6

(b) Probes 7 to 10

Figure 2.17: Power spectral density of X-velocity component time history for NACA-0012 simulated with laminar flow model at specific locations shown in Fig. 2.15.

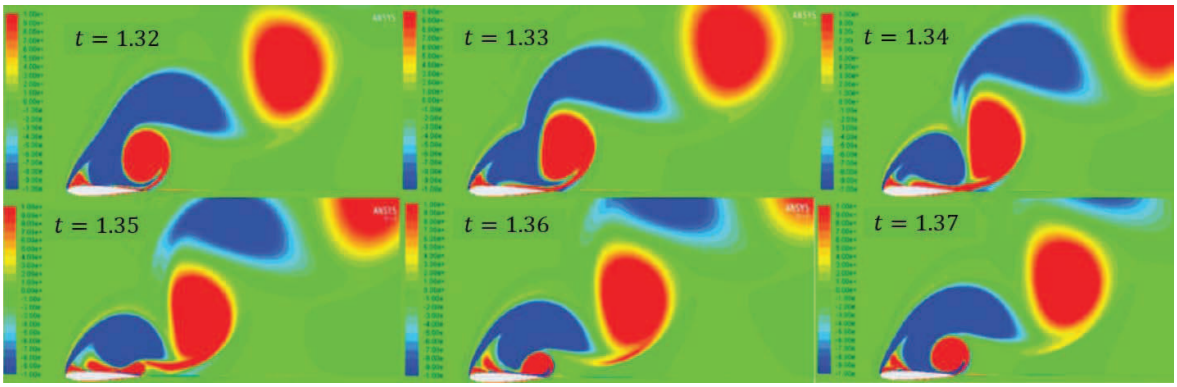

Figure 2.18: Vorticity time stepping for RS model over NACA 0012 at $Re = 79,900$, $\alpha_o = 40°$ (δ t = 0.01 s).

parameters, experimental data in this range of Reynolds numbers are dearth.

Recalling section 2.3.1, the observed peak is around 75 Hz, in which we attribute this difference in the shear layer instability frequencies to the different methodology in both experiments and simulations as well as the difference in the measured quantities. It should be noted that for $70,000 \leq Re_c \leq 100,000$, a flow structure transition occurs at the angle of attack investigated. Either separation bubble formation or bubble bursting can occur for a given Reynolds number. Due to the high sensitivity of the flow to changes in experimental parameters, for this reason, experimental data in this range of Reynolds numbers are dearth.

To conclude this section, the 2D flow over the NACA-0012 wing section at high angles of attack and Re=79,000 is simulated by solving Reynolds averaged Navier-Stokes equations using different turbulence models. The computed mean lift and drag coefficients using Spalart-Allmaras turbulence model are in good agreement with experimental data, but there are noticeable discrepancies in the angle of attack range of 25 to 40 degrees. A more detailed study is conducted to clarify the effects of the turbulence model on vortex shedding and the wake structure at an angle of attack of 40 degrees. The original Sparlart-Allmaras and the modified version predicted highly diffused shear layers emanating from the leading and trailing edges of the airfoil without discernible vortex shedding. The Reynolds stress transport model predicted well-defined vortex street in the wake with shedding frequency of $f = 15$ Hz or a Strouhal number of $St = fCsin\alpha/U_\infty = 0.157$. In the present simulations, the Reynolds number is relatively low, hence laminar boundary layer separation is anticipated from the leading edge, and at the trailing edge separation is fixed by the sharp edge. Thus we expect that turbulence on the airfoil pressure side to play a minor rule in the dynamics of the boundary layer separation. For these reasons, results from a laminar flow simulation showed similar wake structure and shedding frequency as the Reynolds stress transport model.

Analysis of the power spectral density of velocity components showed the dominant frequency to be the vortex shedding frequency. High frequencies typical of free-shear layer instabilities were not pronounced perhaps due the roll-up of the separated shear layer into a coherent vortex on the upper surface before instability sets in. Local peaks in the spectra at twice the shedding frequency are due to secondary vortices induced by the interaction of primary vortices with the upper surface.

2.6 Dynamic Measurements and frequency response

In order to asses the frequency response function of a dynamical system, it is important to define the input and output values. Similar to Theodorsen's representation [28], we construct the frequency response between the quasi-steady lift as an aerodynamic input and the circulatory lift as an aerodynamic output. This is also in accordance with the assumption of Taha et al. [29] that the nonlinearity of lift build-up dynamics may be absorbed in the nonlinear input-output map between the quasi-steady lift and the angle of attack, while the lift dynamics due to changes in the quasi-steady lift may still be considered linear. A supporting finding for this assumption was presented by Pitt Ford and Babinsky [24]. They showed that adding the Wagner's lift [30] to the non-circulatory contributions obtained using potential flow closely matches the measured lift forces near stall. In the current study, the quasi steady lift is determined from the static lift curve using the instantaneous effective angle of attack, α_{eff}. At each mean angle of attack α_0, the plunging motion was performed such that the variation of the effective angle of attack from its mean value is within a small range. The plunging oscillations, $h(t) = h_a \sin(2\pi f t)$, were performed at various reduced frequencies ($0.1 \leq k \leq 0.95$). The oscillation parameters include the amplitude, h_a=$h_o/2$, the plunging frequency, f, and the reduced frequency $k = \pi f c/U_\infty$. By changing the effective angle of attack during the plunging motion, vortices are shed from the leading and trailing edges of the airfoil. The interaction of the shed vortices with the airfoil motion and the shed wake results in a time lag between the airfoil motion and the corresponding aerodynamic load. The frequency response function is a very common means for representing this dynamical behavior. In this work, we use the magnitude of the frequency response function as a measure of the lift enhancement that can be obtained through plunging oscillations of the airfoil. For each combination of mean angle of attack α_0 and reduced frequency k, we define this magnitude as:

$$|G|(k;\alpha_0) = \frac{|C_{L_c}(t;k,\alpha_0)|}{|C_{L_s}(t;k,\alpha_0)|} \tag{2.2}$$

where $|.|$ donates the magnitude, C_{Lc} is the circulatory lift coefficient obtained from the measured lift by subtracting the components due to the moving and added masses and is

given by:

$$C_{L_c}(t) = \left[L(t) - (m_{\text{moving}} + \pi\rho\ell b^2 \cos^2\alpha)\ \ddot{h}(t)\right] / \left[\frac{1}{2}\rho U_\infty^2 c\right] \tag{2.3}$$

and C_{Ls} is the quasi-steady lift defined by the instantaneous angle of attack and can be written as $C_{L_s}(t) = C_L(\alpha_{\text{eff}}(t))$, where the effective angle of attack is given by:

$$\alpha_{\text{eff}}(t) = \alpha_0 + \frac{\dot{h}(t)}{U_\infty} = \alpha_0 + \frac{2kh_a}{c}\cos(2\pi f t) \tag{2.4}$$

In the next set of figures, we show the variations of the quasi-steady lift coefficient as a function of the effective angle of attack $\alpha_{\text{eff}}(t)$ over different ranges of plunging oscillations. In addition to these variations, we show the time variations of C_{Lc}, the calculated circulatory lift from the measured values and α_{eff}.

2.6.1 Frequency Response in the Linear Regime ($\alpha_0 = 0^\circ - 10^\circ$)

Figure 2.19 shows time histories of the quasi steady lift coefficient C_{L_s}, the circulatory lift coefficient C_{L_c}, and the effective angle of attack α_{eff} along with the C_{L_s}-α_{eff} variations for $\alpha_0 = 0^\circ, 5^\circ$ and 10° at selected value of the reduced frequency k. In all cases, the effective angle of attack lies within $\pm 5.7^\circ$ of the mean angle of attack. For all cases shown, the effective angle of attack varies sinusoidally with a period equal to that of the plunging oscillations. Because the static lift coefficient varies linearly with the effective angle of attack, its time variations are also sinusoidal with one period. As for the circulatory lift, its variations are also periodic. For $\alpha_0 = 0^\circ$ and $\alpha_0 = 5^\circ$, C_{Lc} exhibits periodic variations with a period that is equal to that of the forced oscillations. In the case of $\alpha_0 = 10^\circ$, we note that the fluctuations of C_{Lc} have two periodic components. The first one has the same period as that of the oscillations and the second one is a weaker component with a frequency of about 75 Hz, which matches the shedding frequency observed in the spectra of the static lift measurements. Figure 2.20 shows the obtained frequency responses along with Theodorsen's frequency response function for the cases of $\alpha_0 = 0^\circ$, 5°, and 10°. The error bars show the extent of variation of the measured values from different data sets for each operating reduced frequency. Good agreement with Theodorsen's frequency response is noted over this range of mean angles of attack. This agreement is expected for small angles of attack and the no flow separation flat wake assumption is not severely violated. The obtained frequency response

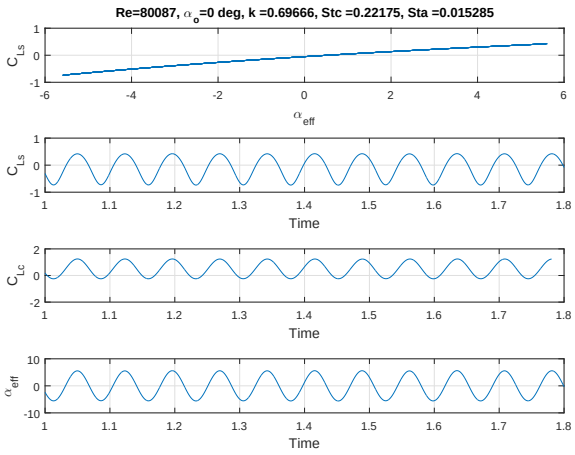

(a) $\alpha_0 = 0^\circ$ and $k = 0.69$

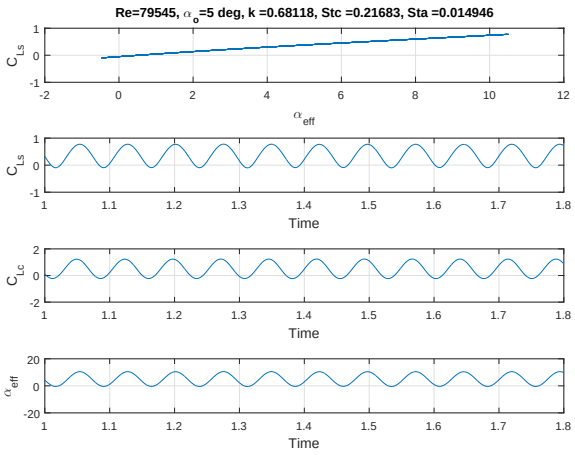

(b) $\alpha_0 = 5^\circ$ and $k = 0.68$

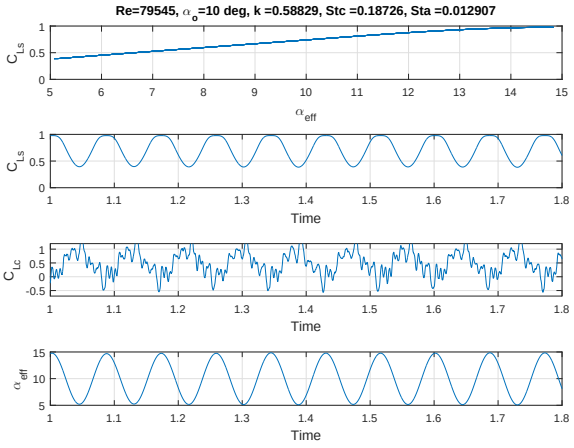

(c) $\alpha_0 = 10^\circ$ and $k = 0.58$

Figure 2.19: Time histories of C_{L_s}, C_{Lc} and α_{eff} at various reduced frequencies along with the C_{L_s}-α_{eff} variation in the linear regime.

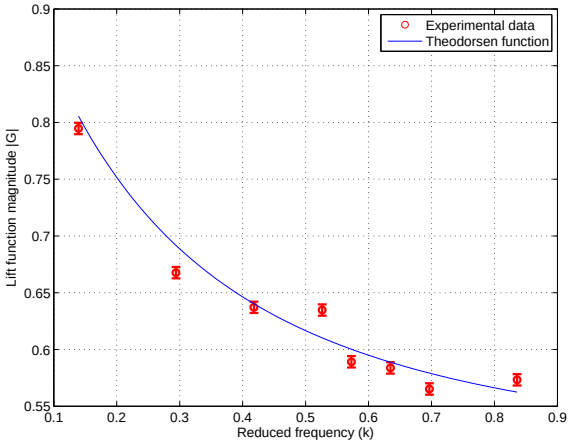

(a) $\alpha_0 = 0^o$

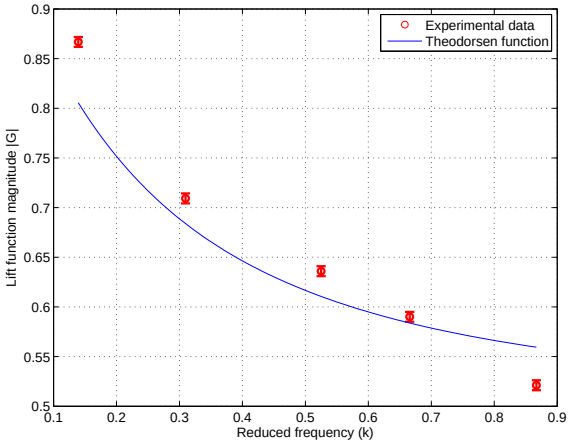

(b) $\alpha_0 = 5^o$

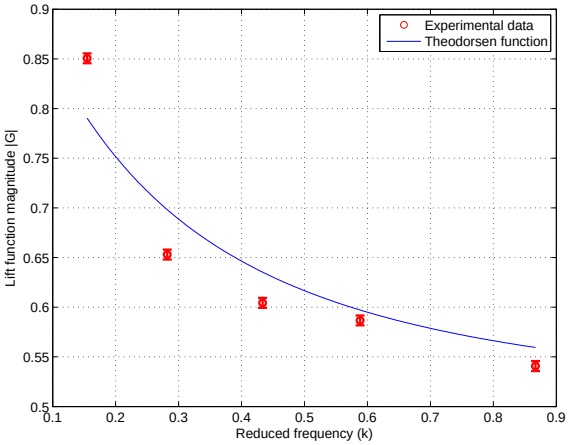

(c) $\alpha_0 = 10^o$

Figure 2.20: Magnitude of the lift frequency response in the linear regime.

is monotonically decreasing as the frequency increases, which is similar to the response of a first-order simple lag system.

2.6.2 Frequency Response in the Stall Regime ($\alpha_0 = 15° - 40°$)

The frequency response in the stall regime cannot be predicted by Theodorsen's model. Even the model of Yan et al. [32], though is geometrically valid for high angles of attack, presumed an attached flow and, hence, does not account for the effects of flow separation. Figure 2.21 shows time histories of C_{L_s}, C_{L_c}, α_{eff}, and the C_{L_s}-α_{eff} variation over the range

$15° \leq \alpha_0 \leq 40°$ for selected values of k. The nonlinearity of the static lift coefficient variation with the effective angle of attack is clearly shown. This nonlinearity can also be noted from the multi-frequency, periodic time-variation of the quasi-steady and circulatory lift although the wing oscillatory motion has a single frequency. Of particular importance is the appearance of superharmonics in the periodic variations of the static lift coefficients that can be associated with the nonlinear variations of C_{Ls} with respect to α_{eff}. Furthermore, figures 2.21(a) and 2.21(b) show periodic variations in C_{Lc} value with many frequency components. These variations are due to a resonance between the different aspects of the flow dynamics resulting from the plunging motion and vortex shedding.

Figure 2.22 shows the magnitudes of the frequency response functions at $\alpha_0 = 15°$, $20°$, $25°$ and $30°$ along with Theodorsen's. As expected, the obtained frequency responses in this regime are quite different from Theodorsen's; both qualitatively and quantitatively. Unlike the monotonically decreasing behavior of Theodorsen's frequency response, we note a decrease in the magnitude of the frequency response as k increases up to values near 0.65 - 0.7. Around that value, we observe an increase in the magnitude of the frequency response, followed by a reduction as k is increased further. This finding is quite important for unsteady aerodynamics applications as it suggests significant enhanced lift generation around $k = 0.7$. This value of reduced frequency corresponds to a Strouhal number based on the oscillation amplitude, h_a, S_{ta}= 0.016 and a Strouhal number based on the chord, c, S_{tc}= 0.23. The observed value of the lift-optimum frequency is consistent with the result obtained by Wang [74]. She used the Navier-Stokes equations to simulate impulsively started flow over a two dimensional wing section. She compared her numerical results to the experimental data of Dichinson et al. [9]. Both results show that the steady-state values of the lift cannot remain indefinitely constant at high angles of attack because of the well known LEV instability for two-dimensional flows (i.e., in the absence of a stabilizing axial or spanwise flows) and because a Von Karman street starts to emerge after about 10 chord lengths of travel. Wang [74] concluded that there is a lift-optimum window for flapping that occurs after the steady state lift is reached, after the Wagner's lift transient behavior, and before the Von Karman oscillations start. We find that this window corresponds to a reduced frequency around $k = 0.7$. Choi et al. [75] used the immersed boundary method to perform a direct numerical simulation of Navier Stokes

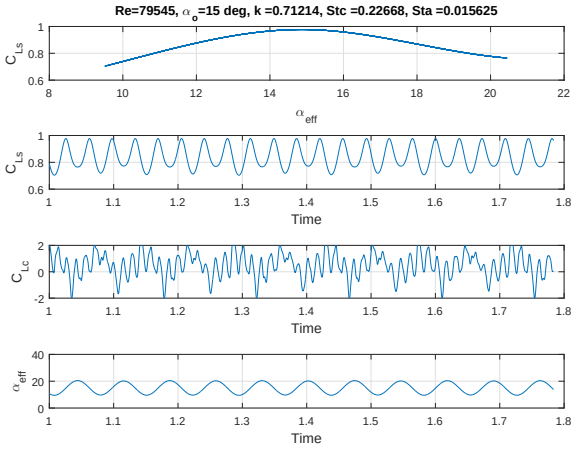

(a) $\alpha_0 = 15^\circ$ and $k = 0.71$

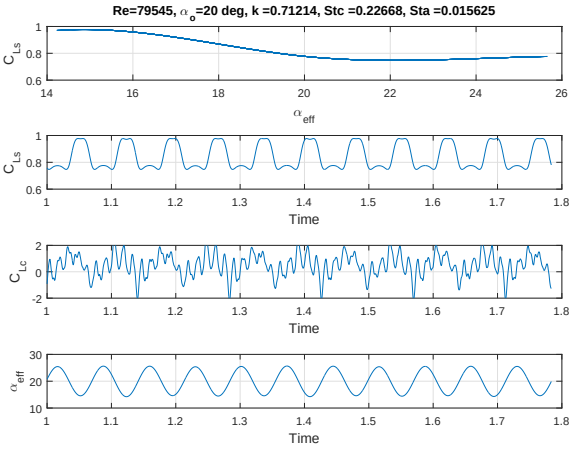

(b) $\alpha_0 = 20^\circ$ and $k = 0.71$

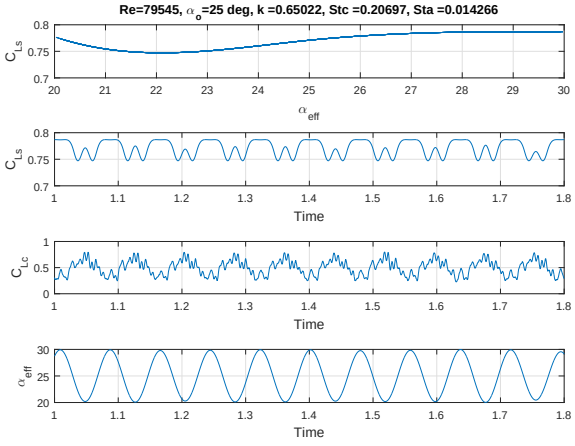

(c) $\alpha_0 = 25^\circ$ and $k = 0.65$

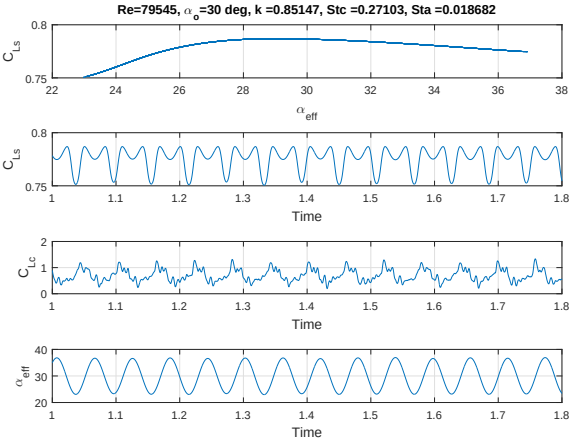

(d) $\alpha_0 = 30^\circ$ and $k = 0.85$

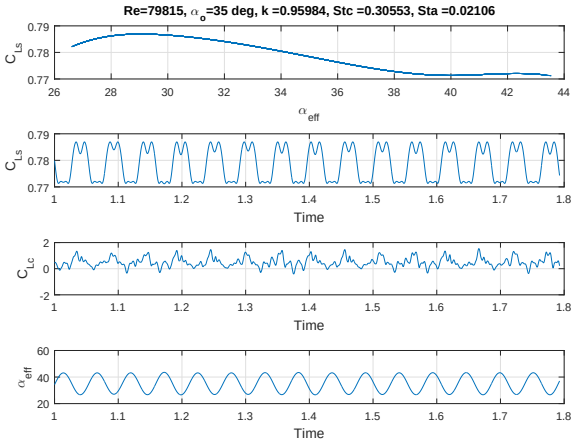

(e) $\alpha_0 = 35^\circ$ and $k = 0.95$

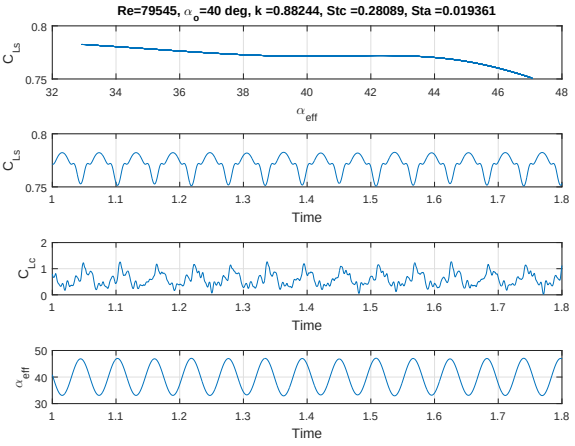

(f) $\alpha_0 = 40^\circ$ and $k = 0.88$

Figure 2.21: Time histories of C_{L_s}, C_{Lc} and α_{eff} at various reduced frequencies along with the C_{L_s}-α_{eff} variation in the stall regime.

equations on a flat plate undergoing surging and plunging. The authors obtained a Fourier transform of the lift coefficient due to surging that is close to the potential flow theoretical prediction of Greenburg [76] at small angles of attack ($\alpha = 5°$). In addition, they found similar lift enhancement for surging airfoils over the same range of reduced frequencies $k = 0.6 - 0.7$ at $\alpha = 15°$. The authors stated that plunging results in a similar behavior. The observed lift enhancement mechanism is also consistent with the experimental findings of Ol. et al. [22], Cleaver et al. [77] and Calderon et al. [78]. Figures 2.22(e) and 2.22(f) show the frequency response functions for $\alpha_0 = 35^o$ and 40^o, respectively. The plots show similar characteristics to the response functions obtained at lower angles of attack within the stall regime but with the lift-optimum frequency shifted to higher values. In fact, this shift can also be observed from the results of Choi et al. [75] as their lift-peak frequency at $Re = 500$ and 57,000 was $k = 0.6$ at $\alpha = 15°$ and $k = 0.7$ at $\alpha = 20°$. We consider the two cases of $\alpha_0 = 35^o$ and 40^o as a transition phase between stall and post-stall regimes.

2.6.3 Frequency Response in the Post-Stall Regime ($\alpha_0 = 45° - 65°$)

Figure 2.23 shows time histories of C_{L_s}, C_{L_c}, α_{eff}, and the C_{L_s}-α_{eff} variation over the post-stall regime (i.e., $45° \leq \alpha_0 \leq 65°$). The results show a time response similar to that of the linear regime that is characterized by sinusoidal variations that have one period and an almost linear variation of C_{L_s} with α_{eff}. Figure 2.24 shows the obtained frequency responses at $\alpha_0 = 45°$, $50°$, $55°$, $60°$, and $65°$ along with that of Theodorsen's. The response functions regained their first-order-like behavior in this post-stall regime. Yet, as expected, the obtained frequency responses are considerably different from that of Theodorsen's. In agreement with the geometrically-exact potential flow theoretical predictions of Yan et al. [32], the obtained magnitude of the lift frequency response in the post-stall regime is considerably smaller than that predicted by Theodorsen's, which can be satisfactorily attributed to flow separation from the leading edge.

2.6.4 Spectral Analysis at Dynamic Conditions

Figure 2.25 shows the frequency spectra of the measured lift due to plunging at various reduced frequencies, $0.1 \leq k \leq 0.9$, which corresponds to a frequency range between 1.9 and

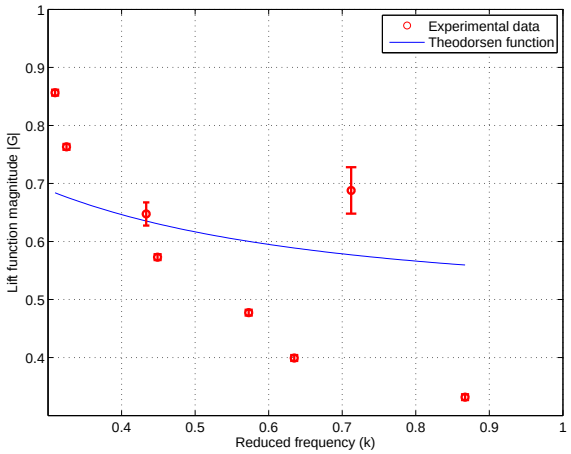

(a) $\alpha_0 = 15^o$

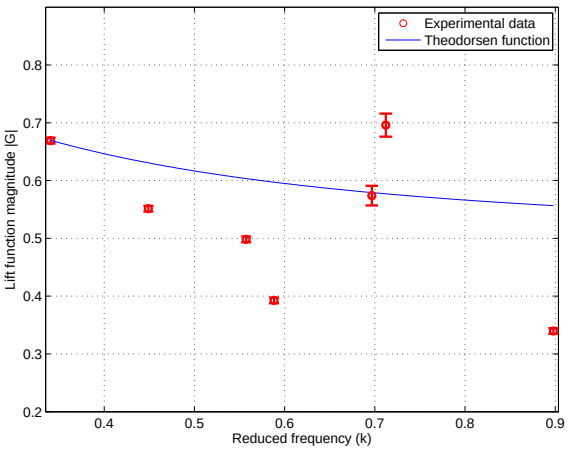

(b) $\alpha_0 = 20^o$

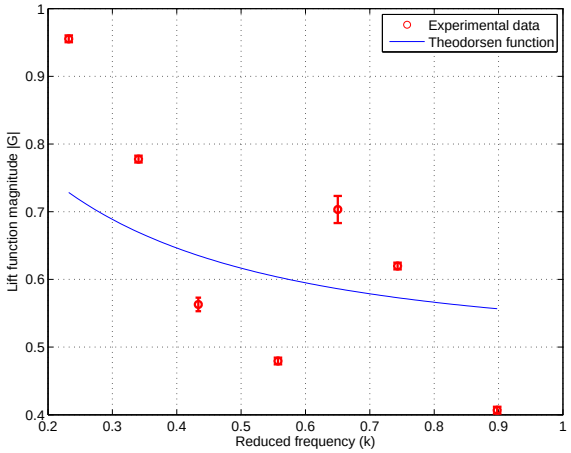

(c) $\alpha_0 = 25^o$

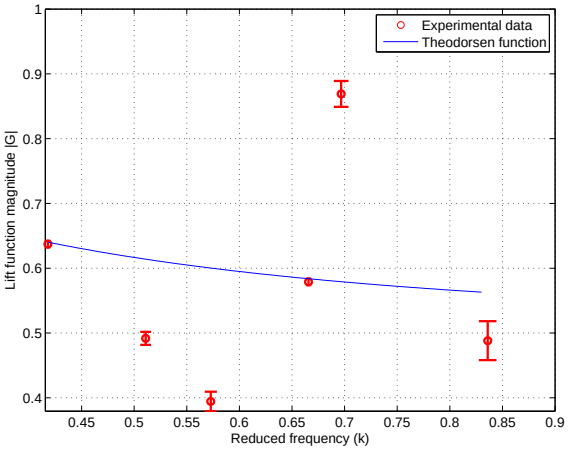

(d) $\alpha_0 = 30^o$

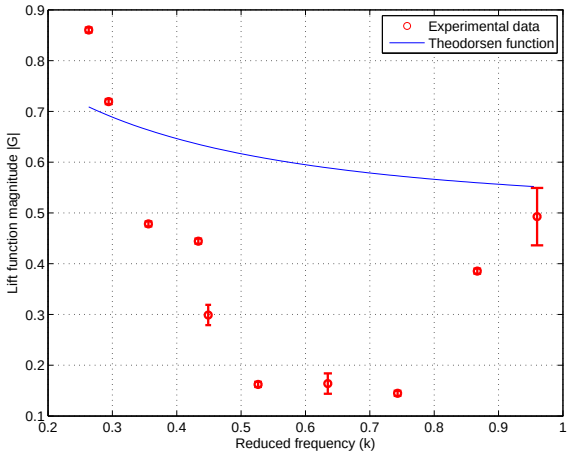

(e) $\alpha_0 = 35^o$

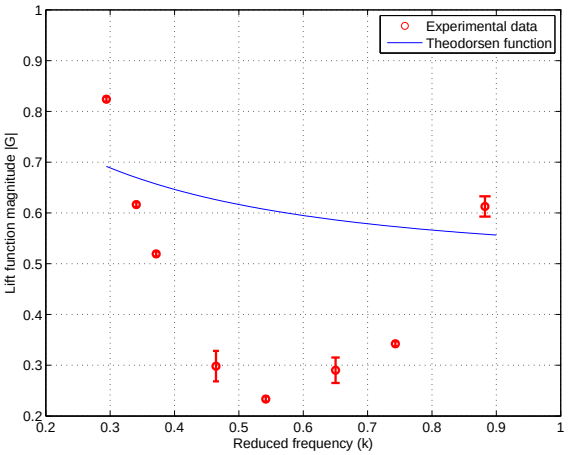

(f) $\alpha_0 = 40^o$

Figure 2.22: Magnitude of the lift frequency response in the stall regime: α_0 varies between 15° and 40°.

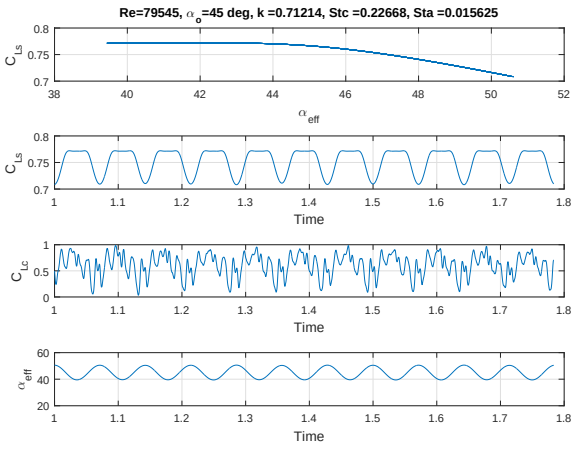

(a) $\alpha_0 = 45°$ and $k = 0.71$

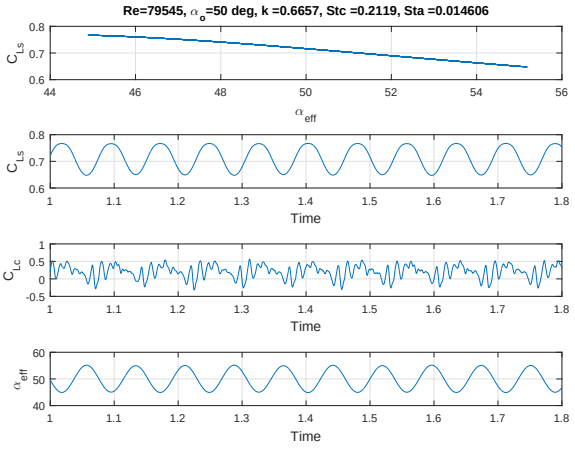

(b) $\alpha_0 = 50°$ and $k = 0.66$

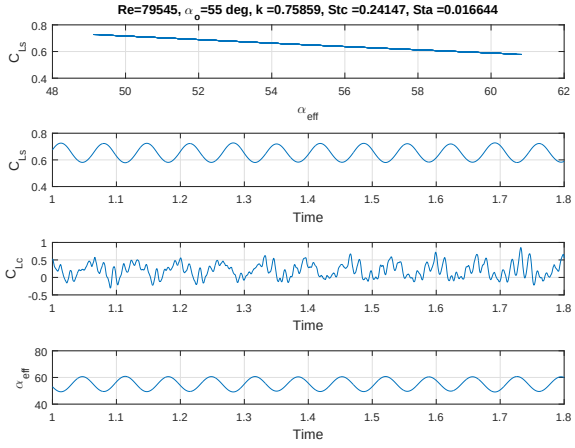

(c) $\alpha_0 = 55°$ and $k = 0.75$

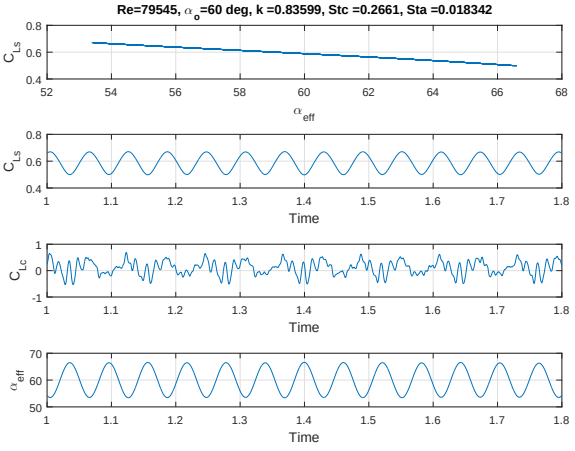

(d) $\alpha_0 = 60°$ and $k = 0.83$

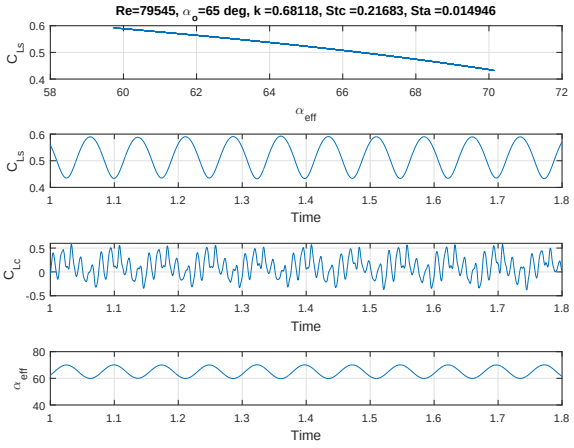

(e) $\alpha_0 = 65°$ and $k = 0.68$

Figure 2.23: Time histories of C_{L_s}, C_{Lc} and α_{eff} at various reduced frequencies along with the C_{L_s}-α_{eff} variation in the post-stall regime.

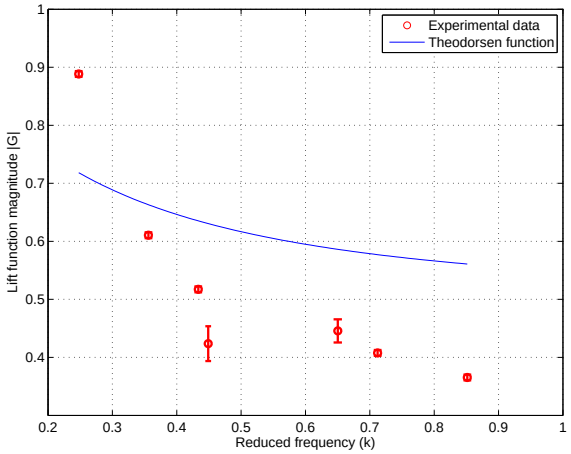

(a) $\alpha_0 = 45^o$

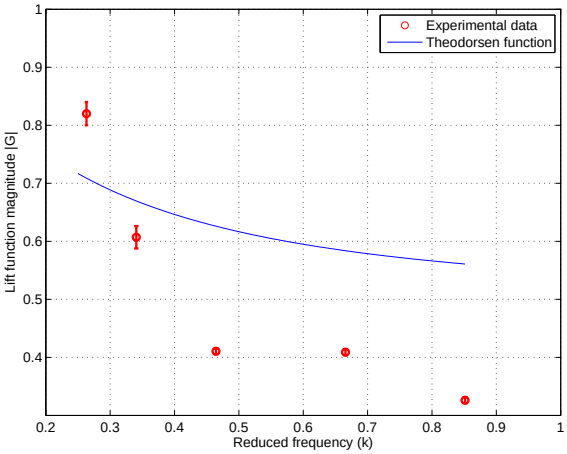

(b) $\alpha_0 = 50^o$

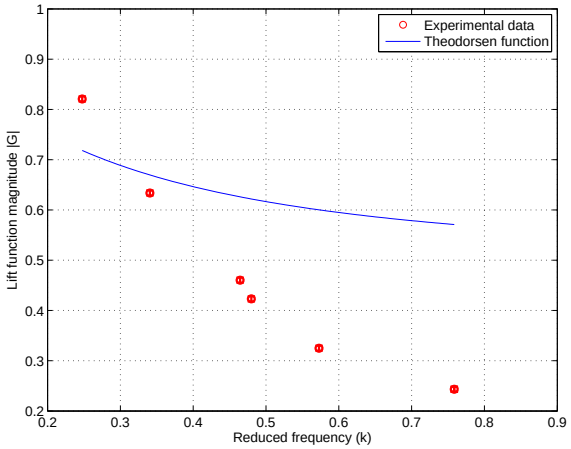

(c) $\alpha_0 = 55^o$

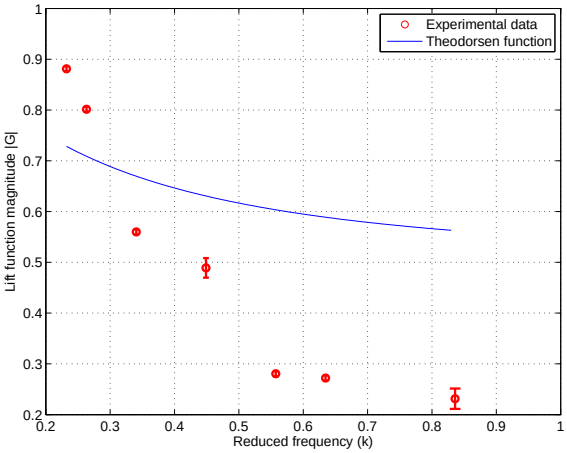

(d) $\alpha_0 = 60^o$

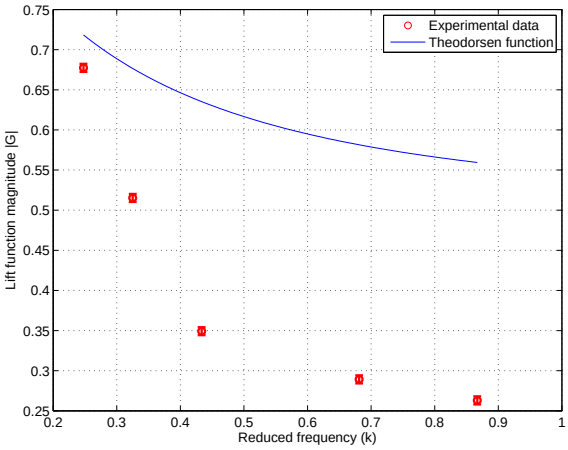

(e) $\alpha_0 = 65^o$

Figure 2.24: Magnitude of the lift frequency response in the post-stall regime: α_0 varies between 45° and 60°.

17.6 Hz and mean angles of attack (α_0 = 0°, 15°, 40°, and 65°). For all cases, a distinct peak is clearly noted at the excitation/forcing frequency. At α_0=0°, 15°, 40° and for k<0.6, most of the energy of the lift fluctuations is concentrated in a frequency equal to that of the excitation frequency. For k>0.6, we note the appearance of peaks at the superharmonics of the excitation frequency, particularly in the range between 50 and 75 Hz which covers the frequency band of the static lift fluctuations. Of particular importance is the case of α_0 = 15° and k=0.7, which shows two peaks with equal magnitudes near f=15 and f=70 Hz indicating perfect resonance between the oscillation of the wing and the formation and shedding of vorticity into the wake. This resonance can also be seen in the time series of the measured lift coefficient presented in Fig. 2.21(a) and disused above. This is also the case of enhanced lift presented in Fig. 2.22(a) where the appearance of these two peaks is indicative of nonlinear interactions in flow dynamics. It should be noted that, while plunging leads to diminishing the natural shedding activities, the higher harmonics due to the nonlinear effects at relatively large reduced frequencies are close to the natural shedding frequency. As such, the observed lift enhancement mechanism may be attributed to the convected LEV lift enhancement mechanism discussed by Gusrul et al. [50] which is found to be effective when the plunging frequency resonates with the natural shedding frequency, its harmonics or sub-harmonics. We will present below flow visualization to determine the flow characteristics resulting in the enhanced lift. In the post-stall regime, represented in Fig. 2.25(d) by α_0=65°, we note that the high frequency components are more present even for small values of reduced frequencies. This is due to the fact that vortex shedding is enhanced at these high angles of attack.

2.7 Physical Insight Through Flow visualization

In order to provide a physical insight into the observed lift enhancement mechanism, flow visualizations were performed by seeding ceramic particles in a water channel facility having a test chamber sectional area of 58 cm width and 83 cm height. The seeded particles were illuminated by a NDYAG laser sheet at the mid section of the used profile. High speed images were recorded at 200 frames per sec using a CCD camera with a resolution of 1024 x 840 pixels

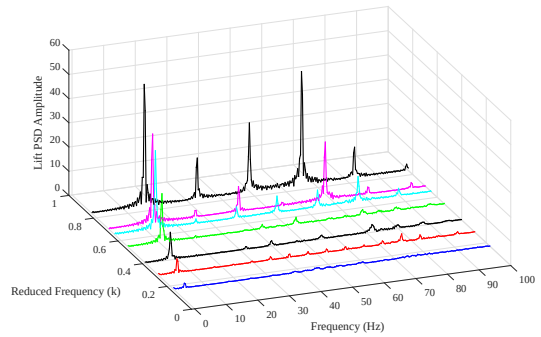

(a) $\alpha_0 = 0°$.

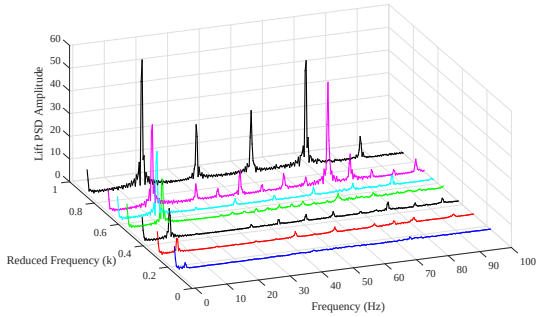

(b) $\alpha_0 = 15°$.

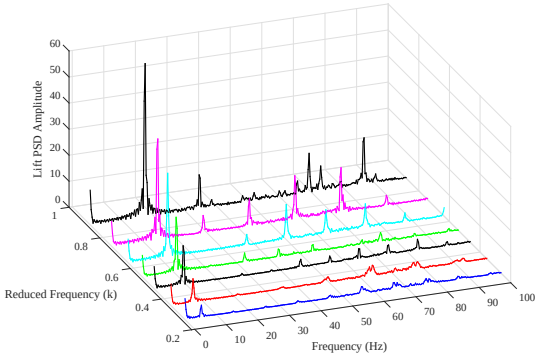

(c) $\alpha_0 = 40°$.

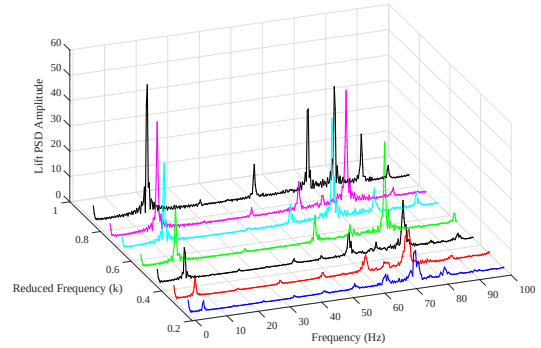

(d) $\alpha_0 = 65°$.

Figure 2.25: Frequency spectra of the measured lift over NACA 0012 at $Re = 79,900$ due to plunging at various reduced frequencies and mean angles of attack.

coupled with 50 mm $f1.2$ Nikon lens. The flow speed was 0.5 m/s, which yielded a Reynolds number of $70,000$. The cases of $k = 0.5$, $k = 0.7$ and $k = 0.9$ were considered because it is the conditions before and after the observed lift enhancement (k=0.7). The turbulence level is 1% and wing experienced less than $0.05c$ tip deflection due to hydrodynamic loading at the maximum operating frequency (1.2 Hz). Moreover the deflection is more negligible near the mid-span section where the visualization was performed. The advantage of using this technique versus a smoke visualization technique is that the generated streamlines would not deteriorate as they would at high flow speeds. The same pitch-plunge mechanism, wing profile (NACA 0012) and chord were used. The wing was painted with a matte black color to prevent reflection. The mechanism was hanged upside down above the test section as shown

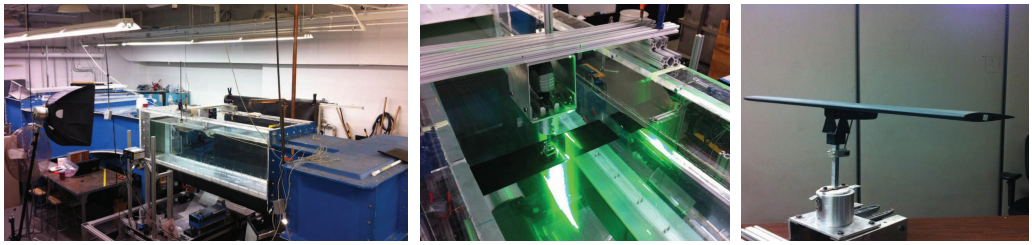

Figure 2.26: Pitch-plunge mechanism mounted in the test chamber of the water channel.

in Fig. 2.26.

Figure 2.27 shows a flow visualization sequence of pictures taken over one period of pure plunging oscillation about $\alpha_0 = 15^o$ at $k = 0.7$. The sequence starts at $t/T = 0$ with the wing at its highest position (a) and having zero velocity. It also shows pictures over constant time separations of $t/T = 1/20$. Because of the plunging velocity of the wing, the effective angle of attack varies between 20.5° at position (f) and 9.5° at position (p) (i.e., $15° \pm 5.5°$). Figure 2.28 shows the plunging cycle related to each picture presented in Fig. 2.27.

Between (a) and (f), the wing accelerates downwards from a zero plunging speed at (a) to a maximum plunging speed of 4.86 cm/s at (f), which corresponds to an increase in the effective angle of attack from 15° at (a) to 20.5° at (f). The vortex over the wing near the trialing edge, shown in (a), is a remnant of a LEV that has formed during the previous cycle. Between (f) and (k), the wing has a downward velocity while decelerating from 4.86 cm/s at (f) to zero velocity at (k). Consequently, the effective angle of attack decreases from 20.5° to 15°. This decrease results in the wing re-approaching the stall conditions. Over this time period, a LEV starts to form at position (f) and grows until it forms a coherent vortex structure at the (j) position. Between positions (k) and (o), the wing is moving upwards, which results in a further decrease in the effective angle of attack from 15° to 9.5°. Meanwhile, the LEV continues its excursion along the upper surface. Between (o) and (t), the wing moves upwards while decelerating, which results in an increase in α_{eff} from 9.5° to 15°. Over this region, the coherent structure becomes less visible indicating vortex breakdown as it leaves the trailing edge.

Figure 2.29 shows a picture sequence from (i) to (p). On each picture, a cm ruler is

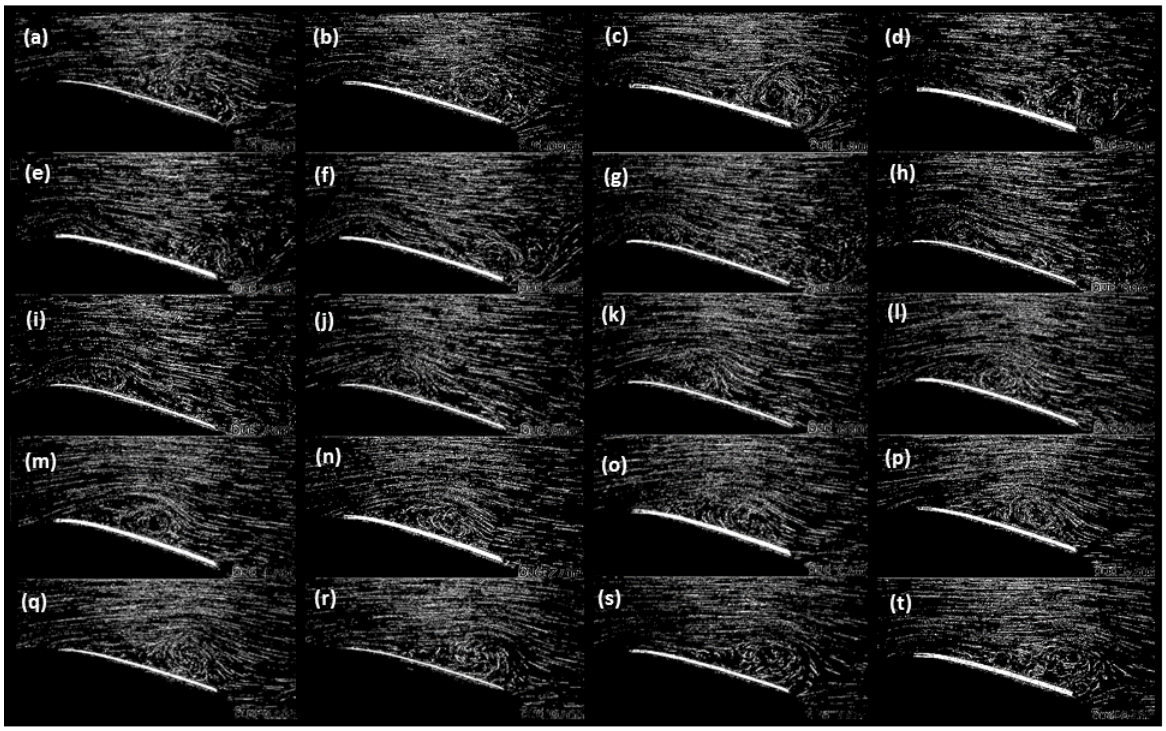

Figure 2.27: Flow visualization sequence of one plunging period with $k = 0.7$ at 15^o AOA. The sequence starts at $t/T = 0$ (top of stroke (a)) and follows in constant steps of 1/20. The effective angle of attack varies between 9.5° to 20.5°.

placed along the airfoil chord to locate the position of the vortex core. Picture (i) shows the LEV at $0.3c$ from the leading edge. By tracing the picture sequence, one can observe a LEV convection velocity along the top surface of approximately 12 $cm/s = 0.24U_\infty$. This relatively slow convection, in comparison to the free stream velocity, indicates that the LEV remains attached to the surface over this period. The presented visualization shows that the vortex forms when α_{eff} is close to 15° and the wing is moving downwards at a decelerating rate which mitigates separation effects. The wing deceleration allows the LEV to remain attached to the top surface. This synchronization between the reduction of the effective angle of attack and the development of the leading edge vortex results in lift enhancement. These observations are similar to those of Cleaver et al. [79] who performed a plunging experiment at a mean angle of attack of 15° and lower Reynolds number ($Re = 10,000$).

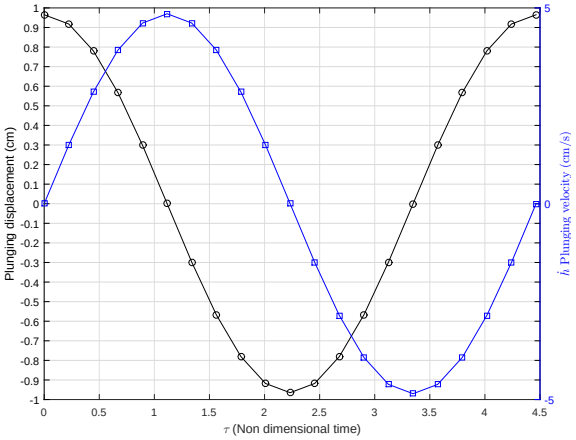

(a) Plunging velocity and displacement versus non-dimensional time

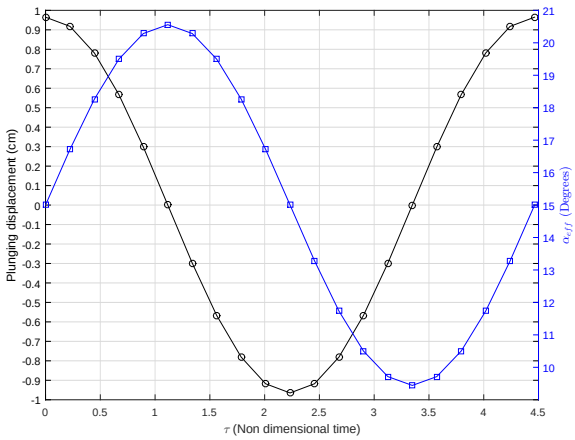

(b) Plunging displacement and effective angle of attack versus non-dimensional time

Figure 2.28: One plunging period with $k = 0.7$ at 15^o AOA

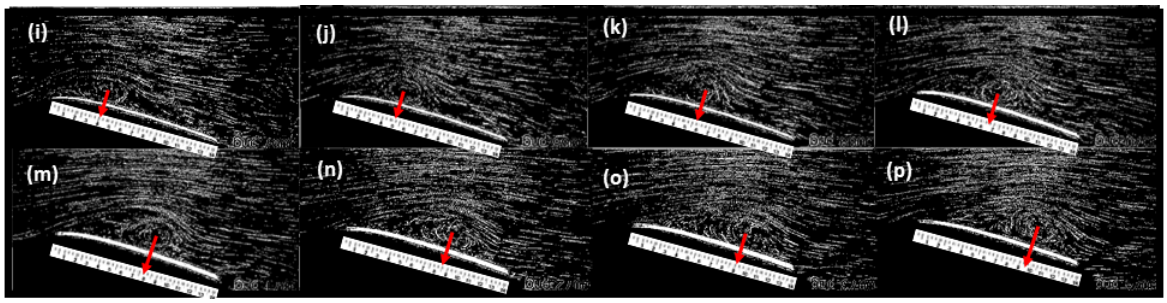

Figure 2.29: Flow Visualization sequence pictures of the LEV convection on the upper surface of NACA 0012 listed in Fig. 2.27. A ruler placed along with the chord line is used to determine the vortex core.

Li and Wu [14] concluded that a LEV convecting downstream on the upper surface of an airfoil enhances the lift when it is near the leading edge and reduces the lift as it approaches the trailing edge. Inspecting Fig. 2.27, we find that, near the mid-stroke region covered by (i)-(l), the LEV maintains a strong core while convecting downstream on the upper surface and remaining close to the leading edge, which results in lift enhancement as suggested by Li and Wu [14] and Chow et al. [80]. This LEV lift enhancement is coincident with the maximum quasi-steady lift at point (k) where $\alpha_{\text{eff}} = 15°$ as shown in Fig. 2.30. Likewise, near the maximum upward plunging speed covered by (p)-(r), the LEV approaches the trailing edge,

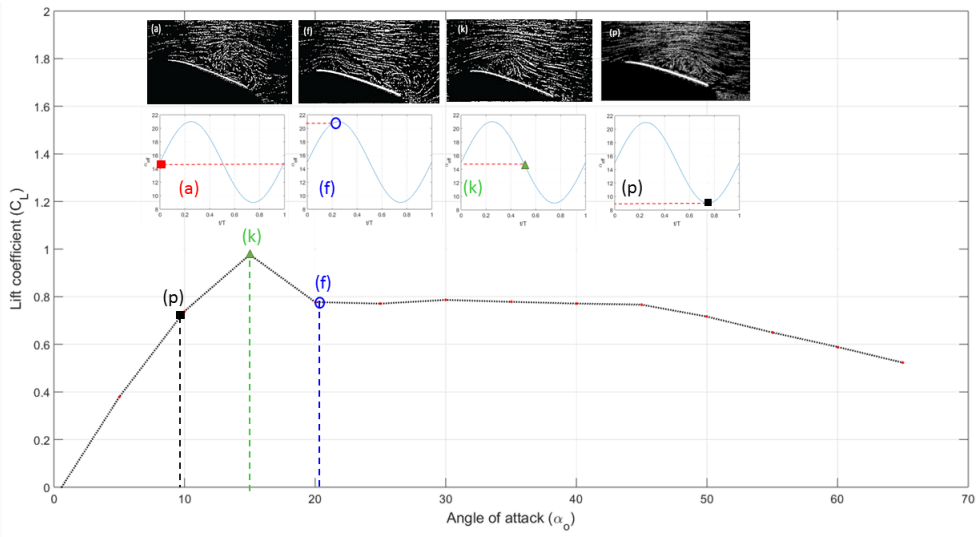

Figure 2.30: Steady C_L-α curve of NACA 0012. The points marked corresponds to the effective angle of attack starting with the wing is at its highest position and going downward (a), at zero position and having a downward velocity (f), at the lowest position and going upward (k) and at zero position with an upward velocity (p).

causing a lift reduction that is also coincident with the lowest quasi-steady lift at point (p) where $\alpha_{\text{eff}} = 9.5°$. Therefore, similar to the conclusions of Choi et al. [75], the observed lift enhancement mechanism is attributed to a synchronization between the motion frequency and LEV shedding time-scale such that the changes in the LEV lift and the quasi-steady lift are coincident.

Figures 2.31 and 2.32 show a full period flow visualization at an angle of attack of 15^o for reduced frequencies $k = 0.5$ and $k = 0.9$, respectively. Similarly to the case of k=0.7, we note that a LEV starts to emanate from the leading edge (i) and moves downstream (t). Then, it starts to amalgamate with a trailing edge vortex towards the end of the plunge cycle. We note that it is hard to identify the vortex core as we were able to do for the case of k=0.7.

To quantize the LEV shedding velocity relative to the free stream, we perform the same procedure as presented in the analysis of Fig 2.29. Fig. 2.33 and Fig. 2.34 show the upstroke as the wing moves upwards for $k = 0.5$ and $k = 0.9$, respectively. Noting the difficulty in

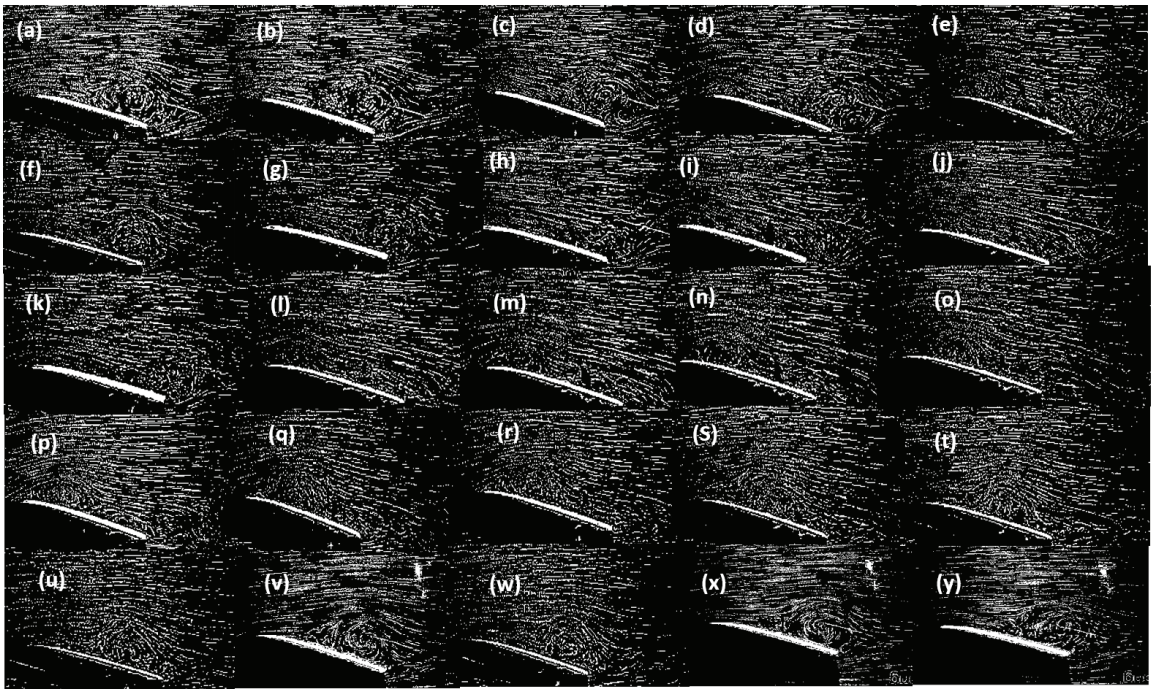

Figure 2.31: Flow visualization sequence of one plunging period with $k = 0.5$ at 15^o AOA. The sequence starts at $t/T = 0$ (top of stroke (a)) and follows in constant steps of 1/25. The effective angle of attack varies between 11° to 19°.

identifying the vortex core, we summarizes in Table 2.2 approximate values for the convection velocities for the three selected cases of reduced frequencies.

It is clear from Table 2.2 that the case $k = 0.7$ shows lower values of LEV convection velocity downstream compared to the other two cases, $k = 0.5$ and $k = 0.9$, which an be associated with the lift enhancement observed for $k = 0.7$ case.

2.8 Optimization based system identification

The flow dynamics in the linear regime can be satisfactorily described by Theodorsen's response. On the other hand, as discussed in the introduction, there is a lack of efficient models governing the dynamics in the stall regime. It should be noted that even the linearized, potential flow models (e.g., Theodorsen's and Wagner's) that also presume flat wake

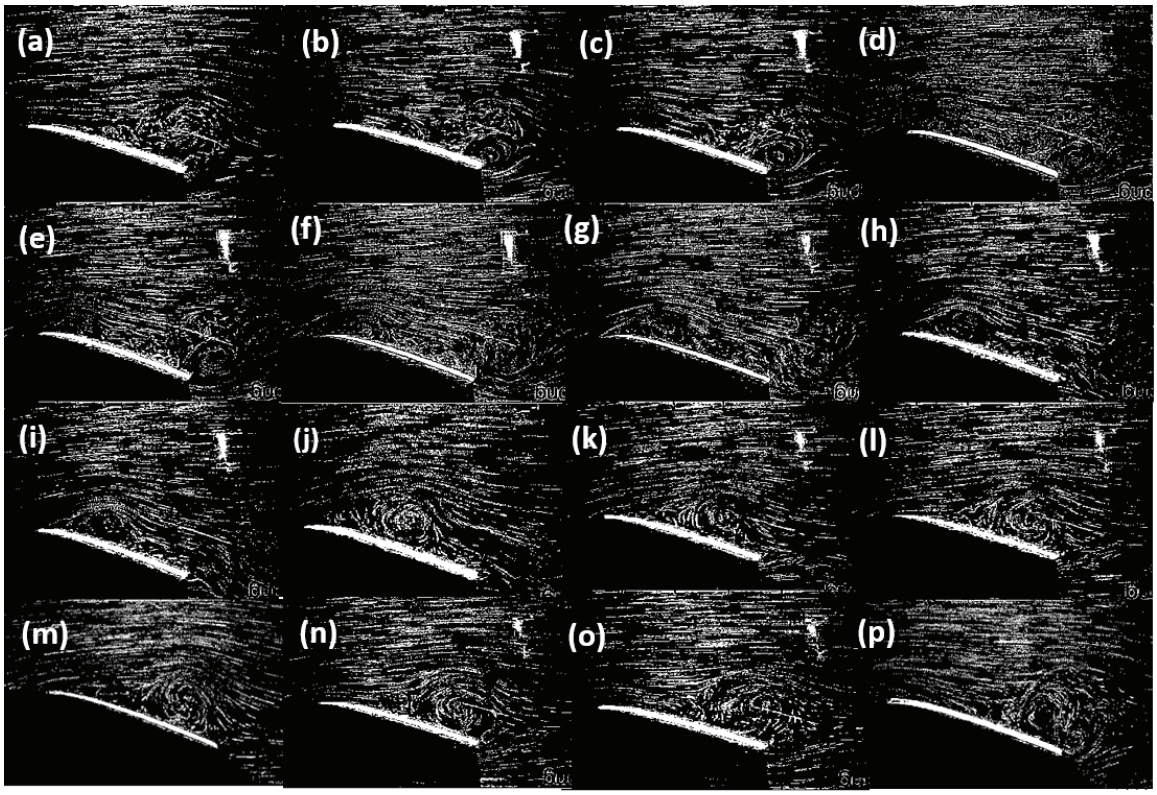

Figure 2.32: Flow visualization sequence of one plunging period with $k = 0.9$ at 15^o AOA. The sequence starts at $t/T = 0$ (top of stroke (a)) and follows in constant steps of 1/16. The effective angle of attack varies between 8° to 23°.

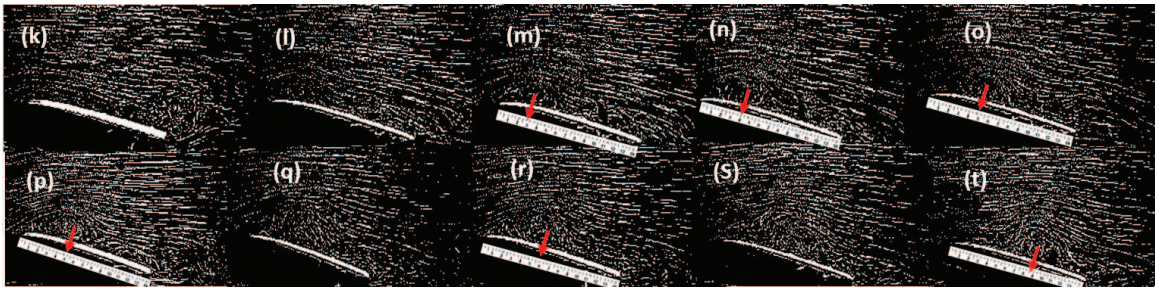

Figure 2.33: Flow Visualization sequence pictures of the LEV convection on the upper surface of NACA 0012 listed in Fig. 2.31. A ruler placed along with the chord line is used to determine the vortex core.

Table 2.2: Leading edge vortex convection velocities based on the flow visualization for three different reduced frequencies.

Reduced frequency (k)	time step (δt)	f_{air} (Hz)	f_{water} (Hz)	Convection velocity (cm/s)
0.9	0.0625	17.7	1	20
0.7	0.0625	13.8	0.8	12
0.5	0.071	9.8	0.56	18

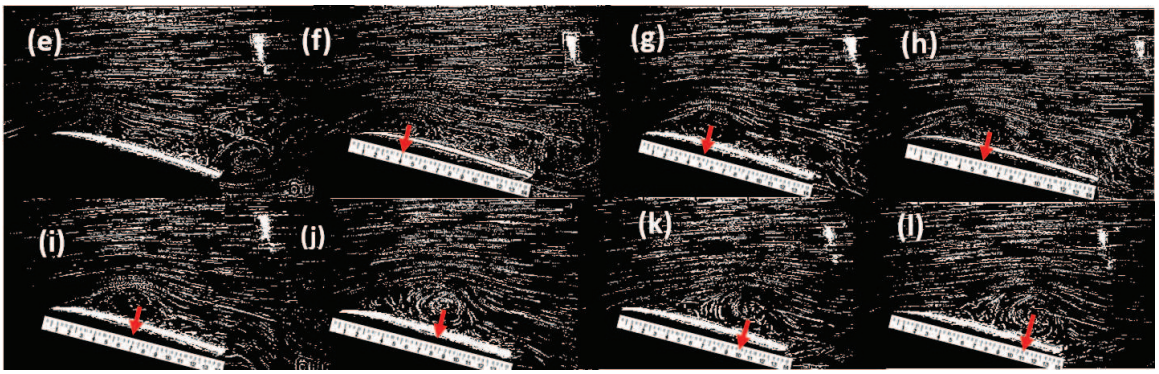

Figure 2.34: Flow Visualization sequence pictures of the LEV convection on the upper surface of NACA 0012 listed in Fig. 2.32. A ruler placed along with the chord line is used to determine the vortex core.

and shedding-by-free-stream result in infinite dimensional dynamical responses. To develop an efficient model that is suitable for optimization, sensitivity analysis, dynamics and control analyses as well as preliminary design of engineering systems, we seek a finite-dimensional approximation to the dynamical behavior (the frequency response) in each of the regimes discussed above. The order of the finite-dimensional approximation is arbitrary. In fact, there is no consensus about the appropriate order of a finite-dimensional approximation even to a linear dynamical response. Useful two dimensional approximation for linear unsteady aerodynamics (i.e., Theodorsen's and Wagner's responses) were developed by Jones [81] and Jones [82]. More recent work on finite-state aerodynamic modeling using Pade approximants can be found in Vepa [83]. In contrast to fitting Theodorsen's and Wagner's responses, finite-state models were derived from the basic principles by Peters and Karunamoorthy [84], Peter et al. [85], and Peter [86], though required a relatively high order (eighth-order) for good

accuracy. In this work, we determined that the minimum order of a dynamical system that can fit the data of the stall-regime, which exhibited the most dynamically-rich response, is four. As such, we write the approximating fourth-order dynamical system as:

$$\begin{aligned}
\frac{d}{d\tau}\begin{pmatrix}\chi_1(\tau)\\ \chi_2(\tau)\\ \chi_3(\tau)\\ \chi_4(\tau)\end{pmatrix} &= \begin{bmatrix} 0 & 1 & 0 & 0\\ 0 & 0 & 1 & 0\\ 0 & 0 & 0 & 1\\ -a_0 & -a_1 & -a_2 & -a_3\end{bmatrix}\begin{pmatrix}\chi_1(\tau)\\ \chi_2(\tau)\\ \chi_3(\tau)\\ \chi_4(\tau)\end{pmatrix} + \begin{pmatrix}0\\0\\0\\1\end{pmatrix} C_{L_s}(\alpha(\tau))\\
C_{L_c}(\tau) &= \begin{bmatrix} b_0 & b_1 & b_2 & b_3\end{bmatrix}\begin{pmatrix}\chi_1(\tau)\\ \chi_2(\tau)\\ \chi_3(\tau)\\ \chi_4(\tau)\end{pmatrix}
\end{aligned} \tag{2.5}$$

where the χ's represent the internal aerodynamic states, $\tau = \frac{U_\infty t}{b}$ is the nondimensional time, and a's and b's are constant coefficients. The transfer function of the system (2.5) is written as:

$$G(p) = \frac{C_{L_c}(p)}{C_{L_s}(p)} = \frac{b_3p^3 + b_2p^2 + b_1p + b_0}{p^4 + a_3p^3 + a_2p^2 + a_1p + a_0} \tag{2.6}$$

where, p is the non-dimensional Laplace variable corresponding to the non-dimensional time-variable τ. To obtain the magnitude of the frequency response of this transfer function, we substitute $p = ik$, which yields:

$$|G(k)| = \sqrt{\frac{(b_0 - b_2\omega^2)^2 + (b_1\omega - b_3\omega^3)^2}{(a_0 - a_2\omega^2 + \omega^4)^2 + (a_1\omega - a_3\omega^3)^2}} \tag{2.7}$$

To determine the coefficients of the transfer function given in Eq. (2.6), we set up and solve, for each α_0, the following optimization problem.

$$\min_{\boldsymbol{x}} \quad e^2_{|G|} = \sum_i^N \left(|G(k_i)| - |G_{\text{meas}}(k_i)|\right)^2 \quad \text{subject to}$$

$$\frac{b_0}{a_0} = 1 \ \text{ and } \ \mathcal{R}\left[\text{roots}(p^4 + a_3p^3 + a_2p^2 + a_1p + a_0)\right] < 0$$

where $\boldsymbol{x} = [a_0, a_1, a_2, a_3, b_0, b_1, b_2, b_3]$ represents the vector of design variables (transfer function coefficients), $|G_{\text{meas}}(k_i)|$ is the measured frequency response at the data point k_i, N is the number of measurements, and $\mathcal{R}$ represents the real part of its argument. The first

(equality) constraint (i.e., unity transfer function dc gain) is dictated by the physics of the problem. That is, the ratio between the unsteady and steady loads at zero frequency must be unity. The second (inequality) constraint is to ensure that the selected transfer function given in Eq. (2.6) has poles with negative real parts; that is, we have stable flow dynamics as suggested by Jefferys et al. [87]. We use sequential quadratic programming to solve the above posed optimization problem.

Figure 2.35 shows the magnitude of the lift frequency response data points from the measurements at $\alpha_0 = 0^o$, 5^o and 10^o along with that of Theodorsen's. Additionally, we show the frequency response of the fitted fourth-order system. The plot shows good matching among the three sets. It should be noted that the infinite dimensional nature of Theodorsen's response renders its magnitude an infinite slope at $k = 0$, which cannot be realized by any finite-dimensional approximation. As such, there will always be a boundary-layer-like range near small values of k over which there is a mismatch between Theodorsen's response and its finite-dimensional approximation. On the other hand, because of Theodorsen's way of defining the circulatory lift, the high frequency gain is non-zero (1/2), which cannot be realized by any realistic dynamical system. A non-zero high-frequency gain comes from a transfer function whose numerator's degree is higher than or equal to its denominator's degree (i.e., non-strictly proper transfer function). This implies a non-zero instantaneous response of the system output. This non-physical behavior is due to Theodorsen's definition of the circulatory lift, which is the common definition in Fung [88]. Interestingly, the majority define the circulatory lift not as the lift due to bound circulation. Rather, they adopt an easily computed definition that incorporates an added-mass component. The former definition would result in an indicial response that has a zero initial value and a frequency response of a zero high-frequency gain. The latter common definition results in the Wagner's indicial response having initial value of 1/2 and the Thodorsen's frequency response having a high-frequency gain of 1/2. This point is discussed in detail in Peters 2008.

Theodorsen's model is based on a linear approximation for the flow dynamics, which results in a frequency response that is independent of the operating condition and/or the amplitude of the aerodynamic input (airfoil motion). However, the geometric and non-planar-wake nonlinearities are expected to result in a different frequency response (i.e., linearized flow

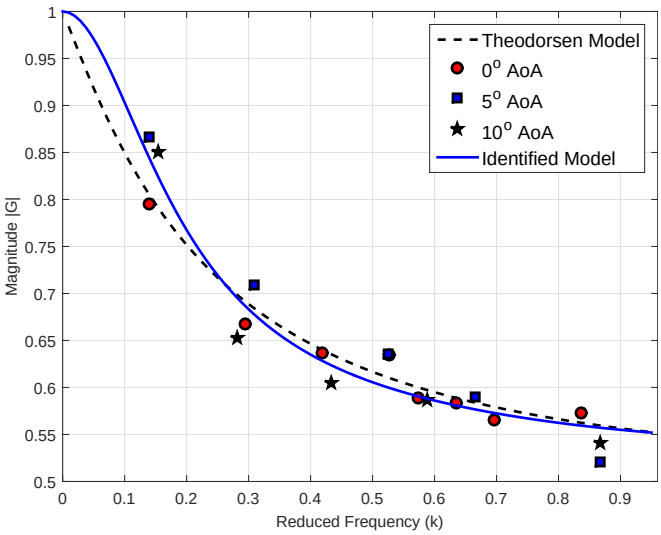

Figure 2.35: Lift frequency response function for the linear regime (0^o - 10^o AOA).

dynamics) at different operating conditions (angles of attack). In addition, it is important to note that if an aeroelastic and/or flight dynamic stability is to be checked around some equilibrium at relatively large angle of attack (i.e., $\alpha > 10^\circ$), Theodorsen's linear model will not be valid even for the sake of linear/local stability analysis. This motivates developing even a linearized model governing the flow dynamics at high angle of attack. Figure 2.36 shows the three sets of frequency response data including the measured points, Theodersen's response and the fitted fourth-order representations for $\alpha_0 = 15^o$, 20^o, 25^o and 30^o. The results show that the proposed fourth order model is able to capture the flow dynamics in the stall regime. Since the frequency responses at $\alpha_0 = 35^o$ and 40^o are different from that of the whole stall regime (lift enhancement shifted towards higher reduced frequencies), we did not consider their data in the optimization process for the stall regime. As mentioned earlier, we consider these cases as a transition phase between stall and post-stall regimes. Figure 2.37 shows show the three sets of frequency response data for $\alpha_0 = 45^o$, 50^o, 55^o, 60^o and 65^o. The results show good matching between the proposed model and the experimental data for all operating angles of attack.

Brunton and Rowley [27], introduced a modification for Theodorsen's frequency response model for unsteady lift that is more suitable for low Reynolds number flow. It should be

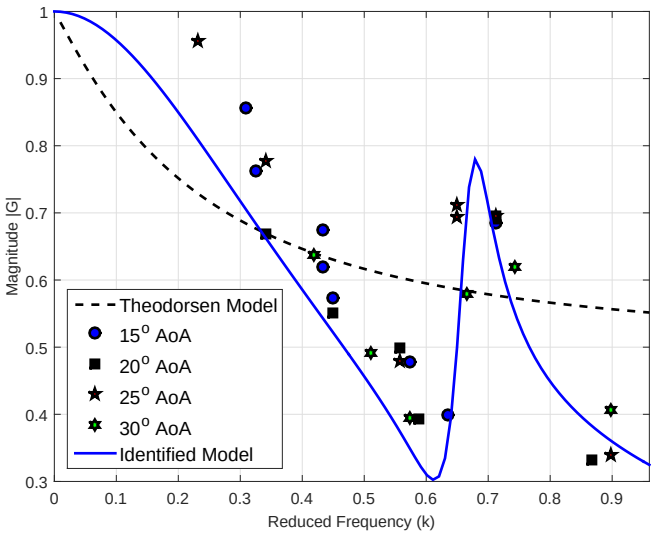

Figure 2.36: Lift frequency response function for the stall regime (15^o - 30^o AOA)

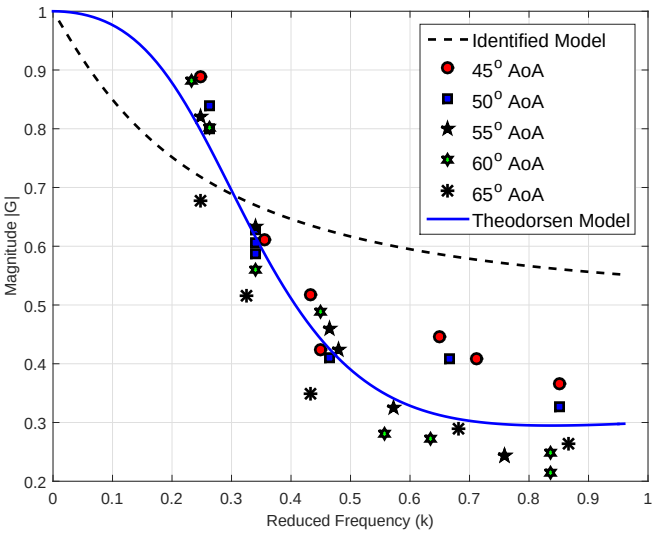

Figure 2.37: Lift frequency response function for the post-stall regime (45^o - 65^o AOA)

noted that, their model does not include the Reynolds number as a varying parameter, as it was obtained at a single value of the Reynolds number ($Re = 100$). As such, it does not naturally yield to Theodrsen's model at for high Reynolds number.

In our problem formulation, the angle of attack is the varying parameter. It is intuitive to

α_0	$a_o = b_o$	a_1	a_2	a_3	b_1	b_2	b_3
Theodorsen	3.1701	30.7108	24.2644	1.2726	-15.8178	-9.2929	-1.2673
Linear	4.6823	32.0823	23.4877	1.3979	-13.0734	-9.3572	0.4512
Stall	0.1207	0.5054	0.7807	1.1556	-0.0676	0.2854	-0.2198
Post-stall	5.1463	22.9454	46.0681	1.1607	-8.3369	12.0981	3.3905

Table 2.3: Optimized coefficient for the proposed reduced-order dynamical system (eq.2.6 and eq.2.5) for the three operating regimes.

aim at glowing the obtained models at different angles of attack so that they naturally yield to Theodorsen for small angles of attack. This should be performed carefully as direct switching between different models may cause fictitious instability. This invokes the Linear Parameter Varying (LPV) control theory as a mathematical analysis tool, which will be considered in future work.

2.9 Unified State Space Modeling

As shown in the previous section, the constructed models in the linear and post-stall regimes do not have a considerable dependence on the operating angle of attach and, as such, are combined in a single response function, each. On the other hand, the frequency response in the stall regime depends on α_o; the frequency and amplitude of the lift peak is different for various operating angles of attack. Since the constructed state space model is of the abstract form:

$$\begin{aligned} \dot{\boldsymbol{x}} &= [\boldsymbol{A}]\boldsymbol{x} + [\boldsymbol{B}]C_{L_s} \\ C_{L_{\text{circulatory}}} &= [\boldsymbol{C}]\boldsymbol{x} \end{aligned} \tag{2.8}$$

We propose combining the obtained linearized dynamics in the stall regimes at various angles of attack by writing the coefficients of the transfer function [89] (consequently, the entries of the matrices) as polynomials functions of the mean angle of attack as:

$$\begin{aligned} \dot{\boldsymbol{x}}(t) &= [\boldsymbol{A_2\alpha(t)^2} + \boldsymbol{A_1\alpha(t)} + \boldsymbol{A_0}]\boldsymbol{x}(t) + [\boldsymbol{B}]C_{L_s}(\boldsymbol{\alpha}(t)) \\ \boldsymbol{C_{L_{\text{circulatory}}}}(t) &= [\boldsymbol{C_2\alpha(t)^2} + \boldsymbol{C_1\alpha(t)} + \boldsymbol{C_0}]\boldsymbol{x}(t) \end{aligned} \tag{2.9}$$

Note that the state space form results in the same $\boldsymbol{B}$ matrix. Figure 2.38 shows the variations of the coefficients of the transfer function (equivalently the state space model) with the

operating angle of attack in the stall regime along with their quadratic fit. Two sets of data are excluded from this fit and kept for validation. These are the experimental data at $\alpha_0 = 25°, 40°$, respectively.

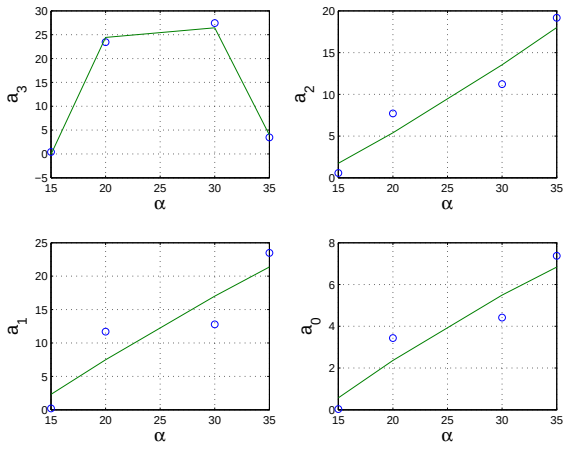

(a) Fourth order transfer function numerator coefficients

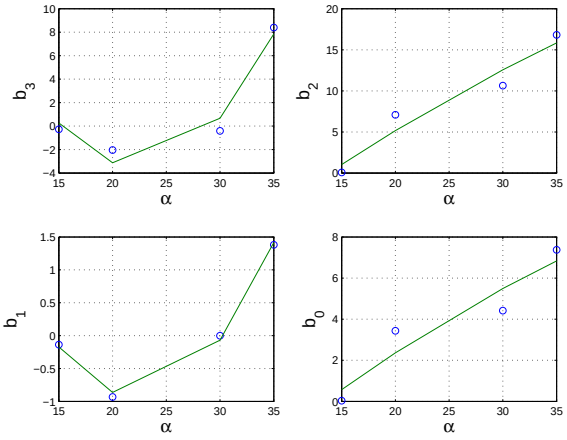

(b) Fourth order transfer function denominator coefficients

Figure 2.38: Variation of the transfer function coefficients with α_0 in the stall regime along with their quadratic fit.

2.10 Results and Validation

The resulting model is then validated in frequency and time domains by comparing the model's prediction against the unsteady measurements for angles of attack $\alpha_0 = 25$ and 40 degrees.

2.10.1 Frequency domain comparison

Figure 2.39 shows the results for the proposed model and the experimental data with the fitted function based on the optimized coefficients. The plots in Fig.2.39 show that the proposed model captures the unsteadiness and the lift enhancement in the neighborhood of the amplitude jump associated with all the unsteady stall regime.

In Fig. 2.39(a), the model characterize an existing lift enhancement at k=0.61, this value corresponds to a maximum lift gain function of one. The model presented in 25^o test case

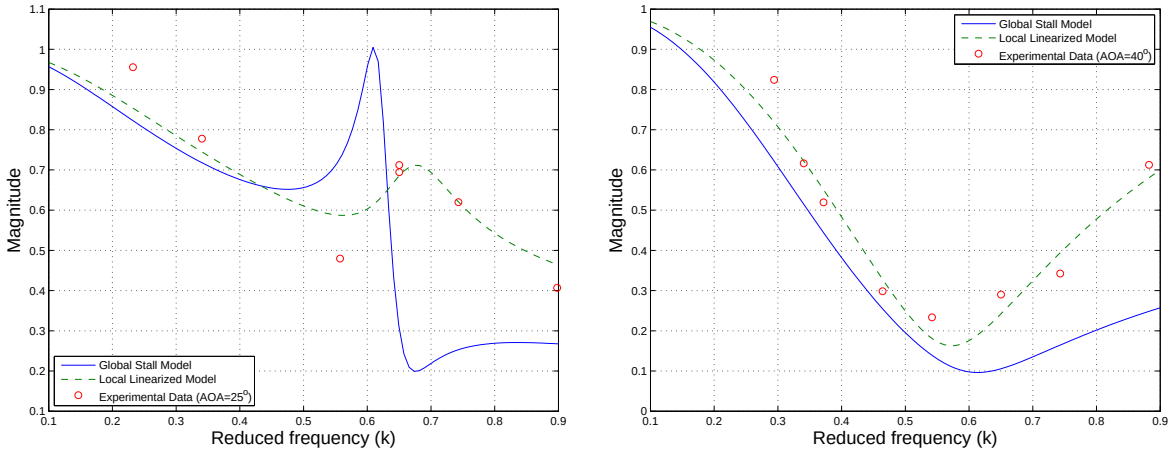

(a) Lift response function for test case $\alpha_o = 25^o$ (b) Lift response function for test case $\alpha_o = 40^o$

Figure 2.39: Global and Local models comparison with test cases

shows an over-predicted trend than the local optimized model. Figure 2.39(b) shows the global model also captured the dynamics at 40^o AOA test case with a slight discrepancy from the local optimized model.

2.10.2 Time domain Comparison

A more rigorous validation for the model presented in eq.2.9 is performed by comparing the time history of the obtained lift with the measured one. It should be noted that in this implementation, the effective angle of attack α_{eff} is used in the place of α in eq.2.9. Figures 2.40(a), 2.41(a), 2.42(a) and 2.43(a), show the time domain comparison between experimental data and the proposed global model at α_o=25^o and a wide range of reduced frequency (k=0.21, 0.35, 0.41 and 0.74), respectively. Figures 2.40(b), 2.41(b), 2.42(b) and 2.43(b), show time histories for the quasi-steady lift coefficient and the corresponding effective angle of attack.

Figure 2.40 shows a good agreement with the experimental data with a slight shift appeared in the proposed model to be greater than the lift function amplitude of the experimental data. The quasi-steady lift coefficient shows a pure sinusoidal motion with time and linearly changes with the effective angle of attack. Increasing the reduced frequency in fig. 2.41 and fig 2.42, the proposed model shows satisfactory results for capturing the dynamics,

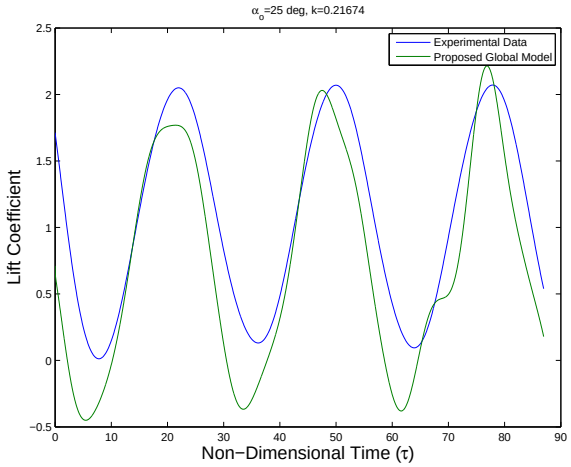

(a) Circulatory lift coefficient at 25^o AOA and k=0.21.

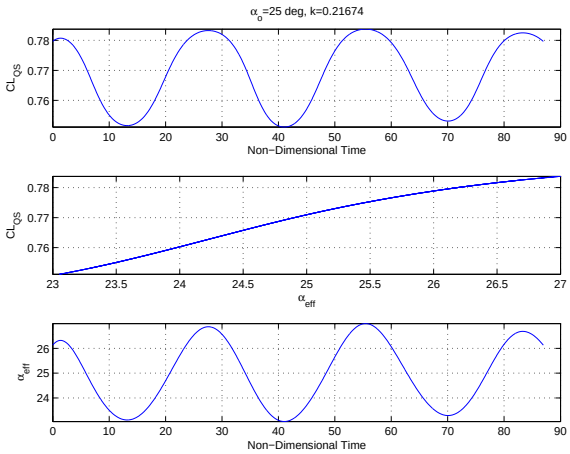

(b) Quasi-steady lift coefficient and α_{eff} at 25^o AOA and k=0.21.

Figure 2.40: Time domain comparison for $\alpha_0 = 25^o$ and k=0.21

while preserving the pure sinusoidal motion of the quasi-steady lift as well as the effective angle of attack. At a greater value of reduced frequency (k=0.74), we notice in fig.2.43 that the quasi-steady lift coefficient time history is no longer a pure sinusoidal. This is because this part of the $C_{L\alpha}$ curve characterized by a lack of monotonically nature (high non-linearity). Summing up the results, the proposed model shows acceptable results at low and high reduced frequency within the range of application.

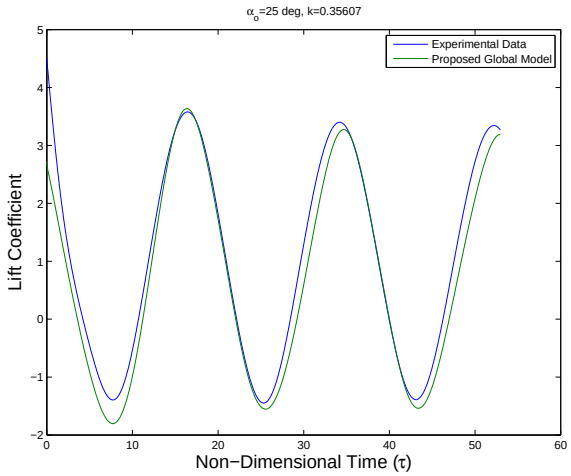

(a) Circulatory lift coefficient at 25^o AOA and k=0.35.

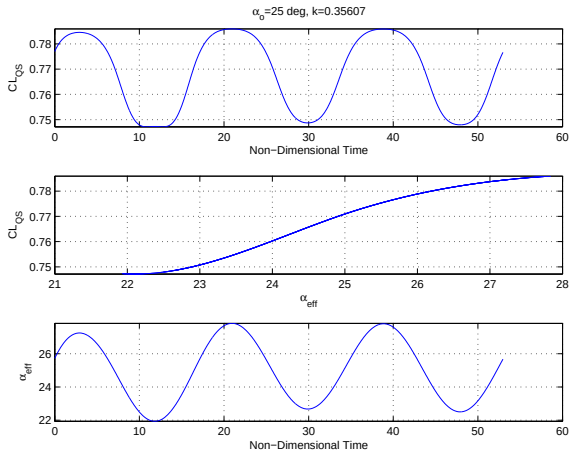

(b) Quasi-steady lift coefficient and α_{eff} at 25^o AOA and k=0.35.

Figure 2.41: Time domain comparison for $\alpha_0 = 25^o$ and k=0.35

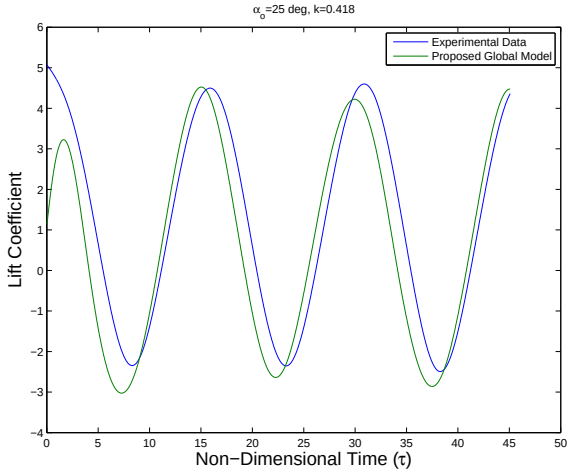

(a) Circulatory lift coefficient at 25^o AOA and k=0.41.

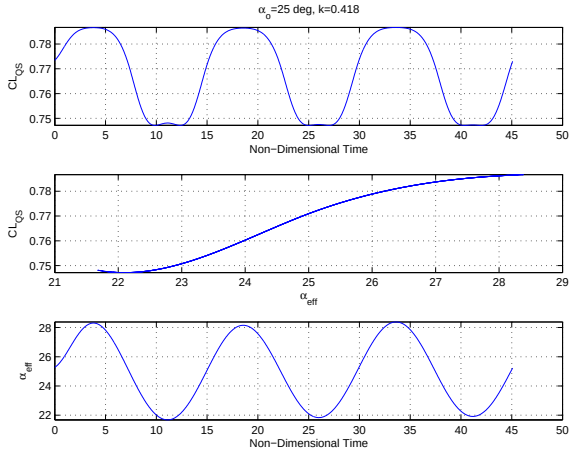

(b) Quasi-steady lift coefficient and α_{eff} at 25^o AOA and k=0.41.

Figure 2.42: Time domain comparison for $\alpha_0 = 25^o$ and k=0.41

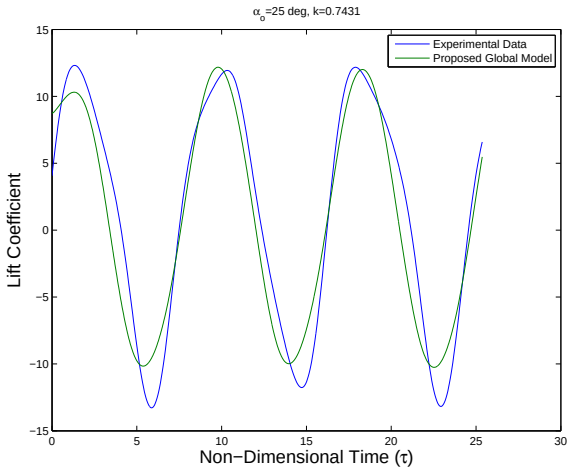

(a) Circulatory lift coefficient at 25^o AOA and k=0.74.

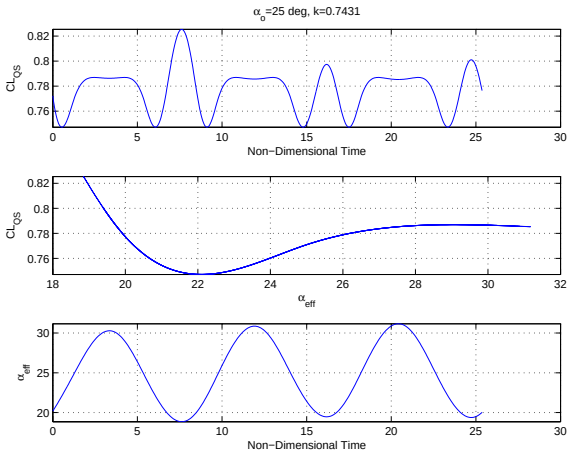

(b) Quasi-steady lift coefficient and α_{eff} at 25^o AOA and k=0.74.

Figure 2.43: Time domain comparison for $\alpha_0 = 25^o$ and k=0.74

Chapter 3

Measurements of oscillating two dimensional airfoil in stationary fluid flow

3.1 Introduction

The concept of the added mass was proposed by *Friedrich Bessel* in 1828 to explain differences between the periods [90]. In his quest to explain the period of oscillations of a pendulum when submerged in fluids and vacuum. He concluded that the inertial mass of the pendulum must be increased to account for the increase in kinetic energy of the fluid around it. For a pendulum with a spherical shape attached to a thin wire, the added mass was found to be one half of the displaced fluid mass. Inviscid potential flow analysis around a sphere accelerating in an otherwise stationary fluid reveals that the force on the sphere is totally due to the pressure gradient on the surface of the sphere that balances the local acceleration $\rho\partial\overrightarrow{V}/\partial t$. The pressure gradient that balances the convective term (non linear) acceleration $V \cdot \bigtriangledown\overrightarrow{V}$ produces zero forces.

On the other hand, fluid viscosity significantly influences the fluid force on a body in unsteady motion not only because of the rate of change of the fluid kinetic energy but also because it modifies the time dependent pressure gradient on the body and other forces due

to shear stress, flow separation and vortex shedding. In classical unsteady aerodynamic problems, the forces are usually split into those due to the relative acceleration between a moving body immersed in a fluid and circulatory forces induced by the vortical structure interaction associated with the wake [91–93]. Yet, such a separation is not very clear in some applications. For instance, an oscillating airfoil in still air may generate its own flow patterns. As such, additional forces are not related to added mass forces only but to forces generated by the vortex shedding and flow separation.

Chen et al. [94] derived a closed-form solution for the added mass and damping coefficient on a cylindrical rod vibrating in a viscous fluid contained in a fixed cylindrical shell. They also performed experimental measurements. Their analytical and experimental results for the added mass coefficient and damping ratio were found to be in good agreement. However, their linear theory was based on the assumption that the vibration amplitude is small. Brennen [95] reviewed the state of knowledge, at that time, concerning the evaluation of the forces imposed by a body in a fluid due to acceleration of either the body or the fluid. He suggested that the added mass for a body of complex geometry might be estimated for each direction of acceleration from the principal dimensions of the projected area in that direction and a corresponding approximate equation. Lissaman and Brown [96] studied the added mass effects on flight dynamics of parafoils. The authors concluded that, for reduced frequency $0.3 \leq k(\pi f c/U_\infty) \leq 0.4$, the effect of vorticity is to cancel the apparent mass effect, which reduces the rate of change of static lift with the angle of attack. They proposed a constant (C) as an alleviating factor for the relative frequency of motion in case that it is not considered in the theoretical unsteady $C_{L\alpha}^{\cdot}$ term.

Yadykin et al. [97] performed a three-dimensional analysis for calculating the added mass of a cantilever plate undergoing first-mode vibrations. Their approach assumes a spanwise half-sine fundamental mode and a single natural mode in the chordwise direction. The thin airfoil theory was used to calculate the forces. Their main findings are: (a) the nondimensional added mass is a function of the plate's aspect ratio and the order of the natural modes of vibration, (b) the increase of the order of the chordwise natural mode of vibration decreases the value of the added mass, (c) decreasing the aspect ratio leads to a decrease of the added mass and attenuates the dependence of the added mass on the order of the chordwise natural

mode. This dependence diminishes as the aspect ratio approaches 0.01. For an aspect ratio that is equal to one, the results obtained by a three-dimensional theory are close to those calculated by a two-dimensional one (A=∞). Finally, the commonly used slender-wing approximation for calculating the added mass tends to overestimate the results for aspect ratios higher than $\approx$0.7, and underestimates these values for lower aspect ratio plates vibrating at the fundamental mode.

Granlund and Simpson [98] showed experimentally that the added mass is linearly dependent on the plunging velocity of a three-dimensional ellipsoid. They supported their experiments by potential flow arguments. Maniaci and Li [99] found that the added mass effect caused a 3.6 % change in thrust for a rapid pitch case of a wind turbine blade and a change in the amplitude and phase of the thrust for a case with 30^o of yaw. Granlund et al. [100] performed experiments in a water tunnel to study the nonlinearity effects of leading and trailing vortex interactions on two cascaded plunging plates. Their results show a quadratic relation for the normalized added mass force with the oscillation frequency at low plunging speeds. In addition, they observed an optimum spacing between the two plunging wings in which the nonlinear interactions takes place.

The current literature does not include a discussion of the unsteady forces for airfoils oscillating at high frequencies as well as high angles of attack in still air. The major challenge that needs to be addressed is the contribution to the total forces by the added mass and the unsteady forces. In this effort, we performed experiments to measure the aerodynamic loads on an airfoil undergoing plunging oscillations over a frequency range between 18 and 100 rad/s and with angles of attack up to 50 *degrees*. We estimated the added forces by subtracting the inertial loads from the total measured forces and compared to the potential flow approximations. This allowed us to determine the contribution of the unsteady forces.

3.2 Potential flow prediction

When an airfoil undergoes oscillations in a fluid, additional pressure forces are required to accelerate the fluid in its vicinity. These forces, which are referred to as the added mass effect, are functions of the local accelerations of the moving body. Based on Theodorsen's theory [91],

the total unsteady force calculated on a thin airfoil with a chord length $\bar{b}$ undergoing a plunging and pitching motion at small angles of attack is given by:

$$L = \rho\pi\bar{b}^2 V\dot{\alpha} - \rho\pi\bar{b}^2\,\ddot{h} + \rho\pi\bar{b}^3 a\ddot{\alpha} + 2\rho\pi V^2\bar{b}^2 C(k)\left\{\alpha + \frac{\dot{h}}{V} + \bar{b}(0.5-a)\frac{\dot{\alpha}}{V}\right\} \tag{3.1}$$

Since we are interested in plunging motion only with no free stream velocity (V=0), the expression for the non circulatory added force can be written as:

$$N_{Plunging} = \rho\pi\bar{b}^2\,\ddot{h} \tag{3.2}$$

Theodosen's formulation for the added mass force given in eq. 3.2 does not account for the angle of attack dependency as it is valid at low angles. In order to account for the angle of attack dependence, we apply Kochin et al. [101] formulation considering the two-dimensional unsteady potential flow induced by an unsteady motion of an elliptic cylinder in a quiescent fluid as shown in Fig. 3.1. Writing the instantaneous velocity of the cylinder center $\overrightarrow{V_c}$ as:

$$\vec{V_c} = U\hat{i} + V\hat{j} \tag{3.3}$$

and its angular velocity as:

$$\vec{\omega} = \omega\hat{k} \tag{3.4}$$

the aerodynamic force on the elliptic cylinder are written as:

$$F_x = -\pi\rho b^2\frac{dU}{dt} + \pi\rho a^2\omega V - \rho\Gamma V \tag{3.5}$$

$$F_y = -\pi\rho a^2\frac{dV}{dt} - \pi\rho b^2\omega U + \rho\Gamma U \tag{3.6}$$

where x and y are the Cartesian coordinates along the major and minor axes of the ellipse, respectively, Γ is the circulation around the cylinder and a and b are the semi major and minor axes.

Next, we consider an elliptic cylinder whose major axis is inclined at an angle α with the horizontal (defined here as an angle of attack), and its center moves vertically with a velocity $W(t)$ as shown in Fig 3.2. Assuming that the circulation around the cylinder is zero, ($\Gamma = 0$), the vertical and horizontal components of the aerodynamic force are given by:

$$F_V = -\pi\rho\left(a^2 cos^2\alpha + b^2 sin^2\alpha\right)\frac{dW}{dt} \tag{3.7}$$

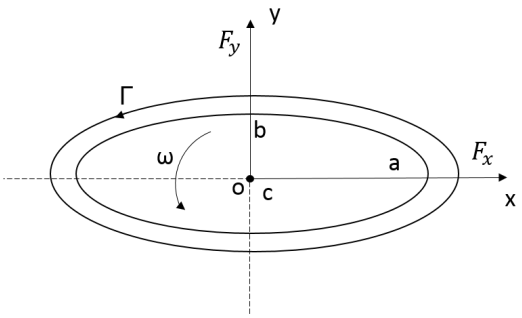

Figure 3.1: Elliptical cylinder moving in quiescent fluid

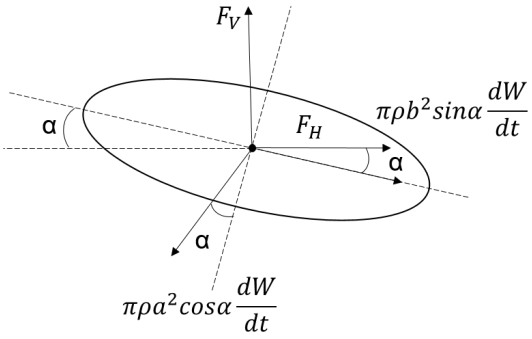

Figure 3.2: Vertical and horizontal aerodynamic forces acting on a two-dimensional ellipse

$$F_H = -\frac{1}{2}\pi\rho \sin 2\alpha (a^2 - b^2)\frac{dW}{dt} \tag{3.8}$$

Considering that the plunging force is the vertical component of the force and assuming the case of a flat plate ($b \to 0$), we obtain a plunging force of the form:

$$N_p = -\rho\pi \left(a^2 cos^2\alpha\right) \ddot{h} \tag{3.9}$$

The non-circulatory lift associated with a plunging flat plat can then be written as:

$$L_{added} = [\rho\pi\bar{b}^2 cos^2(\alpha)\, \ell]\, \ddot{h} \tag{3.10}$$

The theoretical prediction matches with the geometrically unsteady potential flow model developed by Yan et al. [32] for airfoils undergoing large amplitude maneuvers. The issue with the potential flow assumption when it comes to prediction of the added forces is the neglection of other unsteady forces that contributes to the total produced forces by the fluid due to viscous effects. The basic definition of the added mass is the force required to accelerate

the body in a fluid. In viscous quiescent flow, the acceleration of the body may create flow patterns in the vicinity of the body that affect the pressure distribution and consequently contribute to additional unsteady forces associated with the motion.

3.3 Experimental testing

The test rig described in chapter 2 was used in these experiments. The wing section profile is NACA-0012 and has a chord length of 0.14 m and span of 0.63 m and is shown in Fig. 3.9(a). Figure 3.3(b) shows a schematic of the imposed motion during the tests. End plates were attached to the wing tip to reduce the three dimensional flow effects and two MEMS accelerometers were placed on the bracket that held the wing and connected to the main oscillatory rod. The low frequency motion exhibited slight jitter that disappeared as the frequency was increased. In all performed experiments, the maximum displacement of the plunge motion was maintained constant at a value of $h_o = 2h_a$=0.0193 m which corresponds to non dimensional amplitude based on the chord of h_a/c=7%. The geometric reduced frequency was calculated to be $k = h_o/c$=0.137. The weight breakdown for the whole test rig is shown in Table 3.1 and the moving mass contributing to the inertial force was calculated to be $0.477kg \pm 1grams$.

Table 3.1: Mass breakdown for the whole setup.

Device	**Mass** ($grams$)
Driving motor	1355
Bracket	1005
Base	1240
Push-rods (moving)	139
Wing (moving)	235
End plates (moving)	103
Net mass	4077

The acceleration of the wing was measured using a single axis miniature accelerometer of mass 0.5 gm and sensitivity of ±15% at 10 mV/g. The accelerometer was calibrated using a

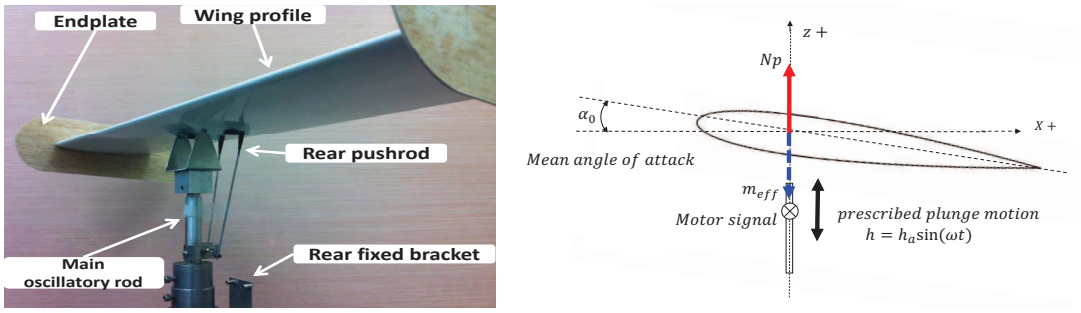

(a) Airfoil model setup and driving mechanism (b) Wing plunging motion schematic diagram

Figure 3.3: Plunge-Pitch apparatus and kinematics.

2 MHz variable phase synthesizer apparatus over a broad range frequencies. The operating angle of attack for the wing was measured using a digital protractor with an accuracy of $\pm$ 0.2 degree. The force measurements were obtained by using a strut mount balance (6-component) and the data was acquired using *National Instruments SCXI-1520* system sampled at 2500 Hz. A low-pass fourth order butter-worth filter with a cut-off frequency of 55 Hz was used. In order to ensure that the forcing frequencies were far away from the eigen-frequency of the strut mount, a mechanical strike-test was performed, whereby we tapped the strut with a rubber hammer and recorded the data. The frequency revealed a natural frequency of 361 rad/s, which is well above the highest frequency of 100 rad/s in our experiments. Another additional effect that should be considered is the fact that the entire span of the wing does not exhibit a uniform motion while oscillating leading to an error caused by slight deflections of the wing tips. For this purpose, we measured the tip deflection by using a high-speed camera that operated at 1000 fps. Using image boundary detection technique, we determined the maximum tip deflection based on two extreme plunging positions at a maximum operating at a frequency of $0.0544\,h_a$. The wing loading and the maximum tip deflection captured from the CCD camera in air are shown in Figure 3.4.

In our experiments, the plunging motion had the form:

$$h(t) = h_a \sin(\omega t) = h_a \sin(2\pi f t) \quad , \tag{3.11}$$

The maximum translation velocity of the plunging airfoil is written as $U_{ref} = 2\pi f h_a$ and

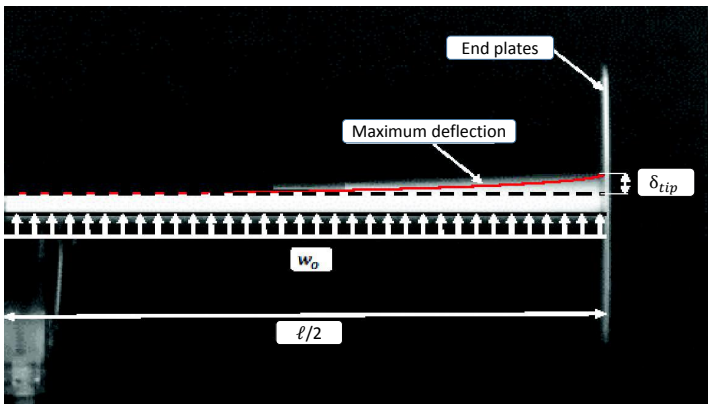

Figure 3.4: High-speed photogrammetry image of the wing showing maximum tip deflection during an oscillating frequency experiments of 100 rad/s.

used as the reference velocity. We also use the non-dimensional which can be written as:

$$\widehat{F} = \frac{\omega c^2}{\nu} \tag{3.12}$$

where ω is the oscillation frequency, c is the chord length and μ is the kinematic viscosity. Based on eq. 3.11, the plunging velocity and acceleration are respectively given by:

$$\frac{dh}{dt} = \dot{h} = \omega h_a \cos(\omega t) \quad . \tag{3.13}$$

and

$$\ddot{h} = -\omega^2 h_a \sin(\omega t) \tag{3.14}$$

The theoretical plunging force obtained by accounting for both inertia and added mass of the wing is then given by:

$$Np_{theoretical}(t) = [m_{moving} + \pi\rho\bar{b}^2 cos^2(\alpha)\ell\,]\ddot{h}(t) \quad . \tag{3.15}$$

Assuming that the measured forces is a function of the frequency and amplitude of the oscillations and the angle of attack, we write the more general expression

$$Np_{measured}(t) = \big[m_{moving} + m_{added}\big](\ddot{h}(t)) + F_{fluid}(\ddot{h}(t), \dot{h}(t), \widehat{\omega}) \tag{3.16}$$

the last term in eq. 3.16 accounts for the unsteady added forces that will be obtained from the measured values.

We defined the added force as:

$$|F_{added}| = |Np_{measured}| - m_{moving}\,\omega^2 h_a \tag{3.17}$$

3.4 Results and Discussion

Figure 3.5 shows the added force as calculated by using equation 3.17 for different plunging frequencies and various angles of attack. The error bars for each data point is based on 95% level of confidence for fifty cycles averaged ensemble from a total record length of ten seconds. The plot also shows theoretical estimates of the added mass from potential flow predictions for 0 and 50 degrees angles of attack. The significant departure from potential flow estimates raises a question about the origin of these added forces associated with the motion. This departure from the potential flow prediction is most likely related to the viscous effects which results in a flow separation and formation of vorticies around the leading and trailing edges. These effects induce additional unsteady forces.

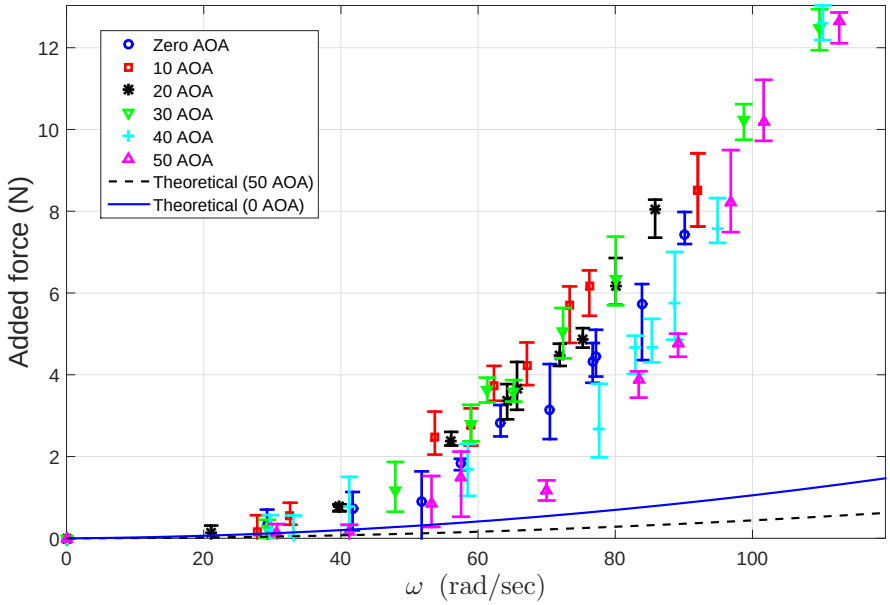

Figure 3.5: Estimates of the measured and theoretically predicted added forces for different angular frequencies and angles of attack.

Figure 3.6, shows curve fits for the added forces with the frequency of oscillations at different angles of attack. Because of the lack of measurements at very low frequencies, there is a significant difference in the slope and intercept of these curves near zero frequency. However, the cubic curve fit seems to represent well the variation of these added forces with operating plunging frequency.

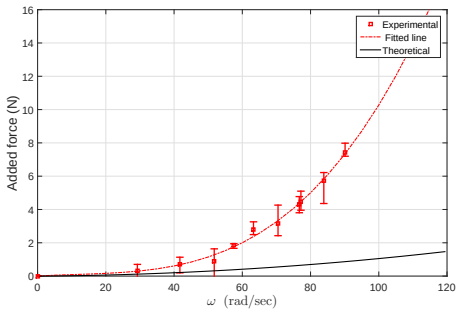

(a) 0° AoA

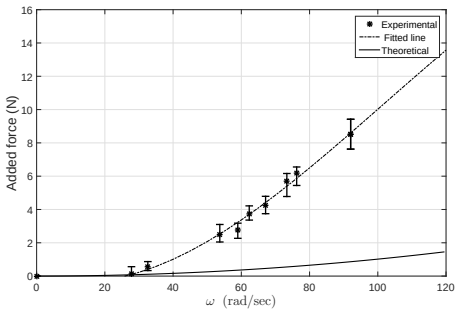

(b) 10° AoA

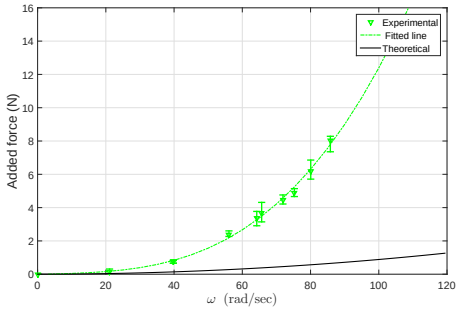

(c) 20° AoA

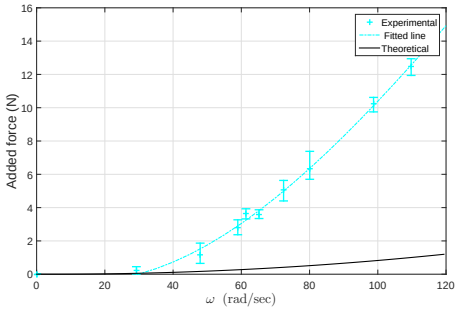

(d) 30° AoA

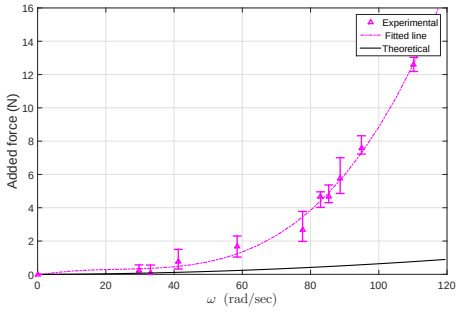

(e) 40° AoA

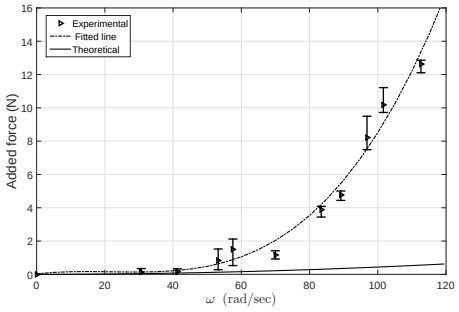

(f) 50° AoA

Figure 3.6: Apparent mass force at different operating angular frequencies and angles of attack

Next, we postulate that the curve fit for the total added force coefficient $C_a = F_a/\rho\pi\bar{b}^2\ell\ddot{h}$ should approach its theoretical value of $\cos^2\alpha$ as $\omega \to 0$ based on theoretical predictions. A linear curve fit of the measured added mass as defined by eq. 3.17, is then written as:

$$C_a = \frac{m_a}{\rho\pi\bar{b}^2\ell\ddot{h}} = \cos^2\alpha + C\frac{\omega c^2}{\nu} \tag{3.18}$$

Figure 3.7 shows linear curve fits of the added force coefficients as a function of the oscillation frequency for different angles of attack. Although the data show significant scatter, there is clear evidence that the added forces increases as the frequency of the oscillation is increased. Figure 3.8 shows a comparison of the fitted curves based on eq. 3.17 for all angles of attack. The results show that the added force values at 10, 20 and 30 degrees are comparable and larger than the values obtained for the case of zero angle of attack. On the other hand, the added mass values for the 40 and 50 degrees angle of attack are smaller than the one obtained for zero angle of attack. These observations lead to the notion that flow separation from the leading and trailing edges, expected to be more significant at the 10 and 20 degrees than at 40 and 50 degrees, is contributing to the added unsteady forces as represented and calculated here. From the results below and recalling eq. 3.18, one can write a hypothesis for the total forces experienced by the wing section after excluding the inertial forces as:

$$F_{fluid} = -C_1\ddot{h} - C_2|\dot{h}|\dot{h} + Shape\ correction \tag{3.19}$$

where C_1 is the coefficient of the added mass force as function of the local acceleration of the body and C_2 is the coefficient of drag forces as function of the square of plunging velocity. It should be noted that the shape correction factor for an airfoil might be a function of the oscillation frequency as well as the leading and trailing edge geometry of the airfoil which needs more investigations to have an appropriate functional form such as the form presented by Lawrence and Weinbaum [102].

3.5 Higher order spectral analysis

One of the very powerful tools to identify the presence of nonlinearities in the system is the higher-order spectral analysis (HOS) [103]. HOS are based on the Fourier transforms of higher-order moment functions, which can be used to obtain more information about the

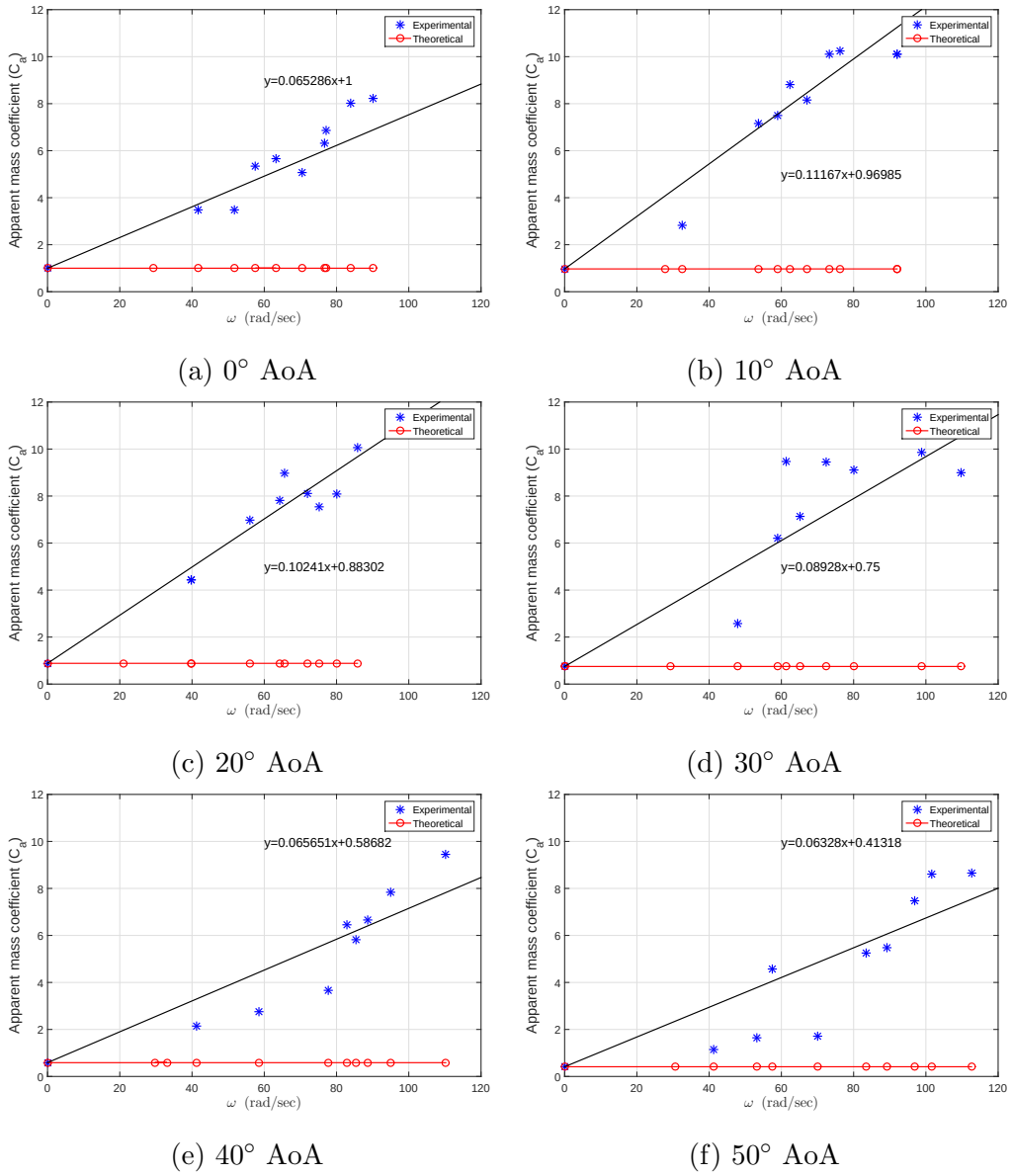

(a) 0° AoA (b) 10° AoA

(c) 20° AoA (d) 30° AoA

(e) 40° AoA (f) 50° AoA

Figure 3.7: Measured apparent mass at different operating frequencies and angles of attack

harmonics generated by nonlinear couplings [104]. The power spectrum is obtained from the Fourier transform of the second-order correlation. The Fourier transform of a time series *x(t)* is given by:

$$X(f) = \int_{-\infty}^{\infty} x(t) e^{-2i\pi ft} dt \quad , \tag{3.20}$$

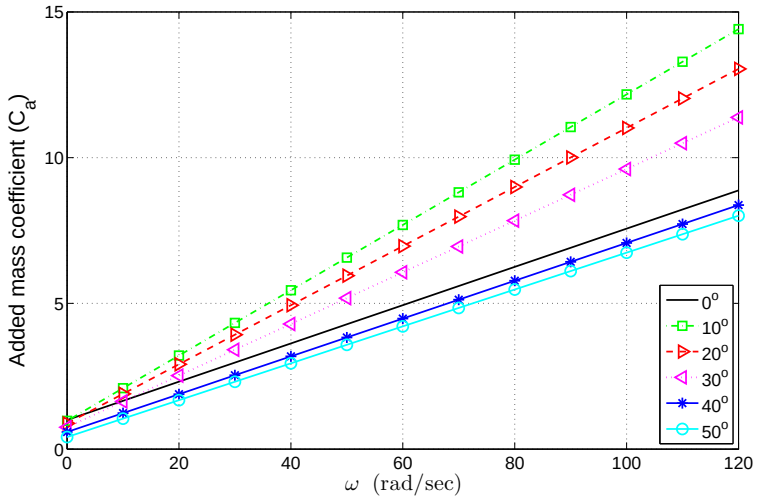

Figure 3.8: Plunging force with frequency at different operating angular frequencies and angles of attack

where f denotes the frequency and $X(f)$ is a complex quantity.

The power spectrum (S_{xx}) is the Fourier transform of the second-order correlation given by:

$$S_{xx}(f) = \lim_{T\to\infty} \frac{1}{T} E[X(f)\ X^*(f)] \quad , \tag{3.21}$$

where $X(f)$ is the Fourier transform, the superscript (*) denotes complex conjugate and E is the expected value, which is calculated by the arithmetic average estimator for M sets of data records [105]. The information embedded in a power spectrum represents the distribution of energy at different frequencies, which fully characterizes a linear system in the frequency domain. The normalized value of the cross-power spectrum captures the phase relation at the same frequency between two different signals. However, for a nonlinear system, higher-order spectrum analysis is needed because the power spectrum cannot portray the energy relation between the various frequency components which is a typical feature of nonlinear systems.

In nonlinear systems, the frequencies can combine with themselves to create new components at their sum or difference frequency. When the frequencies are interacting, the phase of the new component is related to the phases of the primary interacting modes, therefore by inspecting the phase relation it is possible to identify any nonlinear coupling [106]. The detection of quadratic nonlinear couplings among frequency modes relies on the fact that the interaction of two frequency components (f_1 and f_2) and their sum components ($f_1 + f_2$) leads

to significant values of bispectrum. If the system has a quadratic nonlinearity, the complex bispectrum results exhibits a phase relation as showed in Figure 3.9.

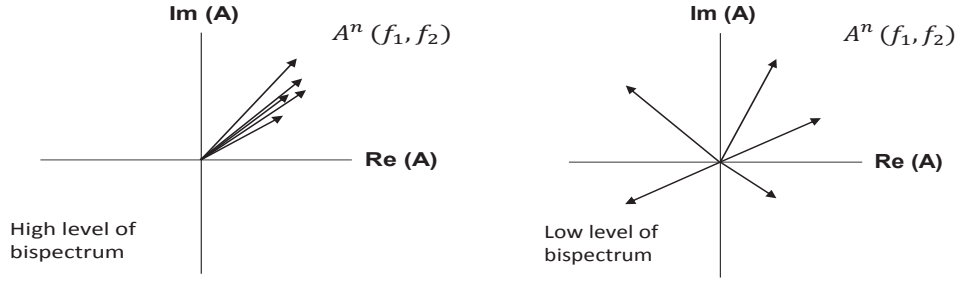

(a) Non-phase relation (b) Phase relation

Figure 3.9: Vector representation of N estimates of bispectrum, where $A^n(f_1, f_2) = X(f_1 + f_2)\ X^*(f_1)\ X^*(f_2)$.

The auto-bispectrum is obtained from the Fourier transform of third-order correlation and can be estimated as:

$$S_{xxx}(f_1, f_2) = \lim_{T\to\infty} (\frac{1}{T}) E[X(f_1 + f_2)\ X^*(f_1)\ X^*(f_2)] \quad , \tag{3.22}$$

The auto-bispectrum is usually normalized with respect to the amplitudes of the individual spectral components to yield the *auto-bicoherence*.

Based on the Schwartz inequality, the auto-bicoherence defined as:

$$b^2_{xxx}(f_1, f_2) = \frac{|S_{xxx}(f_1, f_2)|^2}{E[|X_T(f_1 + f_2)|^2] E[|X_T(f_1) \quad X_T(f_2)|^2]} \quad , \tag{3.23}$$

is bounded by 0 and *one* (i.e. $0 < b^2_{xxx}(f_1, f_j) < 1$). If $b^2_{xxx}(f_1, f_j) = 1$, then the pair of frequency components at f_1 and f_j, as well as their sum $f_1 + f_j$, are quadratically coupled. If $b^2_{xxx}(f_1, f_j) = 0$, frequency components are not coupled, and partially coupled if $0 < b^2_{xxx}(f_1, f_j) < 1$.

To understand the HOS results, one should analyze the bicoherence in a two-dimensional plot of the cut-off planes, which have a range between 0 and 1. Figure 3.10(a) shows the bicoherence plot. The frequencies f_1 and f_2 can be related in four ways: (i) $f_1 + f_2$, (ii) $f_1 - f_2$, (iii) $-f_1 + f_2$ and (iv) $-f_1 - f_2$, which are presented in the four quadrants. Those regions can be divided into eight parts using two dashed lines ($f_1 + f_2 = 0$ and $f_1 - f_2 = 0$) [107]. This

eight regions have similarity relations among themselves and they are named as parts I and II [105]. From these relations, one can infer that regions A and B are enough to represent all the behavior of the frequencies couplings. Figure 3.10(b) shows the method to identify the

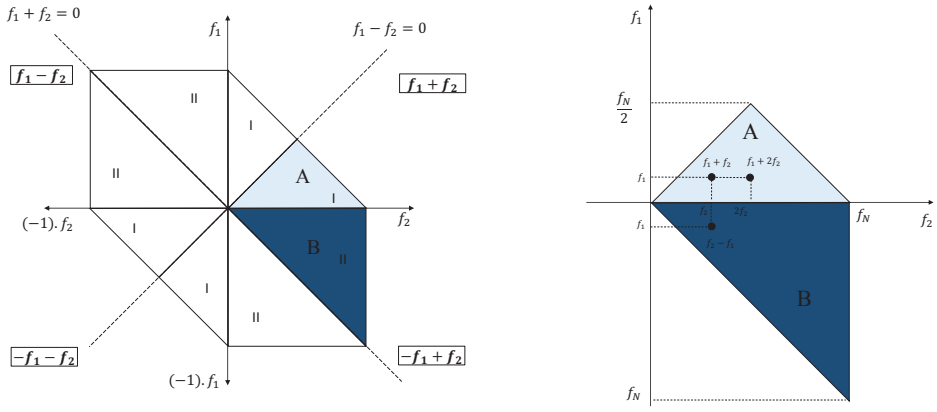

(a) a (b) b

Figure 3.10: (a) Bicoherence computation and its symmetry properties. (b) Countour plot to identify the nonlinear quadratic couplings.

effect of quadratic nonlinearities. In this figure, f_N and $f_N/2$ are the sampling and Nyquist frequency, respectively. One can see the relation between f_1, f_2 and their sum and difference (regions A and B, respectively). For investigation of two different signals (cross-bicoherence) the region B should be also considered.

Figure 3.11 shows power spectra for various angles of attack (0° to 50°). The dotted curve shows the spectrum of the force measured by the balance ($Np_{measured}$) and the solid line shows the spectrum of the acceleration. We note the appearance of super harmonics in all cases for different angles of attack with small amplitudes, which indicates the presence of nonlinearities in the system.

3.5.1 Auto Bicoherence analysis

Figures 3.12 shows the auto-bicoherence for the case of the airfoil set at 20 degrees AoA and plunging frequency of 13.75 Hz.

The plot shows peaks are centered at (f_0,f_0) and at (f_0, $2f_0$), which indicates that the force contains components at twice, trice and four times the forcing frequency. This indicates

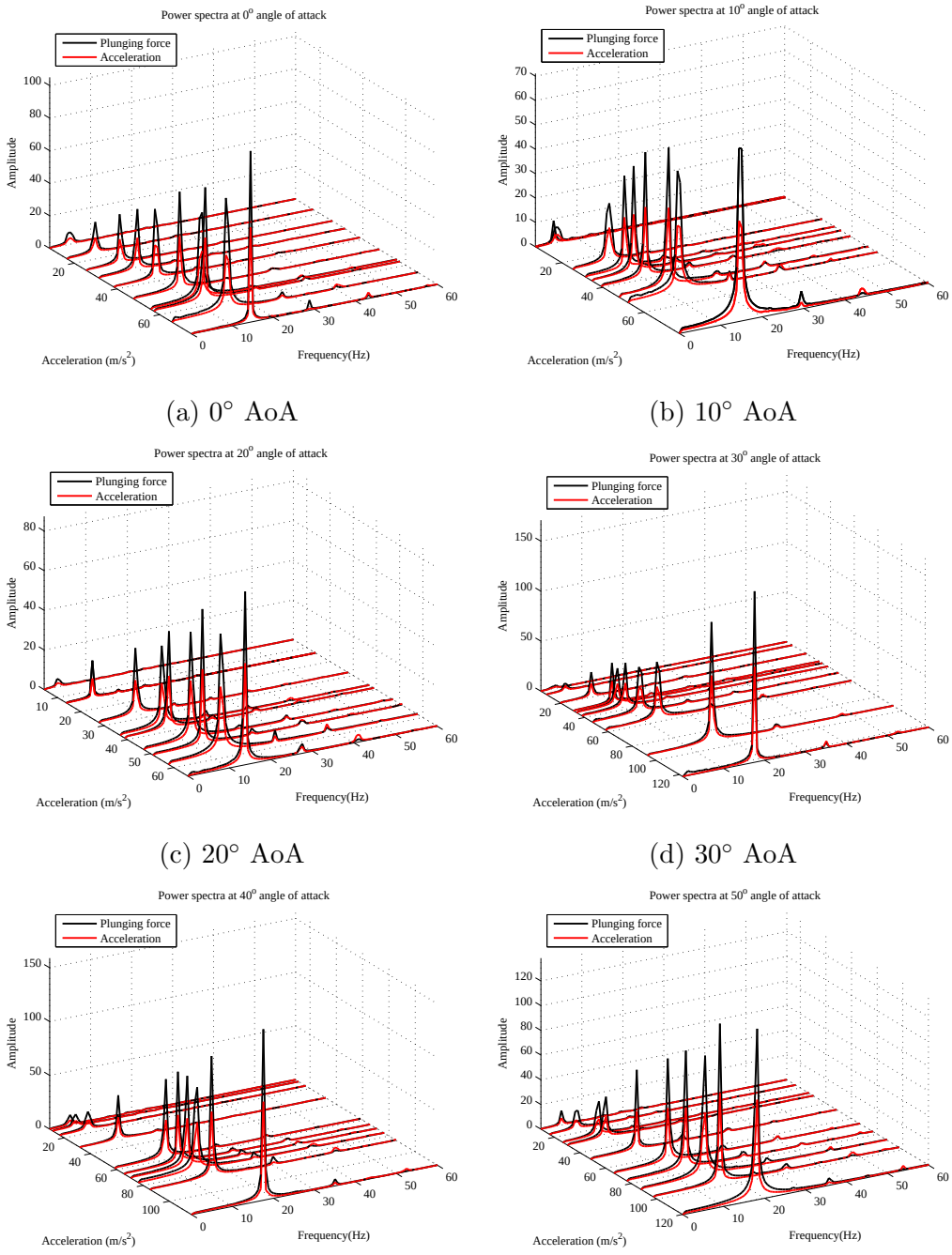

(a) 0° AoA (b) 10° AoA

(c) 20° AoA (d) 30° AoA

(e) 40° AoA (f) 50° AoA

Figure 3.11: 3D Power spectral density for the plunging force and the operating acceleration.

that the force is proportional to terms other than the accelerations.

Figure 3.13 shows the auto bi-coherence plots for two different forcing frequencies, 8.75

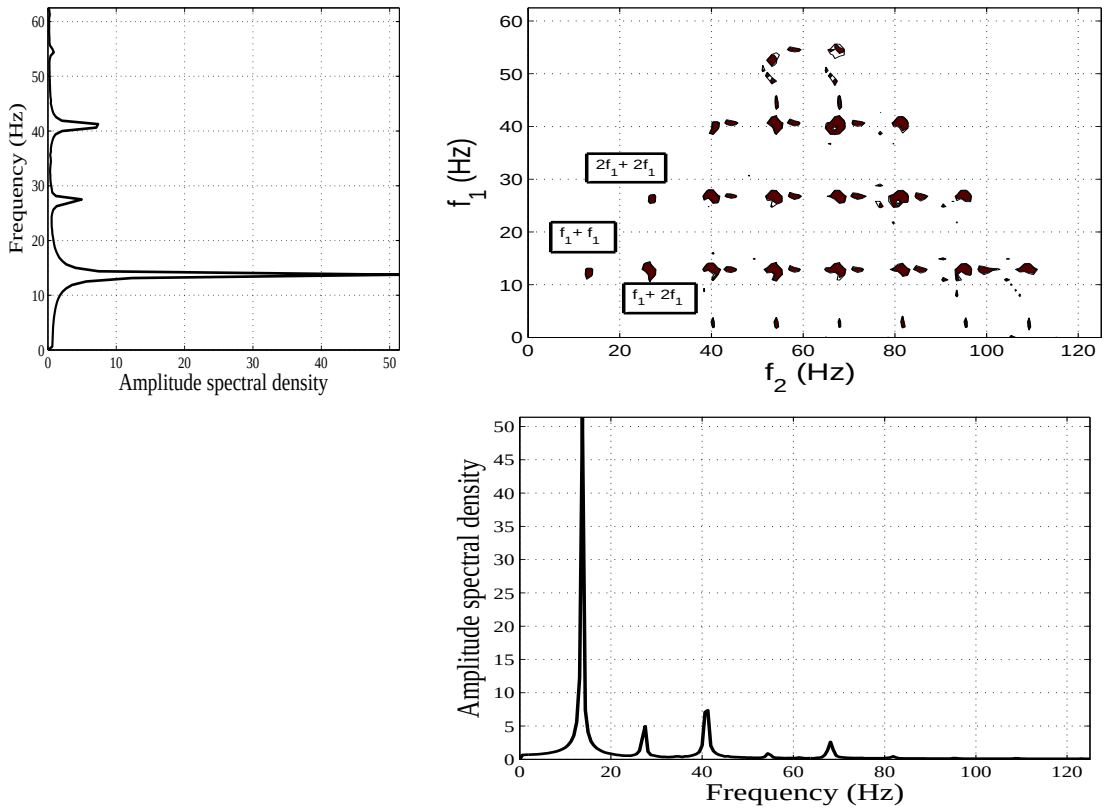

Figure 3.12: Auto-bicoherence of the force at 13.75 Hz and 20 degrees angle of attack.

Hz and 13.75 Hz and various preset angles of attack. The results show that the acceleration signal does not exhibit any nonlinear coupling, which indicates that it consists of a single frequency. On the other hand, the auto-bicoherence plots of the measured forces exhibit coupling between the forced frequency and its harmonic. The highest levels of these couplings is over the range between 10^o and 30^o. This should be considered in concert with the results presented above that showed larger forces at these angles of attack. That is the contributions of the unsteady forces is the highest over this range of angles of attack.

3.5.2 Cross bicoherence analysis

The results shown in this subsection are for specific cases and aim to show the nonlinear dependence on the added force and the acceleration. Figures 3.14, 3.16 and 3.18 show the power spectral density and linear coherence for the added force and acceleration at 0°, 20° and 50° angles of attack. These results are followed by results for the same angles at the same

selected frequency representing the auto and cross bicoherence shown in Figs. 3.15, 3.17 and 3.19. In Figure 3.14, the results show a linear coherence of 0.74 for the added force with the plunging acceleration at the operating frequency for zero angle of attack. However, at 20° the linear coherence is increased to 0.87 and increased again to reach 0.95 for 50∘ AoA. Figure 3.15 shows the cross bispectral analysis for 0^o angle of attack at an operating frequency of 13.5 Hz and a cutoff ratio is 0.93. It is clear that only the auto bispectral analysis for the added force shows coupling with the subharmonics of the signal and concentrating around an operating frequency of 13.5 Hz. At higher angle of attack (20^o), as shown in Fig. 3.17, we observe two high contours. The first is at 27.08 Hz and 13.5 Hz, and the second is 41.66 Hz and 28.1 Hz, respectively. These high contours show the nonlinear quadratic coupling between the added force and the acceleration that results from the interaction between the sub-harmonics (f_o,$2f_o$) and $(3f_o, 2f_o)$. The results in Fig. 3.19 show weak coupling between the added force and the acceleration at $(5f_o, 4f_o)$.

3.6 Flow visualization

In order to provide a physical insight of flow in such case (oscillating airfoil in stationary flow), flow visualizations were performed by seeding ceramic particles in a water channel facility having a test chamber sectional area of 58 cm width and 83 cm height (same procedures were held as explained in section 2.7). The mechanism was hanged upside down above the test section as shown in Fig. 3.20. The maximum operating plunging frequency was 0.4 Hz in water which corresponds to 20 Hz in air based on the nondimensional frequency parameter fc^2/ν (see eq.3.12). The mounted scheme resulting in approximately 0.05c model tip deflection from the hydrodynamic loading at the maximum operating frequency (2 Hz), however the deflection was found to be negligible at the half span location where the visualization takes place. Fig. 3.21 shows the wing section immersed in the water channel and the flow visualization regions of interest. The laser sheet lightening the lower side with the prescribed regions of interest (leading and trailing edges). A shadow appears on the upper side of the wing and a remedy for that is we put a square mirror on the upper side of the free surface to enhance the particle illumination specially at the leading edge region. The

operating frequency was captured using a laser tachometer to count the plunge oscillations that reflected from a patch bonded on the wing tip. Figures 3.22, 3.23, 3.24, 3.25 show a sequence of images recorded at 0°, 10°, 20° and 30° angles of attack for 3/4 of full stroke period. The trailing edge region was taken to be the region of interest for 0° and 10° as there is no evidence for any flow changes at the leading edge region. In Fig. 3.22 (a), the wing is at its highest position creating a strong TEV in a clockwise direction. In (b) and (c), the wing start to move downwards results in decreasing the TEV strength generated in the previous time instant and start to generate another counter rotating vortex (counterclockwise) while being shed away from the trailing edge. In (d), (e) and (f), the asymmetric wake behind the airfoil was observed. The formed vortex structure called the mushroom type observed in flow visualization of a purly heaving foils in a free stream by [45]. However the mechanism is different from the vortex structure observed by Rival et al., where the observed one here is genesis from the trailing edge only due to the high frequency of the plunging airfoil as well as the slow excursion of the formed vorticies constrained such formation. On the other hand, the mushroom type mechanism observed by Rival et al. is based on the leading edge vortex emanated from the leading edge and convected downstream to reach another TEV, then form such type. One should note that, the asymmetric pattern results in the inclined path the generated vorticies could be attributed to the free surface of the water channel. Figures 3.24 and 3.25 show the two regions of interest as illustrated in fig. 3.21. The same vortex structure was observed as in the cases of 0° and 10°. An attached LEV was observed of particular interest, fig. 3.24 (d) and fig. 3.25 (e). The evidence of a attached LEV formation as well as the shedding of a TEV contributes to the added forces associated with the motion.

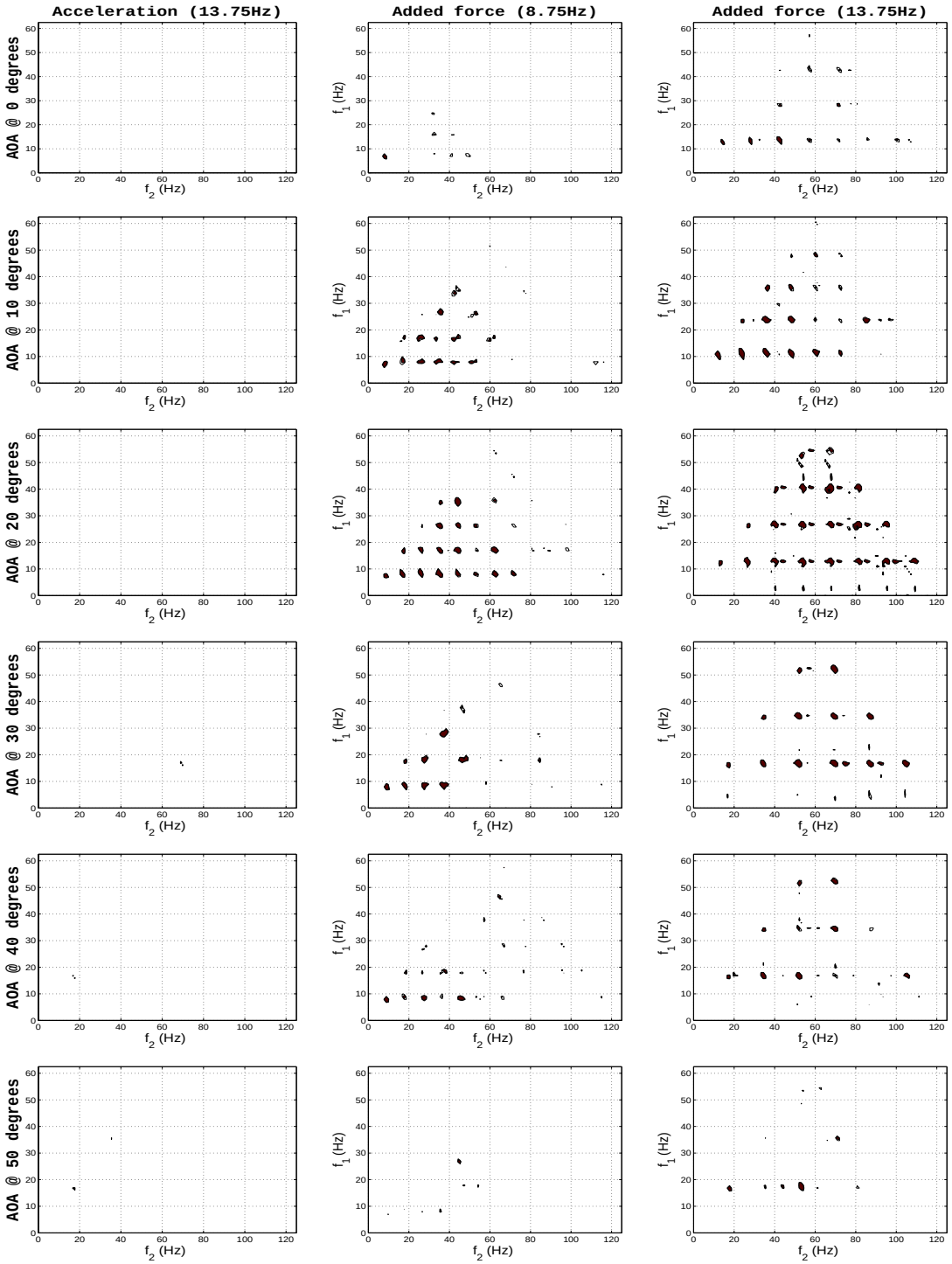

Figure 3.13: Auto bicoherence analysis for the plunging force and operating acceleration at various angles of attack.

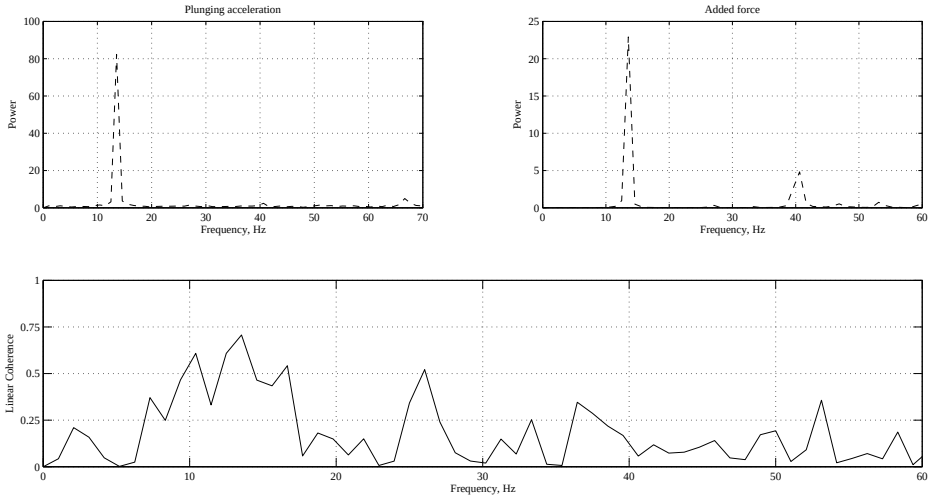

Figure 3.14: PSD for added forces and plunging acceleration and their linear bicoherence at 0° AoA

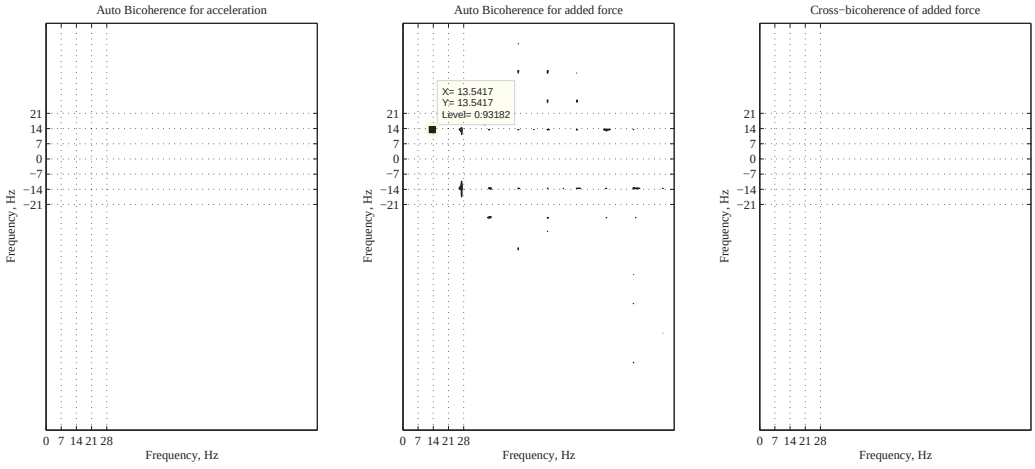

Figure 3.15: Auto and cross bicoherence at 0° AoA

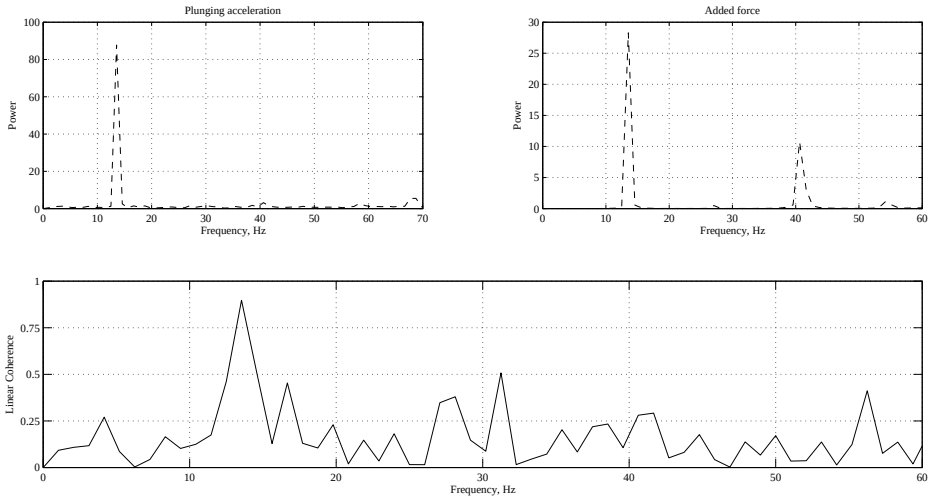

Figure 3.16: PSD for added forces and plunging acceleration and their linear bicoherence at 20° AoA

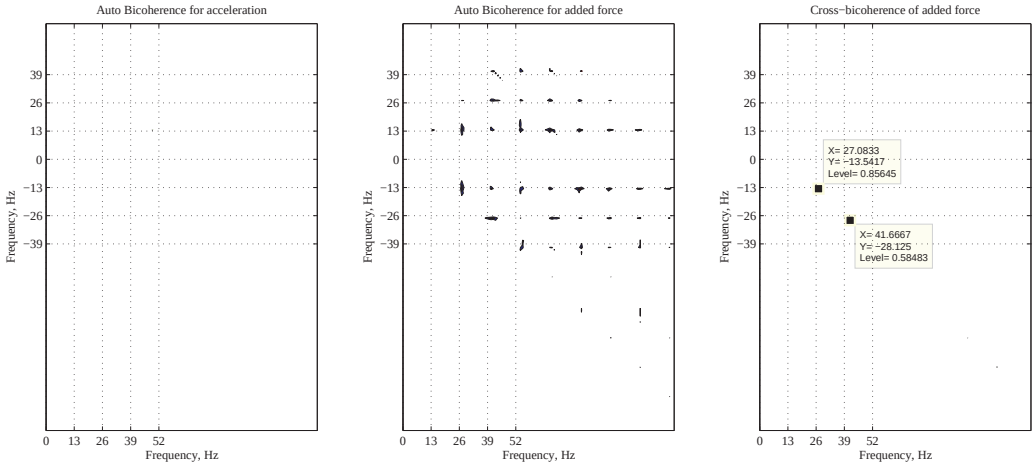

Figure 3.17: Auto and cross bicoherence at 20° AoA

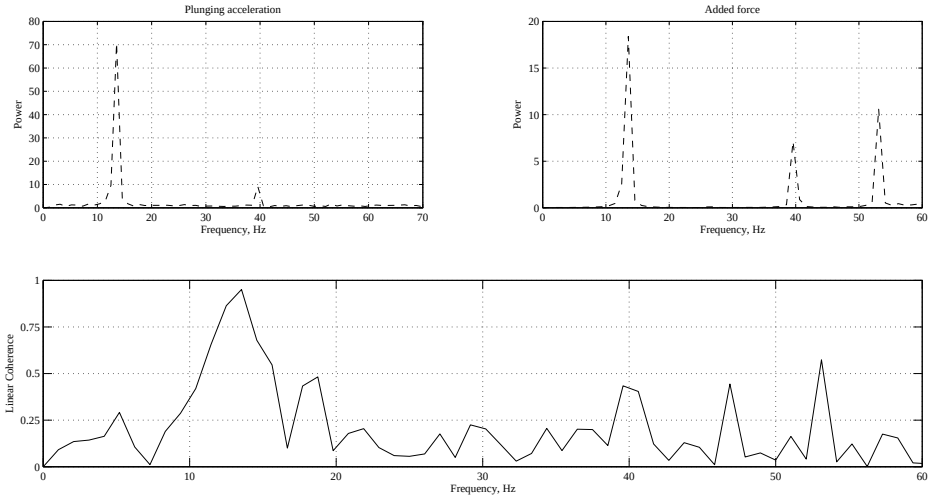

Figure 3.18: PSD for added forces and plunging acceleration and their linear bicoherence at 50° AoA

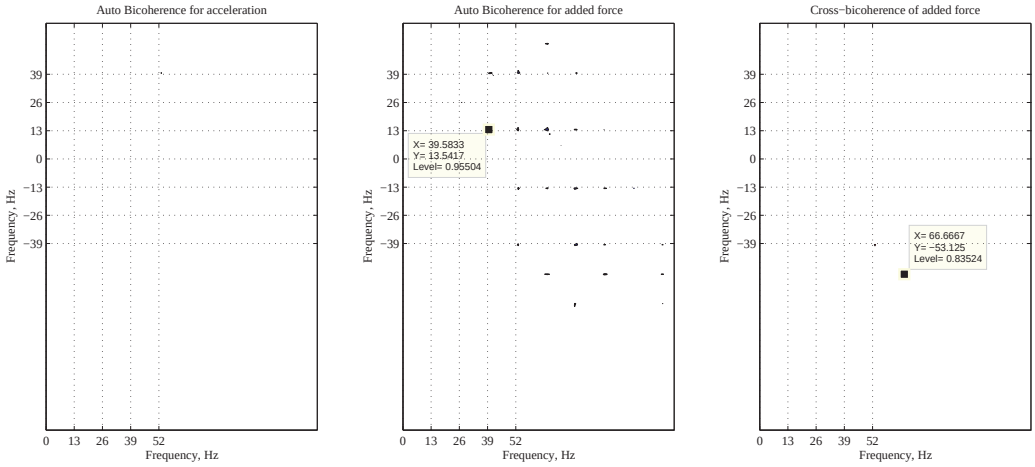

Figure 3.19: Auto and cross bicoherence at 50° AoA

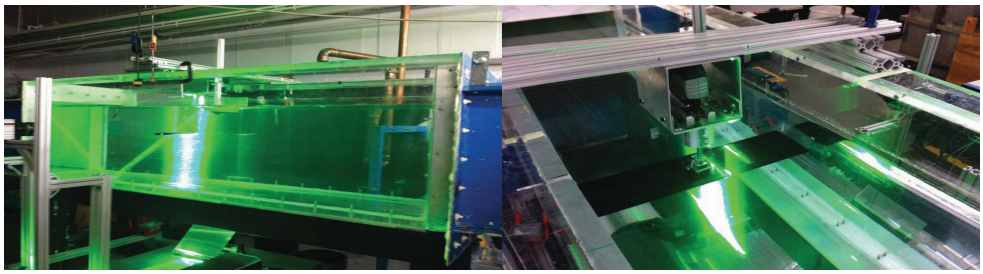

Figure 3.20: Test section and motion apparatus mounted above the test section of the horizontal free surface water tunnel.

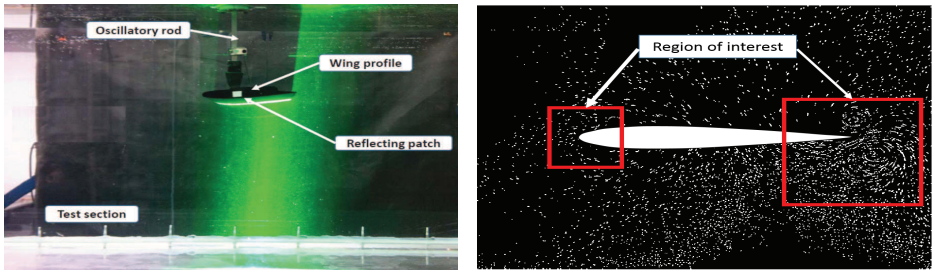

Figure 3.21: Plunge mechanism placed in the test chamber with the laser sheet illuminates the upper surface of the airfoil and region of interest to capture the insight flow.

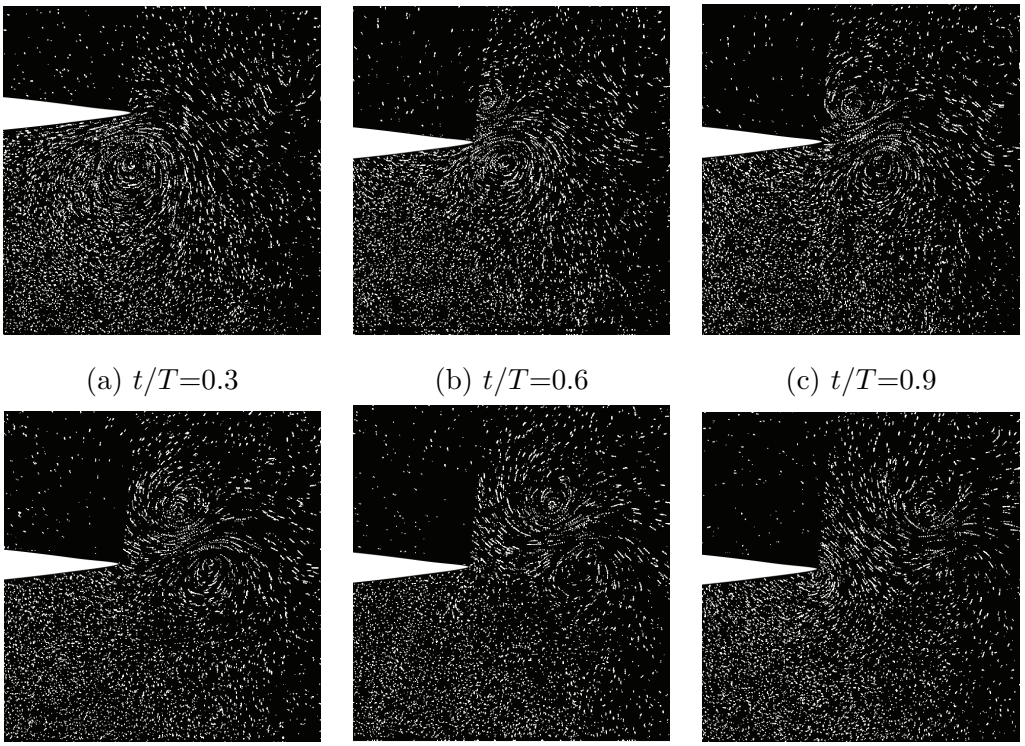

(a) t/T=0.3 (b) t/T=0.6 (c) t/T=0.9

(d) t/T=1.2 (e) t/T=1.5 (f) t/T=1.8

Figure 3.22: Flow visualization of one period for the NACA-0012 captured for the trailing edge at α_o=0° and plunging frequency 0.4 Hz.

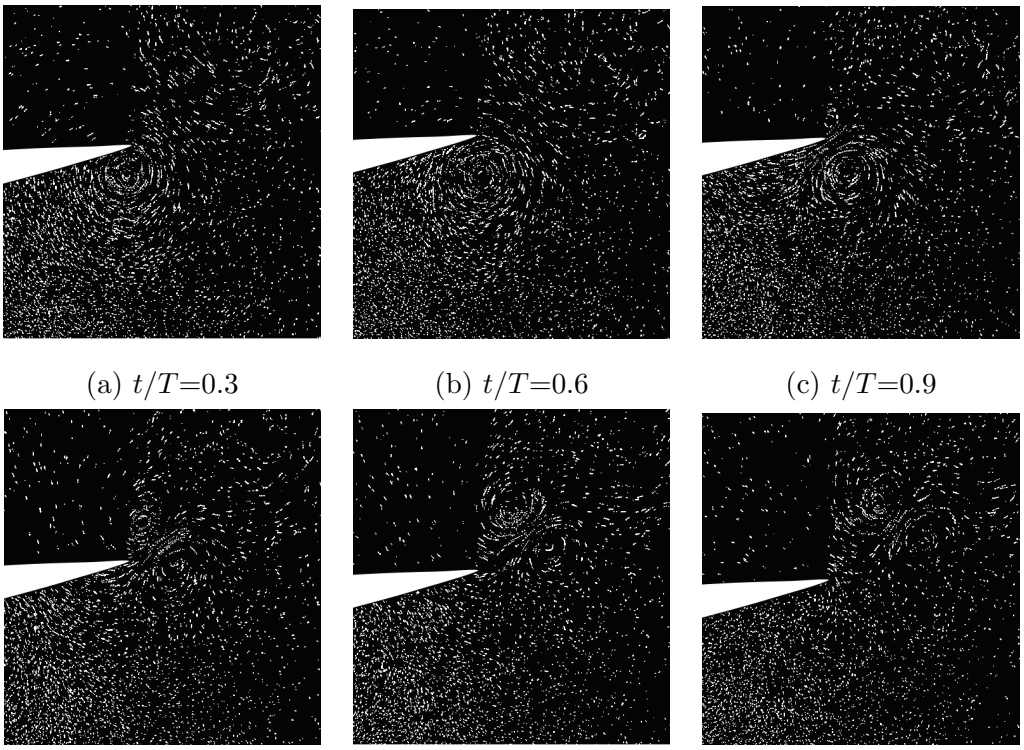

(a) t/T=0.3 (b) t/T=0.6 (c) t/T=0.9

(d) t/T=1.2 (e) t/T=1.5 (f) t/T=1.8

Figure 3.23: Flow visualization of one period for the NACA-0012 captured for the trailing edge at α_o=10° and plunging frequency 0.4 Hz.

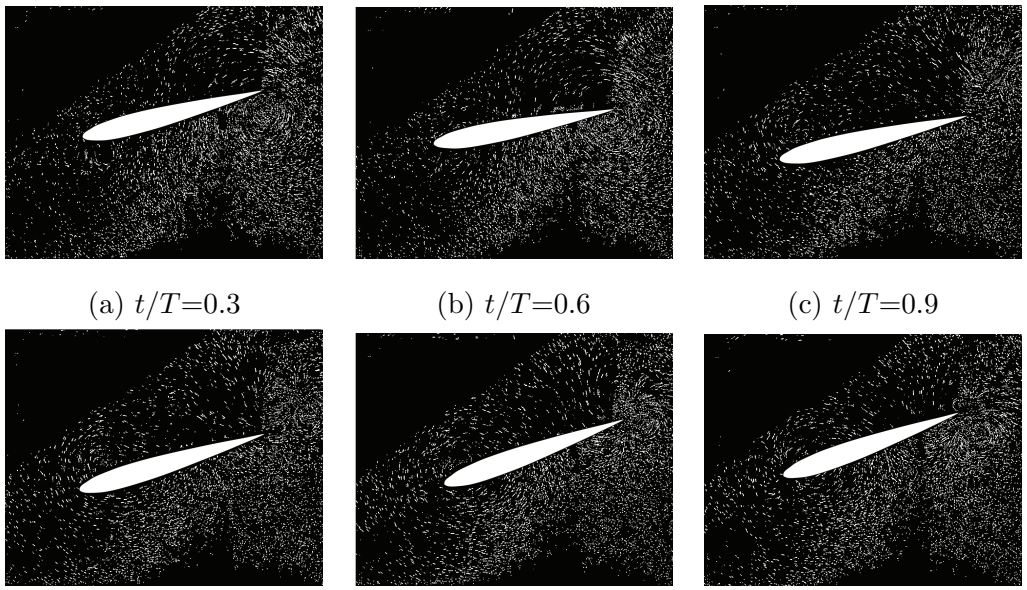

(a) t/T=0.3 (b) t/T=0.6 (c) t/T=0.9

(d) t/T=1.2 (e) t/T=1.5 (f) t/T=1.8

Figure 3.24: Flow visualization of one period for the NACA-0012 captured for the trailing edge at α_o=20° and plunging frequency 0.4 Hz.

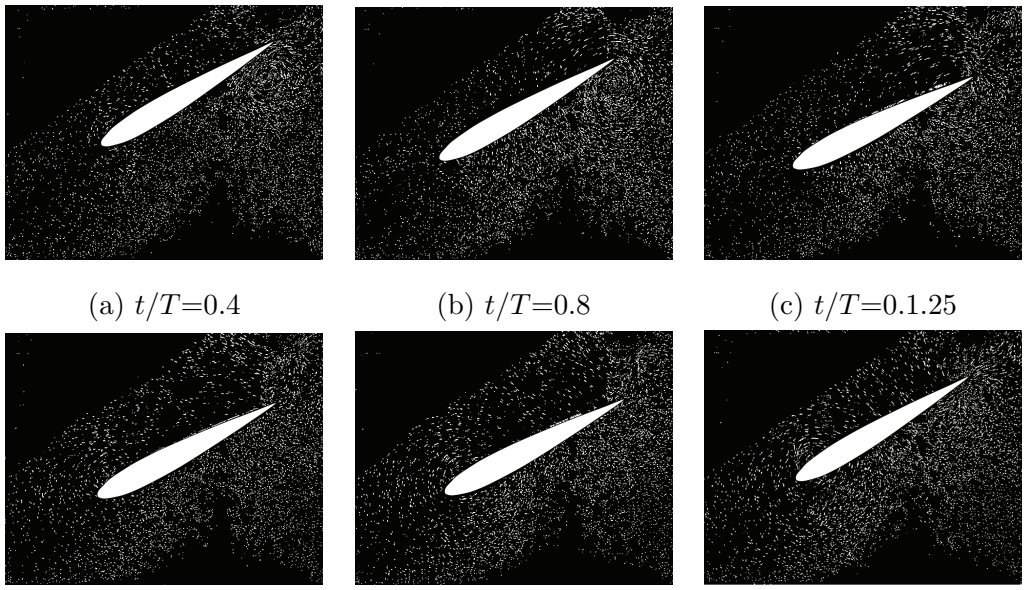

(a) t/T=0.4 (b) t/T=0.8 (c) t/T=0.1.25

(d) t/T=1.6 (e) t/T=2 (f) t/T=2

Figure 3.25: Flow visualization of one period for the NACA-0012 captured for the trailing edge at α_o=30° and plunging frequency 0.4 Hz.

Chapter 4

Applications on flapping wings in Forward flight: Kinematic and shape optimization

4.1 Introduction

Pterosaurs are the earliest vertebrates known to have evolved powered flight. Their wings were formed by a membrane of skin, muscle, and other tissues stretching from the ankles to a dramatically lengthened fourth finger shown in figure 4.1. The first pterosaur fossil was described by the Italian naturalist Cosimo Collini in 1784. Their origin remained a mystery until, in 1801, George Cuvier discovered that the fossils belonged to a flying reptile. Katsufumi Sato, a Japanese scientist, did calculations using modern birds and concluded that it was impossible for a pterosaur to stay aloft [108]. Most of the many studies on pterosaurs describe the fossil remains, and discuss how a new specimen updates the current knowledge base. Several authors have also investigated the flight performance of pterosaurs and flapping flight. A thorough review was done by Middleton and English [109] explaining the challenges and advances in the study of pterosaur flight. Most of those studies are based on analytical considerations. Several projects of pterosaur reconstructions have investigated flapping flight and the role of the membrane in flight.

Derived pterosaurs were believed to be motor-gliders and would not flap their wings continually. The focus of the replica project was mainly to investigate the wing controls during glide. The first replica was derived from an almost complete skeleton of Anhanguera piscator described by Kellner and Tomida [110]. Although not the largest pterosaur found, this animal was believed to have a wingspan of approximately ten meters and was considerably larger than any living flying vertebrate. The quality of the fossils make this specimen valuable and suitable for the study, where by predicting the operating range of the kinematic parameters for the pterosaur, one can build a rigorous aerodynamic model for other species. Although a lot of information about the wing motions can be inferred from the fossils, there is little known information about the wing membrane properties. Strang et al. [111] identify the joint motions that contribute most to propulsive efficiency of pterosaurs. However, computational studies on pterosaur flapping flight have so far been limited, with past analysis conducted by Brooks et al. [112] and Delaurier [113].

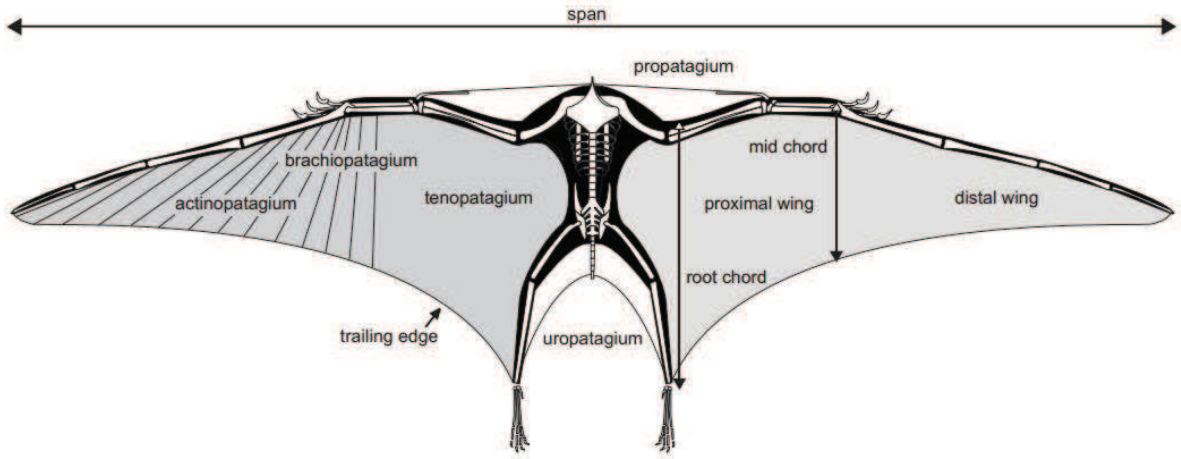

Figure 4.1: Schematic sketch of Pterodactylus as viewed in its inferred flight position from ventral view [1], [2]

The orientations of the Pterodactylus are given in its estimated gliding position, with the wing fully extended as illustrated in Fig. 4.1 [1], [2]. Observations of bird wing motions was documented by Otto Lilienthal [114] in relation to flight. Heaving, plunging and flapping are the three main wing motions studied in the past. Theodorsen [28] and Garrick [115] derived

analytical solutions for the general theory of oscillating airfoils. They derived lift and thrust equations for heaving and pitching airfoils in inviscid two-dimensional flow, then *Küssner* [116] derived the same results independently. Several flapping models were conducted and created by Betteridge and Archer [117], Phlips et al. [118], RT Jones [119], DeLaurier and Harris [120]. There have been numerous studies on the aerodynamics of pterosaurs, including works by Bramwell and Whitfield [121], Brower [122], Chatterjee and Templin [123] have shed new light on the functional morphology and aerodynamic potential of this related pterosaurs. Also, it is now apparent that aeroelasticity of the wing is a key feature of pterosaur flight that was exploited to provide efficient flight control and propulsion. However these studies focus mainly on gliding performance, without studying the details of the flapping motion. In addition, DeLaurier [113] used a three-dimensional aerodynamic model to study the flapping efficiency of the QN (Quetzalcoatlus northropi) replica, developed by Aerovironment under a flapping and twisting motion. This replica is a half-scale wing-flapping flying machine, with a wingspan of 18 feet and weighing 40 lbs when completed, it was the largest known flying ornithopter. QN flying without an aerodynamic tail structure, the replica relied on the use of forward sweep with wash-in at the wing finger joint to achieve pitch stability.

Additional yaw control was added by using the head as a steerable forward fin, and by using the three small finger digits as drag devices. The QN replica incorporates a custom-built flight control system (autopilot) which processes pilot commands and sensor inputs, implements several feedback loops, and delivers command signals to the various servo-actuators. Now on display at the Smithsonian National Air and Space Museum.

Figure 4.2: Paul Maccready's half-scale replica of Quetzalcoatlus Northropi [3]

The minimum power required for a flying vehicle is determined by the physical laws of aerodynamics, animal or man-made, as a function of its shape, size, and weight. In comparing many large birds, it was found that the muscle power available per kilogram for propulsion actually decreases with increasing weight. However, the power required per kilogram increases slowly with increasing weight. This is a consequence of the fact that for flight vehicles of the same shape and density, the larger ones fly faster because they have to carry more weight per square meter of wing area. If the vehicle dimensions is doubled, the wing area increases by a factor of 4, weight by a factor of 8, and the speed and power required per unit weight both increase by 1.4 times as Paul MacCreadys half-scale replica shown in Fig. 4.2 [3].

The stringent weight and power constraints that are imposed on the design process of flapping-wing vehicles invoke the need for optimal designs. As such, there have been many investigations on optimum wing shapes, wing flapping kinematics, and flapping actuation mechanisms. Conventional parametric studies, which merely estimate the sensitivity of the design objectives with respect to each of the design variables independently, do not exploit potential interrelationships between variables. Rakotomamonjy et al. [124] conducted optimization using genetic algorithm to maximize the mean lift. They used a neural network approach to generate functional forms describing the wing motion. Strang et al. [111] used an unsteady three-dimensional vortex-lattice model that captures the main aerodynamic effects of flapping flight and coupled it with a binary genetic algorithm to determine the optimum wing motion under a set of biological constraints. They concluded that the optimization did not find an efficiency advantage for the sweeping motions when accounting for the inertial forces. The required actuated power may increase by about 17% for their estimate of wing mass distribution. Also, they noted that designing an ornithopter wing with a natural frequency close to the designed flapping frequency might be a key design problem to ensure the efficient operation of the motor. Zakaria et al. [125] conducted a parametric study on the effect of reduced frequency on lift, drag, thrust and propulsive power. They concluded that there is a specific value for the dynamic twist angle at which the thrust and propulsive efficiency are independent of the reduced frequency.

Berman and Wang [126] considered optimization of the wing kinematics with respect to the body for hovering insects, namely, the hawk moth, bumble bee, and fruit fly. They

proposed specific functional forms and kinematic parametrization (11 parameters) for the three Euler angles that describe the wing motion with respect to the body. They used the quasi-steady aerodynamic model developed by Pesavento and Wan [127] and Andersen et al. [128, 129]. This model accounts for the translatory (leading edge vortex), rotational, viscous, and added mass effects. They used both gradient-based and global optimization techniques to minimize the average required power (aerodynamic + inertial) under a lift constraint. Kurdi et al. [130] considered the same problem of wing kinematics optimization to minimize the required hovering power under a lift constraint. They also used the quasi-steady aerodynamic model of Pesavento and Wang [127] and Andersen et al. [128, 129]. However, they adopted a different approach for optimization of the shapes of the kinematic functions. They used 30 design variables for each Euler angle to specify the magnitudes of each angle at specific instants during the flapping cycle. Spline interpolation was then performed to obtain differentiable functions. Kurdi et al. [130] determined the effect of the levels of elastic storage and cost to dissipate negative power on the optimization problem. The elastic storage was modeled as a fraction of the inertial power, and the remaining inertial power was modeled as a dissipation cost. All of the above trials have approximated the problem as a finite dimensional optimization problem. Taha et al. [131] formulated the problem as an infinite dimensional optimization problem (i.e., a calculus of variations problem.) They determined that the triangular waveform is the optimum shape of the horizontal flapping angle that results in minimum aerodynamic power while supporting the weight at hover.

Stanford and Beran [132] performed a gradient-based optimization of flapping-wing active-shape-morphing in forward flight. They performed a sensitivity analysis for the three-dimensional unsteady vortex-lattice method to obtain the gradient of their objective function with respect to the design variables. Their objective was to maximize the aerodynamic efficiency under lift and thrust constraints. They represented the wing morphing along with the flapping motions by a finite series of spatial and temporal functions. The spatial functions are the first twisting and bending modes of the wing. As for the design variables, they adopted two techniques. The first technique assumes harmonic functions for the time variation of the generalized coordinates and, as such, the design variables are the amplitudes and phase shifts of the generalized coordinates. The second technique is similar to that of Kurdi et

al. [130], in which the time variations of the kinematic functions are approximated by cubic splines and the amplitudes of the generalized coordinates at specific control points represent the design variables. Ghommem et al. [133] adopted the same approaches using global and hybrid (global and gradient-based) optimization techniques. Stewart et al. [134] performed a multi-objective optimization using the ϵ constraint method where the power and mass are the secondary objective functions which are treated as nonlinear constraints while the cycle-averaged thrust is the primary objective function. The authors stated that the density of the wing material has a significant effect on the optimal wing design which also has been addressed experimentally by Zakaria et al. [135] indicating a considerable variation for the thrust generation due to two membrane wings with different mass densities.

In this chapter, a multi-objective optimization is performed on the wing kinematics and planform of the Pterosaur replica. The design objectives include the cycle-averaged aerodynamic power and the propulsive efficiency. The unsteady aerodynamic model proposed by DeLaurier [113] and modified by zakaria et al. [136] is used.

4.1.1 Wing Kinematics

The wing kinematics and wing sections are illustrated in figure A.26. For a root flapping motion with no spanwise bending, the plunging motion is given by:

$$h(t, y) = y\gamma(t) = \Gamma y \cos(\omega t) \tag{4.1}$$

where γ represents the section's dihedral (flapping) angle, Γ represents its amplitude, and ω is the flapping frequency. The dynamic twist is linearly proportional to the span according to the following relation:

$$\delta\theta = -\beta_0 y \cos(\omega t + \varphi) \tag{4.2}$$

where φ is the phase shift between pitch and plunge. Then, the total pitch angle of the airfoil chord with respect to the free stream velocity U is given by

$$\theta = \overline{\theta}_a + \overline{\theta}_w + \delta\theta \tag{4.3}$$

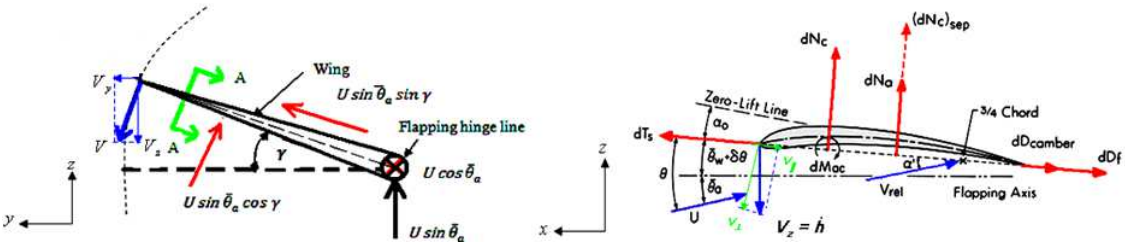

Figure 4.3: A front and section view of flapping wing

In the case of whole wing motion (no flapping axis), θ will be the wing mean pitch angle. Using the leading edge as the reference point, the wing motion can be described by three discrete motions. These are the plunging motion, pitching motion and the forward motion relative to the freestream velocity (U). The component of plunging velocity h in a direction perpendicular to the airfoil chord line seen at each instant of time is $\dot{h}cos(\theta - \overline{\theta}_a)$. In the pitching direction, the $\frac{3}{4}$ chord point is the point of interest. As such, the radius of rotation at that chord location yields a rotational velocity that is equal to $\frac{3}{4}C\dot{\theta}$. As for the forward motion, the instantaneous relative angle of attack is $\delta\theta$ which gives the velocity in vertical direction $U\delta\theta$. The relative angle of attack α at $\frac{3}{4}$ chord location due to wing motion is then given by

$$\alpha = \frac{\dot{h}cos(\theta - \overline{\theta}_a) + \frac{3}{4}C\dot{\theta} + U(\theta - \overline{\theta})}{U} \tag{4.4}$$

4.1.2 Unsteady aerodynamic model

The unsteady aerodynamic model developed by DeLaurier [113] is used to estimate the aerodynamic loads. This model is an extension of the classical Theodorsen's unsteady model [28]. Jones [137] obtained a modified frequency response function over that of Thedorsen's that is suitable for finite but large aspect ratio wings. In his model, DeLaurier [113] used Jones's modification [137] in a strip theory approach to assess the aerodynamic performance of the flying Pterosaur. The model accounts for the unsteady vortex wake effect, viscous friction drag, partial leading edge suction and post-stall behavior. It is considered as one of the most complete models to analyze forward flight of birds and flapping air vehicles.

To calculate the forces generated during a flapping cycle, the flow relative velocity and

flow relative angle of attack should be determined. Using the derived expression of relative angle of attack at $\frac{3}{4}$ chord location due to the wing's motion given by equation (4.4), the flow's relative angle of attach α'at $\frac{3}{4}$ chord location is given by:

$$\alpha' = [C(K)_{Jones}]\alpha - \frac{w_o}{U} \tag{4.5}$$

The coefficient $C(K)_{Jones}$ in equation (4.5) derived by Jones [137] accounts for the wings finite span unsteady vortex wake by means of strip theory model. He uses *modified Theodorsen function* for finite aspect ratio wings which is given by:

$$C(K)_{Jones} = \left(\frac{AR}{2+AR}\right)C'(k) \tag{4.6}$$

$$k = \frac{cw}{2U} \tag{4.7}$$

$C(K)_{Jones}$ is a complex function. It is more convenient to use Scherer's [138] alternative formulation where the complex form of $C'(k)$ is written as:

$$C'(k) = F'(k) + iG'(k) \tag{4.8}$$

Substituting equation (4.8) into equation (4.6) and then substituting the outcome into equation (4.5) with the assumed motion

$$\alpha = Ae^{-wt} \tag{4.9}$$

Eventually, $\acute{\alpha}$ is expressed as:

$$\alpha' = \frac{AR}{2+AR}\left(F'(k)\alpha + \frac{C}{2U}\frac{G'(k)}{k}\dot{\alpha} - \frac{w_o}{U}\right) \tag{4.10}$$

where the downwash term is given by:

$$\frac{w_o}{U} = 2\frac{(\alpha' + \overline{\theta})}{(2+AR)} \tag{4.11}$$

A. Attached flow

1. Normal force

   The normal force on the wing differs depending on whether the flow is attached or separated. To calculate the normal force for the attached flow, the section's normal force due to circulation can be written as:

$$dN_c = \frac{1}{2}\rho U V C_n(y) c dy \tag{4.12}$$

   where, the normal force coefficient is given by:

$$C_n(y) = 2\pi(\alpha' + \alpha_o + \overline{\theta}) \tag{4.13}$$

   Another additional normal force contribution comes from the apparent mass effect or virtual mass force. The acceleration of this mass of air shows up as a virtual mass force which acts at the mid-chord and is given by:

$$dN_a = \frac{\rho\pi c^2}{4}\dot{v_2} dy \tag{4.14}$$

   where $\frac{\rho\pi c^2}{4}$ is the mass of air enclosed in a thin cylinder of width dy and of diameter equal to the chord. $\dot{v_2}$ is the time rate of change of the mid-chord normal velocity component due to the wing's motion and expressed as:

$$\dot{v_2} = U\dot{\alpha} - \frac{1}{4}c\ddot{\theta} \tag{4.15}$$

   The section's total attached flow normal force is

$$dN = dN_a + dN_c \tag{4.16}$$

2. Chordwise force

   The section's circulation distribution likewise generates forces in the chordwise direction, as illustrated in figure A.26. The chordwise force due to camber is given by:

$$dD_{camber} = -2\pi\alpha_o(\alpha' + \overline{\theta})\frac{1}{2}\rho\hat{V}V_n c dy \tag{4.17}$$

Garrick [115] presented a theory where the leading-edge suction is examined for a two-dimensional airfoil. Incorporating his theory into the strip theory model, one gets an expression for the chordwise force due to leading-edge suction as:

$$dT_s = \eta_s 2\pi \left[\alpha' + \overline{\theta} - \frac{1}{4}\left(\frac{c\dot{\theta}}{U}\right)\right]^2 \frac{1}{2}\rho \hat{V} V_n c dy \tag{4.18}$$

where η_s is the leading edge suction efficiency factor. Viscosity also gives a chordwise friction drag as:

$$dD_f = (C_d)_f \frac{1}{2}\rho V_x c dy \tag{4.19}$$

where V_x is the relative flow speed tangent to the section, which can be approximated by:

$$V_x = U\, cos(\theta) - \dot{h}\, sin(\bar{\theta}) \tag{4.20}$$

Thus, the total chordwise force is given by:

$$dF_x = dT_s - dD_{camber} - dD_f \tag{4.21}$$

B. Stall criterion

Prouty [139] has shown that for a pitching airfoil the flow can remain attached at angles of attack larger than the static stall angles of the airfoil. As an advantage the strip theory model allows for an approximation to localized post stall behavior consequently, Prouty uses a dynamic stall-delay effect, represented by an angle $\Delta\alpha$ in order, to account for the difference between the static and effective stall angles, $\Delta\alpha$ is given by:

$$(\alpha_{stall})_{eff} - (\alpha_{stall})_{st} = \Delta\alpha = \xi\sqrt{\frac{c\,\dot{\alpha}}{2U}} \tag{4.22}$$

where ξ is found experimentally and depends on the local Mach number. In this case it was determined that $\Delta\alpha$ is given by:

$$\Delta\alpha = 0.51\Big(\frac{\dot{\alpha}}{\dot{\alpha_{mag}}}\Big)\sqrt{\frac{c\,\dot{\alpha}_{mag}}{2U}} \tag{4.23}$$

where $\alpha_{\dot{mag}}$ is the absolute value of $\dot{\alpha}$. The magnitude value of $\dot{\alpha}$ is to ensure that the term under the square root is positive and the term in the brackets ensures that the correct sign is used. Therefore the criterion for the attached flow over the wing segment is:

$$(\alpha_{stall})_{min} \leq \left[\alpha' + \bar{\theta} - \frac{3}{4}\left(\frac{c\dot{\theta}}{U}\right)\right] \leq (\alpha_{stall})_{max} \tag{4.24}$$

C. Stalled flow

Since, the stall behavior is strictly dependent on the static stall characteristics for the airfoil, it is assumed that negative α' stalling would not occur, hence the lower limit is of no interest. When the upper limit is exceeded, the flow is separated and the normal force under separation condition is expressed as:

$$(dN)_{sep} = (dN_c)_{sep} + (dN_a)_{sep} \tag{4.25}$$

where $(dN_c)_{sep}$ is due to cross-flow drag and is given by:

$$(dN_c)_{sep} = (C_d)_{cf}\frac{1}{2}\rho\hat{V}V_n c dy \tag{4.26}$$

where $(C_d)_{cf}$ is the post stall normal force coefficient and is equal to 1.98 according to Hoerner [140]. $\hat{V}$ is the resultant of the chordwise component and is given by:

$$\hat{V} = \sqrt{{V_x}^2 + {V_n}^2} \tag{4.27}$$

where V_n is the mid-chord normal velocity component due to the wing's motion and is given by:

$$V_n = \dot{h}\, cos(\bar{\theta}) + \frac{1}{2}c\dot{\theta} + U\, sin(\theta) \tag{4.28}$$

and V_x is given in equation (4.20). It is evident that $\hat{V}$ is a nonlinear function of the independent variables $\bar{\theta}$ and h. Also, $(dN_a)_{sep}$ due to apparent mass effects is assumed to be half that of the attached flow value in equation (4.14) and is given by:

$$(dN_a)_{sep} = \frac{1}{2}(dN_a) \tag{4.29}$$

When the attached flow range is exceeded, totally separated flow is assumed to abruptly occur. For that condition, all chordwise forces are negligible.

D. Lift and Thrust

Now, the equations for the segment's instantaneous lift and thrust are:

$$dL = dLcos\theta + dF_x sin\theta \tag{4.30}$$

$$dT = dF_x cos\theta - dN sin\theta \tag{4.31}$$

These may be integrated along the span to give the whole wing's instantaneous lift and thrust as:

$$L(t) = \int_0^{\frac{b}{2}} cos(\gamma(t))dL \tag{4.32}$$

$$T(t) = 2\int_0^{\frac{b}{2}} dT \tag{4.33}$$

The wing's average lift and thrust are obtained by integrating L(t) and T(t) over the cycle.

$$\overline{L} = \frac{1}{2\pi}\int_0^{2\pi} L(\phi)d\phi \tag{4.34}$$

$$\overline{T} = \frac{1}{2\pi}\int_0^{2\pi} T(\phi)d\phi \tag{4.35}$$

E. Aerodynamic Power and Propulsive efficiency

For the attached flow the instantaneous power required to move the section against its aerodynamic loads is given by:

$$dP_{in} = dF_x\dot{h}sin(\theta - \overline{\theta}_a) + dN\left[\dot{h}cos(\theta - \overline{\theta}_a) + \frac{1}{4}c\dot{\theta}\right] + dN_a\left[\frac{1}{4}c\dot{\theta} - dM_\alpha\dot{\theta} - dM_a\dot{\theta}\right] \tag{4.36}$$

where dM_α is the section's pitching moment about its aerodynamic center and depends on the airfoil characteristics. Also dM_a includes apparent-camber and apparent-inertia moments and is given by:

$$dM_a = -\left[\frac{1}{16}\rho\pi c^3\dot{\theta}U + \frac{1}{128}\rho\pi c^4\ddot{\theta}\right]dy \tag{4.37}$$

For the separated flow, equation (4.25) is simplified by ignoring dF_x, $dM_a c$ and dM_a , so we have:

$$dP_{in} = (dN)_{sep}\left[\dot{h}cos(\theta - \overline{\theta}_a) + \frac{1}{2}c\dot{\theta}\right] \tag{4.38}$$

The instantaneous aerodynamic power needed by the whole wing is found from the integration over the span, and the average input power throughout the cycle is obtained by the integration over the flapping cycle (ϕ). Since the flight speed U is constant, one can determine the average output power by multiplying the average thrust by the flight speed, so we have:

$$\overline{P}_{out} = \overline{T}U \tag{4.39}$$

Therefore, the average propulsive efficiency may be calculated from:

$$\overline{\eta} = \frac{\overline{P}_{out}}{\overline{P}_{in}} \tag{4.40}$$

4.1.3 Verification and Validation of the Aerodynamic Model

We start by studying the effects of the number of time samples per cycle and the number of spanwise strips on the convergence of the aerodynamic model. Figure 4.4 shows the effects of the number of time samples per cycle on the variations of the cycle-averaged lift, thrust, input power and propulsive efficiency with the dynamic twist angle. The results show that 20 samples per cycle is an appropriate choice. On the other hand, figure 4.5 shows the effects of the number of spanwise strips on the same variations. It is found that 12 strips per semi-span (24 strips per the whole wing) is a good choice.

The used aerodynamic model has been verified in an earlier work [125] using the results presented and validated against the results of Kamakoti et al. [141] and Benedict [142]. Here, the final results of Zakaria et al. are presented [125]. The airfoil used is *Liebeck LPT* 110A. The used kinematic parameters for the Pterosaur replica and the airfoil parameters are in table 4.1 and table 4.2, respectively.

Table 4.1: Aerodynamic data for Liebeck LPT 110 airfoil

Parameter	Value	Definition
α_o	0.5 (deg)	Zero-lift angle of attack
η_s	0.98	Leading edge suction efficiency
C_{mac}	0.025	Moment coefficient about aerodynamic center
$(\alpha_{stall})_{max}$	13 (deg)	Stall angle

Table 4.2: Kinematic data for *Pterosaur replica* used in Delaurier's design case

	W(kg)	b(m)	f(hz)	U(m/s)	$\Gamma(deg)$	$\overline{\theta}_a$(deg)	$\beta_0(deg/m)$
Pterosaur	18.5	5.48	1.2	13.411	20	7.5	0 - 10

The wing of the Pterosaur replica is divided into twelve strips of equal width ($dy = 0.224m$) as shown in table 4.3. Also 20 time step intervals over the whole cycle were chosen. In applying shape optimization we choose the mid-span location for each strip as the prescribed chord location.

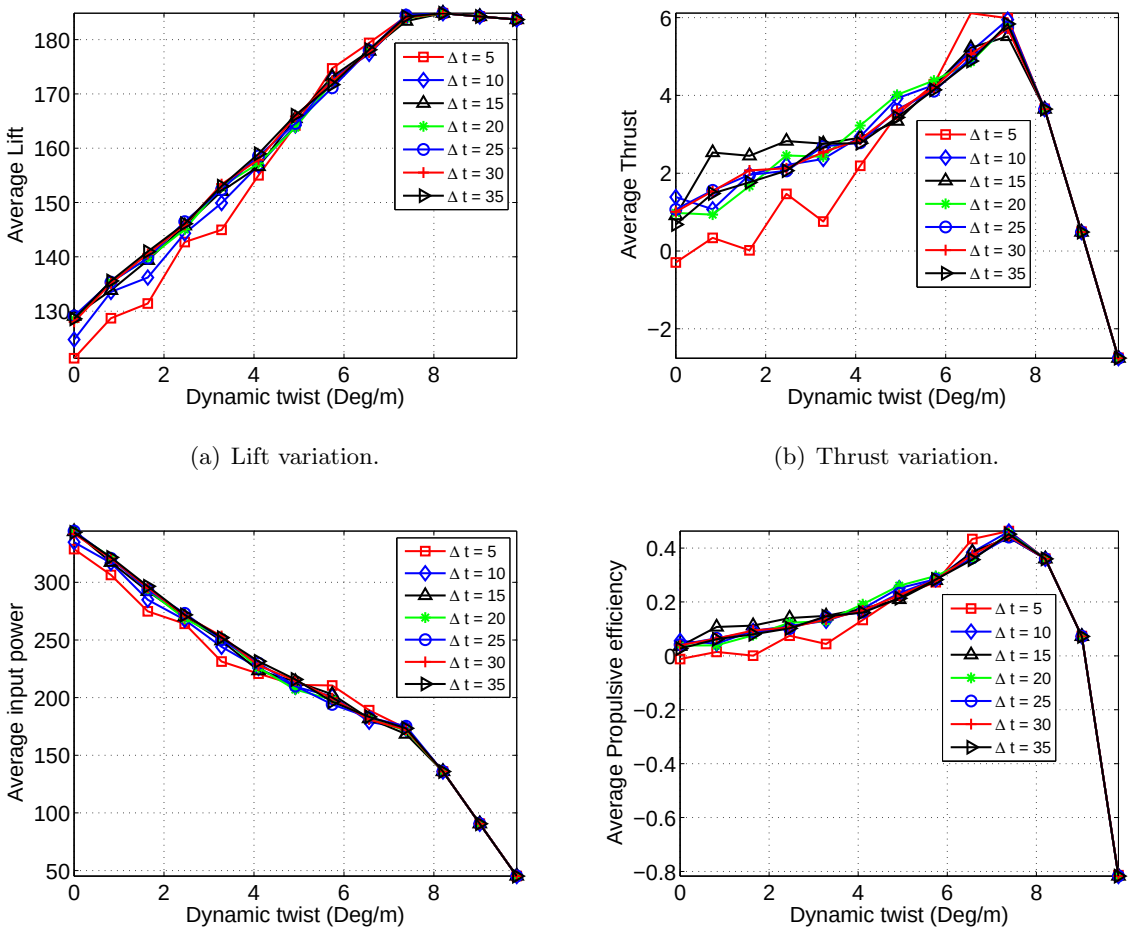

(a) Lift variation.

(b) Thrust variation.

(c) Power variation.

(d) Propulsive efficiency variation.

Figure 4.4: Effect of the number of time samples per cycle on the variations of the cycle-averaged lift, thrust, input power and propulsive efficiency with the dynamic twist angle β_0.

Table 4.3: Mean chord of the twelve strips for pterosaur

Section No.	1	2	3	4	5	6	7	8	9	10	11	12
Chord	0.74	0.6	0.51	0.45	0.41	0.41	0.42	0.36	0.30	0.28	0.23	0.12

The obtained results by Zakaria et al. [125], as presented in figure 4.7, show close agreement with the results obtained by Delaurier [113], Kamakoti et al. [141] and Benedict [142].

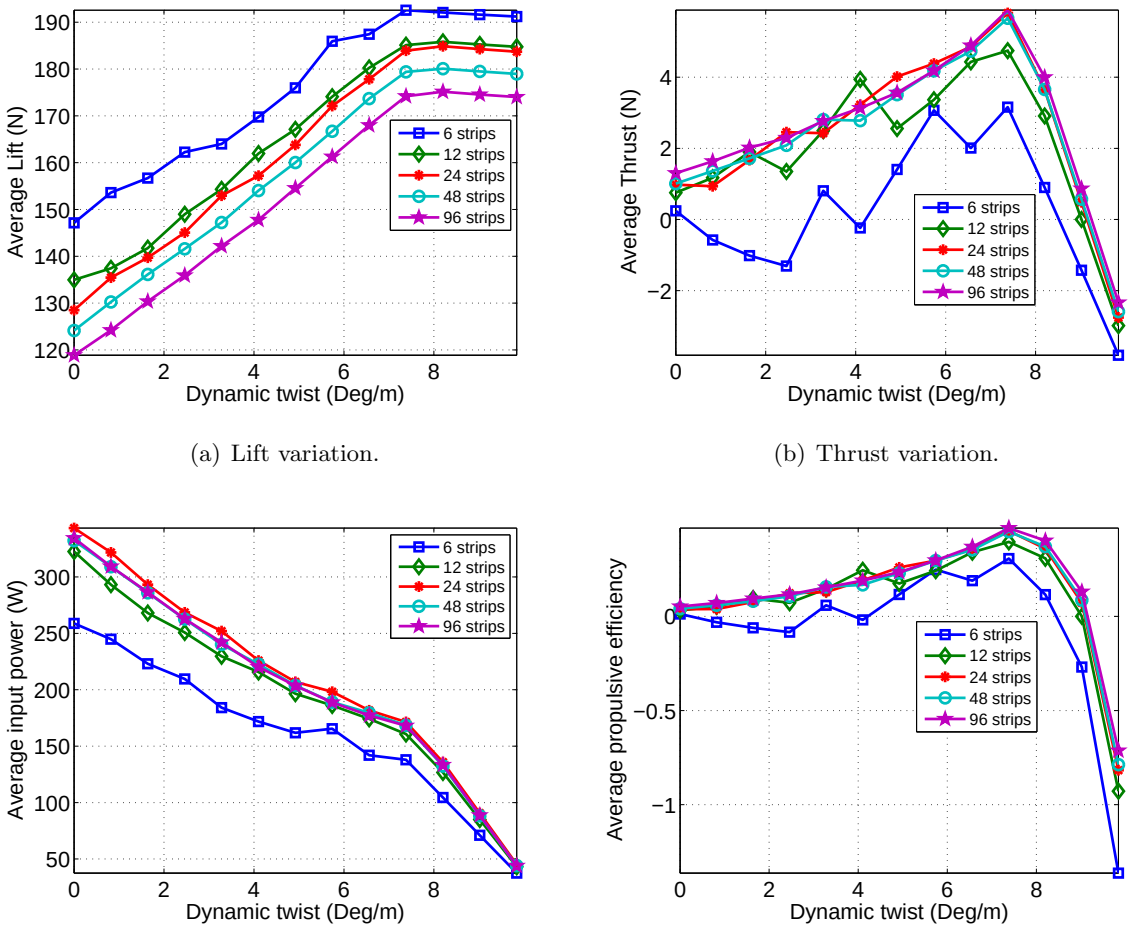

(a) Lift variation.

(b) Thrust variation.

(c) Power variation.

(d) Propulsive efficiency variation.

Figure 4.5: Effect of the number of spanwise strips on the variations of the cycle-averaged lift, thrust, input power and propulsive efficiency with the dynamic twist angle β_0.

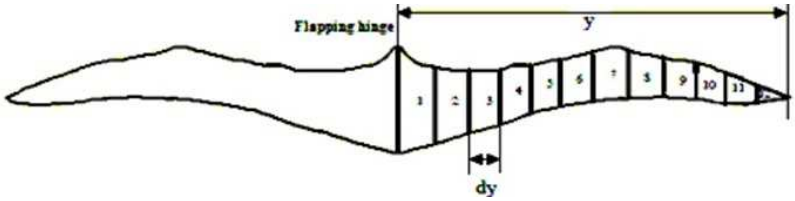

Figure 4.6: Schematic diagram of a Pterosaur Replica wing.

For the given flapping frequency of 1.2 Hz, it is seen that the average generated lift balances the model's weight (18.478 kg) at a flapping-axis angle of 7.5°, the flight speed U is 13.4m/s

and the dynamic twist magnitudes are in excess of 7.3 (deg/m).

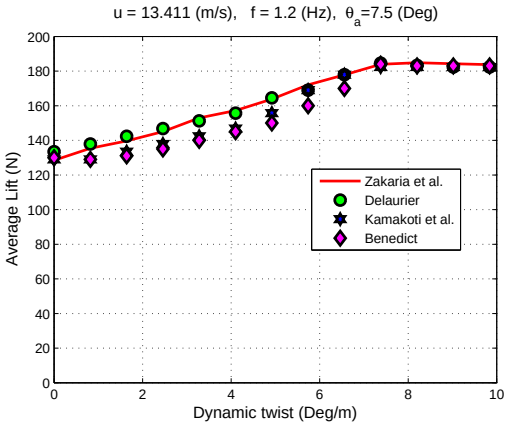

(a) Lift variation.

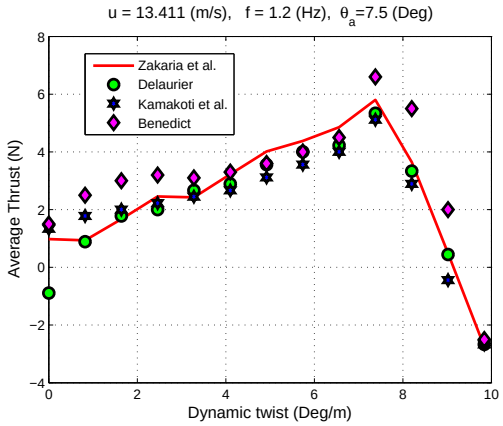

(b) Thrust variation.

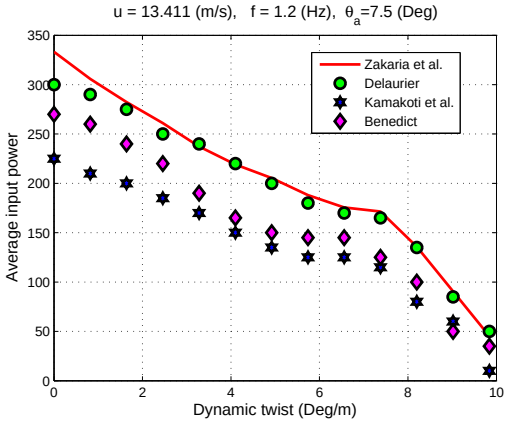

(c) Power variation.

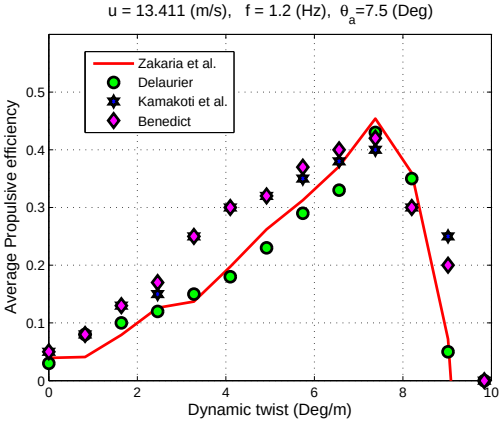

(d) Propulsive efficiency variation.

Figure 4.7: Variation of the cycle-averaged lift, thrust, required power, and propulsive efficiency with the dynamic twist β_0.

4.1.4 Kinematic and Shape Optimization

Two objective functions are considered, namely, the cycle-average of the required power and the propulsive efficiency while satisfying the trim constraints; that is, the cycle-averaged lift and thrust forces balance the weight and drag forces, respectively.

A. Necessity of Inertial Power

Hamdaoui et al. [143] used DeLaurier's model to perform kinematics optimization for flapping micro air vehicles. They showed that DeLaurier's model does not yield a feasible solution for the optimization problem. This deficiency may be attributed to the lack of some of the considerable physical aspects such as the inertial power and body drag. It should be noted that large dynamic twist angles may yield negative aerodynamic power as shown from the trend in figure 4.7(c). Thus, accounting for the inertial power requirements is necessary for a proper formulation of the optimization problem. The total mechanical power requirements include inertial and aerodynamic contributions

$$P_{Mechanical} = P_{Inertia}(t) + P_{Aero}(t) \tag{4.41}$$

Two contributions are considered for the inertial power requirements; for each of the rotational motions in the adopted kinematics. These are the inertial power required for performing the motion about the x-axis (P_γ) and the motion about the y-axis (P_θ). Thus, the inertial power can be written as:

$$P_{Inertial} = P_\gamma + P_\theta$$

where P_γ and P_θ are defined as

$$P_\gamma = I_x \dot{\gamma}\ddot{\gamma} \ , \ \ P_\theta = 2\int_0^{\frac{b}{2}} I'_y(y)\dot{\theta}(y)\ddot{\theta}(y)dy$$

where I_x is the moment of inertia of the whole wing about the x-axis passing through the wing fulcrum and I'_y is the moment of inertia of a wing section about the spanwise axis passing through its centroid. These are given by:

$$I_x = 2\rho_w \tau \int_0^{\frac{b}{2}} c(y)y^2 dy \ \ and \ \ I'_y(y) \simeq \frac{\rho_w \tau c^3(y)}{12}$$

where ρ_w is the density of the wing material and τ is the wing thickness. Thus, P_θ is given by:

$$P_\theta = \frac{\rho\tau\beta_0^2\omega^3 \sin 2(\omega t + \varphi)}{12} \int_0^{\frac{b}{2}} c^3(y)y^2 dy \tag{4.42}$$

Mere consideration of the inertial power requirements without taking into account the elastic storage and cost to dissipate negative power could yield nonphysical results from the kinematic optimization problem. Kurdi et al. [130] recommended the following formulation as a remedy to consider the elastic storage and the cost to dissipate negative power:

$$p_{Mechanical} = \begin{cases} -\alpha_e |P_{Mechanical}| + \beta_e (1-\alpha_e)|P_{Mechanical}|, & \text{if } P_{Mechanical} < 0 \\ P_{Mechanical}, & \text{otherwise} \end{cases} \tag{4.43}$$

where $\alpha_e \in [0,1]$ and $\beta_e \in [0,1]$ are the parameters to determine the percentage of elastic storage and cost to dissipate negative power which can be written as follows:

$$\begin{cases} \alpha_e = 0, & \text{no elastic storage} \\ \alpha_e = 1, & 100\% \text{ elastic storage} \\ \beta_e = 0, & \text{no cost to dissipate negative power} \\ \beta_e = 1, & 100\% \text{ cost to dissipate negative power} \end{cases} \tag{4.44}$$

B. Formulation of the Optimization Problem

The Pareto front of the multi-objective optimization problem is constructed using the ϵ-constraint technique. Using this technique for the problem in hand, one of the two objectives is first handled in a single-objective, unconstrained optimization problem while second objective is overlooked. Next, the second objective is handled in another single-objective, constrained optimization problem where the first objective is taken as the constraint. In doing so, the propulsive efficiency maximization problem is solved first without considering the power requirements. That is, the optimization problem is stated as follows:

$$\min_{\boldsymbol{x}} \quad \frac{1}{\overline{\eta}} \quad \text{subject to}$$

$$\overline{L} - W \geq 0 \ , \ \overline{T} - D_{\text{body}} \geq 0$$

$$\text{and} \ \ \boldsymbol{x}_{\text{LB}} < \boldsymbol{x} < \boldsymbol{x}_{\text{UB}}$$

where $\boldsymbol{x}$ represents the vector of design variables which includes either the kinematic parameters or the planform variables. The kinematic design parameters include the flapping frequency f, the flapping amplitude Γ, the pitching angle $\overline{\theta}_a$ relative to the free-stream, the dynamic twist angle β_0, and the phase angle φ between the pitch and the plunge motion.

The planform variables are taken to be the chord lengths at the specified stations namely, the twelve stations per semi-span, as shown in figure 4.6. $\boldsymbol{x}_{\mathrm{LB}}$ and $\boldsymbol{x}_{\mathrm{UB}}$ denote the lower and upper bounds of the design variables, respectively. Here, fiber composite is used as a material for the wing which density is given by $\rho_w = 2330\ Kg/m^3$ and a wing thickness of 1 mm is used.

Let $\eta_{\max}$ denote the resulting maximum efficiency obtained from solving the problem stated above. Then, the ϵ-constraint technique is used to solve the following optimization problem:

$$\min_{\boldsymbol{x}} \quad C_p \quad \text{subject to}$$

$$\overline{L} - W \geq 0 \ , \ \overline{T} - D_{\mathrm{body}} \geq 0 \ , \ \overline{\eta} \geq \eta_{\max} - \epsilon$$

$$\text{and} \ \ \boldsymbol{x}_{\mathrm{LB}} < \boldsymbol{x} < \boldsymbol{x}_{\mathrm{UB}}$$

where $C_p = \frac{2\overline{P}}{\rho \overline{U}^3 S}$ is the coefficient of the cycle-averaged required power. An initial small value is assigned to ϵ that is then increased gradually until the unconstrained optimal efficiency value is attained.

For each single objective, constrained optimization problem, we use the sequential quadratic programming as a gradient-based method. The gradient-based approach is preferred over the global-based optimization algorithms in this problem because of the expected smooth dependence of the objective and constraints on the design variables. However, similar to all gradient-based methods, the used one is essentially local. To overcome this issue, we solve each optimization problem many times, each starting form a different initial guess in the design space. In fact, we start at the corners and the center. From all these problems, we select the best answer. The constraints are considered via an *active set* procedure, which is also known as the *projection method* [144, 145]. The algorithm comprises two steps. In the first step, we determine a feasible point, if there is any. In the second step, we generate an iterative sequence of feasible points that converges to the optimum point.

C. Kinematic Optimization

The optimum kinematic parameters are now determined for a forward speed $U = 13.41 m/s$ and the prescribed planform of the Pterosaur replica that is shown in figure A.34 (i.e., $\boldsymbol{x} =$

$[f,\ \Gamma,\ \overline{\theta}_a,\ \beta_0,\ \varphi]^T$). Figure 4.8(a) shows the Pareto front for the case of $\alpha_e = 1$ (i.e., full elastic storage). Figure 4.8(b) shows the Pareto front for the case of $\alpha_e = 1$ and $\beta_e = 1$ (i.e, no elastic storage but no cost to dissipate negative power).

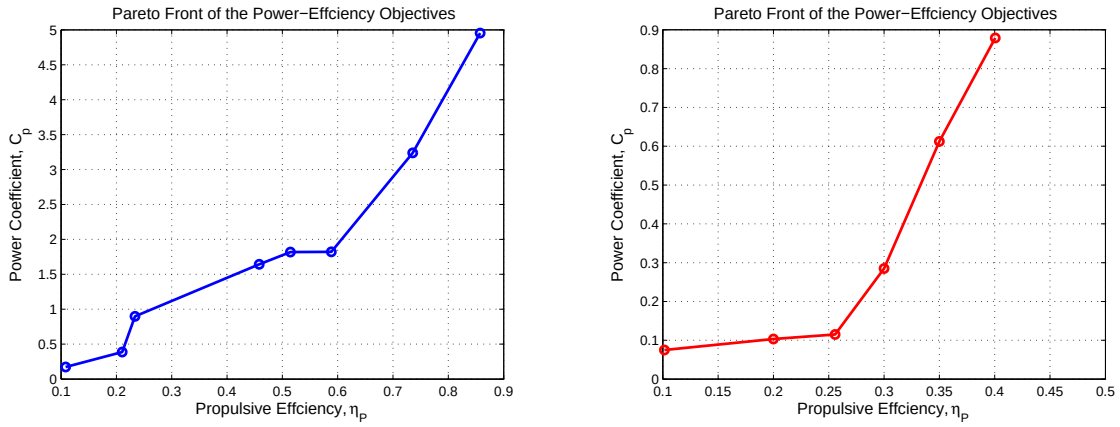

(a) $\alpha_e = 1$. (b) $\alpha_e = 0$ and $\beta_e = 0$.

Figure 4.8: Pareto front of the power-efficiency multi-objective optimization problem for the cases of $\alpha_e = 1$ (full elastic storage) and $\alpha_e = 0$ and $\beta_e = 0$ (no elastic storage but no cost to dissipate negative power).

As stated above, figure 4.8(a) shows that full elastic storage yields unreasonably large power and efficiency values. Therefore, in the following results, we use $\alpha_e = 0$ (no elastic storage) and $\beta_e = 0$ (no cost paid to dissipate negative power). That is, the intermediate case between the two extremes of $\alpha_e = 1$ (full elastic storage) and $\alpha_e = 0$ and $\beta_e = 1$ (no elastic storage and 100% cost paid to dissipate negative power). Figure 4.8(b) shows the Pareto front for the considered case of $\alpha_e = 0$ and $\beta_e = 0$, which gives much more physical results. Table 4.4 shows the optimum kinematics for the two boundary points of the Pareto front (maximum efficiency and minimum power coefficient).

1. Effect of design variables on the objectives

Figure 4.9 shows the variations of the objectives (efficiency and power coefficient) and the constraints (lift-to-weight ratio and thrust-to-drag ratio) with the design variables. When the

Table 4.4: Optimum kinematics for the two boundary points of the Pareto front (maximum efficiency and minimum power coefficient).

Variable	LB	UB	$\boldsymbol{x}^*$ for minimum C_p	$\boldsymbol{x}^*$ for maximum $\overline{\eta}$
Flapping frequency f (Hz)	0	20	1.1	3.4
Flapping amplitude, Γ	0	90°	25.1°	24°
Dynamic twist, β_0	0	$\frac{180^\circ}{b}/m$	$10.5^\circ/m$	$17.7^\circ/m$
Pitching angle, $\overline{\theta}_a$	$\frac{\beta_0 b}{2} - 90^\circ$	$90^\circ - \frac{\beta_0 b}{2}$	7.3°	7.1°
Phase angle, φ	-90°	90°	-90.0°	-75.4°
C_p			0.08	0.88
$\overline{\eta}$			10.2%	40.1%

variation with one of the design variables is considered, the other design variables are set to the values of the maximum efficiency $x = [3.4,\ 24^\circ,\ 7.1^\circ,\ 17.7^\circ/m,\ -75.4^\circ]^T$. Figure 4.9(d) shows that the optimizer yields a local maximum value for the efficiency while satisfying the lift and thrust constraints. For the other three design variables, figures 4.9(a), 4.9(b), and 4.9(c) show the existence of better efficiency design points with an unsatisfactory lift constraint. Thus, the optimizer certainly converges to less efficiency points to satisfy such a design constraint.

Unlike the case of maximum efficiency, figure 4.10 shows that the optimizer results in a local minimum for the power coefficient while satisfying the lift and thrust constraints. Thus, the lift and thrust constraints are the main driving forces for this design optimization problem. Figure 4.10(b) shows the existence of design points with less power coefficients with unsatisfactory thrust constraint. Figure 4.10(c) shows the existence of design points with less power coefficients with unsatisfactory lift constraint, and Figs. 4.10(a) and 4.10(d) show the existence of design points with less power coefficients violating both the lift and thrust constraints.

Recalling the set of parameters that DeLaurier used in his study for the Pterosaur $f = 1.2Hz,\ \Gamma = 20^\circ,\ \overline{\theta}_a = 7.5^\circ,\ \varphi = -90^\circ$, it can be seen that they are very close to the set of

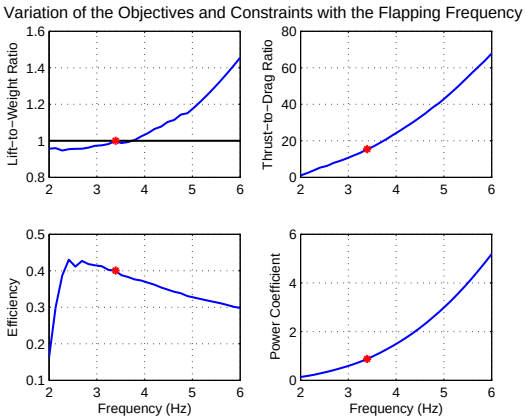

(a) Frequency variation.

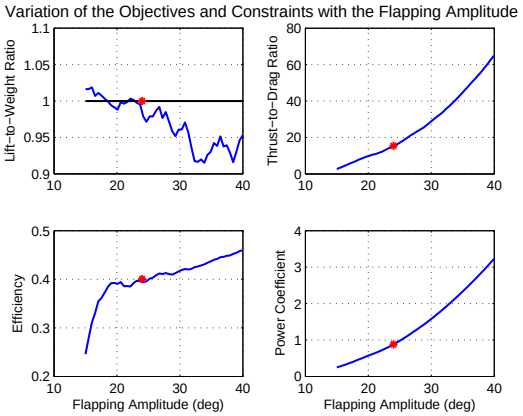

(b) Flapping Amplitude variation.

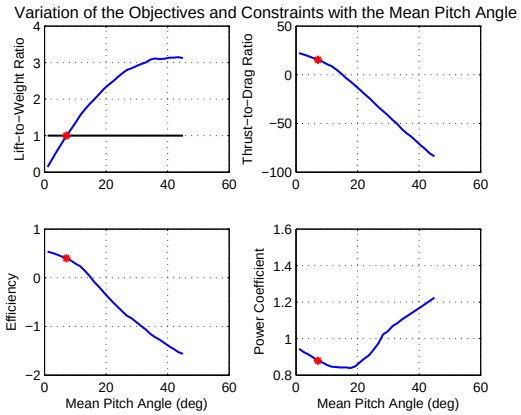

(c) Mean Pitch Angle variation.

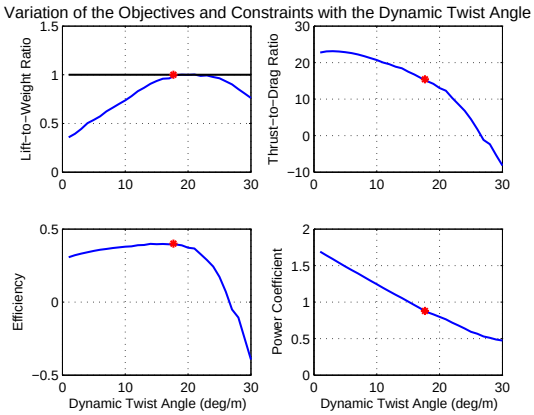

(d) Dynamic Twist Angle variation.

Figure 4.9: Variation of the objectives functions and constraints with the design variables for maximum efficiency. The design point is marked with red dot (∗).

design variables obtained here for a minimum power coefficient. Thus, it can be concluded that DeLaurier's design case study is a minimum power requirement design point.

2. Effect of design variables on the stall angle

As stated in equation (4.24), the maximum stall angle of attack was taken into consideration without considering negative stalling. Thus it is worth to capture the flow separation across the whole wing in the span-wise direction. This can be done by tracing the stalled sections along the span over the whole cycle. Figure 4.11 shows the attached and stalled flow regions

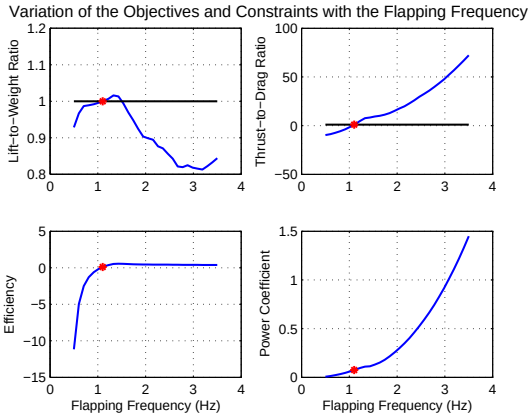

(a) Frequency variation.

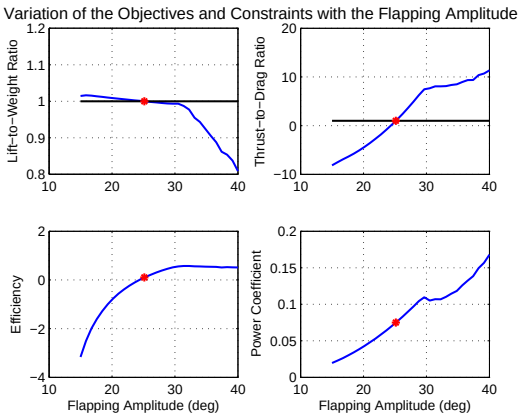

(b) Flapping Amplitude variation.

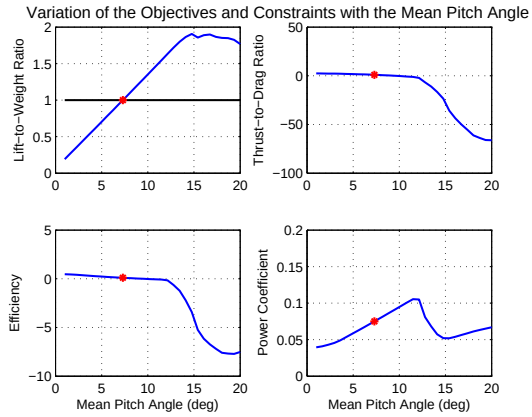

(c) Mean Pitch Angle variation.

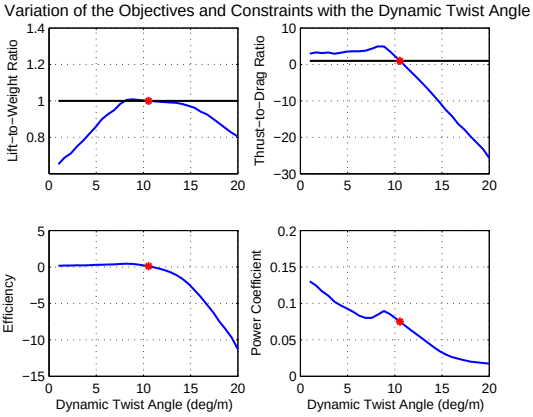

(d) Dynamic Twist Angle variation.

Figure 4.10: Variation of the objectives functions and constraints with the design variables for minimum power coefficient. The design point is marked with red dot (∗).

per section for the prescribed two objectives and Delaurier's design case. The attached section's flow is shown in blue circles and the separated section's flow is in red dots. The results is consistent with the fact that towards the wing tips the stalled section appears with the dynamic twist variation increases (the near root section does not stalled). This implies that for the case of minimum power the lower values of dynamic twist dictates a lower number of stalled sections, on the other hand, the maximum efficiency case with higher dynamic twist value the stalled section was increased to be 9 sections for the whole cycle.

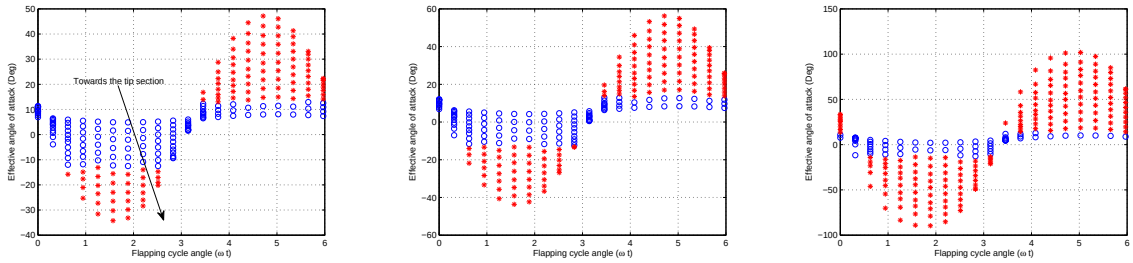

(a) Delaurie's Design case (b) Minimum power coefficient case (c) Maximum propulsive efficiency case

Figure 4.11: Variation of the design variables for the minimum power requirement with the wing section's stall angle

D. Shape Optimization

Finally, we determined the optimum planform shape at forward speed $U = 13.41m/s$ for maximum efficiency. The corresponding optimum kinematic parameters are considered from table 4.4. The design variables are the chord lengths at the twelve considered stations (see figure 4.3). Figure 4.12 shows the obtained optimum planform for maximum efficiency along with the base line shape of the Pterosaur. The leading edge coordinates are shown in black color for both of the actual and optimized shape in figure 4.3. The trailing edge of the optimized shape is shown in red color. It should be noted that, in the optimization problem, the design variables (chord distribution) are given elliptical spanwise weight distribution to account for the three dimensional effects. The obtained maximum efficiency is 46.0%.

An interesting question that is ubiquitously posed by biologists is "How creatures are designed?" More specifically, based on what criterion does the nature design its creatures? A main contribution of this chapter is to try to find an answer to this question regarding the Pterosaur. Noting that our model is of a low-to-medium fidelity and the obtained optimum shape is close to the actual natural shape of the Pterosaur, it seems that, at least for the Pterosaur case, the nature is maximizing efficiency.

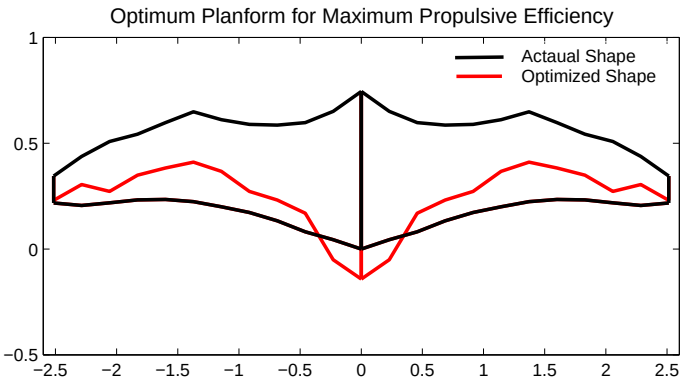

Figure 4.12: Optimum planform for maximum efficiency along with the actual shape of the Pterosaur relpica.

Chapter 5

Applications on Energy Harvesting

5.1 Energy Harvesting from self-induced flutter of a composite beam

Fluid structure interaction phenomena that have been considered for energy harvesting include flutter of wing sections [146], [147], [148], vortex -induced vibrations (VIV) [149] and galloping [150], [151], [152], [153]. In all of these studies, nonlinear phenomena play an important role in determining the level of the harvested energy as shown by others [154], [155]. The previously performed investigations on harvesting energy from fluid-structure interactions are based on attaching a moving structure to a beam with a piezoelectric patch. This setup adds to the weight and volume of the energy harvester and causes a reduction in its energy density, which takes away from the advantage of using piezoelectric transduction to minimize the volume of the harvester.

One important phenomenon that has been observed when it comes to aeroelastic performance of flexible wings is the effects of large wing deformations on the structural frequencies, aerodynamic loads and aeroelastic response in terms of flutter speed and ensuing the limit cycle oscillations. Patil et al. [156], [157] performed a nonlinear aeorleastic analysis on a flexible wing that curved under constant distributed loading to the point where a tip displacement of around 25% of the wing span was achieved. Their results showed significant changes in the frequencies of the torsional and edge-wise bending moments and a decrease of

the flutter speed by more than 50% for such large deformations. In this section, we design an energy harvester that exploits the fact that large deformations can reduce the flutter speed of a cantilever beam. Particularly, we subject a flexible composite beam, held at static angle of attack at the beam root, to airflow. This setup has the advantage of dispensing of the secondary structure needed to induce the beam vibration as in previous setups. By setting the beam at a non-zero angle of attack, it is subjected to a differential aerodynamic loading which results in a uniform static deflection that has the shape of the first bending mode. When this deflection is large enough, the geometric nonlinearities affect the beam's stiffness and induce a change in its natural frequencies, which, in turn, cause the torsional and second bending frequencies to coalesce. This coalescence results in self-induced flutter of the beam. Beyond this bifurcation, the combination of the static deflection and geometric and aerodynamic nonlinearities causes self-sustained limit cycle oscillations (LCO) of the beam that can be efficiently exploited for energy harvesting. Below, we provide details of the performed experiments used to determine the effects of the preset angle of attack, wind speed and load resistance on the levels of the harvested energy from self-induced flutter of a composite beam.

5.1.1 Experimental Setup

The experiments were performed in the subsonic wind tunnel facility of the Department of Engineering Mechanics at Virginia Tech. The tunnel is a suction-type open circuit wind tunnel. The test chamber has a cross section that is 52 cm $\times$ 52 cm. The tests were performed by fixing the composite beam, having the properties listed in table 5.1, to the center of the roof of the test section as shown in figure 5.1. The beam was attached to a stepper motor connected to a controller that was used to set the static angle of attack at the beam root. The measurements were performed over a range of angle of attacks between 0^o and 14.4^o degrees with a step change of 1.8^o degrees. Figure 5.2 shows the schematic diagram of the experimental set-up and the devices used. The system is composed of the plate attached to an MFC connected to a stepper motor to perform the variation in the static angle of attack. The output voltage of the MFC was measured using digital multi-meter and also connected in parallel with USB-6009 National Instruments data acquisition card to measure the cyclic actual volt in time series. The LCO frequency was measured using the spectral analysis

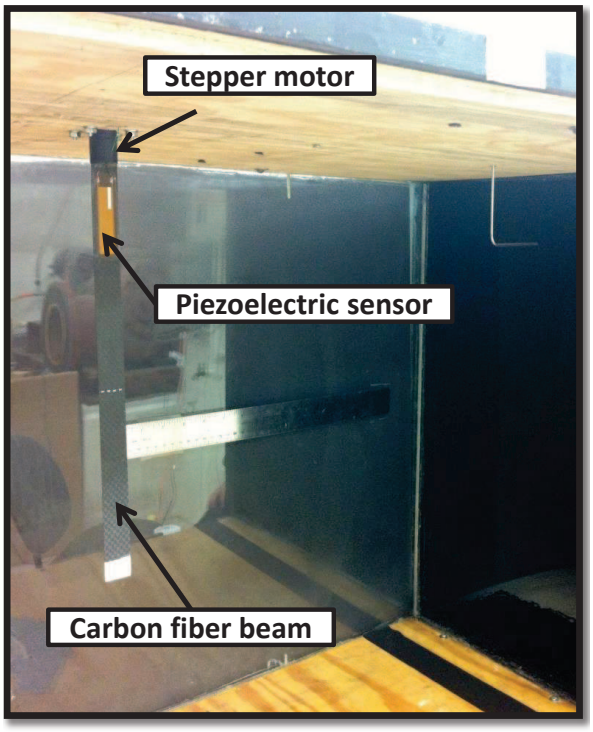

Figure 5.1: Picture of the tested beam as set in the center of the roof of the test section.

through Fast Fourier Transform (FFT) of the AC output voltage signal.

The composite beam was manufactured from two layers of un-sized plainweave $SGP196$ ($IM7-GP$) carbon fiber fabric (6K filaments count in a tow). The composite was constructed using well dried carbon fibers with a polymeric matrix made from epoxy resin/hardener (*Aeropoxy*). The composite matrix layers were fabricated using two thermoset polymers namely, PR 2032 (epoxy resin), and PH3665 (Epoxy hardener). Tests were performed in the ESM machining lab shown in figure 5.3 to obtain the stress-strain curve of a test sample of dimension 4 cm x 2 cm. The stress-strain curve obtained from a three point bending test results which corresponds to a modulus of elasticity of E=29 GPa as shown in figure 5.4. The mechanical properties of the fabricated beam are listed in table (5.1).

A PHOTRON ultima APX-RS high CCD camera was used to measure the static deflection and amplitude of the ensuing limit cycle oscillations. The camera was adjusted to capture 1000 fps with 1024 x 1024 pixel resolution. The camera was installed 1.5 meters downstream the test section. The beam edge facing the camera was painted white to evaluate the bending

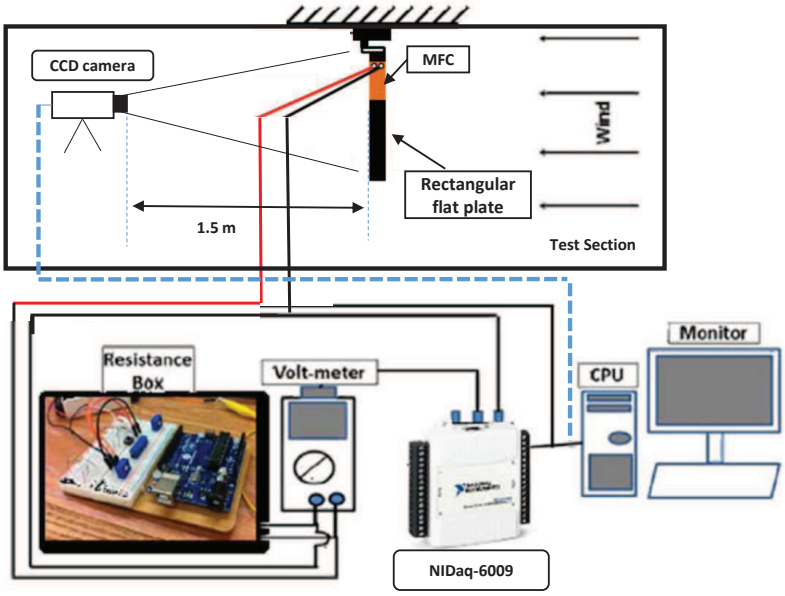

Figure 5.2: Schematic drawing for the whole setup

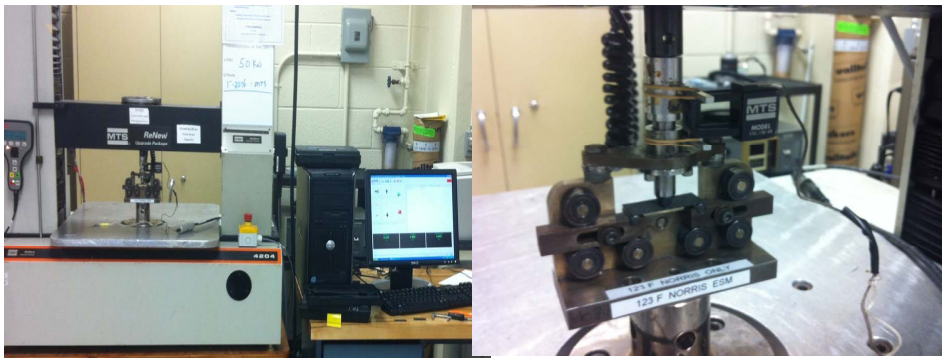

Figure 5.3: ESM machining lab three-point bending test

deflection, also the tip of the beam was painted white to sense the torsional deflection. The camera frustum was adjusted using the enclosed area of the test section as a calibration target, giving an error of ± 2 pixels at the beam view location. Using image acquisition, we were able to split the image colors into two colors with a grey threshold. As such, we were able to measure the static deflections and the LCO amplitudes by tracing the white boundary at each angle of attack from both directions (left and right) to detect the edge at each frame. A straight green line was imposed on the picture to note the beam's original

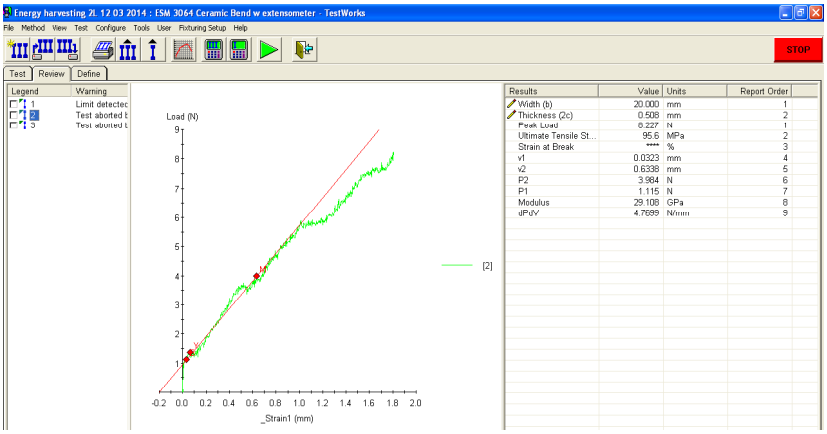

Figure 5.4: Stress displacement curve for the tested beam sample

Table 5.1: Tested carbon fiber cantilever beam properties

Parameter	**Symbol**	**Value (unit)**
Mass	m	0.0028 (kg)
Length	L	0.26 (m)
Thickness	t	0.00049 (m)
Moment of inertia	I_{xx}	$1.96 \times 10^{-13} (m^4)$
Chord	c	0.02 (m)
Young's modulus	E_b	29 (GPa)

position at zero angle of attack (reference position). After scaling the pixels with the beam's dimensions, the static deflection was measured as the lateral distance between the last pixel traced from the white line and the last pixel of the green line with an accuracy of $\pm$ 0.2 mm, which is less than 1.5% and 0.44% of the minimum measured static deflection and LCO amplitude, respectively. Figure 5.5 shows the analyzed images at a flow speeds of 9 m/s for different angles of attack. The measured values of the static deflections and LCO amplitudes are presented in table 5.2. Clearly, there is no static deflection when the angle of attack is zero. At 1.8^o, there is a static deflection with no vibrations. As the angle of attack increased, the amplitudes of both static deflection and LCO increase.

Based on the results in table 5.2, the LCO amplitudes for different angles of attack shows a high potential for exploiting self-induced flutter for the purpose of energy harvesting. For

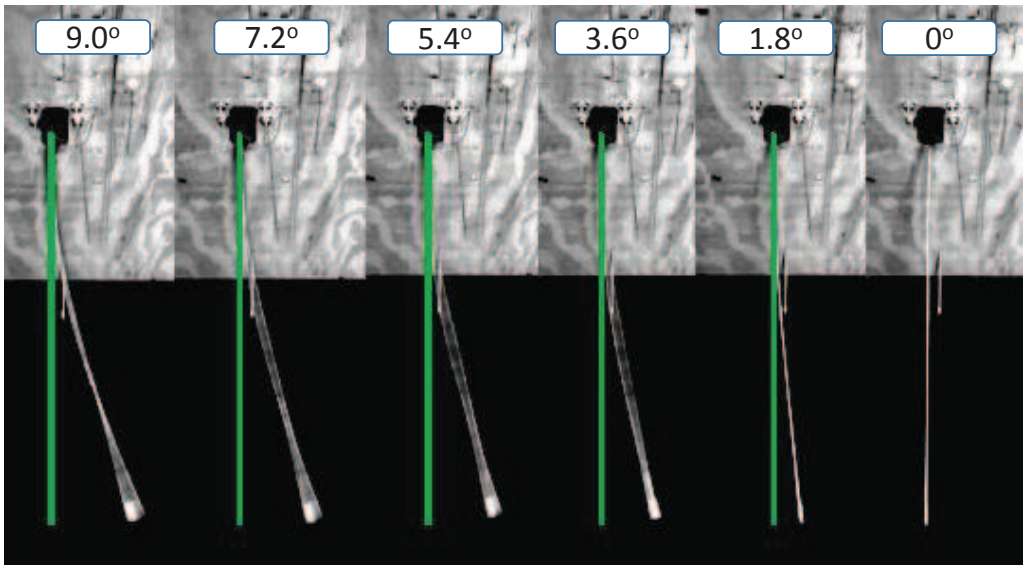

Figure 5.5: Analyzed images of the cantilever beam at 9 m/s with increasing angles of attack

Table 5.2: Static deflections and LCO amplitudes of the beam at 9 m/s (dimensions are in cm)

$\alpha_\circ$	Static deflection (δ_s)	LCO amplitude (δ_{LCO})
0^o	0	0
1.8^o	1.6	0
3.6^o	3.2	0.45
5.4^o	3.5	0.65
7.2^o	4.2	0.8
9^o	4.8	1.1

this purpose, a piezoelectric MFC was attached to the beam 5 mm below the fixed end. The mechanical properties of the Macro-fiber composite and its size are presented in table 5.3. The output voltage of the MFC was acquired at a rate of 2000 Hz. The data segments of the output voltage were recorded over time periods of three seconds. A resistor box was connected to the output wire of the MFC to study the performance of the energy harvester over a broad range of electrical loads that varied between 0.1 MΩ and 10 MΩ.

Table 5.3: Properties and size of the MFC patch

parameter	**Symbol**	**Value (unit)**
Piezoelectric material density	ρ_p	7800 (kg/m^3)
piezoelectric constant	d_{31}	-190 (Pm/V)
Strain permittivity	ε^{33}	15.9 (nF/m)
MFC active length	ℓ_a	40 (mm)
MFC active width	w_a	10 (mm)
MFC thickness	t	0.26 (mm)
MFC total mass	m_{MFC}	2 (gm)

5.1.2 Output power measurements

Figures 5.6(a) and 5.6(b) show the variation of the harvested power with the load resistance respectively for 5.4^o and 7.2^o at airflow speeds between 7 and 10 m/s. The two plots show that the optimal load resistance is 1 $M\Omega$. Furthermore, the level of harvested power increases as the air speed is increased when the angle of attack is set to 5.4^o with the largest value of 0.295 mW obtained at 10 m/s. This is not the case for 7.2^o where, the highest power level was obtained at 9 m/s. The maximum level of harvested power for 7.2^o is 0.272 mW. These results point to the complex relation between the aerodynamic loading and its impact on the static deflection and LCO amplitudes on one hand and the load resistance and level of power harvested on the other hand. The reason is that, both the static deflection and the harvested power impacts the frequency of the beam oscillations. By harvesting energy from a vibrating beam, one is essentially reducing its velocity and as such, is changing its damping. This points to a coupled system where the deflections, oscillations and the level of the harvested energy are coupled.

Figure 5.7 shows the variation of the output power, also presented as power density, with the flow speed for various angles of attack for a load resistance of 1 MΩ. The results show that the maximum harvested power was obtained at 5.4^o angle and 10 m/s. At 7 m/s, the flutter occurs but with small amplitudes yielding low output power levels for all angles of attack. Increasing the flow speed to 8 m/s, the output power is increased with the maximum level attained at the angle of attack of 12.6^o. It is interesting to note that flutter

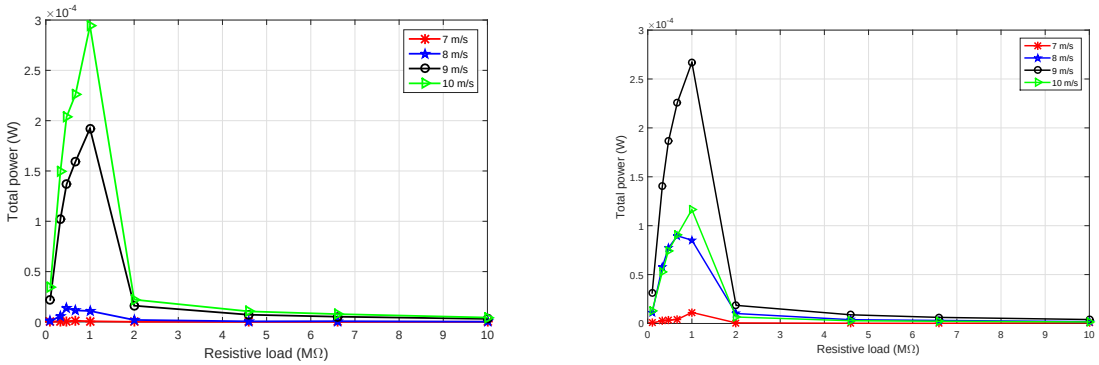

(a) $\alpha_o = 5.4^o$. (b) $\alpha_o = 7.2^o$.

Figure 5.6: Output power versus resistive load at 5.4^o and 7.2^o for various flow speeds.

is not present at the higher angle of attack, 14.4^o. At 5.4^o, the output power is 0.02 mW ($0.0078\ mW/cm^3$). It increases to 0.08 mW ($0.031\ mW/cm^3$) when the angle of attack is set 7.2^o. At 9^o, 10.8^o and 12.6^o, the maximum output power values are near 0.165 mW (0.065 mW/cm^3). The performance of the harvester is completely different at 9 m/s, where the output power increases with increasing the preset angle reaching a maximum value of 0.265 mW ($\simeq 0.104\, mW/cm^3$) at 7.2^o. At larger angles of attack, the level of harvested power is much lower. At 10 m/s, the output power is maximum at 5.4^o and has a value that is close to the one observed at 9 m/s for an angle of attack of 7.2^o.

Figure 5.8 shows the output power versus the flow speed for the case of 1 MΩ and $\alpha_o = 7.2^o$. The plot shows that the power increases as the flow speed is increased and decreases as the flow speed is reduced. The absence of any hysteresis indicates that the bifurcation is super-critical, which means that the beam will not undergo unexpected oscillations due to changes in the air speed such as a gust.

5.1.3 Power spectral analysis

To characterize the global dynamic behavior of the system and the effects of varying the static angle of attack, we present in figure 5.9 the power spectrum for the output voltage at 9 m/s for 5.4^o and 7.2^o. We note that the oscillations frequency is 39 Hz. Increasing the angle of attack to 7.2^o, this frequency shifts to 36.37 Hz. We also note the cubic harmonic in the spectrum which is an exhibit of the role of the system nonlinearities in generating

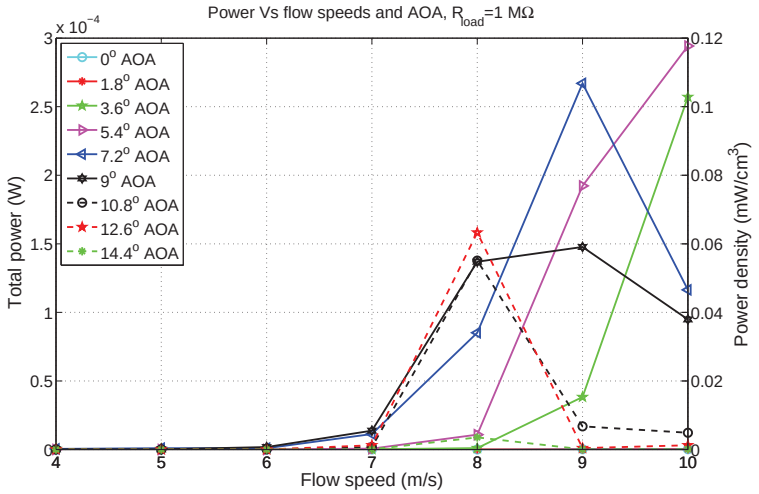

Figure 5.7: Output power versus flow speeds at various static angles of attack when the resistive load is set to 1 MΩ

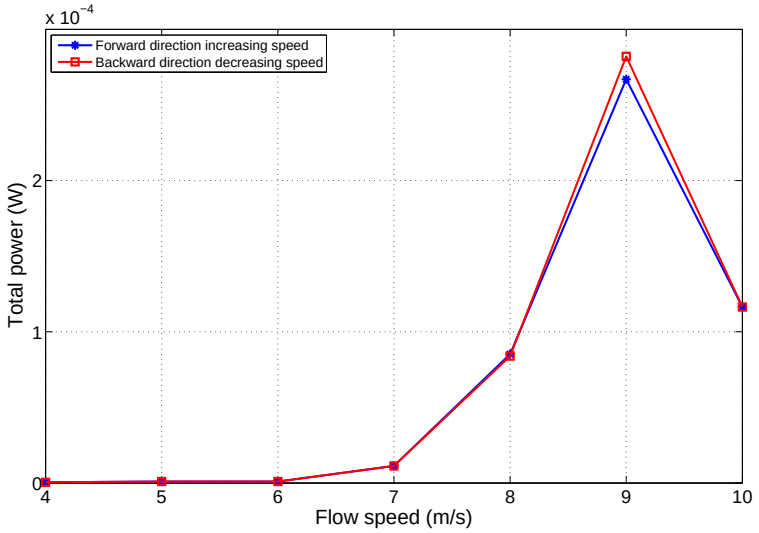

Figure 5.8: Variation of the harvested power as the wind speed is increased and decreased for the case of 1 MΩ at $\alpha_o = 7.2^o$

these dynamic responses. Spectra at other speeds and angles of attack showed these same characteristics. Table 5.5 shows the undeformed beam first and second bending frequencies associated with the corresponding LCO frequencies at various operating flow speeds. As

shown in fig.5.7, the energy harvesting is very effective at 9 m/s and 10 m/s. The closeness of the LCO frequencies at these speeds to that of the second bending mode indicate the significant role played by this mode in the energy harvesting.

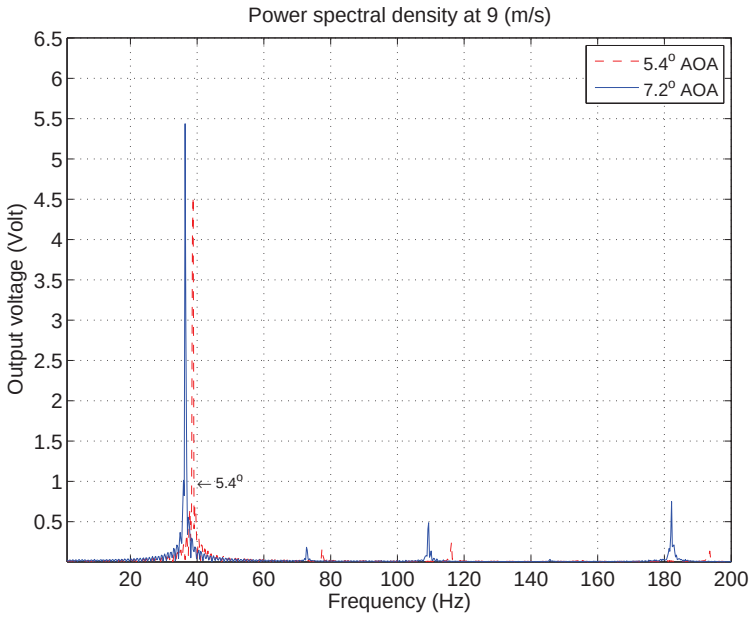

Figure 5.9: Power spectrum of the measured voltage when the air speed is 9 m/s, the electrical load is 1 MΩ

Table 5.4: First two bending modes (no beam deflection) and frequency of LCO for different air speeds at 5.4°

$\omega_1\ (Hz)$	$\omega_2\ (Hz)$	$\omega_{LCO}\ (Hz)$			
-	-	7 m/s	8 m/s	9 m/s	10 m/s
6.3	39.4	53.9	44.9	39	38.1

5.1.4 Torsion frequency detection

The results reported by zakaria et al. [158] does not include the measured torsional frequencies for various angles of attack. It is useful to use the recorded videos to predict the torsional frequencies of the LCO. The idea based on measuring the maximum area enclosed within

the LCO as function of time. This idea stems from the fact that, in each cycle, the twist angle of the beam during the LCO changes from zero minimum value (curved line) to a maximum value (enclosed area). The camera are able to see an increase and decrease in the enclosed area within one period of the LCO. This calculated area was drawn versus the frame number to determine the torsional frequency at specific flow speed. In doing so, A MATLAB code was written to analyze the recorded videos based on the Gaussian mixture to model the background, followed by some morphological operations, and finally the active contour snake model was applied for accurate segmentation of the processed image. A snake model [159] is an active (moving) contour, in which the points are attracted by edges and other image boundaries. To keep the contour smooth, a membrane and thin plate energy were used for contour regularization. This step is followed by computing the gradient along the active contour and moved along its perpendicular direction from left to right. Figure 5.10 represents the analyzed image before and after using the snake model for maximum and minimum strokes for a given LCO frequency. Figures 5.11, 5.12, 5.13 and 5.14 show the area enclosed versus frame number at various angles of attack.

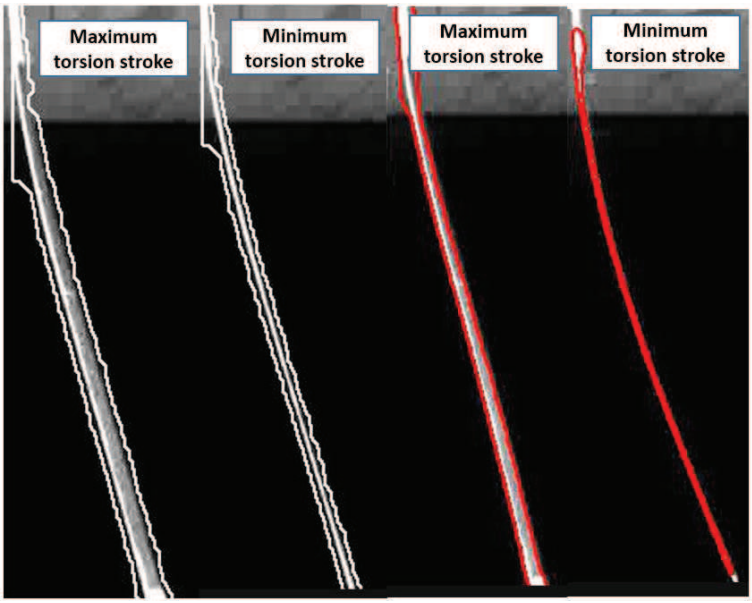

Figure 5.10: Analyzed images before and after applying snake model (left) and after applying it (right) at velocity 9 m/s and 5.4^o AoA

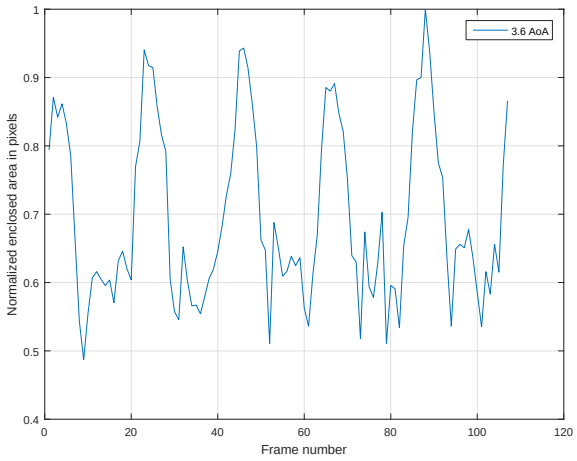

(a) Normalized Area enclosed seen by the camera vs frame number

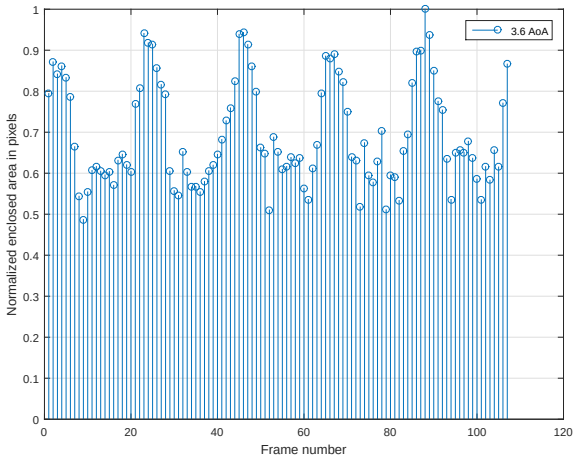

(b) Normalized digitized area points vs frame number

Figure 5.11: plate twist frame history based on maximum and minimum area captured during LCO at 3.6^o AoA

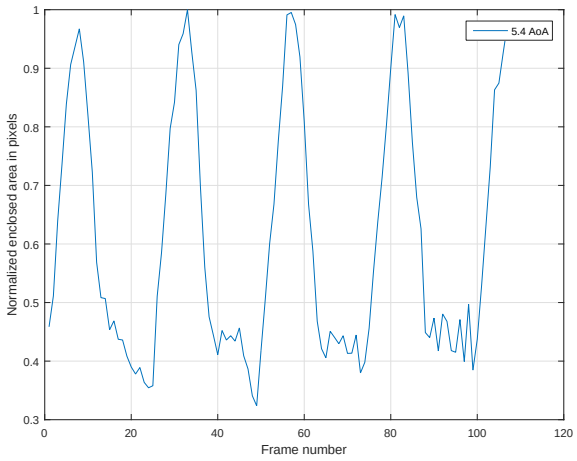

(a) Normalized Area enclosed seen by the camera vs frame number

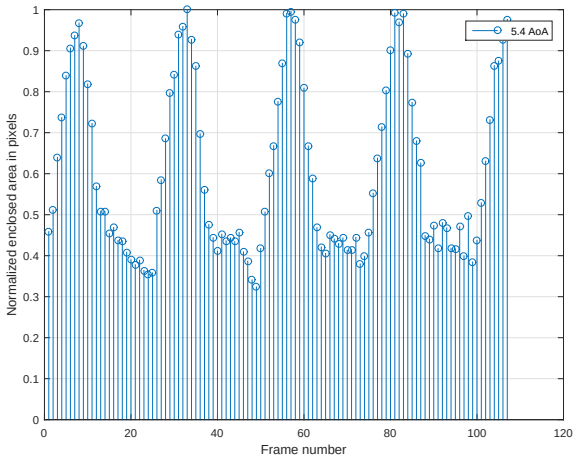

(b) Normalized digitized area points vs frame number

Figure 5.12: plate twist frame history based on maximum and minimum area captured during LCO at 5.4^o AoA

From Figs. 5.11, 5.12, 5.13, 5.14, it is clear that figure 5.14 has the most well defined sinusoidal pattern with less error compared to the prediction at lower angles of attack. Also, one can see that the stem plots in all figures have almost the same lower boundaries $\simeq 0.3$

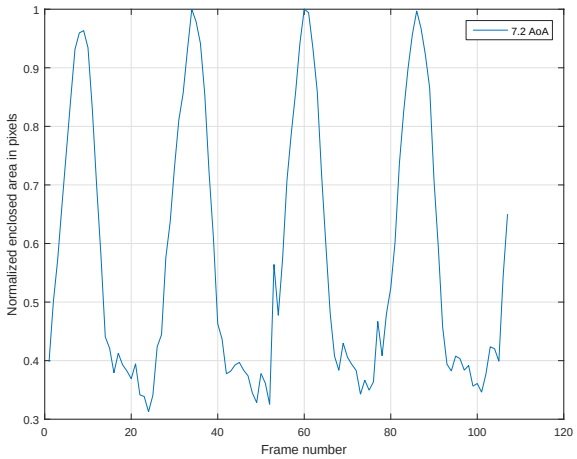

(a) Normalized Area enclosed seen by the camera vs frame number

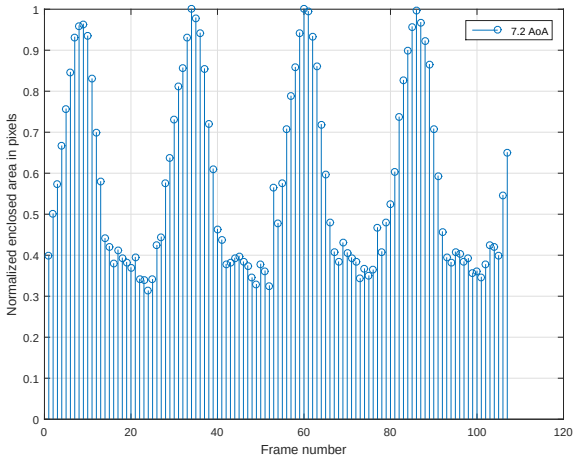

(b) Normalized digitized area points vs frame number

Figure 5.13: plate twist frame history based on maximum and minimum area captured during LCO at 7.2^o AoA

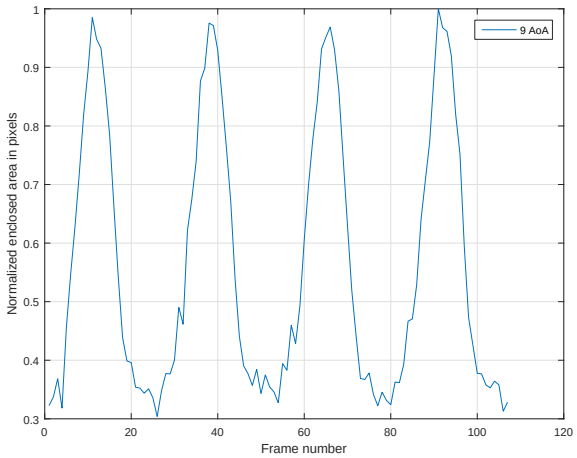

(a) Normalized Area enclosed seen by the camera vs frame number

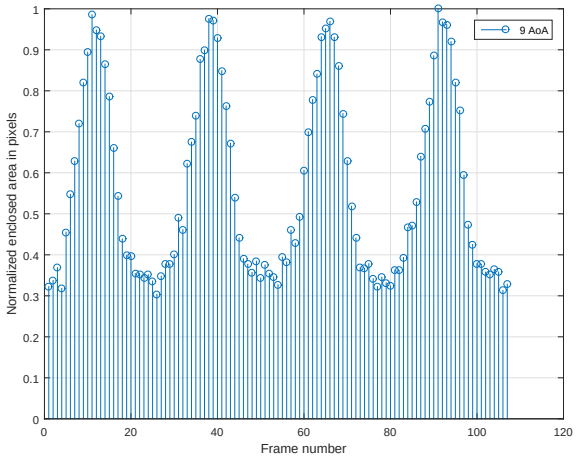

(b) Normalized digitized area points vs frame number

Figure 5.14: plate twist frame history based on maximum and minimum area captured during LCO at 9^o AoA

in area due to the fact that the area is always a positive value. For a line to be detected in the imaging analysis, each line has a thickness along with its length, which in-turn give the minimum area enclosed at zero torsion showed in figure 5.10(b). Table 5.5 shows the undeformed beam first and second bending frequencies associated with the corresponding

LCO frequencies at 9 m/s flow speed. The closeness of the second bending and torsional modes in table 5.5, indicates that the two frequencies coalesce with an error from imaging in torsion by 1.38% error.

Table 5.5: First two modes (bending and torsion with no beam deflection) and the corresponding frequencies of LCO for different air speeds at 5.4°

Mode	$\omega_1\,(Hz)$	$\omega_2\,(Hz)$	$\omega_{LCO}\,(Hz)$
-	-	-	9 m/s
Bending	6.3	39.4	39
Torsion	-	-	38.46

We presented a powerful imaging tool to predict the LCO frequency of a cantilever beam when subjected to a free stream. These oscillations are induced by large static deflections of the beam when placed in an air flow at preset angles of attack. The results show a very good agreement with the MFC sensor output with high precision and accuracy. Also, the results prove that the flutter onset occurs when the bending and torsion frequency coalesce for each angle of attack. The notion presented here is that one can control the LCO amplitudes as well as measuring the frequency of the torsional and bending modes in real time. By exploiting this technique, it is easy to predict the flutter onset and avoid the catastrophic accidents that might happen while doing such experiments in the wind tunnels after any design process.

5.2 Experimental Modeling of Centimeter-scale micro wind turbines

Power needs to operate sensors pose a major limitation when considering their use for monitoring and control. These needs are augmented when the sensors are in remote locations, their number is large, as in the case of wireless sensing networks, or when complementary components, such as cyber security devices, also need to be powered. These needs have raised the interest in developing technologies to harvest energy from ambient media such as solar power, thermal gradients, mechanical vibrations and air and water flows. Table 5.6 shows approximate values for the power density that can be released from these sources [160].

Table 5.6: Energy harvesting sources typical data used for remote wireless environmental sensing.

Power Source	Operating condition	Power density	Area or volume
Solar	Outdoors	7500 $\mu W/cm^2$	1 cm^2
Solar	Indoors	100 $\mu W/cm^2$	1 cm^2
Vibration	1 m/s	100 $\mu W/cm^2$	1 cm^3
Thermal	$\Delta T = 5^oC$	60 $\mu W/cm^2$	1 cm^2

Significant advancements have been made in designing wind turbines over the past thirty years to cover a wide range of applications. Clausen and Wood [161] classified relatively small size wind turbines into three categories based on their typical use by characterizing the wind turbine diameter (D) and the output power (P): micro (1.5 m; 1 kW) to power electric fences, remote telecommunications, equipment on yachts and the like; mid-range (2.5 m; 5 kW) to power a single remote house; and mini (5 m; 20 kW) to power small grids for remote communities. On the other hand, powering individual sensors requires power levels in the range of 10-100 mW. As such, there has been increasing interest in developing centimeter-scale micro wind turbines (CSMWT). For example, such turbines can be placed in air conditioning and ventilation ducts, without a major obstruction effect (duct cross-sectional area divided by wind turbine disk area < 0.18 %), to power micro-wireless sensors, smoke and gas detectors and temperature controllers. At this scale, such turbines need to be carefully designed to operate efficiently at low wind speeds.

Unfortunately, design models and optimal operating conditions proposed for large scale wind turbines do not directly apply towards the design and operation of CSMWT. These turbines have different aerodynamic behavior compared to their large-scale counterparts. The low Reynolds number regime of centimeter-scale micro wind turbines projects a fundamental shift in flow characteristics and in quantities such as lift and drag coefficients at the small scale from the large-scale wind turbine. The rated speed is an another important parameter in the design of CSMWT. This speed is the incoming flow speed of the wind at which the turbine starts to produce power. It depends on both total inertia and internal friction of the system including the rotor, ball bearings and the generator. The rated speed decreases with decreasing wind turbine size due to lower inertia. However, decreasing the size of wind turbine blades reduces the available aerodynamic torque and, thus, increases the rated speed. These opposing factors should be optimized when designing a centimeter-scale micro wind turbine with a desired rated speed and output power. As a measure of the design quality, the power density (output power per unit area) and the efficiency of a micro wind turbine should be improved by reducing frictional losses and improving the generator efficiency. This presents another challenge in terms of achieving the desired number of revolutions of the rotor shaft. Therefore, building an effective small size generator with a low starting torque and a high voltage-to-rpm ratio is a critical design criterion. Overcoming these challenges and optimization of the performance of CSMWT requires good estimates of their aerodynamic power, electromechanical coefficients and overall efficiency. In turn, this requires the development of capabilities to model and simulate the output power of small-size wind turbines.

Many investigations have been performed to evaluate the performance of CSMWT. Howey et al. [5] investigated experimentally and numerically a miniature shrouded ducted type micro wind turbine with a 2 cm rotor diameter and a 3.2 cm outer diameter. They showed that the fabricated MWT can deliver power levels from 80 μW to 2.5 mW over a wind speed range from 3 m/s to 7 m/s. The overall efficiency of that turbine was less than (2%). Hossain et al. [162] studied the effects of scaled MWT in single and grid arrangements using PIV, hot-wire and ultrasonic anemometers. Particularly, they investigated the downwash flow pattern for the smaller scale wind turbine (D= 5 cm) in an array arrangement. They calculated the wake deficit ratio for the inner region, outer region and intermediate region to control the wake by

using a suitable architecture of the micro wind turbines. However, they did not give power levels associated with the different arrangements. Carli et al. [163] maximized the efficiency of their micro wind turbine (D= 6 cm) using a buck-boost converter based maximum power point (MPP) circuit with fixed-frequency discontinuous current mode (FF DCM) to emulate a fixed resistance for minimizing the power loss. They were able to increase their conversion efficiency to 87 % and the overall efficiency of their turbine to about 5%. Leung et al. [4] connected fan-bladed micro wind turbines side by side by using geared meshing to add up the power. They concluded that turbines with high-solidity had higher power coefficients at a specific blade angle. They showed that the five-bladed micro wind turbine with 60-degree blade subtended angle yields an optimal power output. Rancourt et al. [164] examined the effect of the sweep angle on three types of micro wind turbines. They showed that the efficiency of the wind turbine follows the Schmitz theory, even for small diameter turbines (4.2 cm diameter). They obtained an efficiency of 9.5 % in 11.83 m/s wind speed. They also asserted that at low wind speeds the friction in the generator and electric resistance reduced the energy conversion so the maximum efficiency was only 1.85 % and the power provided was 2.4 mW at 5.5 m/s air speed. Haik et al. [165] studied the effectiveness of using an organic capacitor to store energy harvested from a miniature wind turbine. They used a 5 cm diameter fan type CSMWT to deliver a maximum output power is 0.2 Watt at 8 m/s. Table 5.7 summarizes the operating conditions for previous studies related to CSMWTs.

Table 5.7: Maximum performance operating conditions as reported in recent studies and experiments on CSMWTs

Author(s)	**D (cm)**	**Number of blades**	**Air speed** $U(m/s)$	**Power** $P(mW)$	**Efficiency (%)**	**Power density** (mW/cm^2)
Howey et al. [5]	3.2	3-6-12	10	4.3	1.5	1.37
Rancourt et al. [164]	4.2	3	11.8	130	9.5	9.39
Carli et al. [163]	6.3	4	4.7	9.97	5.36	0.32
Fujun Xu et al. [6]	7.6	4	10	10	7.6	0.055
Leung et al. [4]	11.7	8	15	295	1.37	2.74

The above discussion shows that there must be an optimal relation between the rotor type, its diameter, number of blades and flow speed. zakaria et al. [158] developed a model to

predict the generated power from CSMWT that is important for optimizing its performance. In this work, we test and model the performance of a swirl-type centimeter-scale micro wind turbine. Particularly, we measure the harvested power at different speeds, electric loads and yaw angles. Then, we present the developed model for predicting and evaluating the different losses. This model would serve in optimizing the design of centimeter-scale micro wind turbines. Comparisons of the performance of this turbine with others in terms of efficiency and power density over a broad range of wind speeds are also performed. Tests are also conducted to assess the effects of varying the direction of incident flow on the turbine performance.

5.2.1 Experimental setup

A. Swirl type CSMWT

The performance of a centimeter-scale micro wind turbine is based on three major aspects: its geometry, the generator and operating conditions. Various types of CSMWT are shown in figure 5.15. The geometric constraints include the blade twist angle, number of blades, chord length and the prospect of connecting the blade tips with a circular shroud to increase the aerodynamic efficiency by decreasing the tip losses. The fan type is characterized by a small twist angle and few blades, which makes it easy to fabricate. The ducted type (also referred to as shrouded type) studied by Howey et al. [5] has more complicated design elements than the fan type turbine. It consists of a rotor, an inlet shroud, a casing, bearings and an exit diffuser. The MWT generator is embedded between the rear and front casing as bearing magnets (integrated into the shroud). The swirl type used in this study is shown on the right side of figure 5.15. A CAD drawing of this turbine is presented in figure 5.16. Its specifications are presented in Table 5.8.

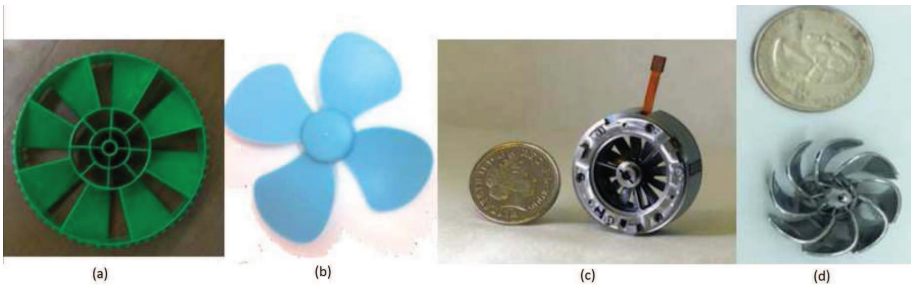

Figure 5.15: Various types of centimeter-scale micro wind turbines. (a) Fan blade with shroud type [4], (b) Fan type, (c) Ducted fan type [5] and (d) Swirl type used in the present study.

Table 5.8: CSMWT swirl type case study specifications

Variable	**Specifications**
Generator volume size (cm)	$1 \times 1.4 \times 1$
Generator material	Permanent magnet
Rotor-blade diameter D (cm)	2.6±0.01
Blade chord c (mm)	5±0.05
Number of blades N	8
Rotor mass (grams)	2
Generator mass (grams)	5
Rated speed (m/s)	3±0.02

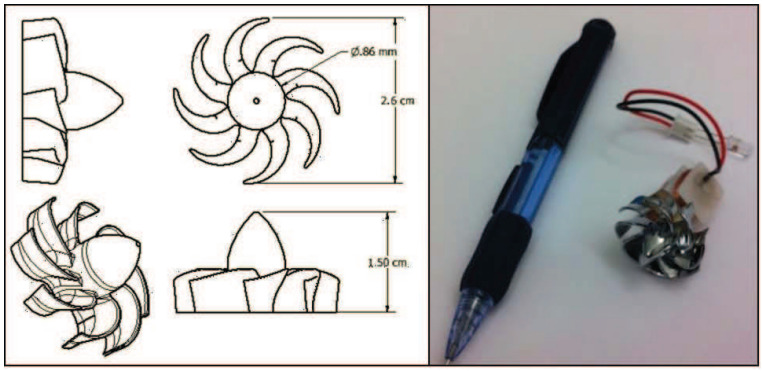

Figure 5.16: CAD drawing of the swirl CSMWT and its scale compared to a pencil.

B. Wind tunnel testing

All experiments were performed in the subsonic wind tunnel facility of the Department of Engineering Science and Mechanics at Virginia Tech. Pictures of the wind tunnel and turbine are shown in figure 5.17. The tunnel is a suction-type open circuit wind tunnel. It is powered by a 15 hp Leeson motor driving a 1 meter centrifugal fan. The air flow is discharged by the fan which forces the flow to pass through a square (1.5 m $\times$ 1.5 m) honeycomb inlet that has a 0.001 m cell size and is 0.09 m long. This inlet is followed by three turbulence reduction screens that ensure a uniform flow with a turbulence intensity that is less than 2 %. The test section dimension is 52 cm $\times$ 52 cm. The maximum attainable speed of the wind tunnel is 25 m/s. The flow velocity is measured with an accuracy of 0.5 % based on the reading recorded from a pitot-static tube connected to a differential pressure scani-valve. All tests were performed in the center of the test section with the Pitot-static tube set 10 cm away from the axis of rotation and 20 cm ahead of the tested CSMWT. The velocity variation across the test section is less than 2.5 %. A data reduction program was implemented to calculate the uncertainties based on Moffat method [56] that considers both bias and precision errors. The results are presented for all experimental data points in the form of error bars.

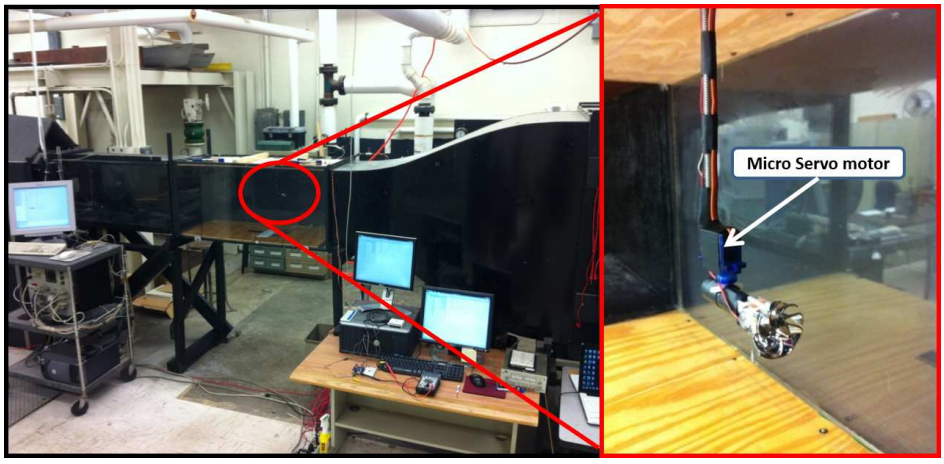

Figure 5.17: Pictures of the wind tunnel facility with mounted CSMWT.

Figure 5.18 shows a schematic of the experimental setup, test-rig and devices used. The swirling CSMWT is connected to a micro-generator that has an area of 1 cm^2. This whole system is connected to a micro-servo motor that can be used to rotate the CSMWT in the

yaw direction. The output voltage of the wind turbine generator was measured using a digital multimeter and was also connected in parallel to a USB 6009 National Instruments data acquisition card to measure the generated voltage. The data sampling rate was set to 200 Hz and data segments were recorded over a period of three seconds. The resistor box was connected to the output wire of the generator to study the performance of the wind turbine under various loading conditions. The measured internal resistance for the whole setup (generator and wire connection) was found to be $R_{in} = 134\ \Omega$. Thus, we selected to measure the output power over a broad range of loading resistance from 20 Ω to 2 $k\Omega$. This range includes the internal resistance of the CSMWT and covers a wide range of small batteries, sensors and controllers. At fixed wind speeds, the load resistance was varied and the corresponding output voltage was recorded. We conducted experiments at six different wind speeds between 3.9 m/s and 8.8 m/s. The angular velocity of the CSMWT was measured using a laser tachometer. The results of these measurements were confirmed by comparing them with the frequency of the generated AC output voltage as shown in figure 5.19. The results in figure 5.19 show a good agreement between the two measurement methods. Of particular interest is the dip around 6 m/s. Because energy is extracted from the rotation of the turbine, one could assume that the rotational speed is dependent on both free stream velocity and the efficiency of energy extraction. That is, the coupled effect of the energy extraction and incoming speed impacts the angular velocity of the turbine. The results presented below will show that the maximum efficiency of power extraction is also near 6 m/s. As such, the dip, observed in figure 5.19, can be related to the fact that the efficiency of the energy extraction is maximum in this range.

5.2.2 Electronic based circuit model

A. Power and optimal load resistance

We aim to use the experimental measurements to develop a model for predicting the output power harvested from a micro wind turbine. The model is based on understanding of the electronic circuit of the overall system and the perquisites set by Xu et al. [6]. When the kinetic energy of the incident air is captured by the micro wind turbine, the rotor rotates

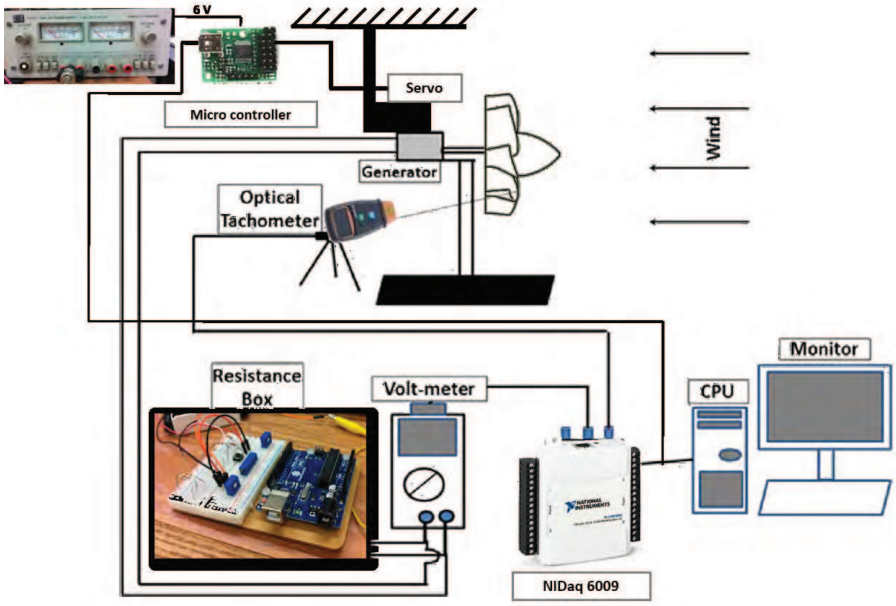

Figure 5.18: Schematic of the experimental setup.

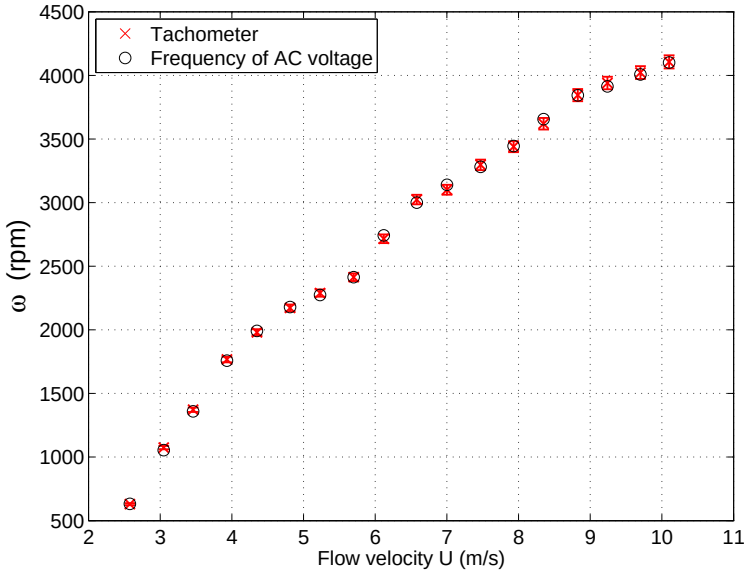

Figure 5.19: Comparison of the variation of the angular velocity as measured by the tachometer and from the frequency of the generated output AC voltage with the free stream velocity.

with a certain angular velocity and the torque generated by the air power, referred to as drive torque, is given by:

$$T_{drive} = \frac{P_{aero}}{\omega} \tag{5.1}$$

where P_{aero} is the aerodynamic power of the incident wind and ω is the angular velocity of the rotor. The driving torque can be subdivided into three components and written as:

$$T_{drive} = T_g + T_a + T_f \tag{5.2}$$

where T_g is the torque associated with the generated power and is given by:

$$T_g = Gi \tag{5.3}$$

Here, i is the generated electric current and G is the electro-mechanical coefficient. It is obtained by assuming a linear relation between the generated voltage, V and the angular velocity, ω; i.e. $V = G\omega$. The inertial torque, T_a, is proportional to the angular acceleration of the rotor $\dot{\omega}$, and is given by:

$$T_a = I\dot{\omega} \tag{5.4}$$

where I is the mass moment of inertia. Finally, T_f is the torque used to overcome the frictional damping between the shaft and the rotor casing. This damping is a function of the angular velocity and is written as:

$$T_f = C_2\omega^2 + C_1\omega + C_o \tag{5.5}$$

The dependence of T_f on the square of the angular velocity is due to the air friction between the shaft and the rotor casing. Its linear dependence on the angular velocity is due to the friction in the generator. The constant value is due to the start-up friction required to initiate the angular motion. Substituting equations (5.3), (5.4) and (5.5) in equation (5.2), the total driving torque is re-written as:

$$T_{drive} = Gi + I\dot{\omega} + C_2\omega^2 + C_1\omega + C_o \tag{5.6}$$

where C_o is independent of the shaft speed (ω). As such, we define:

$$T^*_{drive} = T_{drive} - C_0 \tag{5.7}$$

and write

$$T^*_{drive} = Gi + I\dot{\omega} + C_2\omega^2 + C_1\omega \tag{5.8}$$

Given that the generated voltage is related to the angular velocity, i.e. $V = G\omega$, the generated current is written as:

$$i = \frac{G\omega}{R_{in} + R_L} \tag{5.9}$$

where, R_{in} is the internal resistance of the wind turbine and R_L is the load resistance. Substituting equation (5.9) in equation (5.8), the drive torque as a function of ω and $\dot{\omega}$ is re-written as:

$$T^*_{drive} = \frac{G^2\omega}{R_{in} + R_L} + I\dot{\omega} + C_2\omega^2 + C_1\omega \tag{5.10}$$

For a constant angular velocity, the inertia torque is zero and T^*_{drive} is written as:

$$T^*_{drive} = C_2\omega^2 + \left(\frac{G^2 + C_1(R_{in} + R_L)}{R_{in} + R_L}\right)\omega. \tag{5.11}$$

Equations (5.9) and (5.11) can then be used to relate the generated power P_L to the torque. As such, we write:

$$P_L = \frac{G^2\omega^2 R_L}{(R_{in} + R_L)^2} = \frac{G^2 {T^*_{drive}}^2 R_L}{[G^2 + (C_1 + C_2\omega)(R_{in} + R_L)]^2} \tag{5.12}$$

The optimal resistive load can be obtained by setting the derivative of the output power with respect to the resistive load to zero; i.e. $\frac{d(P_L)}{d(R_L)} = 0$. This yields an expression for the optimum resistive load R_{Lopt} that is given by:

$$R_{Lopt} = R_{in} + \frac{G^2}{(C_1 + C_2\omega)} \tag{5.13}$$

B. Electro-mechanical coefficient

To determine the electromechanical coefficient, we measure the open circuit voltage as a function of the angular velocity ω. For this, we measured the open circuit voltage and the angular velocity for different free-stream velocities. Then, we divided the voltage by the

angular velocity to obtain the electro-mechanical coefficient over a broad range. The results are plotted in figure 5.20 which give an average value for G of $8.3 \times 10^{-3}\ Volt/(rad/s)$.

$$C_2\omega + C_1 = \frac{G^2}{R_{L_{opt}} - R_{in}}, \tag{5.14}$$

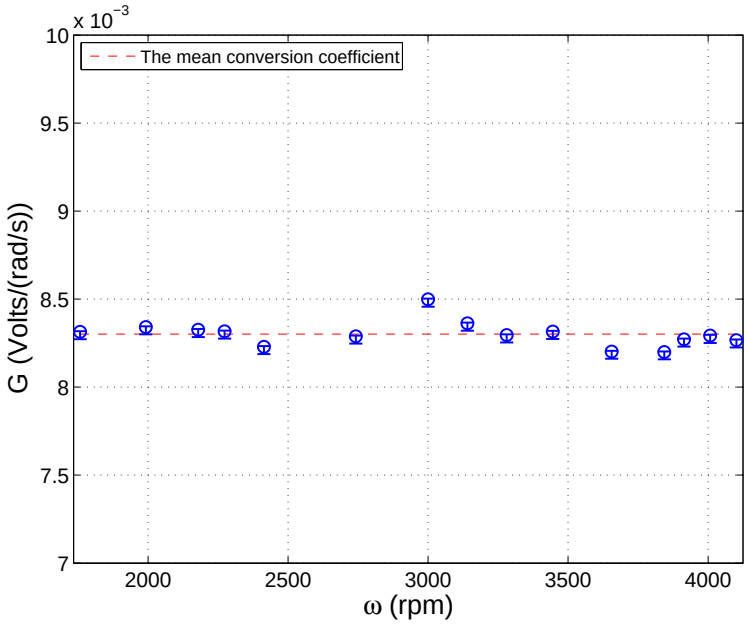

Figure 5.20: Electromechanical coefficient vs angular velocity.

Figure 5.21 shows a curve-fit of the torque from measurements over a broad range of angular velocities. The results show a quadratic relation, as expected from the model presented above. The curve-fit with a value of 0.99 correlation coefficient yields:

$$T^*_{drive} = {T_F}^* = 1.7272 \times 10^{-9}\omega^2 - 3.7404 \times 10^{-7}\omega + 3.294 \times 10^{-5} \tag{5.15}$$

which is in agreement with the model presented in equation 5.5. The values of C_1 and C_2 in equation (5.5) are determined from the curve fit presented in equation (5.15). These values are then used in equation (5.14) to determine the optimal load resistance as a function of the angular velocity with the corresponding free stream velocity as shown in Table 5.9.

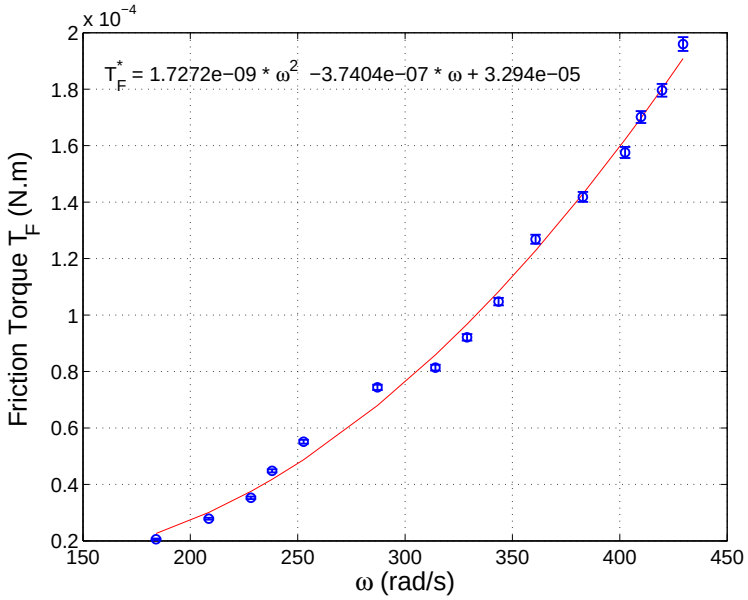

Figure 5.21: Curve fit of the experimental values of the torque vs angular velocity.

Table 5.9: Optimum resistive load for different freestream velocities and corresponding angular velocities.

U: **velocity (m/s)**	3.9	4.3	4.8	5.2	5.7	6.1	6.5	7	7.4	7.9	8.3
ω: **angular velocity (rad/s)**	184	208	228	238	252	287	314	328	343	360	382
R_{Lopt}: **optimal load** (Ω)	750	650	580	500	450	400	400	380	360	330	320

C. Aerodynamic and overall efficiency

The main components of a typical wind turbine are the alternator and the rotor consisting of the blades with aerodynamic surfaces. According to the Betz law, the theoretical maximum aerodynamic power coefficient (Cp) is 59.26 %. In centimeter-scale micro wind turbines the total efficiency is significantly smaller. The major losses are due to: (1) the relatively high viscous drag on the blades at low Reynolds number, (2) the friction and thermal losses which can be significant in a centimeter-scale micro wind turbines and (3) the high electromagnetic interference. These losses reduce the total efficiency of small-scale wind turbine having a rotor-tip-diameter of less than 10 cm and a direct drive generator without a gearbox to about 14.8 % [6].

Figure 5.22 shows a schematic for the efficiency at different stages in power generation

from the swirl-micro wind turbine for a specific speed of 6.5 m/s. The white boxes show the values that were measured experimentally. The gray ones show the predicted values for the different efficiencies, which include the aerodynamic efficiencies of the wind turbine (C_p) of the generator power (η_g) and of the rectifier (η_{Rec}) .

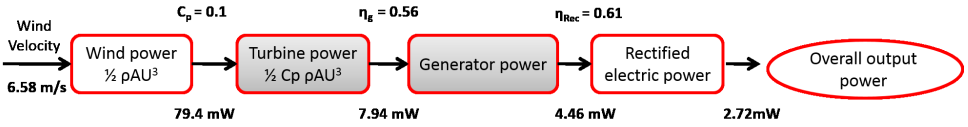

Figure 5.22: Efficiency at different stages of power generation.

Given the diameter of the wind turbine ($D = 2.6cm$) and for a free-stream velocity of 6.5 (m/s), the total power of the incoming flow is 79.4 mW. The maximum power that can be extracted from the ambient wind, P_{aero} can be expressed by:

$$P_{aero} = \frac{C_p(\lambda, \theta)\rho A U^3}{2}, \tag{5.16}$$

where $C_p(\lambda, \theta)$ is the aerodynamic efficiency of the rotor. It is a function of the pitch angle θ and the tip speed ratio λ, which represents the dimensionless relation between the tangential speed of the tip of the rotor blade and the incoming flow ($\lambda = \frac{\omega D}{2U}$). Following [6, 166], C_p is given by:

$$C_p(\lambda, \theta) = c_1 \left[\frac{c_2}{\lambda_i} - c_3\theta - c_4\theta^{c_5} - c_6\right] e^{-\frac{c_7}{\lambda_i}}, \tag{5.17}$$

where

$$\lambda_i = \frac{1}{\frac{1}{\lambda + c_8\theta} - \frac{c_9}{\theta^3 + 1}}, \tag{5.18}$$

and $(c_1 - c_9)$ are constants. Xu et al. [6] obtained experimentally the values of these constants for a small wind turbine of 7.6 cm diameter over a range of different air speed velocities. These values, presented in Table 5.10, were also shown to be independent of the free-stream velocity. In this work, we use them as approximations of the C_p coefficients in equations 5.17 and 5.18. Based on a tip speed ratio of λ=0.55 and a mean pitch angle (θ) of 32^o, we estimated the value of C_p to be 0.11. This is a slightly smaller value than the theoretical value of 0.148 presented by Xu et al. [6].

Table 5.10: Values of the constants (c_1 - c_9) used in the estimation of the aerodynamic efficiency of the rotor of a centimeter scale micro wind turbine [6].

C_p coefficient	c_1	c_2	c_3	c_4	c_5	c_6	c_7	c_8	c_9
CSMWT	0.6	160	0.93	0	0	9.3	9.8	0.037	0

5.2.3 Results and discussion

Figure 5.23(a) shows the measured and modeled variations of the output DC voltage as a function of the load resistance for different incident flow speeds. The plots show that the output voltage increases as the incident velocity is increased. Furthermore, the output voltage increases as the load resistance is increased and asymptomatically approaches a maximum value at high values of the load resistance. Figure 5.23(b) shows the measured and modeled variations of the output power as a function of the resistive load for different incident flow speeds. The results show that, for each speed, there is a maximum power level at a specific load resistance; as expected from equation 5.14. Figure 5.24 shows a plot of the normalized output power ($P_{out}/\frac{1}{2}\rho U^3 A$), also referred to as total efficiency, as a function of the load resistance for three free stream velocities. The plots show a maximum value of 3.2 % at U = 6.5 m/s (Re = 1810 based on the chord of the blade, c). Comparing figures 5.23b and 5.24, we note that although increasing the free stream velocity increases the level of harvested power, there is an optimal value of the free stream velocity for which the normalized power efficiency is maximized. This difference is also noted when looking at the plots in figures 5.25a and 5.25b which respectively show the maximum output and maximum normalized power as a function of the Reynolds number. Although the maximum power level increases as the Reynolds number is increased, the normalized level reaches a maximum value at Re = 1810. This is because the friction losses are a quadratic function of the angular velocity.

A comparison of the power density of the tested wind turbines with those of previously tested wind turbines is presented in figure 5.26. A closer look at the results shows that the power density is also a function of the diameter of the micro wind turbine. The tested wind turbine with a diameter of 2.6 cm has a power density that varies between 0.1 mW/cm^2 and

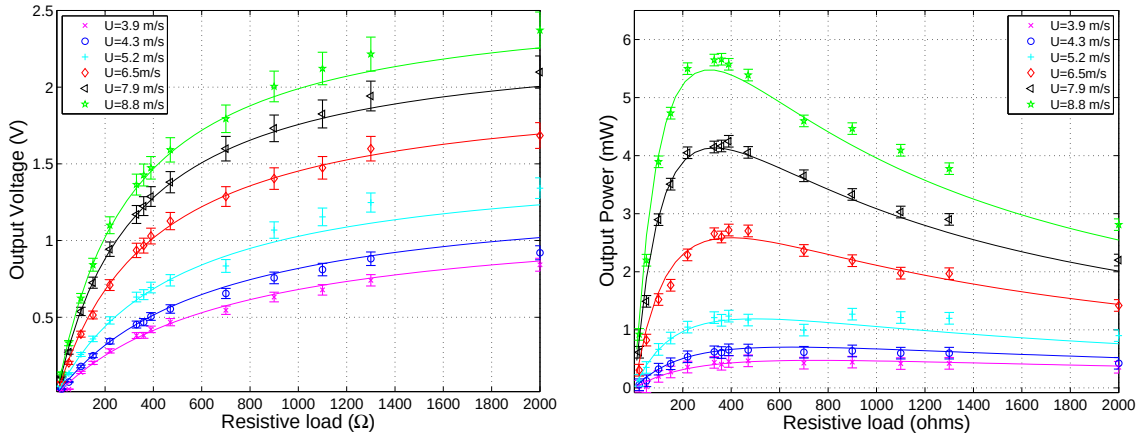

Figure 5.23: Experimental and predicted (solid lines) variations of the output voltage and power of the tested swirl CSMWT with the load resistance.

2 mW/cm^2 over a range of incident wind speeds between 4 and 10 m/s. The wind turbine of Howey et al. [5], with a diameter of 3.2 cm has a relatively smaller power density but in the same range. Larger wind turbines have power densities that varied between 0.2 and 10 mW/cm^2. Figure 5.27 shows the efficiency of the tested and previously investigated micro wind turbines as a function of the diameter of the turbine. The plot shows that the efficiency increases from about 2% to 3% for wind turbines having a diameter of 2 to 3 cm to about 6% to 8% for turbines with diameters between 6 and 8 cm and to higher efficiency of about 12% to 16% for turbines with diameters between 10 to 12 cm. The experiments of Rancourt et al. [164] show a higher efficiency of 9.5% at 11.83 m/s but the maximum efficiency at the lower speed near 5.5 m/s was relatively low with a value near 1.85 %. The dependence of the efficiency level on the size of the turbine raises a question as to whether staggering relatively small wind turbines would be more efficient than using a single turbine when the size is a constraining parameter. Issues such as cost and mutual interference between the turbines would need to be balanced against the levels of generated power from different configurations or designs.

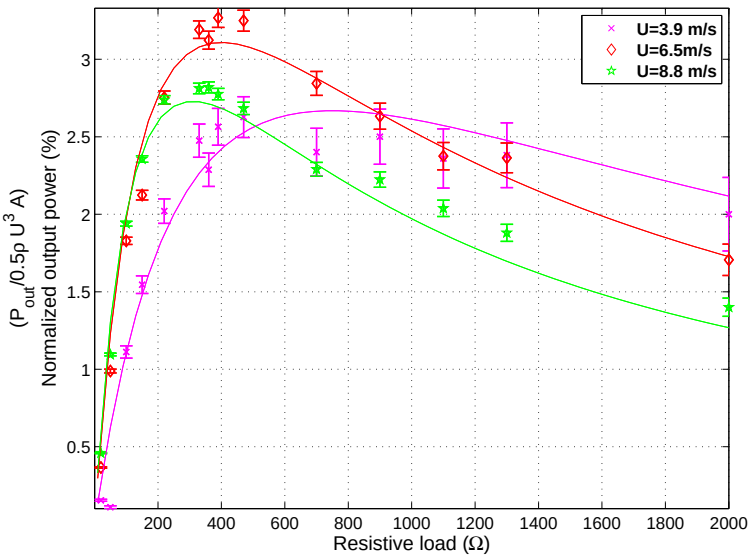

Figure 5.24: Normalized output power (total efficiency) vs resistive load. The solid lines are obtained from the model presented in section 3.

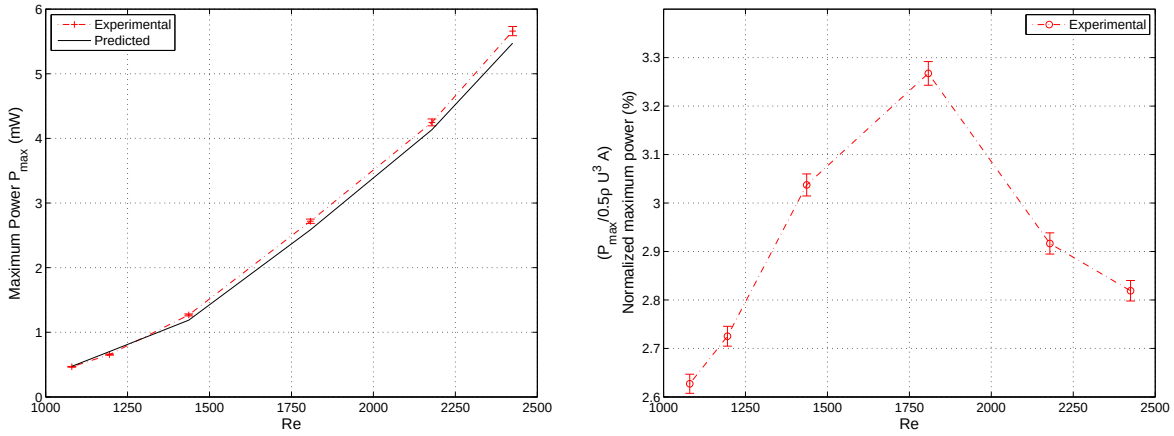

(a) (b)

Figure 5.25: Power variation with Reynolds number ($\frac{Uc}{\nu}$)

Another performance metric for the operation of the tested centimeter-scale micro wind turbine would be to determine its effectiveness under varying incident flow directions. Experiments were conducted over a range of yaw angles from 0 to 30 degrees. The motion was automated using a micro-controller-based device connected to a computer. Figure 5.28 shows the total output power versus the flow speed operating at different yaw angles, β, for

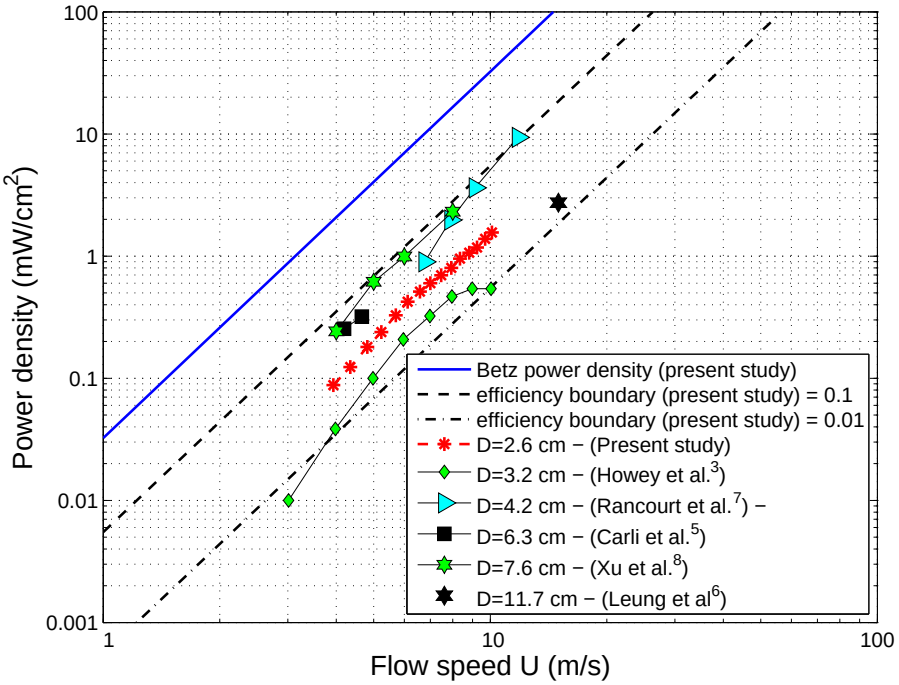

Figure 5.26: Comparison of the power density of the tested swirl type and other CSMWT as a function of the flow speed.

the case of optimum resistive load of 330Ω. Figure 5.28(a) which presents the power as a function of the air speed, shows that the output power at 0° and ± 10° yaw angles are almost equal. At larger yaw angles, the generated power decreases by about 25% for yaw angles of ± 20° and by 52% for yaw angles of ± 30°. Furthermore, there is no difference in the power generated for positive and negative yaw angles. The reason is that the geometry of the swirl is axisymmetric. Figure 5.28(b) presents the output power as a function of (Ucos β)^3, where $Ucos(\beta)$ is the velocity component that is perpendicular to the plane of the swirl. We note that over the range of relatively low speeds, the power output is proportional to $U^3cos^3(\beta)$ indicating that the total efficiency is constant. There is a departure from the linear relation at the higher speeds indicating a reduction in the efficiency. Of particular importance is the significant drop in the generated output power as the yaw angle is increased to 30° in comparison to the values obtained at 0°, 10° and 20° yaw angles. This drop shows that the total efficiency decreases significantly as the yaw angle is increased beyond 20°. This reduction is in

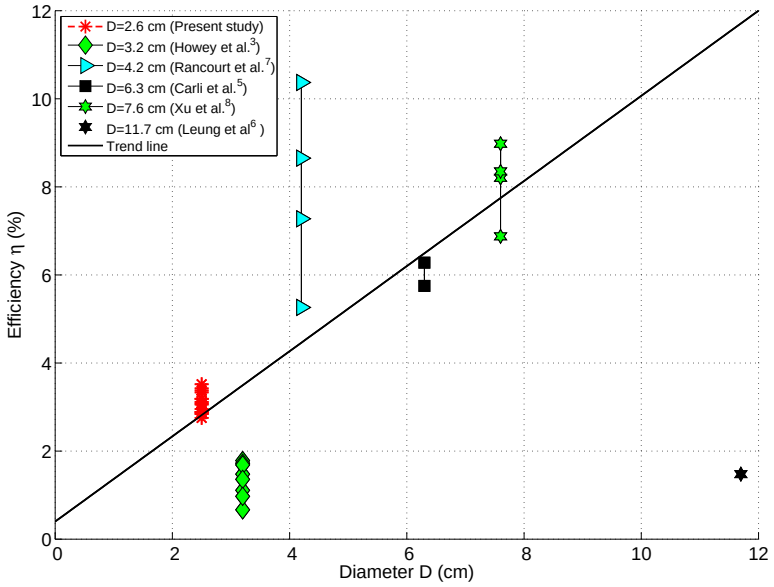

Figure 5.27: Efficiency versus diameter of the tested swirl type and other CSMWT.

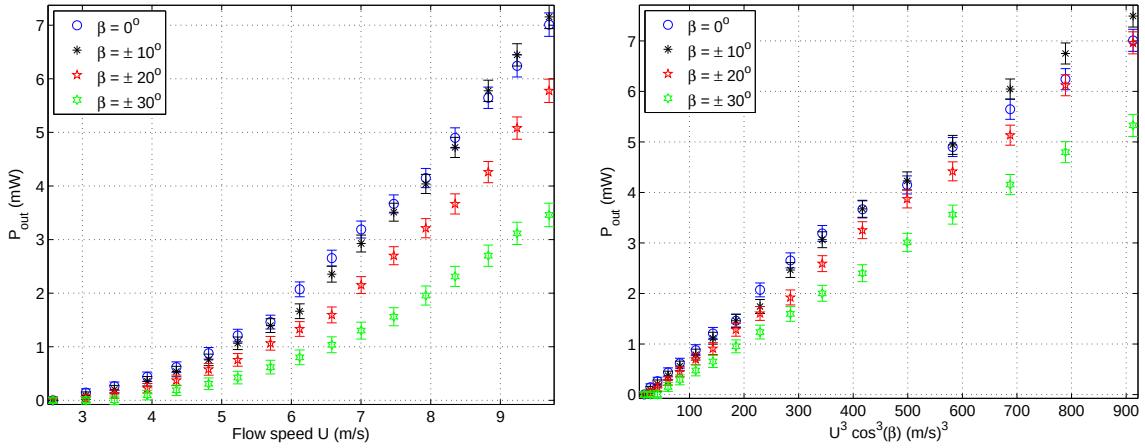

(a) (b)

Figure 5.28: Power variation of the yaw angle, β, as a function of (a) the velocity U and (b) $(\mathrm{U}\cos\beta)^3$

qualitative agreement with published data in [167] and [168]. Still, these numbers represent a satisfactory performance when compared to other small-scale micro wind turbines. Also, we tested the swirl type wind turbine in a turbulent flow by using a simple commercial bladed

fan. The output power from the turbine is higher compared to power obtained in the wind tunnel, which has a lower turbulence intensity.

Chapter 6

Conclusions and Future Recommendations

6.1 Summary

In this dissertation, we made three major contributions towards providing models for unsteady aerodynamics. First, we developed a state-space model to predict lift enhancement for airfoils undergoing plunging oscillations at high angles of attack and high reduced frequencies. Second, we gained insight into the flow to explore the lift enhancement phenomenon that resulted from the observed leading edge vortex by performing flow visualization experiments in a water channel. Finally, we developed a simple model based on experimental data to represent the added mass forces associated with plunging oscillations of an airfoil. In addition, we considered specific applications of unsteady aerodynamics that include flapping flight and energy harvesting from limit cycle oscillations of a fluttering beam. we give below a summary of our contributions along with suggestions for future work in this field.

In Chapter 2, we presented the work performed on a plunging experiment of a two-dimensional NACA 0012 airfoil. The plunging oscillations were performed at various mean angles of attack between 0° and 65° and with reduced frequencies between 0.1 to 0.95. For each combination of a mean angle of attack and a reduced frequency, the lift time-history was measured along with the wing plunging acceleration. This acceleration was used to

estimate the inertial and added mass loads and, therefore, the circulatory lift was extracted from the measured lift forces. In addition, the measured plunging acceleration is integrated to determine the plunging velocity and, consequently, the effective angle of attack. As such, the quasi-steady lift was calculated based on the measured steady lift characteristics. Then, the frequency response, defined as the ratio between the circulatory lift and the quasi-steady lift was constructed for each mean angle of attack. The results show that, in the linear range ($0^o - 10^\circ$), the obtained frequency responses match Theodorsen's frequency response function. Over the stalled region between 15^o to 40^o, there is a considerable qualitative and quantitative difference from Theodorsen's frequency response.

The time series of the lift coefficients exhibit more than a single period indicating significant nonlinear effects. The lift frequency response exhibits a peak near a reduced frequency of 0.7. This peak can be utilized in maximizing the lift over oscillatory wings performed near this reduced frequency. In the post-stall region, the obtained frequency response regains its monotonically decreasing (first-order) dynamical nature with a much smaller lift amplitude than that of Theodorsen's. The results of the flow visualization revealed that the lower convection speed of the formed LEV for the case of k=0.7, yield to the observed lift enhancement in the frequency response. An optimization-based fourth-order dynamical system model approximation is developed to match the obtained frequency responses at each mean angle of attack. A global optimized frequency response for each regime was developed by combining the obtained models. These models are then written in a state space form. To combine the obtained models, the entries of the state space matrices are written as quadratic in the operating angle to attack. The developed model is then validated in the frequency and time domains against data set that were not included in the fitting process. These results provide a basis for the development of efficient though rich unsteady models operating at high angles of attack that can be used in control design applications where unsteady aerodynamics play a major role.

The results presented in Chapter 3 provide measured data of the forces associated with the added mass on an airfoil undergoing plunging oscillations at high frequencies and high angles of attack in still air. The results show a cubic variation of these forces with the frequency of the oscillations. This variation indicates that the added force is dependent on

the oscillation frequency. The results also show that the added force is largest for angles of attack between 10 and 20 degrees and lowest for angles of attack between 40 and 50 degrees. The dependence of the added force on the frequency of the oscillations and the angle of attack indicate a significant effect of the flow pattern generated by the oscillating airfoil and its contribution to the added force. So, one question that needs to be addressed is whether and how the generated unsteady loads due to the oscillatory motion should be separated from the added mass.

In Chapter four; section one, kinematics and shape optimization for a flapping Pterosaur in forward flight have been performed as an application for unsteady aerodynamics. In addition to the classical unsteady considerations, the used aerodynamic model accounts for the viscous friction, partial leading edge suction, and post-stall behavior. A multi-objective design optimization problem was formulated in which the cycle-averaged propulsive efficiency is maximized and the cycle-averaged required input power is minimized. It is found that inclusion of the inertial power requirements is necessary for a physical and proper formulation of the optimization problem. Furthermore, mere addition of the inertial power requirements is not enough to obtain reasonable results from the optimization problem. Rather, one has to consider a partial (or even zero) elastic energy storage. By doing so, it is found that for minimum power and maximum efficiency requirements, two variables remain approximately constant, flapping angle ($\Gamma \approx 25^\circ$) and mean pitch angle ($\overline{\theta}_a \approx 7.2^\circ$). On the other hand, to attain minimum power requirements the flapping frequency (f) is 1.1 (Hz) and the dynamic twist angle (β_o) is 10.5° which indicates low inertial power cost paid and a propulsive efficiency of 10.2%. In the case of maximum propulsive efficiency, the flapping frequency and dynamic twist angle are 3.4 (Hz) and 17.7%. The smaller values for the flapping frequency and dynamic twist of the minimum-power design in comparison to those of the maximum-efficiency design are consistent with the fact that the inertial power requirements increase as the flapping frequency and dynamic twist increase.

Chapter Five encompassed two interesting applications in energy harvesting from air flow. We presented an energy harvester that exploits self-excited oscillations of a cantilever beam. These oscillations are induced by large static deflections of the beam when placed in an air flow at preset angles of attack. When the deflection is large enough, the geometric nonlinearities

affect the beam's stiffness and induce a change in its natural frequencies, which, in turn cause the torsional and second bending frequencies to coalesce. This coalescence results in self- excited oscillations of the beam. By exploiting this phenomenon, we eliminated the need to attach a structure to the beam to initiate vibrations and, as such, decreased the energy significantly. The results shows that optimal levels of harvested power are obtained at specific settings of the angle of attack depending on the flow speed. The results also show a strong dependence of the frequency of oscillations on the air speed and angle of attack. This is of interest because it shows that small variations in the aerodynamic loads cause variations in the beam stiffness when subjected to large deformations. The nonlinear effects of the designed system are detected by the observed harmonics in the spectra of the signal of the harvested voltage. In addition, I investigated experimentally the performance of a swirl type centimeter-scale micro wind turbine. The results in terms of power density and efficiency show that its performance is better than the performance of ducted turbines of similar size. The results show an optimal combination between the rotor diameter and the number of rotor revolutions. The maximum output power of the CSMWT was 2.72 mW with a wind speed of 6.5 m/s at an operating resistive load of 330 Ω , which corresponds to a maximum system efficiency of 3.42 %. We also modeled and validated the performance of the tested turbine and its dependence on the angular velocity. The results show that the torque in the tested turbine is a function of the square of the angular velocity which becomes significant at high angular velocities. As such, the generated power starts to decrease once a critical speed is surpassed for a specific load resistance. Finally, we tested the effects of varying incident flow direction on the turbine performance. The results showed no reduction in the power generated for yaw angles less than 10^o which is quite significant.

6.2 Conclusions

1. We obtained good estimates of the lift enhancement at specific reduced frequencies (e.g k=0.7) and discussed the factors that affect the leading edge vortex convection velocity (e.g effective angle of attack variation).

2. We found that the total forces on a plunging wing in stationary fluid at high reduced

frequencies is affected by the unsteady pressure loads. These loads contribute to an additional unsteady forces due to the drag effects as well as the vortex shedding.

3. We optimized the shape and kinematics for a flapping bird by maximizing the propulsive efficiency and minimizing the drag. The findings were consistent with the fact that inertial power requirements increase as the flapping frequency and dynamic twist increase.

4. We harvested energy using MFC patch connected to a composite beam by exploiting the self-induced flutter to sustain a limit cycle oscillations with different amplitudes by varying the inflow angle of attack.

5. We experimentally assessed the performance of swirl type centimeter-scale micro wind turbines. we found that the output power generated from this type is larger than micro turbines built in a configuration similar to that of large wind turbines.

6.3 Recommendations for Future Work

There remains several open questions that can be related to this effort.

6.3.1 Optimal control based on the developed models

It is of particular interest to use the models developed in this dissertation for control design of flying vehicles. The low-dimensional, state-space form of these models will be ideal for use with modern control techniques which could be switched from one mode to another based on the maneuver. Comparison of control methods based on Theodorsen's model and the more accurate models in this dissertation would be of great value. It will be particularly interesting to compare the flight controllers developed for models at small angles of attack (linear regime), 0° to 10°, where Theodorsen's model is most accurate, with controllers at higher angles of attack, where linear models fail and how to switch from a regime model to another.

6.3.2 Unified nonlinear model

Developing nonlinear models based on the multi-models presented in this dissertation will be a challenging and worthwhile endeavor. Of particular interest, merging the three linearized dynamical models developed in Chapter two to obtain a global model that describes the whole range of a flight vehicle operation should be sought. Nonlinear system identification (ex. Volterra series) may provide valuable information about the form of the nonlinearity in such a model.

6.3.3 Design optimization for micro harvesters

For enhancing the performance of micro energy harvesters, it is worthy to use optimization techniques while designing such harvesters. Maximizing power density as well as minimizing power losses should be stringent objectives for high levels of power extraction. As such, one can relate the amount of power harvested from MFC sensors attached with a cantilever beam to the position of the sensor on the beam as well as MFC sensor type (electro-mehanical conversion). On the other hand, optimized wind turbines blades operated at low rated speeds might enhance the output power harvested from such micro turbines.

Appendix A

Unsteady aerodynamics tools

A.1 Steady and Quasi steady flow

When modeling the aerodynamic forces acting on an airfoil in motion, it is natural to start with a quasi-steady approximation. Instead of dealing with the full unsteady problem, one assumes that the airfoil's center of mass, h, and angle of attack, α, motions are gradually enough for the flow field to locally equilibrate to the motion. In this way, the unsteady terms in the flow equations are set to zero and the motion is accounted for by translating $\dot{h}$ into an effective angle of attack and $\dot{\alpha}$ into an effective camber. Finally, applying the assumption of a thin airfoil, we obtain a quasi-steady estimate for the lift coefficient. To deal with a sudden change in angle of attack by applying a step input, one of the simplest and reasonable assumption could be the steady or quasi steady assumption. For example, for an airplane to have a sudden change in angle of attack, it takes time (Δt) for the wings to build up lift (ΔC_L) corresponds to the positive change in AOA. on the other hand for the body dynamics to have a compact response due this sudden aerodynamic load it takes also time ΔT ,in which this ΔT considered very large compared to Δt. So, mathematically when talking about steady or quasi steady analysis, we consider that we have a system of algebraic equation that can be solved together to give us the steady lift ($C_L = f(\alpha, \dot{\alpha}, ...)$). For the unsteady case, one can solve a system of differential equations for the unsteady lift accounting for the time history for the lift built up time ($\dot{C}_L = f(\alpha, \dot{\alpha}, ...)$)

A.2 Classical unsteady aerodynamic models

In dynamical systems there are two basic types of response, step response and frequency response. the basic classical unsteady theories are based on these two types of response. The indicial response evolved by wagner 1925 and the frequency response evolved by Theodorson 1935.

A.2.1 Step response Wagner

Indicial functions are used to model the response to a step change in some quantity, which is applied instantaneously at time zero and held constant afterward. These functions may be derived analytically, or determined from computational or experimental data. Both experiments and simulations have shown that the aerodynamic forces acting on a wing accelerating from rest are lower than the values predicted by quasi-steady models (which assume steady-state forces are produced at each instant in time). A transition period is needed before the forces reach the steady-state value. This latency in the establishment of lift was first proposed by Wagner (1925) and studied experimentally by Walker (1931) [169]. When an inclined wing starts impulsively from rest, the circulation around it does not immediately attain its steady-state value. Instead, the circulation rises slowly to the steady-state estimate. This delay in reaching the steady-state values may result from a combination of two phenomena. First, there is inherent latency in the viscous action on the stagnation point and thus a finite time before the establishment of Kutta condition. Second, during this process, vorticity is generated and shed at the trailing edge, and the shed vorticity eventually rolls up in the form of a starting vortex (visualized by Prandtl in 1934 using a water channel and aluminum particles Figure A.2). The velocity field induced in the vicinity of the wing by the vorticity shed at the trailing edge additionally counteracts the growth of circulation bound to the wing. After the starting vortex has moved sufficiently far from the trailing edge, the wing attains its maximum steady circulation. This sluggishness in the development of circulation and is often referred to as the Wagner effect. Wagner effect is defined as the ratio of instantaneous to steady circulation (y-axis) grows as the trailing edge vortex moves away from the airfoil inset), and its influence on the circulation around the airfoil diminishes with

distance (x-axis). Distance is non-dimensionalized with respect to chord lengths traveled. Figure A.2(left) is a schematic diagram of the Wagner effect. It can be seen that the bound vortex has achieved about 80% of its final value after 5 chord lengths. Figure A.2(right) is the impulsively started airfoil experiment showing the starting vortex [Prandtl 1934].

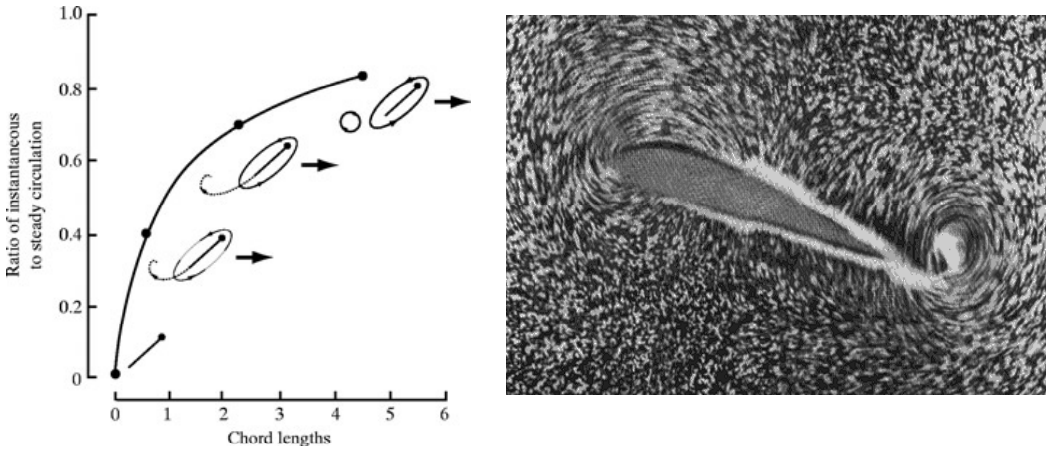

Figure A.1: Wagner effect(Left) and starting vortex (Right)A.2

When designing either an aircraft or a bio-inspired robot, engineers have to explore many design alternatives to optimize performances of the device. This can be very time-consuming. That is why usually only quasi-steady aerodynamic models are employed (which are fast and robust). But those models do not take into account the possible unsteady effects that can occur during rapid maneuvers or takeoff, such as the Wagner effect. Using linearized thin-airfoil theory for the impulsive motion of an airfoil in an incompressible flow, a relation can be derived for the unsteady lift generated, as a function of time [170]. The unsteady lift for an airfoil of chord 2b , impulsively started to velocity U , has the following form:

$$L = 2\pi b \rho U w \Phi(\tau) \tag{A.1}$$

where, $\Phi(\tau)$ is called Wagner's function. It corrects the quasi-steady models when obtaining the aerodynamic forces during the transitional period. The angle of attack, α , is assumed small, w is the downwash velocity and τ is the non dimensional quantity proportional to time.

For a response due to step input, the output could be first order or second order based

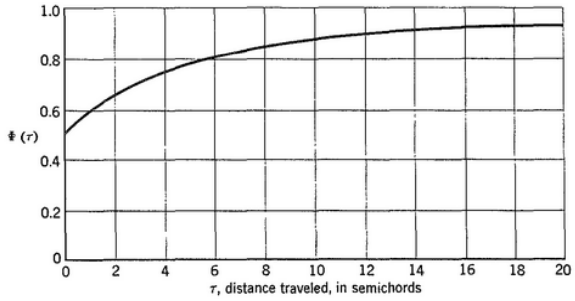

Figure A.2: Wagner's function for an impulsively started airfoil in an incompressible fluid. The value of lift starts at 50% of the steady-state value.

on the system behavior. Wagner describes the lift coefficient as function of steady lift ($2\pi\alpha$) and $\phi(s)$.

$$C_L = C_{L steady}\phi(s) \tag{A.2}$$

where the value of $\phi(s)$ starts from 0.5 at time equals zero and reaches steady state at value equals 1.

Wagner's function, $\phi(s)$, models the circulatory lift response of a thin airfoil undergoing a step change in angle of attack in incompressible flow as a function of reduced time, where S is given by:

$$S = \frac{2}{C}\int_0^t V dt \tag{A.3}$$

The reduced time parameter is commonly used in unsteady aerodynamics, as it represents the distance the airfoil has traveled through the flow in terms of semi-chords. It is a useful indicator of the relative position of the airfoil and features of its shed wake. The application of Wagners function to a time domain simulation of the arbitrary motion of an airfoil is accomplished by treating each time-step as a step change in the angle of attack and pitch rate of the airfoil. The effect of the shed wake over time may then be captured through the superposition of these indicial responses with the Duhamel integral. For a general linear time-invariant system, the Duhamel integral can be written as:

A.2.2 State Space finite Model for Wagner

R T Jones proposed an approximate expression for Wagner function as follows:

$$\phi(s) = 1 - A_1\, e^{-c_1\, s} - A_2\, e^{-c_2\, s} \tag{A.4}$$

where $A_1 = 0.165, A_2 = 0.335, c_1 = 0.0455, c_2 = 0.3$ and s is the reduced time parameter and is given by Ut/b

In time domain the frequency response output due to step input is given by:

$$\phi(t) = 1 - 0.165\, e^{0.0455\, Ut/b} - 0.335\, e^{0.3\, Ut/b} \tag{A.5}$$

By taking the Laplace transform with an operator P:

$$\phi(P) = \frac{1}{P} - \frac{A_1}{P + \frac{c_1 U}{b}} - \frac{A_2}{P + \frac{c_3 U}{b}} \tag{A.6}$$

The transfer function is written as:

$$G(P) = \frac{Y(P)}{U(P)} = \frac{\phi(P)}{1/P} = 1 - \frac{A_1\, P}{P + \frac{c_1 U}{b}} - \frac{A_2\, P}{P + \frac{c_3 U}{b}} \tag{A.7}$$

$$G(P) = \frac{(P + \frac{c_1 U}{b})(P + \frac{c_2 U}{b}) - A_1 P\, (P + \frac{c_2 U}{b}) - A_2 P\, (P + \frac{c_1 U}{b})}{(P + \frac{c_1 U}{b})(P + \frac{c_2 U}{b})} \tag{A.8}$$

$$G(P) = \frac{(1 - A_1 - A_2)P^2 + \left(\frac{c_1 U}{b}\,(1 - A_2) + \frac{c_2 U}{b}\,(1 - A_1)\right)P\; + \frac{c_1 c_2 U^2}{b^2}}{P^2 + \;(c_1 + c_2)\frac{UP}{b} + \frac{c_1 c_2 U^2}{b^2}} \tag{A.9}$$

A.3 Unsteady Bernoulli Equation

Recall Euler equation (conservation of momentum)

$$\rho\, \overrightarrow{a} = \rho \frac{DV}{Dt} = -\nabla P \tag{A.10}$$

The total(substantial)derivative of the velocity is expanded to be:

$$\rho\big[\frac{\partial V}{\partial t} + \overrightarrow{V}.\nabla \overrightarrow{V}\big] = -\nabla P \tag{A.11}$$

Recalling Bernoulli assumption for irrotional invicid flow

$$\overrightarrow{V} = \nabla\phi \tag{A.12}$$

$$\frac{\partial V}{\partial t} = \nabla\frac{\partial\phi}{\partial t} = \nabla\phi_t \tag{A.13}$$

$$\overrightarrow{V}.\nabla\overrightarrow{V} = \frac{1}{2}\nabla(\overrightarrow{V}.\overrightarrow{V}) - \underbrace{\overrightarrow{V}\times(\nabla\times\overrightarrow{V})} \tag{A.14}$$

For irrotational flow $curl(V) = 0$

$$\rho\big[\nabla\phi_t + \frac{1}{2}\nabla V^2\big] = -\nabla P \tag{A.15}$$

The forces acting on fluid element are pressure and gravity, so the momentum equation becomes

$$\nabla\big[\rho\phi_t + \frac{1}{2}\rho V^2 + \overrightarrow{P} + \rho gz\big] = 0 \tag{A.16}$$

Then, we integrate all the spacial derivatives (i.e. knock the $\bigtriangledown$ out), and we have the unsteady Bernoullis Equation;

$$\rho\phi_t + \frac{1}{2}\rho V^2 + \overrightarrow{P} + \rho gz = F(t) \tag{A.17}$$

where F(t) is some function of t (is the constant of integration)

The major deficiency of unsteady Bernoulli equation is it doesn't account for leading edge suction (LES). Linearizing flow velocity, we assume that $U_\infty = const.$

$$\phi_\infty = U_\infty x \tag{A.18}$$

$$\frac{1}{2}\rho {U_\infty}^2 + P_\infty = \rho\phi_t + \frac{1}{2}\rho U^2 + P \tag{A.19}$$

$$P - P_\infty = -\rho\big[\phi_t + \frac{1}{2}(U^2 - {U_\infty}^2)\big] \tag{A.20}$$

Applying linearization

$$U = U_\infty + \triangle u \tag{A.21}$$

$$U^2 = {U_\infty}^2 + 2U_\infty \triangle u + \triangle u^2 \tag{A.22}$$

Assuming small $\triangle$u ,

$$U^2 - {U_\infty}^2 = 2U_\infty \phi_x \tag{A.23}$$

$$P - P_\infty = -\rho\big[\phi_t + U_\infty \phi_x)\big] \tag{A.24}$$

$$\Delta P = 2\rho\big[\phi_t + U_\infty \phi_x)\big]_{upper} \tag{A.25}$$

For more detailed treatments of the physical concepts, the reader is referred to classic fluid dynamics texts written by Lamb (1945), Landau and Lifshitz (1959), Milne-Thomson (1966) and Batchelor (1973) and books focusing on thin airfoil theory, such as Glauert (1947) and Prandtl and Tietjens (1957b).

A.4 Thoedorsen function

In Theodorsens approach, only three major simplifications are assumed:

- The flow is always attached, i.e. the motion's amplitude is small.
- The wing is a flat plate. The flat plate assumption is not problematic. In fact Theodorsen worked on a flat plate with a control surface (3 DOF), so asymmetric wings can also be handled.
- The wake is flat.
- The wake is shedded with a velocity equal to the undisturbed flow velocity.

If the motion is small (first assumption) then the flat wake assumption has little influence on the results. The model is based on elementary solutions of the Laplace equation. Theodorsen chose to model the wing as a circle that can be mapped onto a flat plate through a conformal transformation. Thoedorsen derivation based on two main contribution, the circulatory and non-circulatory load contributions which can be written as:

A.4.1 Plunging flat plate

$$L_{total} = L_{NC} + L_C \tag{A.26}$$

where, L_{NC} is the non circulatory contribution of the lift due to added mass and L_C is the circulatory contribution due to unsteady effects.

$$L_{NC} = -m_{added}\ a_{\frac{c}{2}} \quad , \quad L_C = L_{QS}\ C(k) \tag{A.27}$$

where m_{added} is the added mass and $a_{\frac{c}{2}}$ is the acceleration of the plate due to plunging

$$L_{NC}(t) = -m_{added}\ \ddot{h} = -\pi\rho b^2(-H\omega^2\ sin(\omega t)) \tag{A.28}$$

The quasi-steady lift is given by:

$$L_{QS} = \frac{1}{2}\ \rho U_\infty^2 c C_L\ \alpha_{eff}(t) \tag{A.29}$$

and the effective angle of attack is given by:

$$\alpha_{eff}(t) = \frac{\dot{h}}{U_\infty}\ =\ \frac{bH\omega}{bU_\infty}\ cos(\omega t)\ =\ k\overline{H}cos(\omega t) \tag{A.30}$$

where, k is the reduced frequency and $\overline{H}$ is the normalized plunging amplitude

$$L_{QS}(t) = \frac{1}{2}\ \rho U_\infty^2\ c\ 2\pi\ k\overline{H}cos(\omega t) \tag{A.31}$$

$$L_C(t) = \pi\rho U_\infty^2 ck\overline{H}\ |C(k)|\ cos(\omega t + \phi) \tag{A.32}$$

where, $|C(k)|$ is the amplitude of complex Theodersen function and ϕ its angle ($phase\ shift$)

A.4.2 Pitching flat plate

For the pitching case the airfoil hinge is located at distance ab from the half chord location and the angle of attack function in time is given by:

$$\alpha(t) = A_\alpha \; sin(\omega t) \tag{A.33}$$

the non-circulatory lift is given by:

$$L_{NC}(t) = -\pi\rho b^2 \; (U_\infty \; \dot{\alpha} - \ddot{\alpha} \; a \; b) \tag{A.34}$$

$$L_{QS} = \frac{1}{2} \; \rho U_\infty^2 c C_L \; \alpha_{eff}(t) \tag{A.35}$$

where the effective angle of attack in this case is at the quarter chord location and is given by:

$$\alpha_{eff} = \alpha + \frac{\dot{\alpha}(\frac{1}{2} - a)}{U_\infty} = \; A_\alpha \; sin(\omega t) + \frac{A_\alpha \omega \; cos(\omega t)(\frac{1}{2} - a) b}{U_\infty} \tag{A.36}$$

$$L_{QS} = \pi\rho U_\infty^2 c A_\alpha \; \left[sin(\omega t) + k(\frac{1}{2} - a) \; cos(\omega t) \right] \tag{A.37}$$

$$L_C = \pi\rho U^2 c A_{alpha} |(C_k)| \; \left[sin(wt + \phi) + k * (\frac{1}{2} - a) \; cos(wt + \phi) \right] \tag{A.38}$$

It is clear that unsteady loads are always less than their quasi-steady counterparts

A.5 State Space representation

The following procedure aims to familiarize the reader of how the equations of motion can be written in state space form, if we can represent the deficiency function $C(k)$ as a fractional polynomial $\frac{N(p)}{D(p)}$ in Laplace operator p .

We have:

$$\dot{y} = Ay + By \frac{N(p)}{D(p)} \tag{A.39}$$

Let $L_C = y\frac{N(p)}{D(p)}$, where $L_1 = y_1\frac{N(p)}{D(p)}, ...L_{Ny} = y_{Ny}\frac{N(p)}{D(p)}$ and N_y is the length of y.

Introducing intermediate variable h such that :

$$\frac{L_1}{h}\frac{h}{y_1} = \frac{N(p)}{D(p)} \tag{A.40}$$

Let $\frac{L_1}{h} = N(p)$ and $\frac{h}{y_1} = \frac{1}{D(p)}$, expanding N and D in terms of p leads to :

$$y_1 = h[p^n + d_{n-1}p^{n-1} + ...d_0] \tag{A.41}$$

$$L_1 = h[a_m p^m + a_{m-1}p^{m-1} + ...a_0] \tag{A.42}$$

Equation (A.41) can be written in state space form as :

$$\begin{bmatrix} \frac{d^n h}{dt^n} \\ \frac{d^{n-1}h}{dt^{n-1}} \\ . \\ . \\ . \\ \frac{dh}{dt} \end{bmatrix} = \begin{bmatrix} -d_{n-1} & -d_{n-2} & ..... & d_0 \\ 1 & 0 & ..... & 0 \\ 0 & 1 & ..... & 0 \\ . & . & 1 & 0 \\ . & . & . & 0 \\ . & . & . & 0 \end{bmatrix} \begin{bmatrix} \frac{d^{n-1}h}{dt^{n-1}} \\ \frac{d^{n-2}h}{dt^{n-2}} \\ . \\ . \\ . \\ h \end{bmatrix} + \begin{bmatrix} 1 \\ 0 \\ . \\ . \\ . \\ 0 \end{bmatrix} y_1 \tag{A.43}$$

In matrix form :

$$\dot{H} = A_c H + B_c y_1 \tag{A.44}$$

From eq A.41 : $\frac{d^n h}{dt^n} = y_1 - d_{n-1}\frac{d^{n-1}h}{dt^{n-1}} - d_{n-2}\frac{d^{n-2}h}{dt^{n-2}}..... - d_0 h$

for the case of $n = m$ (it's always the case), substitute in (A.42)

$$L_1 = \begin{bmatrix} (a_{m-1} - a_m d_{n-1}) & (a_{m-2} - a_m d_{n-2}) & ..... & (a_0 - a_m d_0) \end{bmatrix} \begin{bmatrix} \frac{d^{n-1}h}{dt^{n-1}} \\ \frac{d^{n-2}h}{dt^{n-2}} \\ . \\ . \\ . \\ h \end{bmatrix} + [a_m]y_1 \tag{A.45}$$

In matrix form :

$$L_1 = C_c H + D_c y_1 \tag{A.46}$$

(A.46) and (A.44) is repeated N_y times such that :

$$\begin{bmatrix} \dot{H} \\ . \\ . \\ \dot{H} \end{bmatrix} = \begin{bmatrix} A_c & [0] & ... & [0] \\ [0] & A_c & ... & [0] \\ . & .. & .. & [0] \\ [0] & .. & .. & A_c \end{bmatrix} \begin{bmatrix} H \\ . \\ . \\ H \end{bmatrix} + \begin{bmatrix} B_c & [0] & ... & [0] \\ [0] & B_c & ... & [0] \\ . & .. & .. & [0] \\ [0] & .. & .. & B_c \end{bmatrix} \begin{bmatrix} y_1 \\ y_2 \\ . \\ y_{N_y} \end{bmatrix} \tag{A.47}$$

$$\begin{bmatrix} L_1 \\ . \\ . \\ L_{N_y} \end{bmatrix} = \begin{bmatrix} C_c & [0] & ... & [0] \\ [0] & C_c & ... & [0] \\ . & .. & .. & [0] \\ [0] & .. & .. & C_c \end{bmatrix} \begin{bmatrix} H \\ . \\ . \\ H \end{bmatrix} + \begin{bmatrix} D_c & [0] & ... & [0] \\ [0] & D_c & ... & [0] \\ . & .. & .. & [0] \\ [0] & .. & .. & D_c \end{bmatrix} \begin{bmatrix} y_1 \\ y_2 \\ . \\ y_{N_y} \end{bmatrix} \tag{A.48}$$

In matrix form :

$$\dot{M} = A_C M + B_C y \tag{A.49}$$

$$L_C = C_C M + D_C y \tag{A.50}$$

Combining (A.5) and (A.50) with (A.39) leads to :

$$\begin{bmatrix} \dot{y} \\ \dot{M} \end{bmatrix} = \begin{bmatrix} A + B.D_C & B.C_C \\ B_C & A_C \end{bmatrix} \begin{bmatrix} y \\ M \end{bmatrix} \tag{A.51}$$

Introducing a new variable $Z = \begin{bmatrix} y \\ M \end{bmatrix}$, eq (A.51) can be written as :

$$\therefore \dot{Z} = A_{new} Z \tag{A.52}$$

Where :

$$A_{new} = \begin{bmatrix} A + B.D_C & B.C_C \\ B_C & A_C \end{bmatrix}$$

A.5.1 Steady State modeling procedures

In order to model an infinite dimensional dynamics onto a two dimensional system, a second order transfer function can be written as:

$$\frac{Y}{U} = \frac{b_2 P^2 + b_1 P + b_0}{P^2 + a_1 P + a_0} = \frac{Y}{X} \frac{X}{U} \tag{A.53}$$

where X is the internal states of the system, so now we can write the system as follows:

$$\frac{X}{U} = \frac{1}{P^2 + a_1 P + a_0} \tag{A.54}$$

$$\frac{Y}{X} = \frac{b_2 P^2 + b_1 P + b_0}{1} \tag{A.55}$$

starting from

$$XP^2 + Xa_1 P + Xa_0 = U$$

then applying Laplace inverse we get:

$$\ddot{X} + a_1 \dot{X} + a_o X = U$$

then let $X_1 = X$ and $X_2 = \dot{X}$

Also we can write

$$Y = Xb_2 P^2 + Xb_1 P + b_0 X = b_2 \ddot{X} + b_1 \dot{X} + b_o X \tag{A.56}$$

, we have

$$Y = b_2(U - a_o X_1 - a_1 X_2) + b_1 X_2 + b_o X_1 \tag{A.57}$$

By writing these equation in a matrix form $\dot{X} = AX + BU$ and $y = CX + DU$

$$\frac{d}{dt}\begin{pmatrix} X_1 \\ X_2 \end{pmatrix} = \begin{bmatrix} 0 & 1 \\ -a_o & -a_1 \end{bmatrix}\begin{pmatrix} X_1 \\ X_2 \end{pmatrix} + \begin{pmatrix} 0 \\ 1 \end{pmatrix} U \tag{A.58}$$

$$y = \begin{bmatrix} b_o - b_2 a_o & b_1 - b_2 a_1 \end{bmatrix}\begin{pmatrix} X_1 \\ X_2 \end{pmatrix} + \begin{pmatrix} b_2 \end{pmatrix} U \tag{A.59}$$

Regarding to the quasi-steady lift

$$L_{QS} = \rho U \Gamma = 2\pi \rho U b \, W_{3/4} \tag{A.60}$$

where $W_{3/4}$ is the normal velocity component and is given by:

$$W_{3/4} = U sin(\alpha) + \dot{\alpha}[\frac{b}{2} - a]$$

$$L_c(t) = 2\pi\rho U b \begin{bmatrix} b_o - b_2 a_o & b_1 - b_2 a_1 \end{bmatrix} \begin{pmatrix} X_1 \\ X_2 \end{pmatrix} + [b_2] W_{3/4} \tag{A.61}$$

The experiments give us the instantaneous lift force coefficient during a few oscillation periods for a pure plunging motion. After obtaining the measured amplitudes and phase shifts for the circulatory and quasi-steady lift coefficients, we construct the frequency response based on that results for combinations of α_o and ω. Then, the magnitude of the frequency response is obtained as:

$$|G| = \frac{|A_c|}{|B_{QS}|} \tag{A.62}$$

and the phase shift is given by

$$\angle G = -\omega t_{\text{lag}} \tag{A.63}$$

where t_{lag} is the time lag between the steady state circulatory lift and the quasi-steady one far out in time.

In order to model our infinite dimensional dynamics we first project the dynamics onto a two dimensional system. This implies that our second order transfer function can be written as:

$$G(s) = \frac{b_2 s^2 + b_1 s + b_0}{s^2 + a_1 s + a_0}$$

. To obtain the phase and the amplitude of this transfer function we substitute $s = i\omega$ and therefore the amplitude and phase are given by

$$|G(\omega)| = \sqrt{\frac{(b_0 - b_2\omega^2)^2 + b_1^2\omega^2}{(a_0 - \omega^2)^2 + a_1^2\omega^2}} \tag{A.64}$$

$$\angle G(\omega) = \arctan\left(\frac{b_1\omega}{b_0 - b_2\omega^2}\right) - \arctan\left(\frac{a_1\omega}{a_0 - \omega^2}\right) \tag{A.65}$$

The amplitude given above is the ratio of output to input amplitudes and the phase is the phase shift between output and input angles. Next, we use this function to obtain the linear unsteady model which is of the form

$$\begin{aligned} \dot{\vec{x}} &= A\vec{x} + BU \\ C_L &= C\vec{x} + DU \end{aligned} \tag{A.66}$$

where the matricesA, B, C, D are given by

$$A = \begin{pmatrix} 0 & 1 \\ -a_0 & -a_1 \end{pmatrix}, B = \begin{pmatrix} 0 \\ 1 \end{pmatrix}, C = \begin{pmatrix} b_0 - a_0 b_2 & b_1 - a_1 b_2 \end{pmatrix} \text{and} D = b_2$$

Bibliography

[1] Elgin, R. A., Hone, D. W., and Frey, E., "The extent of the pterosaur flight membrane," *Acta Palaeontologica Polonica*, Vol. 56, No. 1, 2011, pp. 99–111.

[2] Wellnhofer, P., "The Pterodactyloidea (Pterosauria) of the Upper Jurassic laminated limestone layers of South Germany (Translated from German)," *Abh Bayer Akad Wiss NF*, Vol. 141, 1970, pp. 1–133.

[3] MacCready Jr, P. B., "The great pterodactyl project," *Engineering and Science*, Vol. 49, No. 2, 1985, pp. 18–24.

[4] Leung, D., Deng, Y., and Leung, M., "Design optimization of a cost-effective micro wind turbine," *WCE 2010-World Congress on Engineering 2010*, Vol. 2, International Association of Engineers., 2010, pp. 988–993.

[5] Howey, D., Bansal, A., and Holmes, A., "Design and performance of a centimetre-scale shrouded wind turbine for energy harvesting," *Smart Materials and Structures*, Vol. 20, No. 8, 2011, pp. 085021.

[6] Xu, F., Yuan, F.-G., Liu, L., Hu, J., and Qiu, Y., "Performance Prediction and Demonstration of a Miniature Horizontal Axis Wind Turbine," *Journal of Energy Engineering*, Vol. 139, No. 3, 2013, pp. 143–152.

[7] Prandtl, L., "Über die Entstehung von Wirbeln in der idealen Flüssigkeit, mit Anwendung auf die Tragflügeltheorie und andere Aufgaben," *Vorträge aus dem Gebiete der Hydro-und Aerodynamik (Innsbruck 1922)*, Springer, 1924, pp. 18–33.

[8] Birnbaum, W., "Der Schlagflugelpropeller und die Kleinen Schwingungen elastisch befestigter Tragfluegel." *Z Flugtech Motorluftschiffahrt*, Vol. 15, 1924, pp. 128–134.

[9] Dickinson, M. H. and Gotz, K. C., "Unsteady Aerodynamic Performance of Model Wings at Low Reynolds Numbers." *Journal of Experimental Biology*, Vol. 174, No. 1, 1993, pp. 45–64.

[10] Ellington, C. P., Van Den Berg, C., Willmott, A. P., and Thomas, A. L. R., "Leading-edge vortices in insect flight," *Nature*, Vol. 384, 1996, pp. 626–630.

[11] Dickinson, M. H., Lehmann, F.-O., and Sane, S. P., "Wing rotation and the aerodynamic basis of insect flight." *Science*, Vol. 284, No. 5422, 1999, pp. 1954–1960.

[12] Ramamurti, R. and Sandberg, W., "A three-dimensional computational study of the aerodynamic mechanisms of insect flight," *Journal of Experimental Biology*, Vol. 205, No. 10, 2002, pp. 15071518.

[13] Saffman, P. G. and Sheffield, J. S., "Flow over a wing with an attached free vortex," *Studies in Applied Mathematics*, Vol. 57, 1977, pp. 107–117.

[14] Li, J. and Wu, Z.-N., "Unsteady lift for the Wagner problem in the presence of additional leading/trailing edge vortices," *Journal of Fluid Mechanics*, Vol. 769, 2015, pp. 182–217.

[15] Minotti, F. O., "Unsteady two-dimensional theory of a flapping wing," *Physical Review E*, Vol. 66, No. 5, 2002, pp. 051907.

[16] Jones, M. A., "The separated flow of an inviscid fluid around a moving flat plate," *Journal of Fluid Mechanics*, Vol. 496, 2003, pp. 405–441.

[17] Yongliang, Y., Binggang, T., and Huiyang, M., "An analytic approach to theoretical modeling of highly unsteady viscous flow excited by wing flapping in small insects," *Acta Mechanica Sinica*, Vol. 19, No. 6, 2003, pp. 508–516.

[18] Pullin, D. I. and Wang, Z., "Unsteady forces on an accelerating plate and application to hovering insect flight," *Journal of Fluid Mechanics*, Vol. 509, 2004, pp. 1–21.

[19] Ansari, S. A., Żbikowski, R., and Knowles, K., "Non-linear unsteady aerodynamic model for insect-like flapping wings in the hover. Part 1: methodology and analysis," *Proceedings of the Institution of Mechanical Engineers, Part G: Journal of Aerospace Engineering*, Vol. 220, No. 2, 2006, pp. 61–83.

[20] Ramesh, K., Gopalarathnam, A., Granlund, K., Ol, M. V., and Edwards, J. R., "Discrete-vortex method with novel shedding criterion for unsteady aerofoil flows with intermittent leading-edge vortex shedding," *Journal of Fluid Mechanics*, Vol. 751, 2014, pp. 500–538.

[21] Ramesh, K., Murua, J., and Gopalarathnam, A., "Limit-cycle oscillations in unsteady flows dominated by intermittent leading-edge vortex shedding," *Journal of Fluids and Structures*, Vol. 55, 2015, pp. 84–105.

[22] V. OL, M., Eldredge, J. D., and Wang, C., "High-amplitude pitch of a flat plate: an abstraction of perching and flapping," *International Journal of Micro Air Vehicles*, Vol. 1, No. 3, 2009, pp. 203–216.

[23] Wang, C. and Eldredge, J. D., "Low-order phenomenological modeling of leading-edge vortex formation," *Theoretical and Computational Fluid Dynamics*, 2012, pp. 1–22.

[24] Pitt Ford, C. and Babinsky, H., "Lift and the leading-edge vortex," *Journal of Fluid Mechanics*, Vol. 720, 2013, pp. 280–313.

[25] Savage, S. B., Newman, B. G., and Wong, D. T.-M., "The role of vortices and unsteady effects during the hovering flight of dragonflies," *The Journal of Experimental Biology*, Vol. 83, No. 1, 1979, pp. 59–77.

[26] Hemati, M. S., Eldredge, J. D., and Speyer, J. L., "Improving vortex models via optimal control theory," *Journal of Fluids and Structures*, Vol. 49, 2014, pp. 91–111.

[27] Brunton, S. L. and Rowley, C. W., "Empirical state-space representations for Theodorsens lift model," *Journal of Fluids and Structures*, Vol. 38, 2013, pp. 174–186.

[28] Theodorsen, T., "General Theory of Aerodynamic Instability and the Mechanism of Flutter," Tech. Rep. 496, NACA, 1935.

[29] Taha, H. E., Hajj, M. R., and Beran, P. S., "State-space representation of the unsteady aerodynamics of flapping flight," *Aerospace Science and Technology*, Vol. 34, 2014, pp. 1–11.

[30] Wagner, H., "Uber die Entstehung des dynamischen Auftriebes von Traflgugeln," *Zeitschrift fur Angewandte Mathematic und Mechanik*, Vol. 35, 1925, pp. 17.

[31] Sun, M. and Du, G., "Lift and power requirements of hovering insect flight," *Acta Mech. Sin.*, Vol. 19, No. 5, 2003, pp. 458–469.

[32] Yan, Z., Taha, H. E., and Hajj, M. R., "Geometrically-Exact Unsteady Model for Airfoils Undergoing Large Amplitude Maneuvers," *Aerospace Science and Technology*, Vol. 39, 2014, pp. 293–306.

[33] Taha, H. E., Yan, Z., and Hajj, M. R., "Geometrically-Exact Extension of Theodorsens Frequency Response Model," *53rd AIAA Aerospace Sciences Meeting*, 2015, p. 1502.

[34] Eldredge, J. D., Wang, C., and Ol, M. V., "A computational study of a canonical pitch-up, pitch-down wing maneuver," AIAA-Paper 2009-3687, 2009.

[35] Ramesh, K., Gopalarathnam, A., Edwards, J. R., Ol, M. V., and Granlund, K., "An unsteady airfoil theory applied to pitching motions validated against experiment and computation." *Theoretical and Computational Fluid Dynamics*, 2013, pp. 1–22.

[36] Leishman, J. G. and Nguyen, k. Q., "State-Space Representation of Unsteady Airfoil Behavior," *AIAA Journal*, Vol. 28, No. 5, 1990, pp. 836–844.

[37] Ellington, C. P., Van Den Berg, C., Willmott, A. P., and Thomas, A. L., "Leading-edge vortices in insect flight," 1996.

[38] Jones, K., Dohring, C., and Platzer, M., "Wake structures behind plunging airfoils: a comparison of numerical and experimental results," *AIAA paper*, Vol. 78, 1996, pp. 1996.

[39] Commerford, G. and Carta, F. ., "Unsteady aerodynamic response of a two-dimensional airfoil at high reduced frequency," *AIAA Journal*, Vol. 12, No. 1, 1974, pp. 43–48.

[40] Triantafyllou, G., Triantafyllou, M., and Grosenbaugh, M., "Optimal thrust development in oscillating foils with application to fish propulsion," *Journal of Fluids and Structures*, Vol. 7, No. 2, 1993, pp. 205–224.

[41] Anderson, J., Streitlien, K., Barrett, D., and Triantafyllou, M., "Oscillating foils of high propulsive efficiency," *Journal of Fluid Mechanics*, Vol. 360, No. 1, 1998, pp. 41–72.

[42] Ohmi, K., Coutanceau, M., Daube, O., and Loc, T. P., "Further experiments on vortex formation around an oscillating and translating airfoil at large incidences," *Journal of Fluid Mechanics*, Vol. 225, 1991, pp. 607–630.

[43] Wang, Z. J., "Dissecting insect flight," *Annu. Rev. Fluid Mech.*, Vol. 37, 2005, pp. 183–210.

[44] Cleaver, D. J., Wang, Z., and Gursul, I., "Bifurcating flows of plunging aerofoils at high Strouhal numbers," *Journal of Fluid Mechanics*, Vol. 708, 2012, pp. 349–376.

[45] Rival, D. and Tropea, C., "Characteristics of pitching and plunging airfoils under dynamic-stall conditions," *Journal of Aircraft*, Vol. 47, No. 1, 2010, pp. 80–86.

[46] Rival, D. E., Kriegseis, J., Schaub, P., Widmann, A., and Tropea, C., "Characteristic length scales for vortex detachment on plunging profiles with varying leading-edge geometry," *Experiments in Fluids*, Vol. 55, No. 1, 2014, pp. 1–8.

[47] Usherwood, J. R. and Ellington, C. P., "The aerodynamics of revolving wings I. Model hawkmoth wings," *Journal of Experimental Biology*, Vol. 205, 2002, pp. 1547 1564.

[48] Panah, A. E. and Buchholz, J. H., "Parameter dependence of vortex interactions on a two-dimensional plunging plate," *Experiments in Fluids*, Vol. 55, No. 3, 2014, pp. 1–19.

[49] Baik, Y. S., Bernal, L. P., Granlund, K., and Ol, M. V., "Unsteady force generation and vortex dynamics of pitching and plunging aerofoils," *Journal of Fluid Mechanics*, Vol. 709, 2012, pp. 37–68.

[50] Gursul, I., Cleaver, D., and Wang, Z., "Control of low Reynolds number flows by means of fluid–structure interactions," *Progress in Aerospace Sciences*, Vol. 64, 2014, pp. 17–55.

[51] Graftieaux, L., Michard, M., and Grosjean, N., "Combining PIV, POD and vortex identification algorithms for the study of unsteady turbulent swirling flows," *Measurement Science and Technology*, Vol. 12, No. 9, 2001, pp. 1422.

[52] Brooks, T. F., Marcolini, M. A., and Pope, D. S., "Airfoil trailing edge flow measurements and comparison with theory incorporating open wind tunnel corrections," *AIAA Paper*, 1984, pp. 84–2266.

[53] Rae, W. H. and Pope, A., *Low-speed wind tunnel testing*, John Wiley, 1984.

[54] Mangler, W., "The lift distibution of wings with end plates," Tech. rep., Technical Memorandum NASA TM 856, NASA, 1938.

[55] Garner, H. C., Rogers, E., Acum, W., and Maskell, E., "Subsonic wind tunnel wall corrections," Tech. rep., DTIC Document, 1966.

[56] Moffat, R. J., "Using uncertainty analysis in the planning of an experiment," *Journal of Fluids Engineering*, Vol. 107, No. 2, 1985, pp. 173–178.

[57] Tang, D. and Dowell, E. H., "Experimental aerodynamic response for an oscillating airfoil in buffeting flow," *AIAA journal*, Vol. 52, No. 6, 2014, pp. 1170–1179.

[58] Polhamus, E. C., "A Concept of The Vortex Lift of Sharp-Edge Delta Wings Based on a Leading-Edge-Suction Analogy," Tech. Rep. NASA TN D-3767, Langely Research Center, Langely Station, Hampton, Va, 1966.

[59] Berman, G. J. and Wang, Z. J., "Energy-minimizing kinematics in hovering insect flight," *Journal of Fluid Mechanics*, Vol. 582, No. 1, 2007, pp. 153,168.

[60] Carmichael, B., *Low Reynolds number airfoil survey*, National Aeronautics and Space Administration, Langley Research Center, 1981.

[61] Yarusevych, S., Sullivan, P. E., and Kawall, J. G., "On vortex shedding from an airfoil in low-Reynolds-number flows," *Journal of Fluid Mechanics*, Vol. 632, 2009, pp. 245–271.

[62] Huang, R. F. and Lin, C. L., "Vortex shedding and shear-layer instability of wing at low-Reynolds numbers," *AIAA journal*, Vol. 33, No. 8, 1995, pp. 1398–1403.

[63] Yarusevych, S., Sullivan, P. E., and Kawall, J. G., "On vortex shedding from an airfoil in low-Reynolds-number flows," *Journal of Fluid Mechanics*, Vol. 632, 2009, pp. 245–271.

[64] Huang, R. F. and Lee, H. W., "Turbulence effect on frequency characteristics of unsteady motions in wake of wing," *AIAA journal*, Vol. 38, No. 1, 2000, pp. 87–94.

[65] Yarusevych, S. and H. Boutilier, M. S., "Vortex shedding of an airfoil at low Reynolds numbers," *AIAA journal*, Vol. 49, No. 10, 2011, pp. 2221–2227.

[66] Huang, M.-K. and Chow, C.-Y., "Trapping of a free vortex by Joukowski airfoils," *AIAA Journal*, Vol. 20, No. 3, 1982, pp. 292–298.

[67] Huang, R. F. and Lin, C. L., "Vortex shedding and shear-layer instability of wing at low-Reynolds numbers," *AIAA journal*, Vol. 33, No. 8, 1995, pp. 1398–1403.

[68] J. Wells, A. Salem-Said, S. A. R., *Effects of Turbulence Modeling on RANS Simulations of Tip Vortices*, 48th AIAA Aerospace Sciences Meeting Including the New Horizons Forum and Aerospace Exposition, Orlando, Florida, 2010.

[69] Zakaria, M. Y., Taha, H. E., Hajj, M. R., and Hussein, A. A., "Experimental-Based Unified Unsteady Nonlinear Aerodynamic Modeling For Two-Dimensional Airfoils," *33rd AIAA Applied Aerodynamics Conference*, 2015, p. 3167.

[70] Spalart, P. R. and Allmaras, S. R., "A one equation turbulence model for aerodinamic flows." *AIAA journal*, Vol. 94, 1992.

[71] Dacles-Mariani, J., Zilliac, G. G., Chow, J. S., and Bradshaw, P., "Numerical/experimental study of a wingtip vortex in the near field," *AIAA journal*, Vol. 33, No. 9, 1995, pp. 1561–1568.

[72] Dacles-Mariani, J., Kwak, D., and Zilliac, G., "On numerical errors and turbulence modeling in tip vortex flow prediction," *International journal for numerical methods in fluids*, Vol. 30, No. 1, 1999, pp. 65–82.

[73] Taulbee, D. B., "An improved algebraic Reynolds stress model and corresponding nonlinear stress model," *Physics of Fluids A: Fluid Dynamics (1989-1993)*, Vol. 4, No. 11, 1992, pp. 2555–2561.

[74] Wang, Z., "Vortex shedding and frequency selection in flapping flight," *Journal of Fluid Mechanics*, Vol. 410, 2000, pp. 323–341.

[75] Choi, J., Colonius, T., and Williams, D. R., "Surging and plunging oscillations of an airfoil at low Reynolds number," *Journal of Fluid Mechanics*, Vol. 763, 2015, pp. 237–253.

[76] Greenberg, J. M., "Airfoil in sinusoidal motion in a pulsating stream," Tech. rep., NACA, 1947.

[77] Cleaver, D., Wang, Z., and Gursul, I., "Investigation of high-lift mechanisms for a flat-plate airfoil undergoing small-amplitude plunging oscillations," *AIAA journal*, Vol. 51, No. 4, 2013, pp. 968–980.

[78] Calderon, D., Wang, Z., and Gursul, I., "Lift-enhancing vortex flows generated by plunging rectangular wings with small amplitude," *AIAA journal*, Vol. 51, No. 12, 2013, pp. 2953–2964.

[79] Cleaver, D. J., Wang, Z., Gursul, I., and Visbal, M., "Lift enhancement by means of small-amplitude airfoil oscillations at low Reynolds numbers," *AIAA journal*, Vol. 49, No. 9, 2011, pp. 2018–2033.

[80] Chow, C.-Y., Huang, M.-K., and Yan, C.-Z., "Unsteady flow about a Joukowski airfoil in the presence of moving vortices," *AIAA journal*, Vol. 23, No. 5, 1985, pp. 657–658.

[81] Jones, R. T., "Operational treatment of the nonuniform lift theory to airplane dynamics," Tech. Rep. 667, NACA, 1938.

[82] Jones, W. P., "Aerodynamic forces on wings in non-uniform motion," Tech. Rep. 2117, British Aeronautical Research Council, 1945.

[83] Vepa, R., "On the use of Pade approximants to represent unsteady aerodynamic loads for arbitrarily small motions of wings," AIAA, 14th Aerospace Sciences Meeting, Washington, DC, Jan 26-28 1976, pp. 7–17.

[84] Peters, D. A. and Karunamoorthy, S., "State-space inflow models for rotor aeroelasticity," AIAA-paper 94-1920-CP, 1994.

[85] Peters, D. A., Karunamoorthy, S., and Cao, W., "Finite-state induced flow models, Part I: two-dimensional thin airfoil." *Journal of Aircraft*, Vol. 44, 1995, pp. 1–28.

[86] Peters, D. A., "Two-dimensional incompressible unsteady airfoil theoryAn overview," *J. Fluids and Structures*, Vol. 24, 2008, pp. 295312.

[87] Jefferys, E., Broome, D., and Patel, M., "A transfer function method of modeling systems with frequency-dependent coefficients," *Journal of Guidance, Control, and Dynamics*, Vol. 7, No. 4, 1984, pp. 490–494.

[88] Fung, Y.-c., *An introduction to the theory of aeroelasticity*, Courier Corporation, 1995.

[89] Zakaria, M. Y., Taha, H. E., Hajj, M. R., and Hussein, A. A., "Experimental-Based Unified Unsteady Nonlinear Aerodynamic Modeling For Two-Dimensional Airfoils," *33rd AIAA Applied Aerodynamics Conference*, 2015, p. 3167.

[90] Stokes, G. G., *On the effect of the internal friction of fluids on the motion of pendulums*, Vol. 9, Pitt Press, 1851.

[91] Theodorsen, T., "General Theory of Aerodynamic Instability and the Mechanism of Flutter," Tech. Rep. 496, NACA, 1935.

[92] Kussner, H., "Untersuchung der Bewegung einer Platte beim Eintritt in eine Strahlgrense," *Luftfahrt forschung*, Vol. 13, No. 425, 1936.

[93] Von Karman, T., "Airfoil theory for non-uniform motion," *Journal of the Aeronautical Sciences (Institute of the Aeronautical Sciences)*, Vol. 5, No. 10, 1938, pp. 379–390.

[94] Chen, S., Wambsganss, M. t., and Jendrzejczyk, J., "Added mass and damping of a vibrating rod in confined viscous fluids," *Journal of Applied Mechanics*, Vol. 43, No. 2, 1976, pp. 325–329.

[95] Brennen, C., "A review of added mass and fluid inertial forces," 1982.

[96] Lissaman, P. and Brown, G. J., "Apparent mass effects on parafoil dynamics," *AIAA paper*, Vol. 1236, 1993, pp. 10–13.

[97] Yadykin, Y., Tenetov, V., and Levin, D., "The added mass of a flexible plate oscillating in a fluid," *JOURNAL of Fluids and Structures*, Vol. 17, No. 1, 2003, pp. 115–123.

[98] Granlund, K. and Simpson, R., "Modeling Unsteady Maneuvers of Slender Bodies," *AIAA Paper*, Vol. 6721, 2007, pp. 2007.

[99] Maniaci, D. C. and Li, Y., *Investigating the influence of the added mass effect to marine hydrokinetic horizontal-axis turbines using a General Dynamic Wake wind turbine code*, IEEE, 2011.

[100] Granlund, K. O., Michael, V., and Bernal, L. P., "Non-linearity of apparent mass for multi-element bodies," .

[101] Kochin, Nikola Evgrafovich, A. K. I. and Roze, *Theoretical hydromechanics*, Interscience, 1964.

[102] Lawrence, C. t. and Weinbaum, S., "The unsteady force on a body at low Reynolds number; the axisymmetric motion of a spheroid," *Journal of Fluid Mechanics*, Vol. 189, 1988, pp. 463–489.

[103] Nayfeh, A. H. and Balachandran, B., *Applied Nonlinear Dynamics*, John Wiley & Sons, New York, 1995.

[104] Hajj, M., Miksad, R., and Powers, E., "Perspective: Measurements and analyses of nonlinear wave interactions with higher-order spectral moments," *Journal of fluids engineering*, Vol. 119, No. 1, 1997, pp. 3–13.

[105] Kim, Y. C. and Powers, E. J., "Digital bispectral analysis and its applications to nonlinear wave interactions," *IEEE Transactions on Plasma Science*, Vol. 7, No. 2, 1979, pp. 120–131.

[106] Hajj, M. R. and Beran, P. S., "Higher-Order Spectral Analysis of Limit Cycle Oscillation of Fighter Aircraft," *Journal of Aircraft*, Vol. 45, No. 6, NOV-DEC 2008, pp. 1917–1923.

[107] Silva, W. and Dunn, S., "Higher-Order Spectral Analysis of F-18 Flight Flutter Data," *46th AIAA/ASME/ASCE/AHS/ASC Structures, Structural Dynamics and Materials Conference*, , No. April 2005, 2005, pp. 1–20.

[108] Dalla Vecchia, F. M., "Triassic pterosaurs," *Geological Society, London, Special Publications*, Vol. 379, No. 1, 2013, pp. 119–155.

[109] Middleton, K. and English, L., "Challenges and advances in the study of pterosaur flight 1," *Canadian Journal of Zoology*, Vol. 92, No. 999, 2014, pp. 1–15.

[110] Alexander, W. and Tomida, Y., "Description of a new species of Anhangueridae (Pterodactyloidea) with comments on the pterosaur fauna from the Santana Formation (Aptian-Albian), northeastern Brazil," *National Science Museum Monographs*, Vol. 17, 2000, pp. ix–137.

[111] Strang, K. A., Kroo, I., Gerritsen, M., and Delp, S., "Efficient flight of pterosaurs-an unsteady aerodynamic approach," *47th AIAA Aerospace Sciences Meeting (Proceedings), Orlando World Center Marriott, Orlando, FL*, 2009, pp. 5–8.

[112] Brooks, A., MacCready, P., Lissaman, P., and Morgan, W., "Development of a wing-flapping flying replica of the largest pterosaur," *AIAA/SAE/ASME/ASEE 21 st Joint Propulsion Conference*, 1985.

[113] DeLaurier, J. D., "An aerodynamic model for flapping-wing flight," *Aeronautical Journal*, Vol. 97, No. 964, 1993, pp. 125–130.

[114] Lilienthal, O., *Birdflight as the basis of aviation: a contribution towards a system of aviation, compiled from the results of numerous experiments made by O. and G. Lilienthal*, Markowski International Publishers, 2001.

[115] Garrick, I., *Propulsion of a flapping and oscillating airfoil*, National Bureau of Standards, 1936.

[116] Küssner, H., "Lösungen der klassischen Wellengleichung für bewegte Quellen," *ZAMM-Journal of Applied Mathematics and Mechanics/Zeitschrift für Angewandte Mathematik und Mechanik*, Vol. 24, No. 5-6, 1944, pp. 243–250.

[117] DS, B. and Archer, R., "STUDY OF MECHANICS OF FLAPPING WINGS," *Aeronautical Quarterly*, Vol. 25, No. MAY, 1974, pp. 129–142.

[118] Phlips, P., East, R., and Pratt, N., "An unsteady lifting line theory of flapping wings with application to the forward flight of birds," *Journal of Fluid Mechanics*, Vol. 112, 1981, pp. 97–125.

[119] Jones, R., "Wing flapping with minimum energy," 1980.

[120] DeLaurier, J. and Harris, J., "Experimental study of oscillating-wing propulsion," *Journal of Aircraft*, Vol. 19, No. 5, 1982, pp. 368–373.

[121] Bramwell, C. D. and Whitfield, G., "Biomechanics of Pteranodon," *Philosophical Transactions of the Royal Society of London. Series B, Biological Sciences*, 1974, pp. 503–581.

[122] Brower, J. C., "The aerodynamics of Pteranodon and Nyctosaurus, two large pterosaurs from the Upper Cretaceous of Kansas," *Journal of Vertebrate Paleontology*, 1983, pp. 84–124.

[123] Chatterjee, S. and Templin, R., *Posture, locomotion, and paleoecology of pterosaurs*, Vol. 376, Geological Society of America, 2004.

[124] Rakotomamonjy, T., Ouladsine, M., and Moing, T. L., "Modelization and kinematics optimization for a flapping-wing microair vehicle," *Journal of Aircraft*, Vol. 44, No. 1, 2007, pp. 217–231.

[125] Zakaria M.Y., Elshabka A., B. A. and O.F., A. E., "Numerical Aerodynamic Characteristics of Flapping Wings," *13th International Conference on Aerospace Sciences & Aviation Technology, ASAT-13, May*, Vol. 26, 2009, p. 15.

[126] Berman, G. J. and Wang, Z. J., "Energy-minimizing kinematics in hovering insect flight," *Journal of Fluid Mechanics*, Vol. 582, No. 1, 2007, pp. 153,168.

[127] Pesavento, U. and Wang, Z. J., "Navier-stokes solutions, model of fluid forces, and center of mass elevation," *Phys. Rev. Lett.*, Vol. 93, 2004, pp. 144501,144504.

[128] Andersen, A., Pesavento, U., and Wang, Z., "Unsteady aerodynamics of fluttering and tumbling plates," *Journal of Fluid Mechanics*, Vol. 541, 2005, pp. 65,90.

[129] Andersen, A., Pesavento, U., and Wang, Z. J., "Analysis of Transitions Between Fluttering, Tumbling and Steady Descent of Falling Cards," *Journal of Fluid Mechanics*, Vol. 541, 2005, pp. 91,104.

[130] Kurdi, M., Stanford, B., and Beran, P., "Kinematic Optimization of Insect Flight for Minimum Mechanical Power," AIAA paper 2010-1420, Jan 2010.

[131] Taha, H. E., Hajj, M. R., and Nayfeh, A. H., "Wing Kinematics Optimization for Hovering Micro Air Vehicles Using Calculus of Variation," *Journal of Aircraft*, Vol. 50, No. 2, 2013, pp. 610–614.

[132] Stanford, B. K. and Beran, P. S., "Analytical Sensitivity Analysis of an Unsteady Vortex-Lattice Method for Flapping-Wing Optimization," *Journal of Aircraft*, Vol. 47, No. 2, 2010, pp. 647–662.

[133] Ghommem, M., Hajj, M. R., Mook, D. T.and Stanford, B. K., Beran, P. S.and Snyder, R. D., and Watson, L. T., "Global optimization of actively morphing flapping wings," *Journal of Fluids and Structures*, Vol. 33, 2012, pp. 210–228.

[134] Stewart, E. C., Patil, M. J., Canfield, R. A., and Snyder, R. D., "Aeroelastic Shape Optimization of a Flapping Wing," 2014.

[135] Zakaria M.Y., Bayoumy A., E. A. and O.F, A. E., "Experimental Aerodynamic Characteristics of Flapping Membrane Wings," *13th International Conference on Aerospace Sciences & Aviation Technology, ASAT-13, May*, Vol. 26, 2009, p. 18.

[136] Zakaria, M. Y., Taha, H. E., and Hajj, M. R., "Design Optimization of Flapping Ornithopters: The Pterosaur Replica in Forward Flight," *Journal of Aircraft*, 2015, pp. 1–12.

[137] Jones, R. T., *The unsteady lift of a wing of finite aspect ratio*, Vol. 681, NACA, 1940.

[138] Scherer, J. O., "Experimental and Theoretical Investigation of Large Amplitude Oscillation Foil Propulsion Systems," Tech. rep., DTIC Document, 1968.

[139] Prouty, R. W., "Airfoils for Rotor Blades," *Helicopter Performance, Stability and control, PWS Engineering, Boston*, 1986.

[140] Hoerner, S., "Skin-friction drag," *Fluid-Dynamic Drag*, , No. 2, 1965, pp. 1–16.

[141] Kamakoti, R., Berg, M., Ljungqvist, D., and Shyy, W., "A computational study for biological flapping wing flight," *Transactions of the Aeronautical Society of the Republic of China*, Vol. 32, No. 4, 2000, pp. 265–279.

[142] Benedict, M., *Aeroelastic Design and Manufacture of an Efficient Ornithopter Wing Dual Degree Project Report*, Ph.D. thesis, Indian Institute of Technology, Bombay, 2004.

[143] Hamdaoui, M., Mouret, J.-B., Doncieux, S., and Sagaut, P., "Optimization of kinematics for birds and UAVs using evolutionary algorithms." *Proceedings of World Academy of Science: Engineering & Technology*, Vol. 42, 2008.

[144] Gill, P. E., Murray, W., S., M. A., and Wright, M. H., "Procedures for optimization problems with a mixture of bounds and general linear constraints," *ACM Transactions on Mathematical Software (TOMS)*, Vol. 10, No. 3, 1984, pp. 282–298.

[145] Gill, P. E., "Numerical linear algebra and optimization," 2007.

[146] Bryant, M. and Garcia, E., "Modeling and testing of a novel aeroelastic flutter energy harvester," *Journal of vibration and acoustics*, Vol. 133, No. 1, 2011, pp. 011010.

[147] Erturk, A., Vieira, W., De Marqui Jr, C., and Inman, D., "On the energy harvesting potential of piezoaeroelastic systems," *Applied Physics Letters*, Vol. 96, No. 18, 2010, pp. 184103.

[148] Abdelkefi, A., Nayfeh, A. H., and Hajj, M., "Modeling and analysis of piezoaeroelastic energy harvesters," *Nonlinear Dynamics*, Vol. 67, No. 2, 2012, pp. 925–939.

[149] Mehmood, A., Abdelkefi, A., Hajj, M., Nayfeh, A., Akhtar, I., and Nuhait, A., "Piezoelectric energy harvesting from vortex-induced vibrations of circular cylinder," *Journal of Sound and Vibration*, Vol. 332, No. 19, 2013, pp. 4656–4667.

[150] Sirohi, J. and Mahadik, R., "Harvesting wind energy using a galloping piezoelectric beam," *Journal of vibration and acoustics*, Vol. 134, No. 1, 2012, pp. 011009.

[151] Abdelkefi, A., Yan, Z., and Hajj, M. R., "Modeling and nonlinear analysis of piezoelectric energy harvesting from transverse galloping," *Smart materials and Structures*, Vol. 22, No. 2, 2013, pp. 025016.

[152] Abdelkefi, A., Scanlon, J., McDowell, E., and Hajj, M., "Performance enhancement of piezoelectric energy harvesters from wake galloping," *Applied Physics Letters*, Vol. 103, No. 3, 2013, pp. 033903.

[153] Ding, L., Zhang, L., Wu, C., Mao, X., and Jiang, D., "Flow induced motion and energy harvesting of bluff bodies with different cross sections," *Energy Conversion and Management*, Vol. 91, 2015, pp. 416–426.

[154] Gammaitoni, L., Neri, I., and Vocca, H., "Nonlinear oscillators for vibration energy harvesting," *Applied Physics Letters*, Vol. 94, No. 16, 2009, pp. 164102.

[155] Stanton, S. C., McGehee, C. C., and Mann, B. P., "Reversible hysteresis for broadband magnetopiezoelastic energy harvesting," *Applied Physics Letters*, Vol. 95, No. 17, 2009, pp. 174103.

[156] Patil, M. J. and Hodges, D. H., "On the importance of aerodynamic and structural geometrical nonlinearities in aeroelastic behavior of high-aspect-ratio wings," *Journal of Fluids and Structures*, Vol. 19, No. 7, 2004, pp. 905–915.

[157] Patil, M. J., Hodges, D. H., and Cesnik, C. E., "Characterizing the Effects of Geometrical Nonlinearities on Aeroelastic Behavior of High-Aspect Ratio Wings," *NASA CONFERENCE PUBLICATION*, NASA, 1999, pp. 501–510.

[158] Zakaria, M. Y., Pereira, D. A., and Hajj, M. R., "Experimental investigation and performance modeling of centimeter-scale micro-wind turbine energy harvesters," *Journal of Wind Engineering and Industrial Aerodynamics*, Vol. 147, 2015, pp. 58–65.

[159] Kass, M., Witkin, A., and Terzopoulos, D., "Snakes: Active contour models," *International Journal of Computer Vision*, Vol. 1, No. 4, 1988, pp. 321–331.

[160] Mathuna, C. O., ODonnell, T., Martinez-Catala, R. V., Rohan, J., and OFlynn, B., "Energy scavenging for long-term deployable wireless sensor networks," *Talanta*, Vol. 75, No. 3, 2008, pp. 613–623.

[161] Clausen, P. and Wood, D., "Research and development issues for small wind turbines," *Renewable Energy*, Vol. 16, No. 1, 1999, pp. 922–927.

[162] Hossain, M., Hirahara, H., Nonomura, Y., and Kawahashi, M., "The wake structure in a 2D grid installation of the horizontal axis micro wind turbines," *Renewable energy*, Vol. 32, No. 13, 2007, pp. 2247–2267.

[163] Carli, D., Brunelli, D., Bertozzi, D., and Benini, L., "A high-efficiency wind-flow energy harvester using micro turbine," *Power electronics electrical drives automation and motion (SPEEDAM), 2010 international symposium on*, IEEE, 2010, pp. 778–783.

[164] Rancourt, D., Tabesh, A., and Fréchette, L. G., "Evaluation of centimeter-scale micro windmills: aerodynamics and electromagnetic power generation," *Proc. PowerMEMS*, 2007, pp. 28–29.

[165] Al-Haik, M. Y., Zakaria, M. Y., Hajj, M. R., and Haik, Y., "Storage of energy harvested from a miniature turbine in a novel organic capacitor," *Journal of Energy Storage*, 2016.

[166] Heier, S., *Grid Integration of Wind Energy Conversion Systems*, Wiley, 1998.

[167] Grant, I., Parkin, P., and Wang, X., "Optical vortex tracking studies of a horizontal axis wind turbine in yaw using laser-sheet, flow visualisation," *Experiments in fluids*, Vol. 23, No. 6, 1997, pp. 513–519.

[168] Adaramola, M. and Krogstad, P.-Å., "Experimental investigation of wake effects on wind turbine performance," *Renewable Energy*, Vol. 36, No. 8, 2011, pp. 2078–2086.

[169] Walker, P., "Growth of circulation about a wing and an apparatus for measuring fluid motion," *ARC report*, 1931.

[170] Fung, Y.-c., *An introduction to the theory of aeroelasticity*, Courier Dover Publications, 2002.